

Acta Naturae

Animal Models of Mitochondrial Diseases
Associated with Nuclear Gene Mutations



**RIPK3 EXPRESSION IN FIBROBLASTS
IN AN *IN VIVO* AND *IN VITRO* SKIN
WOUND MODEL: A CONTROVERSIAL
RESULT**

P. 65

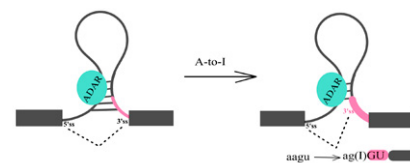
***IN VITRO* ANTIVIRAL ACTIVITY
OF A NEW INDOL-3-CARBOXYLIC
ACID DERIVATIVE AGAINST
SARS-CoV-2**

P. 83

Cooperation and Competition of RNA Secondary Structure and RNA–Protein Interactions in the Regulation of Alternative Splicing

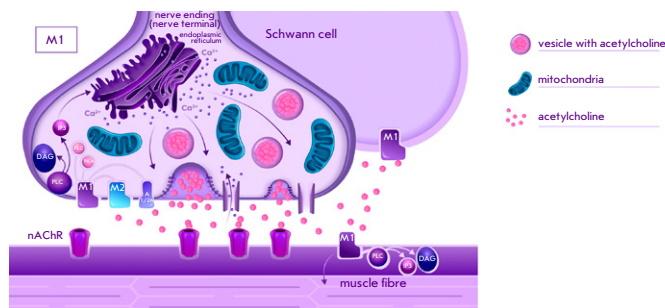
M. A. Vorobeva, D. A. Skvortsov, D. D. Pervouchine

The regulation of alternative splicing in eukaryotic cells is carried out through the coordinated action of a large number of factors, including RNA-binding proteins and RNA structure. The RNA structure influences alternative splicing by blocking *cis*-regulatory elements, or bringing them closer or farther apart. In combination with RNA-binding proteins, it generates transcript conformations that help to achieve the necessary splicing outcome. However, the binding of regulatory proteins depends on RNA structure and, vice versa, the formation of RNA structure depends on the interaction with regulators. Therefore, RNA structure and RNA-binding proteins are inseparable components of common regulatory mechanisms. This review highlights examples of alternative splicing regulation by RNA-binding proteins, the regulation through local and long-range RNA structures, as well as how these elements work together, cooperate, and compete.



The combined effect of RNA secondary structure and RNA-protein interactions

Muscarinic Cholinoreceptors in Skeletal Muscle: Localization and Functional Role



Schematic representation of the localization of M1 subtype muscarinic acetylcholine receptors and the associated signaling pathways in the neuromuscular synapse of vertebrates

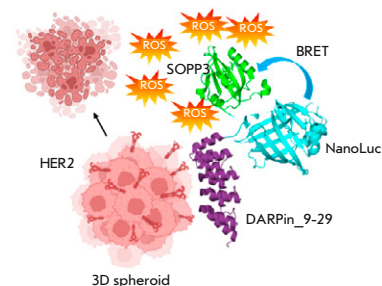
I. V. Kovyazina, A. A. Khamidullina

The review focuses on the modern concepts of the functions of muscarinic cholinoreceptors in skeletal muscles, particularly, in neuromuscular contacts, and that of the signaling pathways associated with the activation of various subtypes of muscarinic receptors in the skeletal muscles of cold-blooded and warm-blooded animals. The review discusses various approaches to the study of the functions of muscarinic receptors in motor synapses, as well as the problems arising when interpreting experimental data. The final part of the review is devoted to an analysis of some of the intracellular mechanisms and signaling pathways that mediate the effects of muscarinic agents on neuromuscular transmission.

System for Self-excited Targeted Photodynamic Therapy Based on the Multimodal Protein DARP-NanoLuc-SOPP3

E. I. Shramova, A. Yu. Frolova, V. P. Filimonova, S. M. Deyev, G. M. Proshkina

This study proposes a fully biocompatible system based on the DARP-NanoLuc-SOPP3 multimodal protein for targeted HER2-specific self-excited photodynamic therapy (PDT). The operating principle of the system relies on bioluminescence resonance energy transfer. This system allows to overcome the problem related to the restricted depth of penetration of exciting light into tissues, as well as the problem of sunlight-induced photodermatoses resulting from aberrant accumulation of chemical photosensitizers in the skin.



System based on multimodal protein DARP-NanoLuc-SOPP3 for targeted BRET-induced PDT

Acta Naturae

OCTOBER–DECEMBER 2023 VOL. 15 № 4 (59)
since april 2009, 4 times a year

Founders

Acta Naturae, Ltd,
National Research University
Higher School of Economics

Editorial Council

Editors-in-Chief: A.G. Gabibov, S.N. Kochetkov

V.V. Vlassov, P.G. Georgiev, M.P. Kirpichnikov,
A.A. Makarov, A.I. Miroshnikov, V.A. Tkachuk,
M.V. Ugryumov

Editorial Board

Managing Editor: V.D. Knorre

K.V. Anokhin (Moscow, Russia)
I. Bezprozvanny (Dallas, Texas, USA)
I.P. Bilenkina (Moscow, Russia)
M. Blackburn (Sheffield, England)
S.M. Deyev (Moscow, Russia)
V.M. Govorun (Moscow, Russia)
O.A. Dontsova (Moscow, Russia)
K. Drauz (Hanau-Wolfgang, Germany)
A. Friboulet (Paris, France)
M. Issagouliants (Stockholm, Sweden)
M. Lukic (Abu Dhabi, United Arab Emirates)
P. Masson (La Tronche, France)
V.O. Popov (Moscow, Russia)
I.A. Tikhonovich (Moscow, Russia)
A. Tramontano (Davis, California, USA)
V.K. Švedas (Moscow, Russia)
J.-R. Wu (Shanghai, China)
N.K. Yankovsky (Moscow, Russia)
M. Zouali (Paris, France)

Project Head: N.V. Soboleva

Editor: N.Yu. Deeva

Designer: K.K. Oparin

Art and Layout: K. Shnaider

Copy Chief: Daniel M. Medjo

Web Content Editor: O.B. Semina

Address: 101000, Moscow, Myasnitskaya Ulitsa, 13, str. 4
Phone/Fax: +7 (495) 727 38 60
E-mail: actanaturae@gmail.com

Reprinting is by permission only.

© ACTA NATURAE, 2023

Номер подписан в печать 30 декабря 2023 г.

Тираж 15 экз. Цена свободная.

Отпечатано в типографии: НИУ ВШЭ,
г. Москва, Измайловское шоссе, 44, стр. 2



*Founder and Chairman
of the Editorial Board (from 2009 to 2023)
of the journal Acta Naturae
Academician Grigoriev Anatoly Ivanovich*

Indexed in PubMed, Web of Science,
Scopus, and RISC

Impact Factor: 2.0 (WOS); 3.5 (Scopus)

CONTENTS

REVIEWS

O. A. Averina, S. A. Kuznetsova, O. A. Permyakov,
P. V. Sergiev

**Animal Models of Mitochondrial Diseases
Associated with Nuclear Gene Mutations 4**

M. A. Vorobeva, D. A. Skvortsov, D. D. Pervouchine
**Cooperation and Competition of RNA Secondary
Structure and RNA–Protein Interactions
in the Regulation of Alternative Splicing 23**

S. A. Golyshev, E. P. Kazakov, I. I. Kireev,
D. G. Reunov, I. V. Malyshev
**Soft X-ray Microscopy in Cell Biology:
Current Status, Contributions and Prospects 32**

CONTENTS

I. V. Kovyazina, A. A. Khamidullina Muscarinic Cholinoreceptors in Skeletal Muscle: Localization and Functional Role	44
E. V. Lapshin, Y. G. Gershovich, A. V. Karabelsky The Potential and Application of iPSCs in Gene and Cell Therapy for Retinopathies and Optic Neuropathies	56

RESEARCH ARTICLES

I. S. Izumov, M. S. Shitova, M. S. Sabirov, S. A. Sheleg, O. L. Cherkashina, E. P. Kalabusheva, E. A. Vorotelyak, E. I. Morgun RIPK3 Expression in Fibroblasts in an <i>in vivo</i> and <i>in vitro</i> Skin Wound Model: A Controversial Result	65
--	----

A. V. Mashkovskaia, S. S. Mariasina, M. V. Serebryakova, M. P. Rubtsova, O. A. Dontsova, P. V. Sergiev Testing a Hypothesis of 12S rRNA Methylation by Putative METTL17 Methyltransferase	75
---	----

A. N. Narovlyansky, M. V. Filimonova, N. G. Tsyshkova, A. V. Pronin, T. V. Grebennikova, E. V. Karamov, V. F. Larichev, G. V. Kornilayeva, I. T. Fedyakina, I. V. Dolzhikova, M. V. Mezentseva, E. I. Isaeva, V. V. Poloskov, L. S. Koval, V. P. Marinchenko, V. I. Surinova, A. S. Filimonov, A. A. Shitova, O. V. Soldatova, A. V. Sanin, I. K. Zubashev, A. V. Ponomarev, V. V. Veselovsky, V. V. Kozlov, A. V. Stepanov, A. V. Khomich, V. S. Kozlov, S. A. Ivanov, P. V. Shegai, A. D. Kaprin, F. I. Ershov, A. L. Gintsburg <i>In Vitro</i> Antiviral Activity of a New Indol-3-carboxylic Acid Derivative Against SARS-CoV-2	83
--	----

A. Yu. Frolova, S. V. Kutyaikov, V. I. Martynov, S. M. Deyev, A. A. Pakhomov BODIPY Dye Derivative for Irreversible Fluorescent Labeling of Eukaryotic Cells and Their Simultaneous Cytometric Analysis	92
--	----

E. I. Shramova, A. Yu. Frolova, V. P. Filimonova, S. M. Deyev, G. M. Proshkina System for Self-excited Targeted Photodynamic Therapy Based on the Multimodal Protein DARP-NanoLuc-SOPP3	100
--	-----

O. K. Gasymov, M. J. Bakhishova, R. B. Aslanov, L. A. Melikova, J. A. Aliyev Membrane Partitioning of TEMPO Discriminates Human Lung Cancer from Neighboring Normal Cells ..	111
---	-----

Guidelines for Authors	121
-------------------------------------	-----



IMAGE ON THE COVER PAGE
(see the article by Averina)

Animal Models of Mitochondrial Diseases Associated with Nuclear Gene Mutations

O. A. Averina^{1,2,3}, S. A. Kuznetsova^{1*}, O. A. Permyakov^{1,3}, P. V. Sergiev^{1,2,3}

¹Institute of Functional Genomics, Lomonosov Moscow State University, Moscow, 119991 Russian Federation

²Belozersky Institute of Physico-Chemical Biology, Lomonosov Moscow State University, Moscow, 119991 Russian Federation

³Department of Chemistry, Lomonosov Moscow State University, Moscow, 119991 Russian Federation

*E-mail: svetlana@belozersky.msu.ru

Received: August 25, 2023; in final form, October 05, 2023

DOI: 10.32607/actanaturae.25442

Copyright © 2023 National Research University Higher School of Economics. This is an open access article distributed under the Creative Commons Attribution License, which permits unrestricted use, distribution, and reproduction in any medium, provided the original work is properly cited.

ABSTRACT Mitochondrial diseases (MDs) associated with nuclear gene mutations are part of a large group of inherited diseases caused by the suppression of energy metabolism. These diseases are of particular interest, because nuclear genes encode not only most of the structural proteins of the oxidative phosphorylation system (OXPHOS), but also all the proteins involved in the OXPHOS protein import from the cytoplasm and their assembly in mitochondria. Defects in any of these proteins can lead to functional impairment of the respiratory chain, including dysfunction of complex I that plays a central role in cellular respiration and oxidative phosphorylation, which is the most common cause of mitopathologies. Mitochondrial diseases are characterized by an early age of onset and a progressive course and affect primarily energy-consuming tissues and organs. The treatment of MDs should be initiated as soon as possible, but the diagnosis of mitopathologies is extremely difficult because of their heterogeneity and overlapping clinical features. The molecular pathogenesis of mitochondrial diseases is investigated using animal models: i.e. animals carrying mutations causing MD symptoms in humans. The use of mutant animal models opens new opportunities in the study of genes encoding mitochondrial proteins, as well as the molecular mechanisms of mitopathology development, which is necessary for improving diagnosis and developing approaches to drug therapy. In this review, we present the most recent information on mitochondrial diseases associated with nuclear gene mutations and animal models developed to investigate them.

KEYWORDS mitochondrial diseases, nDNA, mutations, animal models.

ABBREVIATIONS MD – mitochondrial disease; mtDNA – mitochondrial DNA; nDNA – nuclear DNA; OXPHOS – oxidative phosphorylation; NADH – reduced form of nicotinamide adenine dinucleotide; FGF – fibroblast growth factor.

INTRODUCTION

Mitochondrial diseases (MDs), which are caused by nuclear gene mutations, are a heterogeneous group of inherited diseases affecting all mitochondrial processes. Nuclear DNA (nDNA) encodes not only most of the structural proteins of the oxidative phosphorylation (OXPHOS, approximately 80 proteins) system, but also all the proteins necessary for OXPHOS protein import from the cytoplasm and their assembly in mitochondria. Defects in any of these proteins can lead to functional impairment of the respiratory chain

and, therefrom, the development of MDs. Similar negative effects can also be induced by dysfunction in the proteins that control the stability and/or integrity of mitochondrial DNA (mtDNA). MDs are also caused by some disorders associated with the dysfunction of proteins from other organelles, such as WFS1, in the endoplasmic reticulum, or EIF2S3, in the cytoplasm [1, 2].

nDNA mutations associated with MDs are autosomal-dominant or recessive and can be located on the X chromosome as well. They are found in more

than 300 genes, which accounts for 78.5% of the total number of genes whose mutations are associated with MDs [3, 4].

Oxidative phosphorylation provides energy to most mammalian cells and tissues. The OXPHOS system includes five multisubunit protein complexes comprising more than 80 nDNA-encoded proteins and 13 mtDNA-encoded subunits. Mutations in the individual components of OXPHOS result in a heterogeneous group of inborn errors of metabolism – primary MDs.

The most common cause of MDs is a dysfunction in complex I, the largest OXPHOS enzyme complex, which plays a central role in cellular respiration and oxidative phosphorylation [5]. Complex I deficiency symptoms most often manifest in childhood: approximately 75% of patients do not survive beyond the age of 10 years, and almost 50% of them die before the age of 2 years [6]. The first report of a mutation in an nDNA-encoded complex I subunit, causing Leigh syndrome, happened in 1998 [7]. Leigh syndrome is diagnosed in almost 80% of children with complex I deficiency, and approximately 70% of these are associated with nDNA mutations. Leigh syndrome patients experience encephalopathy, hypotonia, developmental retardation, psychomotor dysfunction, dystonia, seizures, dysphagia, respiratory dysfunction, and early mortality [8]. Complex I (NADH:ubiquinone oxidoreductase) is a 1 MDa L-shaped multiprotein complex comprising 45 different subunits arranged into six modules (N, Q, ND1, ND2, ND4, and ND5) located on hydrophobic and hydrophilic (peripheral) arms. Mutations in 39 different nuclear genes are associated with MDs caused by complex I deficiency. Most nuclear gene mutations associated with MDs are located in the NADH dehydrogenase subunit and hydrophilic arm Q-module genes. Mutations have been found both in the main catalytic subunits (NDUFV1, NDUFV2, NDUFS1, NDUFS2, NDUFS3, NDUFS7, and NDUFS8) and in the subunits responsible for complex I assembly and stability (NDUFS4, NDUFS6, NDUFA2, NDUFA12, NDUFA13, NDUFA1, NDUFA6, NDUFA8, NDUFA9, NDUFA10, NDUFA11, NDUFB3, NDUFB8, NDUFB9, NDUFB10, NDUFB11, and NDUF2), which cumulatively are responsible for NADH:ubiquinone oxidoreductase deficiency. Destabilization of complex I also leads to several additional defects, including changes in the mitochondrial network morphology, membrane potential, and intracellular calcium homeostasis, as well as overproduction of reactive oxygen species. Data on mutations in 13 genes associated with MDs, *NDUFA5*, *NDUFAB1*, *NDUFS5*, *NDUFB4*, *NDUFV3*, *NDUF2*, *NDUFB1*, *NDUFB2*, *NDUFB5*, *NDUFB6*, *NDUFA7*, *ECSIT*, and *NDUFA3* have not yet been obtained and/or reported. However, due to

the increasing application of exome or whole-genome sequencing, new pathological mutations may be identified in the near future [3, 5].

Diagnosis of MD, which includes the assessment of serum lactate, alanine, glucose, and FGF levels, electron microscopic and histochemical analysis of mitochondrial ultrastructure, and evaluation of the enzymatic activity of OXPHOS components, is a complex task. The heterogeneous clinical manifestations of MDs complicate the achievement of a correct diagnosis and choice of an appropriate therapy. Many MD symptoms share the features of other hereditary diseases, such as diabetes mellitus, stroke, or cardiomyopathy [4]. These issues can be addressed by using animal MD models. Mutant animal models may shed light on the mechanisms that underlay MD development and the functions of the genes that encode mitochondrial proteins. Highly conserved mitochondrial proteins offer a wide array of choices of models that can be tapped to study the consequences of mutations in humans.

ANIMAL MODELS OF MITOCHONDRIAL DISEASES

The choice of an animal MD model is always a matter of much debate. No model is inherently “good” or “bad”; the value of a particular model may only be assessed in the context of a specific project. The choice of the species, sex, and genetic properties of a model animal is based on the direction and aims of the research to achieve the most adequate transfer of the results obtained in animals to humans. It is also necessary to evaluate the possibility of using organisms from a lower step on the evolution ladder to obtain representative results without compromising their quality. The choice of a model animal should account for the factors of its availability, ease of manipulation, cost of research, ease of maintenance, and genetic and physiological homology. Genetic divergence between humans and other mammals is about 90 million years. For example, this divergence between humans and model animals such as dwarf pigs (*Porcula salvania*) and sheep (*Ovis aries*) or rabbits (*Oryctolagus cuniculus*) and rats (*Rattus norvegicus*) amounts to 94 and 87 million years, respectively [9]. For this reason, the genomes of all mammals are considered relatively similar. However, it is the laboratory mouse (*Mus musculus*) that has remained the quintessential model animal used to study human genetic MDs for many years. In general, mice and humans have almost the same set of genes. The protein-coding regions of the mouse and human genomes are approximately 85% identical. Almost every gene found in one species is identified as a closely related form in the other; in this case,

some genes are 99% identical, while others are only 60% identical [10].

The first genetic studies in mice were based not on changes in the disease-modeling genotype, but on the disease-resembling phenotypes resulting from random spontaneous mutations or exposure to mutagenic factors. The advent of mouse genome editing techniques has eliminated the need to select the appropriate phenotype after random mutagenesis and enabled the generation of specific mutations in the mouse genome and the investigation of their consequences. Thus, mouse models are extremely important for elucidating the functions of genes and studying the pathological processes associated with mutations in these genes [11].

Mice with altered genomes, which model more than 50% of MDs associated with nuclear gene mutations, have been generated. However, complete inactivation of the gene under study leads to 50% embryonic lethality, although this pathological mutation can cause death at an early age [3–5, 12]. To overcome this obstacle in disease modeling, animals with heterozygous mutations in the gene of interest are examined. While some heterozygous mutants do not display a pathological phenotype, others become model animals; e.g., heterozygous *Risp*^{+/*P224S*} mice exhibit obviously reduced activity of mitochondrial complex III [13], and *Tfam*^{+/-} mice are characterized by mtDNA depletion syndrome (severe decrease in mtDNA content) characteristic of people with a mutation in this gene [14]. Another approach to the investigation of vital genes is the generation of conditional tissue-specific knockouts of these genes. These knockouts have been developed for almost all lethal mutations in the nuclear genes of MDs in the tissues and organs that are most affected by each specific mutation [3–5, 12]. In the case of embryonic lethality, the ideal study object is the eggs of the *Danio rerio* fish and the *Xenopus laevis* amphibian and their fry and tadpoles, respectively [15–17]. These models have recommended themselves well in genome editing studies [18]. At early developmental stages, *D. rerio* and *X. laevis* are translucent, which enables continuous, real-time assessment and monitoring of the development of major internal organs. In this case, *D. rerio* and *X. laevis* develop independently of the parent organism and are available for direct exposure to agents at different embryogenesis stages [19]. In addition, a battery of behavioral tests has been developed to analyze neurodegenerative disorders in these animals [20, 21].

Unfortunately, there are situations when the mouse genome manipulations that should lead to MD development do not reflect the clinical picture associated with the pathological mutation in humans [22]. On the one hand, such results are associated with a high-

er resistance of mice to MDs [23], and on the other, some mutations in humans can manifest themselves in combination with more complex factors, such as lifestyle and concomitant diseases [24]. In these cases, a solution may be to use another animal model. For example, people carrying a mutation in the gene encoding a mitochondrial protein involved in cytochrome *c* oxidase assembly are diagnosed with Leigh syndrome, but constitutive *SURF1*^{-/-} knockout mice do not reproduce the severity of the clinical phenotype in humans. In this case, *SURF1*^{-/-} mutant pigs characterized by failure to thrive, muscle weakness, delayed central nervous system development in newborn piglets, and highly reduced life span become appropriate model animals [25].

It is worth noting the contribution of alternative research objects to the modeling of basic mitochondrial processes and some aspects of human pathologies:

The zebrafish *D. rerio* is considered an optimal alternative to mice. It can be used to model Leigh syndrome, in particular with liver dysfunction, and MDs involving the nervous, immune, and cardiovascular systems. Also, as mentioned above, there exist behavioral tests to assess motor and sensory response impairments typical of clinical MD manifestations [26].

The *Caenorhabditis elegans* nematode and *Drosophila melanogaster* fruit fly, despite their significant divergence from humans (686 million years [9]), have emerged as powerful genetic MD models, with great potential in early high-throughput screening for therapeutic agents [27, 28].

Microorganisms are also used to study MDs. For example, mitochondrial functions in humans and *Saccharomyces cerevisiae* (yeast) are highly similar. Yeast can be used to reproduce pathogenic mutations leading to mitochondrial dysfunction in humans. Yeast is a good alternative model for studying MDs [29] and screening therapeutic agents [30].

Therefore, the generation of reliable animal models enables us to study the functions of mitochondrial protein-encoding genes and the molecular mechanisms of MD development, which is necessary to improve diagnostics and develop approaches to drug therapy.

ANIMAL MODELS OF HUMAN MITOCHONDRIAL DISEASES ASSOCIATED WITH NUCLEAR GENE MUTATIONS (SUMMARY TABLE)

Based on an analysis of publications devoted to various MDs [4, 5] and information gleaned from the periodically updated resources Genomics England PanelApp [3] and Online Mendelian Inheritance in Man [12], we prepared a table that summarizes the most recent data on MDs associated with nuclear

gene mutations. The data are correlated to the corresponding animal models. The table provides information about clinical MD manifestations, the specific nuclear gene mutations that cause certain MDs, inheritance modes, and detailed descriptions of the animal models corresponding to these MDs. This summary table may be useful both for planning and analyzing exploratory and clinical studies and for writing scientific papers and publications.

CONCLUSION

Mitochondrial diseases are some of the most common genetic diseases. They arise at birth or develop throughout life. The genetic mutations that cause these diseases are diverse. So, researchers describing the phenotypic effect of a certain mutation have faced the problem that the mutation consequences can be mapped on a wide range of clinical manifestations. Therefore, researchers face a challenge in describing the phenotypes of mitochondrial muta-

tions and identifying the mechanisms through which certain mutations in mitochondrial protein-coding genes manifest themselves at the level of the organism. This problem may be addressed using modeling of MDs in animals. Manipulations with the genome of model animals, in particular mice, are often able to accurately reproduce the clinical picture of human MDs, providing the opportunity to study the molecular mechanisms of pathological processes, test drugs, predict their efficacy, and select new treatment modalities. ●

Conflict of interest. The authors declare no conflict of interest.

This study was supported by a grant of the Russian Science Foundation No. 17-75-30027 and partially financed from the budget of the Institute of Functional Genomics, Lomonosov Moscow State University.

Animal models of human mitochondrial diseases associated with nuclear gene mutations

Gene	Clinical picture	Inheritance mode
Mitochondrial complex I deficiency		
<i>ACAD9</i> acyl-CoA dehydrogenase family, member 9	<ul style="list-style-type: none"> • hypertrophic cardiomyopathy, • reduced exercise tolerance, • mild beta oxidation deficiency 	Autosomal recessive
<p><i>Acad9</i> knockout mice [31]:</p> <ul style="list-style-type: none"> • complete <i>Acad9</i> inactivation leads to embryonic lethality; • cardiac-specific <i>Acad9</i> knockout is associated with the lack of expression of <i>Acadvl</i> (encodes long-chain acyl-CoA dehydrogenase) and <i>Ecsit</i> (encodes a protein involved in complex I assembly) genes in cardiac tissue; expression of <i>Acadm</i>, encoding medium-chain acyl-CoA dehydrogenase, is reduced; complex I dysfunction; cardiomyopathy with atrial and ventricular thickening is diagnosed by day 14 of life; • muscle tissue-specific <i>Acad9</i> knockout is associated with reduced exercise tolerance and lactic acidosis. 		

REVIEWS

<i>NDUFS1</i> NADH-ubiquinone oxidoreductase Fe-S protein 1	<ul style="list-style-type: none"> • Leigh syndrome • cavitating leukoencephalopathy 	Autosomal recessive
Homozygous <i>Ndufs1</i> knockout in mice is lethal [32].		
<i>NDUFS4</i> NADH-ubiquinone oxidoreductase Fe-S protein 4	<ul style="list-style-type: none"> • combined complex I and III deficiency, • Leigh syndrome, • hypertrophic cardiomyopathy 	Autosomal recessive
<p>Complete <i>Ndufs4</i> knockout mice [33–35]:</p> <ul style="list-style-type: none"> • Leigh-like syndrome, • ataxia, neurological disorders, • developmental delay, • development of blindness by day 21 of life, • early mortality. <p>Tissue-specific <i>Ndufs4</i> knockout targeting neurons and glia [36]:</p> <ul style="list-style-type: none"> • progressive lethal encephalopathy, • reactive glial cell phenotype, neuronal loss, ataxia; • respiratory disturbance. <p>Cardiac-specific <i>Ndufs4</i> knockout [37, 38]:</p> <ul style="list-style-type: none"> • hypertrophic cardiomyopathy. <p><i>Ndufs4</i> point mutation [39]:</p> <ul style="list-style-type: none"> • embryonic lethality of homozygous <i>Ndufs4</i>^{-/-} mice, • reduced activity of complex I in heterozygous mice upon stable activity of complex II. reduced activity of complex I in heterozygous mice upon stable activity of complex II. 		
<i>NDUFS6</i> NADH-ubiquinone oxidoreductase Fe-S protein 6	<ul style="list-style-type: none"> • lactic acidosis with fatal outcome in the neonatal period, • mitochondrial encephalomyopathy, • Leigh syndrome 	Autosomal recessive
<i>Ndufs6</i> knockdown mice [40, 41]:		
<ul style="list-style-type: none"> • cardiomyopathy, systolic dysfunction, • renal disease associated with ultrastructural changes. 		
<i>NDUFV1</i> NADH-ubiquinone oxidoreductase flavo protein 1	<ul style="list-style-type: none"> • mitochondrial encephalomyopathy, • cerebral ataxia, • Leigh syndrome 	Autosomal recessive
Transgenic <i>Caenorhabditis elegans</i> (soil nematode) strain with mutations in the <i>Nuo-1</i> gene, the <i>Ndufv1</i> homolog [42]:		
<ul style="list-style-type: none"> • lactic acidosis, • decreased NADH-dependent mitochondrial respiration, • hypersensitivity to exogenous oxidative stress. 		
<i>NUBPL</i> nucleotide-binding protein-like protein	<ul style="list-style-type: none"> • leukoencephalopathy 	Autosomal recessive
Homozygous <i>Nubp1</i> knockout in mice is lethal [32].		
<i>NDUFAF7</i> NADH dehydrogenase (ubiquinone) complex I, assembly factor 7	<ul style="list-style-type: none"> • pathological myopia 	
<p>Lethality of homozygous <i>Ndufaf7</i> knockout mice [15].</p> <p>Morpholino-mediated <i>Ndufaf7</i> knockdown in <i>D. rerio</i> [15]:</p> <ul style="list-style-type: none"> • delayed hatching time, • morphological abnormalities, • decreased complex I activity. 		
<i>NDUFS7</i> NADH-ubiquinone oxidoreductase Fe-S protein 7	<ul style="list-style-type: none"> • Leigh syndrome 	Autosomal recessive
Homozygous <i>Ndufs7</i> knockout in mice is lethal [32].		
<i>NDUFA1</i> NADH-ubiquinone oxidoreductase subunit a1	<ul style="list-style-type: none"> • Leigh syndrome 	X-linked recessive
<p>Mutant mice with targeted destruction of complex I subunit mRNA, <i>Ndufa1</i> [43]:</p> <ul style="list-style-type: none"> • complex I deficiency, increased levels of reactive oxygen species, • optic nerve and retinal lesions. 		

REVIEWS

<p><i>NDUFA13</i> NADH-ubiquinone oxidoreductase subunit a13 or <i>GRIM19</i> gene associated with retinoid- & interferon-induced mortality 19</p>	<ul style="list-style-type: none"> encephalopathy associated with sensory deprivation, Leigh syndrome, thyroid cancer 	Autosomal recessive
<p>Mutant mice deficient in <i>Grim19</i> [44]:</p> <ul style="list-style-type: none"> <i>Grim19</i>^{-/-} embryos die by day 9.5 of embryonic development, delayed and abnormal development of <i>Grim19</i>^{-/-} blastocysts associated with abnormal mitochondrial structure and defective complex I (<i>GRIM-19</i> physically resides in complex I and is responsible for its assembly), heterozygous <i>Grim19</i>^{+/-} mice lack physiological or phenotypic abnormalities. 		
<p><i>NDUFA8</i> NADH-ubiquinone oxidoreductase subunit a8</p>	<ul style="list-style-type: none"> developmental delay, microcephaly, epilepsy, weight loss and failure to thrive, speech development defects 	Autosomal recessive
<p>Homozygous <i>Ndufa8</i> knockout in mice is lethal [32].</p>		
<p><i>NDUFB11</i> NADH-ubiquinone oxidoreductase 1 beta subcomplex, 11</p>	<ul style="list-style-type: none"> multiple congenital malformations, microphthalmia with linear skin defects (MLS syndrome), embryonic male lethality, lactic acidosis, histiocytoid cardiomyopathy, microphthalmia, skin defects 	X-linked
<p><i>Ndufb11</i> knockdown in <i>Drosophila</i> [45]:</p> <ul style="list-style-type: none"> reduced life span, decreased metabolic rate, complex I assembly defects, increased lactate and pyruvate levels. 		
<p>Mitochondrial electron transport chain defects; OXPHOS disturbance</p>		
<p>UCP2 uncoupling protein 2</p>	<ul style="list-style-type: none"> obesity 	Not found
<p><i>Ucp2</i> knockout mice [46, 47]:</p> <ul style="list-style-type: none"> no obesity, normal response to cold or a high-fat diet, resistant to <i>Toxoplasma gondii</i> infection (forms brain cysts) thanks to an increased level of reactive oxygen species in macrophages, glucose-induced insulin secretion increases, typical of type II diabetes mellitus. <p>Mutant mice with increased <i>Ucp2</i> expression in hypocretin (orexin) neurons [48]:</p> <ul style="list-style-type: none"> these mutant mice have increased temperature of the hypothalamus, which leads to an overall decrease in body temperature by 0.3–0.5°C, these mutants have increased energy efficiency and a longer average life span. <p><i>Ucp1</i> knockout mice [49]:</p> <ul style="list-style-type: none"> sensitive to cold, which indicates impaired thermoregulation, accumulate excess fat in brown adipose tissue, but do not become fat, <i>Ucp1</i> knockout is compensated by <i>Ucp2</i> that is expressed in brown epididymal fat. <p><i>Ucp3</i> knockout mice [50]:</p> <ul style="list-style-type: none"> <i>Ucp3</i> inactivation is associated with <i>Ucp1</i> and <i>Ucp2</i> upregulation in brown adipose tissue, in skeletal muscles, an increased state 3/state 4 ratio due to proton leak, in skeletal muscles, increased production of reactive oxygen species and decreased mitochondrial aconitase. 		
<p>PDHA1 pyruvate dehydrogenase, alpha-1</p>	<ul style="list-style-type: none"> impaired glycolysis–tricarboxylic acid cycle relationship, Leigh syndrome, deficiency of pyruvate dehydrogenase E1-alpha, neurological dysfunction, lactic acidosis, growth retardation, early mortality 	X-linked dominant
<p>Inactivation of the mouse pyruvate dehydrogenase <i>Pdha1</i> gene is embryonic-lethal [51]. <i>D. rerio</i> mutants with visual function defects – no optokinetic response a (noa) – are deficient in dihydrolipoamide-S-acetyltransferase (<i>Dlat</i>), the PDH E2 subunit [16]:</p> <ul style="list-style-type: none"> a phenotype similar to pyruvate dehydrogenase complex deficiency syndrome in humans (neurological dysfunction, lactic acidosis, growth retardation, early death). 		

REVIEWS

<i>PDSS2</i> renyl diphosphate syn- thase, subunit 2	<ul style="list-style-type: none"> defect in ubiquinone (CoQ10) synthesis, encephalomyopathy, tubulopathy, ataxia 	Autosomal recessive
<p>Embryonic lethality of <i>Pdss2</i> knockout mice [52]. Tissue-specific <i>Pdss2</i> knockout targeting glomerular podocytes [52]:</p> <ul style="list-style-type: none"> nephrotic syndrome without changes in the coenzyme Q level in kidney homogenates. <p>Tissue-specific <i>Pdss2</i> knockout targeting hepatocytes [52]:</p> <ul style="list-style-type: none"> coenzyme Q depletion in liver homogenates, mitochondrial respiratory chain dysfunction, disruption of basic metabolic processes. <p>Tissue-specific <i>Pdss2</i> knockout targeting the kidney (<i>Pdss2^{kd/kd}</i>) [53]:</p> <ul style="list-style-type: none"> mitochondrial renal ultrastructural abnormalities, renal CoQ deficiency, decreased respiratory chain activity, increased oxidative stress, development of nephropathy and proteinuria, up to fatal renal failure, cerebellar abnormalities. 		
<i>COQ9</i> coenzyme Q9	Coenzyme Q10 (ubiquinone) deficiency	Autosomal recessive
<p>Mice with a truncating R239X mutation in the <i>Coq9</i> gene [54]:</p> <ul style="list-style-type: none"> impaired mitochondrial respiration with loss of ATP and complex I activity, encephalomyopathy, neuronal death, demyelination, vacuolization, spongiform degeneration, and astrogliosis, cardiac fibrosis, impaired locomotor activity and progressive paralysis, early mortality. 		
<i>CYCS</i> cytochrome C somatic isoform	<ul style="list-style-type: none"> thrombocytopenia 	Autosomal dominant
<p>Cyt <i>c</i> deficiency in mice causes embryonic lethality and attenuates stress-induced apoptosis [55]. Mice expressing mutant cyt <i>c</i> (KA allele) that retains the electron transfer function, but is incapable of Apaf-1 activation [56]:</p> <ul style="list-style-type: none"> exencephaly and hydrocephalus, cachexia, lymphopenia. 		
<i>COQ2</i> coenzyme Q2, polypren- yltransferase	<ul style="list-style-type: none"> encephalomyopathy, tubulopathy, ataxia 	Autosomal recessive
	<ul style="list-style-type: none"> tendency to multiple system atrophy 	Autosomal recessive/ dominant
Homozygous <i>Coq2</i> knockout in mice is lethal [32].		
Mitochondrial complex II deficiency		
<i>SDHD</i> succinate dehydrogenase complex, subunit D, inte- gral membrane protein	<ul style="list-style-type: none"> paraganglioma and gastric stromal sarcoma, pheochromocytoma 	Autosomal recessive/ dominant
Homozygous <i>Sdhd</i> knockout in mice is lethal [57, 58].		
<i>SDHA</i> succinate dehydrogenase complex, subunit A, flavo protein	<ul style="list-style-type: none"> Leigh syndrome, cardiomyopathy 	Autosomal recessive
	<ul style="list-style-type: none"> neurodegeneration and ataxia, optic nerve atrophy, paraganglioma 	Autosomal dominant
Homozygous <i>Sdha</i> knockout in mice is lethal [32].		

REVIEWS

Mitochondrial complex III deficiency		
<p><i>BCS1L</i> BCS1 homolog, ubiquinol-cytochrome c reductase complex chaperone</p>	<ul style="list-style-type: none"> • encephalopathy, • tubulopathy, • liver dysfunction, • Bjornstad syndrome, • GRACILE syndrome 	Autosomal recessive
<p>Mice with a homozygous <i>Bcs1l</i> mutation [59]:</p> <ul style="list-style-type: none"> • mouse model of GRACILE syndrome – neonatal MD involving the liver and kidneys, • growth retardation and short life span, • hepatic glycogen depletion, steatosis, fibrosis, cirrhosis, tubulopathy, • lactic acidosis, • complex III deficiency in the liver, heart, and kidneys. 		
<p><i>UQCRCF1</i> ubiquinol-cytochrome c reductase, rieske iron-sulfur or <i>RISP</i> Rieske iron-sulfur protein</p>	<ul style="list-style-type: none"> • hypertrophic cardiomyopathy, • thrombocytopenia, • hypotonia, • increased serum lactate and alanine levels, • slightly impaired motor skills and reduced muscle strength 	Autosomal recessive
<p>Homozygous <i>Risp</i> mutation is lethal in mice [13]. Heterozygous <i>Risp</i>^{+P224S} mutant mice [13]:</p> <ul style="list-style-type: none"> • reduced complex III activity associated with a decreased level of the iron-sulfur protein RISP, • decreased overall metabolic rate and life span in males, but not females. <p>Conditional knockout (cKO) of the <i>Risp</i> gene in mouse neurons using the Cre-loxP system [60]:</p> <ul style="list-style-type: none"> • short life span, • sudden death with minimal behavioral changes, • weight loss, • cyclic hyperactivity, • decreased performance, • extensive oxidative stress, • neurodegenerative diseases, neuronal death, piriform and somatosensory cortex damage associated with a CIII defect. <p>Mutant mice with <i>Risp</i> inactivation in Treg cells [61]:</p> <ul style="list-style-type: none"> • Treg-specific deficiency of complex III, • early lethal inflammatory disease, • loss of the ability to suppress T cells without changing Treg cells proliferation and survival, • increased DNA methylation. 		
Mitochondrial complex IV deficiency		
<p><i>COX4I2</i> or <i>COX4-2</i> cytochrome C oxidase, subunit 4i2/IV, isoform 2</p>	<ul style="list-style-type: none"> • exocrine pancreatic insufficiency, • dyserythropoietic anemia, • calvarial hyperostosis, • lung-specific Cox4 CIV subunit isoform 	Autosomal recessive
<p>Mutant mice with <i>Cox4I2</i> gene inactivation [62]:</p> <ul style="list-style-type: none"> • pulmonary pathology with inflammation and Charcot-Leyden crystal formation (in sputum in bronchial asthma). 		
<p><i>COX6A2</i> cytochrome C oxidase, subunit 6a2</p>	<ul style="list-style-type: none"> • early hypotonia, • weakness of the facial muscles and limbs, • high palatal vault, • respiratory distress, • cardiomyopathy, • impaired mental development 	Autosomal recessive
<p>Mutant <i>Cox6a2</i>^{-/-} mice [63]:</p> <ul style="list-style-type: none"> • stable, abnormally low weight even upon a high-fat diet due to ineffective energy metabolism, increased energy expenditure, and adaptive thermogenesis, • high Ucp1 and 2 expression levels in the heart and adipose tissue, • increased size of muscle mitochondria, • enhanced glucose tolerance and insulin sensitivity, which is associated with increased phosphorylation and constitutive Ampk activation. 		

REVIEWS

<p>COX10 cytochrome C oxidase assembly factor</p>	<ul style="list-style-type: none"> • mitocomplex IV deficiency, • ataxia, • acidosis, • hypoglycemia, • hypotonia, • mitochondrial encephalopathy, • muscle weakness, • droopy upper eyelid, • pyramidal syndrome, • proximal tubulopathy, • epileptic clouded state, • cardiomyopathy, • hypotrophy, • lactic acidosis, • Leigh syndrome 	<p>Autosomal recessive</p>
<p>Mice with muscle tissue-specific <i>Cox10</i> gene inactivation [64]:</p> <ul style="list-style-type: none"> • regressive myopathy and weakness, • early death, • progressive decrease in COX activity and increase in SDH activity in muscles, • neuromuscular pathology, histologically proven signs of torn red fibers, • abnormal mitochondria. <p>Mice with neuronal tissue-specific <i>Cox10</i> gene inactivation [65]:</p> <ul style="list-style-type: none"> • decreased COX activity in the cerebral cortex and hippocampus, • early mortality, • decreased size and density of forebrain cells, • behavioral defects. <p>Mice with liver tissue-specific <i>Cox10</i> gene inactivation [66]:</p> <ul style="list-style-type: none"> • early mortality, • mitochondrial hepatopathy, • reduced body weight and general activity, • severe liver dysfunction, • decreased COX activity and increased SDH activity, • increased mitochondrial proliferation and decreased ATP levels, • lipid accumulation and glycogen depletion. <p>A conditional <i>Cox10</i> knockout is characterized by dysfunction of oligodendrocytes and Schwann cells to form COX [67]:</p> <ul style="list-style-type: none"> • severe neuropathy with demyelination, abnormal Remak bundles in the peripheral nervous system, • muscle atrophy, palsy, • impaired mitochondrial respiration. 		
<p>SURF1 surfeit 1</p>	<p>Leigh syndrome, Charcot–Marie–Tooth amyotrophy</p>	<p>Autosomal recessive</p>
<p>Mice with inactivation of the <i>Surf1</i> gene encoding the complex IV (COX) assembly factor. <i>Neo</i>^{-/-} mutants (replacement of exons 5–7 by a neomycin-resistance cassette) [68]:</p> <ul style="list-style-type: none"> • 90% embryonic lethality (presumably not due to Surf1 inactivation, but due to the neo cassette or deletions of regulatory elements), • reduced life span, • decreased motor activity, coordination, muscle strength, and endurance without obvious brain morphology abnormalities or neurological symptoms, • suppressed fertility in both sexes, • histochemical analysis of the skeletal muscles and liver revealed decreased COX activity and increased SDH activity, • a drop in COX activity to 23–40% of normal values in various tissues. <p><i>Surf1loxP</i>^{-/-} mutants (insertion of the loxP sequence into exon 7 generating a stop codon at position 225 and elimination of 81 C-terminal amino acids) [69]:</p> <ul style="list-style-type: none"> • no embryonic lethality, • increased life span, • histochemical analysis of skeletal muscles revealed decreased COX activity and increased SDH activity, • reduction in COX activity by 50–70% in various tissues, • there are no neurological defects, but there is resistance to Ca²⁺-mediated damage to isolated neurons and the whole brain, • mitochondria retain normal morphology and membrane potential. <p><i>SURF1</i>^{-/-} mutant pigs[25]:</p> <ul style="list-style-type: none"> • overall developmental delay, • delay in central nervous system development in newborns, • muscle weakness, • short life span, • cytochrome c-oxidase deficiency in the jejunum villi (histochemical analysis). 		

REVIEWS

SCO2 SCO cytochrome C oxidase assembly protein 2	<ul style="list-style-type: none"> Leigh syndrome, hypertrophic cardiomyopathy, neuropathy 	Autosomal recessive
	<ul style="list-style-type: none"> myopia 	Autosomal dominant
<p>The <i>Sco2</i>^{-/-} knockout mouse model is embryonic-lethal [70]. Homozygous mice with an insertion in the <i>Sco2</i> gene or a mutation in the compound heterozygous state are viable and exhibit respiratory chain failure, defects in complex IV assembly, decreased mitochondrial copper content, and overall muscle weakness [70].</p>		
COX15 cytochrome C oxidase assembly factor	<ul style="list-style-type: none"> Leigh syndrome, hypertrophic cardiomyopathy 	Autosomal recessive
<p>Homozygous <i>Coα15</i>^{-/-} knockout mice are embryonic-lethal [71]. Mice with a skeletal muscle tissue-specific mutation develop severe myopathy [71].</p>		
<p>Mitochondrial complex V (ATP synthase) deficiency</p>		
<p>ATP synthase defects are most often associated with mtDNA mutations. Regarding nuclear gene mutations, there are five genes associated with human MDs. Three of them – <i>ATP5A1</i>, <i>ATP5D</i>, and <i>ATP5E</i> – encode structural α-, δ-, and ε-subunits of the enzyme, respectively, and the other two, <i>ATPAF2</i> and <i>TMEM70</i>, encode specific auxiliary factors that facilitate ATP synthase biogenesis. All of these defects have a similar phenotype that is characterized by a pronounced generalized decrease in the ATP synthase complex level:</p> <ul style="list-style-type: none"> neonatal hypotension, lactic acidosis, hyperammonemia, hypertrophic cardiomyopathy, 3-methylglutaconic aciduria. <p>Mutations in the <i>ATP5A1</i>, <i>ATP5D</i>, <i>ATP5E</i>, and <i>ATPAF2</i> genes are very rare, and animal models with these mutations are mostly lethal. In contrast, <i>TMEM70</i> gene mutations are the most common cause of ATP synthase deficiency.</p>		
TMEM70 transmembrane protein 70	<ul style="list-style-type: none"> encephalopathy, facial dysmorphism, hypertrophic cardiomyopathy, lactic acidosis 	Autosomal recessive
<p><i>Tmem70</i>^{-/-} homozygous knockout mice [72]:</p> <ul style="list-style-type: none"> embryonic-lethality, embryos are characterized by delayed cardiovascular system development and impairment of the myocardial mitochondrial ultrastructure with an irregular crista structure. <p><i>Tmem70</i>^{+/-} heterozygous knockout mice [72]:</p> <ul style="list-style-type: none"> viable, normal postnatal growth and development of the mitochondrial OXPHOS system, mild deterioration in cardiac function. <p><i>Tmem70</i> knockout rats generated using the SHR strain genetic background and under the control of the universal EF-1α promoter [73]:</p> <ul style="list-style-type: none"> viable model, genetic complementation restored <i>Tmem70</i> expression in various tissues, to complete restore the physiological function of mitochondria biochemical complement of ATP synthase biogenesis in the liver, 20% of the <i>TMEM70</i> protein and single-allelic <i>Tmem70</i> are sufficient, and in the heart at least 40% of <i>TMEM70</i> and both transgenic alleles. 		
<p>Depletion (decrease in content) of mtDNA</p>		
TYMP thymidine phosphorylase	<ul style="list-style-type: none"> mtDNA depletion syndrome, mitochondrial neurogastrointestinal encephalomyopathy 	Autosomal recessive
<p><i>Upp1/Tymp</i> double knockout mice [74, 75]:</p> <ul style="list-style-type: none"> critical <i>Tymp</i> deficiency, increased thymidine and deoxyuridine levels in tissues, high levels of mitochondrial deoxythymidine triphosphate, partial mtDNA depletion, respiratory chain complex deficiency, and encephalopathy, intense brain damage due to increased plasma pyrimidine levels and subsequent axonal swelling. 		

REVIEWS

<i>ANT1</i> adenine nucleotide trans-locator 1	• mtDNA depletion syndrome	Autosomal dominant/recessive
	• hypertrophic cardiomyopathy, • hypotonia	Autosomal recessive
	• progressive external ophthalmoplegia	Autosomal dominant
<p><i>Ant1</i> gene inactivation in mice [76, 77]:</p> <ul style="list-style-type: none"> • mitochondrial myopathy, hypertrophic cardiomyopathy, metabolic acidosis, • mitochondrial proliferation in the skeletal muscles and heart, • inhibition of complexes I, III, and IV of the mitochondrial respiratory chain, oxidative stress in muscle and heart tissues, • accumulation of multiple mtDNA deletions, mtDNA destabilization. <p><i>Ant4</i> gene inactivation in mice [78]:</p> <ul style="list-style-type: none"> • spermatogenesis defect, male infertility. <p>Simultaneous <i>Ant1</i> and <i>Ant2</i> inactivation in the mouse liver [79]:</p> <ul style="list-style-type: none"> • complex IV activity and COI and cytochrome <i>c</i> levels are increased to compensate for OXPHOS ATP deficiency, • Ca²⁺ excess is required for mtPTP activation, and pores cannot be regulated by Ant ligands, including adenine nucleotides, • hepatocytes are able to respond to induction of cell death, • liver mitochondria exhibit an increase in the respiration rate and no response to ADP addition and an increase in the membrane potential. 		
<i>TWINK</i> twinkle mtDNA helicase	• mtDNA depletion (sharp decrease in content) syndrome, • Alpers syndrome/progressive infantile poliiodystrophy, • Perrault syndrome (a type of female hypogonadism), • infantile spinocerebellar ataxia	Autosomal recessive
	• progressive external ophthalmoplegia	Autosomal dominant
<p>Mutant mice with Twinkle overexpression [80]:</p> <ul style="list-style-type: none"> • abnormal increase in the mtDNA copy number in the muscles and heart. <p>Mice with a PEO-associated mutation, carrying a substitution of threonine for alanine at position 360 of the mouse Twinkle protein (Twinkle^{AT}) [81]:</p> <ul style="list-style-type: none"> • mild myopathy phenotype. <p>Deleter mice with a PEO-associated mutation, carrying an in-frame duplication of amino acids 353–365 (Twinkle^{dup}) [81, 82]:</p> <ul style="list-style-type: none"> • mitochondrial myopathy; the myofibrillar structure is replaced by large mitochondria with concentric cristae and proliferation, • mitochondrial proliferation in cerebellar Purkinje cells, hippocampal pyramidal neurons, and neurons of the indusium griseum (a gray matter layer covering the superior surface of the corpus callosum), • reduced mtDNA levels in the brain (but not in the muscles and heart), • lipid metabolism disorders, • gene expression profiles in skeletal muscle with mitochondrial myopathy revealed induction of several transcripts involved in the response to amino acid and lipid starvation and activation of the Akt and fibroblast growth factor-21 (starvation hormone) signaling. 		
<i>POLG</i> polymerase, DNA, gamma	• progressive external ophthalmoplegia, • SANDO syndrome – a systemic disease characterized by ataxia, balance disturbance, and nerve disorders, such as sensory ataxia, neuropathy, dysarthria, and ophthalmoparesis, • parkinsonism	Autosomal dominant/recessive
	• mtDNA depletion (sharp decrease in content) syndrome, • Alpers syndrome/progressive infantile poliiodystrophy, • mitochondrial neurogastrointestinal encephalomyopathy	Autosomal recessive
<p>D257A (proofreading-deficient PolgA) mice [83–88]:</p> <ul style="list-style-type: none"> • increased levels of mtDNA point and somatic mutations, induction of apoptotic markers, • reduced life span, decreased subcutaneous fat, alopecia, kyphosis, osteoporosis, anemia, decreased fertility, enlarged heart, anemia, loss of intestinal crypt cells, weight, and hearing, sarcopenia, • PolgA deficiency in mouse embryos causes early developmental arrest. 		

REVIEWS

<i>TK2</i> thymidine kinase, mitochondrial	<ul style="list-style-type: none"> • myopathy, • mtDNA depletion (sharp decrease in content) syndrome, • progressive external ophthalmoplegia 	Autosomal recessive
<p><i>Tk2</i>^{-/-} with a his126-to-asn (H126N) mutation in the <i>Tk2</i> gene [89, 90]:</p> <ul style="list-style-type: none"> • growth retardation, decreased activity, generalized gross tremor, and gait disturbance, • mortality at 2 weeks of age, • mtDNA depletion, most remarkable in the brain, • decreased activity of mitochondrial respiratory chain enzymes, ATP levels, and ATP/ADP ratio in the brain, • degeneration and dysfunction of certain types of neurons, • abnormal vacuolar changes in spinal cord neurons, • activated glial cells in the spinal white matter and cerebral cortex, <p>rapidly progressive encephalomyelopathy.</p>		
<i>DGUOK</i> deoxyguanosine kinase	<ul style="list-style-type: none"> • mtDNA depletion (sharp decrease in content) syndrome, • Alpers syndrome/progressive infantile poliodystrophy, • non-cirrhotic portal hypertension/Banti's syndrome, • progressive external ophthalmoplegia 	Autosomal recessive
<p><i>Dguok</i>^{-/-} mutant mice [91]:</p> <ul style="list-style-type: none"> • weight loss, reduced adipose tissue, • mtDNA deficiency in the liver, brain, heart, and skeletal muscles, • lipofuscin accumulation in liver tissues and increased oxidative stress, • increased catabolic lipid metabolism, • increased relative weight of the liver, kidneys, and heart, • abnormal fur pigmentation (lightening). 		
<i>MPV17</i> mitochondrial inner membrane protein	<ul style="list-style-type: none"> • mtDNA depletion (sharp decrease in content) syndrome, • Alpers syndrome/progressive infantile poliodystrophy, • peroneal muscular atrophy (Charcot–Marie–Tooth disease) 	Autosomal recessive
<p><i>Mpv17</i>^{-/-} mutant mice [92]:</p> <p>mtDNA depletion in the liver associated with an increased transcription rate, mtDNA depletion in skeletal muscles, moderate decrease in the enzymatic activity of the mitochondrial respiratory chain and mild changes in cytoarchitecture in the liver, abnormal fur pigmentation (lightening), cochlear sensory epithelium degeneration, focal segmental glomerulosclerosis with massive proteinuria, short life span.</p>		

REVIEWS

<p>TFAM mitochondrial transcription factor A</p>	<ul style="list-style-type: none"> • mtDNA depletion (sharp decrease in content) syndrome 	<p>Autosomal recessive</p>
<p>Homozygous <i>Tfam</i>^{-/-} mice [14]:</p> <ul style="list-style-type: none"> • embryonically lethal depletion of mtDNA. <p>Heterozygous <i>Tfam</i>^{+/-} mice [14]:</p> <ul style="list-style-type: none"> • reduced mtDNA copy number and mitochondrial respiratory chain activity in the heart. <p>Heart and muscle tissue-specific <i>Tfam</i> knockout [93]:</p> <ul style="list-style-type: none"> • early mortality associated with mosaic cardiac-specific progressive respiratory chain deficiency, dilated cardiomyopathy, and atrioventricular blockage, • depletion of mtDNA and <i>Tfam</i> protein, complex I and IV deficiency in the heart and muscles. <p>Skeletal muscle tissue-specific <i>Tfam</i> knockout in mice [94, 95]:</p> <ul style="list-style-type: none"> • progressive myopathy, decreased muscle strength associated with increased levels of mitochondrial Ca²⁺ and decreased release of Ca²⁺ from the sarcoplasmic reticulum, • enlarged mitochondria with deformed cristae, • decreased mtDNA and mitochondrial transcript levels, respiratory chain function, and ATP production. <p>Midbrain dopamine neuron-specific <i>Tfam</i> knockout in mice (MitoPark) [96]:</p> <ul style="list-style-type: none"> • parkinsonian-like phenotype with behavioral disturbances, loss of dopamine neurons, and the presence of Lewy bodies, • decreased mtDNA expression and respiratory chain deficiency in midbrain dopamine neurons. <p>T cell-specific <i>Tfam</i> knockout in mice [97]:</p> <ul style="list-style-type: none"> • premature signs of aging, including metabolic, cognitive, physical, and cardiovascular changes, • a cytokine storm was an inducer of senescence, • early mortality. <p>Pancreatic β-cell tissue-specific <i>Tfam</i> knockout in mice [98]:</p> <ul style="list-style-type: none"> • mitochondrial diabetes, • elevated glucose levels, a gradual decrease in the β-cell mass and pancreatic endo/exocrine tissue ratio, • mutant β-cells exhibit reduced COX activity, normal SDH activity, and abnormally large mitochondria. <p>Neocortical neuron-specific <i>Tfam</i> knockout in mice [99]:</p> <ul style="list-style-type: none"> • mouse model of mitochondrial neurodegeneration (MILON) with late onset (around 4–6 months), • reduced respiratory chain activity and mtDNA and mtRNA levels in neurons, • increased vulnerability to excitotoxic stress, • short life span at the final stage, progressive neurodegeneration, and massive cell death in the hippocampus and neocortex. <p>P1 artificial chromosome (PAC) mutant mice expressing human TFAM in the setting of stable expression of mouse TFAM [100]:</p> <ul style="list-style-type: none"> • net TFAM overexpression, • increased mtDNA copy number upon normal respiratory chain capacity and total mitochondrial mass, • combination of mice with TFAM overexpression and TFAM knockout demonstrated that the mtDNA copy number is directly proportional to the total TFAM protein levels. 		
<p>Iron metabolism disorders</p>		
<p><i>ABCB7</i> ATP-binding cassette, subfamily b, member 7</p>	<ul style="list-style-type: none"> • sideroblastic anemia with ataxia 	<p>X-linked recessive</p>
<ul style="list-style-type: none"> • the lethality of a complete <i>Abcb7</i> knockout is associated with a defect in the extra-embryonic visceral endoderm that predominantly contains the X-chromosome as an active allele [101], • X-inactivations and tissue-specific deletions revealed that <i>Abcb7</i> is essential for the development of all tissues except hepatocytes and endothelial cells [101], • loss of <i>Abcb7</i> in the liver caused mild mitochondrial damage, impaired cytosolic Fe-S cluster assembly, and altered iron sensing, but was not fatal [101]. 		

REVIEWS

<i>FXN</i> frataxin or <i>FRDA</i>	<ul style="list-style-type: none"> • Friedreich ataxia 	Autosomal recessive
<p>Mutant mice with a <i>Frda</i> exon 4 deletion [102]:</p> <ul style="list-style-type: none"> • homozygous <i>Frda</i>^{-/-} model is embryonic-lethal, • embryonic mortality is not associated with abnormal iron accumulation. <p>A viable line of tissue-specific frataxin deficient mice was generated by breeding of conditional <i>Frda</i> allele homozygotes and <i>Frda</i> exon 4 deletion heterozygotes supplemented with the <i>Cre/Lox</i> excision system under the control of the muscle creatine kinase promoter (MCK mutant mouse line) or neuron-specific enolase (NSE mutant mouse line) [103, 104]:</p> <ul style="list-style-type: none"> • NSE mutants had no obvious signs of pathology, and post-mortem studies revealed no iron deposits, • early deficiency of complexes I–III and aconitase activity in the hearts of mutant MCK mice (day 7 of life), • MCK mutant mice develop gradual mitochondrial degeneration from 4 weeks of age, • lipid and protein oxidation levels in the hearts of MCK mutant mice decrease from 7 weeks of age, • intramitochondrial iron deposits in MCK mutant mice form at the terminal stage (10–12 weeks of life) after inactivation of Fe/S enzymes (4 weeks of life) and the development of cardiac dilatation, with left ventricular hypertrophy (5 weeks of life). <p>Tissue-specific <i>Frda</i> knockout in mouse hepatocytes [105]:</p> <ul style="list-style-type: none"> • high level of oxidative stress in the liver, • impaired mitochondrial respiration, decreased ATP levels and Fe/S enzyme activity, • reduced OXPHOS, • multiple liver tumors, • decreased life span. <p>Double heterozygous mutants generated by breeding of mice with a GAA repeat insertion in the <i>Frda</i> gene (in humans, intronic expansion of GAA triplets in the <i>FXN</i> gene causes frataxin deficiency and, as a consequence, Friedreich ataxia) and mice with a frataxin gene knockout [106–108]:</p> <ul style="list-style-type: none"> • GAA repeat length controls the age of onset of somatic instability and the mutation rate and magnitude, • <i>Frda</i>^{-/230GAA} mice are viable and do not exhibit a pronounced pathological phenotype, • this model demonstrates that dysregulation of the peroxisome proliferator-activated receptor gamma (PPARγ) pathway underlies the increased lipogenesis in skeletal muscle and changes in cardiac fiber composition, which are consistent with insulin resistance and cardiomyopathy. <p><i>Drosophila</i> with inactivation of the <i>Dfh</i> gene, a homologue of frataxin [109, 110]:</p> <ul style="list-style-type: none"> • prolonged larval stage and reduced life span of adult animals, • increased size of larvae, • impaired expression of ferritin only in adults, • H₂O₂ is an important pathological substrate underlying the phenotypes resulting from frataxin deficiency in <i>Drosophila</i>. 		
Mutations in nuclear antioxidant defense genes		
<i>SOD1</i> superoxide dismutase 1	<ul style="list-style-type: none"> • amyotrophic lateral sclerosis, • spastic tetraplegia, • axial hypotonia 	Autosomal recessive/ dominant
<p>Mutant mice overexpressing <i>Sod1</i> are a basic model of amyotrophic lateral sclerosis. There are several transgenic mouse strains with different forms of <i>Sod1</i> mutations overexpressed at different levels. Mice with the SOD1G93A mutation are the most commonly used model of amyotrophic lateral sclerosis [111–113].</p> <p>Mice with Cu/ZnSOD deficiency and a <i>Sod1</i> knockout [114, 115]:</p> <ul style="list-style-type: none"> • increased amounts of mitochondria and lipofuscin granules in hepatocytes, • widespread oxidative damage, • hepatocarcinogenesis, • retinal dysfunction, • short life span. 		

REVIEWS

<i>SOD2</i> superoxide dismutase 2	<ul style="list-style-type: none"> • microangiopathy in diabetes mellitus 	Not determined
<p>Mice with MnSOD deficiency, <i>Sod2</i> knockout, generated on the genetic background of a C57BL6/J2 inbred line [116]:</p> <ul style="list-style-type: none"> • severe anemia, neuronal degeneration in the basal ganglia and brain stem, • progressive motor disorders associated with weakness, fatigue, and rotational behavior, • extensive mitochondrial damage in degenerating neurons and cardiac myocytes, • increased susceptibility to oxidative mitochondrial damage. <p>Mice with MnSOD deficiency, <i>Sod2</i> knockout, generated on the genetic background of a CD1 outbred line [117, 118]:</p> <ul style="list-style-type: none"> • short life span, • dilated cardiomyopathy, • accumulation of lipids in the liver and skeletal muscles, • metabolic acidosis, • iron-sulfur center, aconitase, citrate synthase, and complex II and I deficiency in the heart and brain, • accumulation of oxidative DNA damages, • organic aciduria. <p>Heterozygous <i>Sod2</i>^{+/-} mice [119]:</p> <ul style="list-style-type: none"> • model of the free radical aging theory – chronic oxidative damage to tissues and cells, • chronic oxidative damage to lipids of the inner mitomembrane in middle-aged mice increases proton output, • middle-aged and elderly mice have highly sensitized mtPTP, which is associated with a threefold increase in apoptotic hepatocytes, • decreased mitochondrial function accompanied by an increased activity of respiratory chain enzymes. 		
<i>GPX1</i> glutathione peroxidase 1	<ul style="list-style-type: none"> • hemolytic anemia due to glutathione peroxidase deficiency 	Autosomal recessive
<p>Inactivation of the <i>GPx1</i> gene in mice revealed [120–122]:</p> <ul style="list-style-type: none"> • GPx1 is highly expressed in the liver, brain, and renal cortex, but very weakly in the heart and skeletal muscle, • Gpx1 plays a critical role in oxidative stress protection and antioxidant defense mechanisms, • <i>GPx1</i>^{-/-} mice are viable, but they have reduced body weight and chronic growth retardation, • <i>GPx1</i>^{-/-} mitochondria release 4-fold more H₂O₂ in the liver, but not in the heart, which is presumably due to catalase in cardiac mitochondria. <p>Overexpression of <i>GPx1</i> in the heart of myocardial infarction model mice (left coronary artery ligation) resulted in better indicators and survival compared with those in wild-type mice [123].</p>		
Mutations in nuclear genes of mitochondrial dynamics		
<i>MFN2</i> mitofusin 2	<ul style="list-style-type: none"> • axonal Charcot–Marie–Tooth disease 	Autosomal dominant/recessive
	<ul style="list-style-type: none"> • hereditary motor sensory neuropathy 	Autosomal dominant
<p>Cerebellar tissue-specific inactivation of the <i>Mfn2</i> gene in mice [124, 125]:</p> <ul style="list-style-type: none"> • model of neurodegeneration caused by loss of mitochondrial fusion, • 50% mortality in litter; destruction of the giant cell layer of the placental trophoblast in embryos; fragmented mitochondria in embryonic fibroblasts, • <i>Mfn2</i>^{-/-} Purkinje cells have abnormal morphology, short, thin, and less branched dendritic trees with a reduced number of spines; and changes in the morphology, ultrastructure, and distribution of mitochondria with decreased activity of complexes I and IV and increased activity of complex II, • survived mice possess 75% cerebellar atrophy due to a decreased number and quality of Purkinje cells; dystaxia. <p>Tissue-specific inactivation of the <i>Mfn2</i> gene in peripheral motor neurons [126]:</p> <ul style="list-style-type: none"> • homozygous animals lack the ability to flex their hind legs with atrophy of the anterior calf muscles; shortened, deformed tails with bends and thickenings; • <i>Mfn2</i>^{-/-} motor axons are less numerous and have mitochondrial distribution abnormalities (formation of dense clusters). 		

REVIEWS

<p><i>OPA1</i> OPA1 mitochondrial dynamin-like GTPase</p>	<ul style="list-style-type: none"> • optic nerve atrophy 	Autosomal dominant
	<ul style="list-style-type: none"> • Behr syndrome, • mtDNA depletion syndrome 	Autosomal recessive
	<ul style="list-style-type: none"> • tendency to develop glaucoma 	Not determined
<p>Mice with a mutation in the <i>Opa1</i> gene encoding nuclear dynamin-related GTPase occurring in mitochondria [127, 128]:</p> <ul style="list-style-type: none"> • 50% decrease in the <i>Opa1</i> protein level, • homozygous mutation is embryonic-lethal, • heterozygous animals exhibit age-related degeneration of retinal ganglion cells and decreased visual function, • the number of axons in <i>Opa1</i>^{+/-} optic nerves is reduced; the remaining axons have an abnormal shape, irregular myelination, decreased number of neurofibrils, and morphologically abnormal mitochondria with disorganized cristae, • morphological changes in <i>Opa1</i>^{+/-} fibroblasts, increased mitochondrial fission and fragmentation. 		
<p>Defects in mitochondrial and peroxisomal fission</p>		
<p><i>DNM1L</i> dynamin 1-like</p>	<ul style="list-style-type: none"> • encephalopathy, • microcephaly, • optic nerve atrophy, • lactic acidosis 	Autosomal dominant/recessive
<p>Homozygous <i>Drp1</i> knockout in mice is lethal [129]:</p> <ul style="list-style-type: none"> • <i>Drp1</i>^{-/-} embryos exhibit impaired heart and liver development, depletion of the neural tube cell layer, and enlarged mitochondria, • asymmetric cytokinesis in <i>Drp1</i>^{-/-} fibroblasts, • neuronal cells are highly sensitive to Ca²⁺-dependent apoptosis. <p>Mice with a neural cell-specific <i>Drp1</i> deletion (<i>NS-Drp1</i>^{-/-}) [129]:</p> <ul style="list-style-type: none"> • infant mortality due to hypoplasia and apoptosis of the brain, • analysis of primary <i>NS-Drp1</i>^{-/-} forebrain culture revealed that aggregated mitochondria were not properly distributed in nerve cell processes, • neuronal cells are highly sensitive to Ca²⁺-dependent apoptosis. <p>Heterozygous <i>Dnm1l</i> knockdown in mice causes elongation of the mitochondrial network of retinal ganglion cells, but not axonal degeneration in the optic nerve [130].</p>		
<p>Mitochondrial enzyme cofactor deficiency</p>		
<p><i>SLC19A2</i> solute carrier family 19 (thiamine transporter), member 2</p>	<ul style="list-style-type: none"> • thiamine (vitamin B1)-responsive megaloblastic anemia (TRMA) 	Autosomal recessive
<p>Mutant mice with inactivation of the <i>Slc19a2</i> gene encoding the high-affinity thiamine transporter Thtr-1 [131, 132]:</p> <ul style="list-style-type: none"> • lack of a high-affinity component of thiamine transport, • diabetes mellitus with decreased insulin secretion and increased response to insulin, • sensorineural deafness, loss of inner hair cells in the cochlea, • abnormal bone marrow with megaloblastosis. 		

REFERENCES

1. Dogan S.A., Trifunovic A. // *Physiol. Res.* 2011. V. 60. № SUPPL. 1.
2. Mayr J.A., Haack T.B., Freisinger P., Karall D., Makowski C., Koch J., Feichtinger R.G., Zimmermann F.A., Rolinski B., Ahting U., et al. // *J. Inherit. Metab. Dis.* 2015. V. 38. № 4. P. 629–640.
3. Martin A.R., Williams E., Foulger R.E., Leigh S., Daugherty L.C., Niblock O., Leong I.U.S., Smith K.R., Gerasimenko O., Haraldsdottir E., et al. // *Nat. Genet.* 2019. V. 51. № 11. P. 1560–1565.
4. Rambani V., Hromnikova D., Gasperikova D., Skopkova M. // *Endocr. Regul.* 2022. V. 56. № 3. P. 232–248.
5. Fernandez-Vizarra E., Zeviani M. // *FEBS Lett.* 2021. V. 595. № 8. P. 1062–1106.
6. Koene S., Rodenburg R.J., van der Knaap M.S., Willemsen M.A.A.P., Sperl W., Laugel V., Ostergaard E., Tarnopolsky M., Martin M.A., Nesbitt V., et al. // *J. Inherit. Metab. Dis.* 2012. V. 35. № 5. P. 737–747.
7. Loeffen J., Smeitink J.A.M., Triepels R., Smeets R., Schuelke M., Sengers R., Trijbels F., Hamel B., Mullaart R., van den Heuvel L. // *Am. J. Hum. Genet.* 1998. V. 63. № 6. P. 1598–1608.
8. Chang X., Wu Y., Zhou J., Meng H., Zhang W., Guo J. // *Medicine.* 2020. V. 99. № 5. P. e18634.
9. Kumar S., Suleski M., Craig J.M., Kasprovicz A.E., Sand-erford M., Li M., Stecher G., Hedges S.B. // *Mol. Biol.* 2022. V. 39. № 8. P. 1–6.
10. Law M., Shaw D.R. // *Methods Mol. Biol.* 2018. V. 1757. P. 141–161.
11. Gurumurthy C.B., Kent Lloyd K.C. // *DMM Disease Models and Mechanisms.* 2019. V. 12. № 1. P. dmm029462
12. Amberger J.S., Bocchini C.A., Scott A.F., Hamosh A. // *Nucl. Acids Res.* 2019. V. 47. № D1. P. D1038–D1043.
13. Hughes B.G., Hekimi S. // *PLoS One.* 2011. V. 6. № 10. P. e26116.
14. Larsson N.G., Wang J., Wilhelmsson H., Oldfors A., Rustin P., Lewandoski M., Barsh G.S., Clayton D.A. // *Nat. Genet.* 1998. V. 18. № 3. P. 231–236.
15. Zurita Rendón O., Silva Neiva L., Sasarman F., Shoubridge E.A. // *Hum. Mol. Genet.* 2014. V. 23. № 19. P. 5159–5170.
16. Taylor M.R., Hurley J.B., van Epps H.A., Brockerhoff S.E. // *Proc. Natl. Acad. Sci. USA.* 2004. V. 101. № 13. P. 4584–4589.
17. Nenni M.J., Fisher M.E., James-Zorn C., Pells T.J., Ponfer-rada V., Chu S., Fortriede J.D., Burns K.A., Wang Y., Lotay V.S., et al. // *Front. Physiol.* 2019. V. 10. № 26. P. 154.
18. Naert T., Vleminckx K. // *Drug. Discov. Today Technol.* England. 2018. V. 28. P. 41–52.
19. Menegola E., Battistoni M., Metruccio F., Di Renzo F. // *Curr. Opin. Toxicol.* 2023. V. 34. P. 100387.
20. Zeng S.L., Sudlow L.C., Berezin M.Y. // *Expert. Opin. Drug Discov.* 2020. V. 15. № 1. P. 39–52.
21. Langova V., Vales K., Horka P., Horacek J. // *Front. Psy-chiatry.* 2020. V. 11. P. 1–22.
22. Ruzzenente B., Rötig A., Metodiev M.D. // *Hum. Mol. Genet.* 2016. V. 25. № R2. P. R115–R122.
23. Wallace D.C. // *Am. J. Med. Genet.* 2001. V. 106. № 1. P. 71–93.
24. Ishikawa K., Nakada K. // *Biochim. Biophys. Acta Gen. Subj.* 2021. V. 1865. № 3. P. 129835.
25. Quadalti C., Brunetti D., Lagutina I., Duchi R., Perota A., Lazzari G., Cerutti R., Di Meo I., Johnson M., Bottani E., et al. // *Biochim. Biophys. Acta Mol. Basis Dis.* 2018. V. 1864. № 6 Pt A. P. 2131–2142.
26. Steele S.L., Prykhozhiy S.V., Berman J.N. // *Transl. Res.* 2014. V. 163. № 2. P. 79–98.
27. Maglioni S., Ventura N. // *Mitochondrion.* 2016. V. 30. P. 117–125.
28. Sen A., Cox R.T. // *Curr. Top. Dev. Biol.* 2017. V. 121. P. 1–27.
29. Baile M.G., Claypool S.M. // *Front. Biosci.* 2013. V. 18. № 1. P. 241–278.
30. Garrido-Maraver J., Cordero M.D., Moñino I.D., Perei-ra-Arenas S., Lechuga-Vieco A.V., Cotán D., De la Mata M., Oropesa-Ávila M., De Miguel M., Bautista Lorite J., et al. // *Br. J. Pharmacol.* 2012. V. 167. № 6. P. 1311–1328.
31. Sinsheimer A., Mohsen A.-W., Bloom K., Karunanidhi A., Bharathi S., Wu Y.L., Schiff M., Wang Y., Goetzman E.S., Ghaloul-Gonzalez L., et al. // *Mol. Genet. Metab.* 2021. V. 134. № 1–2. P. 156–163.
32. Dickinson M.E., Flenniken A.M., Ji X., Teboul L., Wong M.D., White J.K., Meehan T.F., Weninger W.J., Westerberg H., Adisu H., et al. // *Nature.* 2016. V. 537. № 7621. P. 508–514.
33. Kruse S.E., Watt W.C., Marcinek D.J., Kapur R.P., Schenkman K.A., Palmiter R.D. // *Cell Metab.* 2008. V. 7. № 4. P. 312–320.
34. Leong D.W., Komen J.C., Hewitt C.A., Arnaud E., McKenzie M., Phipson B., Bahlo M., Laskowski A., Kinkel S.A., Davey G.M., et al. // *J. Biol. Chem.* 2012. V. 287. № 24. P. 20652–20663.
35. van de Wal M.A.E., Adjobo-Hermans M.J.W., Keijzer J., Schirris T.J.J., Homberg J.R., Wieckowski M.R., Grefte S., van Schothorst E.M., van Karnebeek C., Quintana A., et al. // *Brain.* 2022. V. 145. № 1. P. 45–63.
36. Quintana A., Zanella S., Koch H., Kruse S.E., Lee D., Ramirez J.M., Palmiter R.D. // *J. Clin. Invest.* 2012. V. 122. № 7. P. 2359–2368.
37. Sterky F.H., Hoffman A.F., Milenkovic D., Bao B., Paganelli A., Edgar D., Wibom R., Lupica C.R., Olson L., Larsson N.-G. // *Hum. Mol. Genet.* 2012. V. 21. № 5. P. 1078–1089.
38. Karamanlidis G., Lee C.F., Garcia-Menendez L., Kolwicz S.C., Suthamarak W., Gong G., Sedensky M.M., Mor-gan P.G., Wang W., Tian R. // *Cell Metab.* 2013. V. 18. № 2. P. 239–250.
39. Ingraham C.A., Burwell L.S., Skalska J., Brookes P.S., Howell R.L., Sheu S.S., Pinkert C.A. // *Mitochondrion.* 2009. V. 9. № 3. P. 204–210.
40. Ke B.X., Pepe S., Grubb D.R., Komen J.C., Laskowski A., Rodda F.A., Hardman B.M., Pitt J.J., Ryan M.T., Lazarou M., et al. // *Proc. Natl. Acad. Sci. USA.* 2012. V. 109. № 16. P. 6165–6170.
41. Forbes J.M., Ke B.X., Nguyen T.V., Henstridge D.C., Penfold S.A., Laskowski A., Sourris K.C., Groschner L.N., Cooper M.E., Thorburn D.R., et al. // *Antioxid. Redox Signal.* 2013. V. 19. № 4. P. 331–343.
42. Grad L.I., Lemire B.D. // *Hum. Mol. Genet.* 2004. V. 13. № 3. P. 303–314.
43. Qi X., Lewin A.S., Sun L., Hauswirth W.W., Guy J. // *Ann. Neurol. United States.* 2004. V. 56. № 2. P. 182–191.
44. Huang G., Lu H., Hao A., Ng D.C.H., Ponniah S., Guo K., Lufei C., Zeng Q., Cao X. // *Mol. Cell. Biol.* 2004. V. 24. № 19. P. 8447–8456.
45. Kohda M., Tokuzawa Y., Kishita Y., Nyuzuki H., Moriyama Y., Mizuno Y., Hirata T., Yatsuka Y., Yamashita-Sugahara Y., Nakachi Y., et al. // *PLoS Genet.* 2016. V. 12. № 1. P. e1005679.
46. Arsenijevic D., Onuma H., Pecqueur C., Raimbault S., Manning B.S., Miroux B., Couplan E., Alves-Guerra M.C., Gubern M., Surwit R., et al. // *Nat. Genet.* 2000. V. 26. № 4. P. 435–439.
47. Zhang C.Y., Baffy G., Perret P., Krauss S., Peroni O., Grujic D., Hagen T., Vidal-Puig A.J., Boss O., Kim Y.B., et al. // *Cell.* 2001. V. 105. № 6. P. 745–755.

48. Conti B., Sanchez-Alavez M., Winsky-Sommerer R., Morale M.C., Lucero J., Brownell S., Fabre V., Huitron-Resendiz S., Henriksen S., Zorrilla E.P., et al. // *Science*. 2006. V. 314. № 5800. P. 825–828.
49. Enerbäck S., Jacobsson A., Simpson E.M., Guerra C., Yamashita H., Harper M.E., Kozak L.P. // *Nature*. 1997. V. 387. № 6628. P. 90–94.
50. Vidal-Puig A.J., Grujic D., Zhang C.Y., Hagen T., Boss O., Ido Y., Szczepanik A., Wade J., Mootha V., Cortright R., et al. // *J. Biol. Chem.* 2000. V. 275. № 21. P. 16258–16266.
51. Johnson M.T., Mahmood S., Hyatt S.L., Yang H.S., Soloway P.D., Hanson R.W., Patel M.S. // *Mol. Genet. Metab.* 2001. V. 74. № 3. P. 293–302.
52. Peng M., Falk M.J., Haase V.H., King R., Polyak E., Selak M., Yudkoff M., Hancock W.W., Meade R., Saiki R., et al. // *PLoS Genet.* 2008. V. 4. № 4. P. e1000061.
53. Quinzii C.M., Garone C., Emmanuele V., Tadesse S., Krishna S., Dorado B., Hirano M. // *FASEB J.* 2013. V. 27. № 2. P. 612–621.
54. García-Corzo L., Luna-Sánchez M., Doerrier C., García J.A., Guarás A., Acín-Pérez R., Bulles-Peregrín J., López A., Escames G., Enríquez J.A., et al. // *Hum. Mol. Genet.* 2013. V. 22. № 6. P. 1233–1248.
55. Li K., Li Y., Shelton J.M., Richardson J.A., Spencer E., Chen Z.J., Wang X., Williams R.S. // *Cell*. 2000. V. 101. № 4. P. 389–399.
56. Hao Z., Duncan G.S., Chang C.C., Elia A., Fang M., Wakeham A., Okada H., Calzascia T., Jang Y., You-Ten A., et al. // *Cell*. 2005. V. 121. № 4. P. 579–591.
57. Piruat J.I., Pintado C.O., Ortega-Sáenz P., Roche M., López-Barneo J. // *Mol. Cell Biol.* 2004. V. 24. № 24. P. 10933–10940.
58. Bayley J.P., van Minderhout I., Hogendoorn P.C.W., Cornelisse C.J., van der Wal A., Prins F.A., Teppema L., Dahan A., Devilee P., Taschner P.E.M. // *PLoS One*. 2009. V. 4. № 11. P. 1–7.
59. Levéen P., Kotarsky H., Mörgelin M., Karikoski R., Elmér E., Fellman V. // *Hepatology*. 2011. V. 53. № 2. P. 437–447.
60. Diaz F., Garcia S., Padgett K.R., Moraes C.T. // *Hum. Mol. Genet.* 2012. V. 21. № 23. P. 5066–5077.
61. Weinberg S.E., Singer B.D., Steinert E.M., Martinez C.A., Mehta M.M., Martínez-Reyes I., Gao P., Helmin K.A., Abdala-Valencia H., Sena L.A., et al. // *Nature*. 2019. V. 565. № 7740. P. 495–499.
62. Hüttemann M., Lee I., Gao X., Pecina P., Pecinova A., Liu J., Aras S., Sommer N., Sanderson T.H., Tost M., et al. // *FASEB J.* 2012. V. 26. № 9. P. 3916–3930.
63. Quintens R., Singh S., Lemaire K., De Bock K., Granvik M., Schraenen A., Vroegrijk I.O.C.M., Costa V., van Noten P., Lambrechts D., et al. // *PLoS One*. 2013. V. 8. № 2. P. e56719.
64. Diaz F., Thomas C.K., Garcia S., Hernandez D., Moraes C.T. // *Hum. Mol. Genet.* 2005. V. 14. № 18. P. 2737–2748.
65. Fukui H., Diaz F., Garcia S., Moraes C.T. // *Proc. Natl. Acad. Sci. USA*. 2007. V. 104. № 35. P. 14163–14168.
66. Diaz F., Garcia S., Hernandez D., Regev A., Rebelo A., Oca-Cossio J., Moraes C.T. // *Gut*. 2008. V. 57. № 2. P. 232–242.
67. Fünfschilling U., Supplie L.M., Mahad D., Boretius S., Saab A.S., Edgar J., Brinkmann B.G., Kassmann C.M., Tzvetanova I.D., Möbius W., et al. // *Nature*. 2012. V. 485. № 7399. P. 517–521.
68. Agostino A., Invernizzi F., Tiveron C., Fagiolari G., Prella A., Lamantea E., Giavazzi A., Battaglia G., Tatangelo L., Tiranti V., et al. // *Hum. Mol. Genet.* 2003. V. 12. № 4. P. 399–413.
69. Dell'Agnello C., Leo S., Agostino A., Szabadkai G., Tiveron C.C., Zulian A.A., Prella A., Roubertoux P., Rizzuto R., Zeviani M. // *Hum. Mol. Genet.* 2007. V. 16. № 4. P. 431–444.
70. Yang H., Brosel S., Acín-Pérez R., Slavkovich V., Nishino I., Khan R., Goldberg I.J., Graziano J., Manfredi G., Schon E.A. // *Hum. Mol. Genet.* 2009. V. 19. № 1. P. 170–180.
71. Viscomi C., Bottani E., Civileto G., Cerutti R., Moggio M., Fagiolari G., Schon E.A., Lamperti C., Zeviani M. // *Cell. Metab.* 2011. V. 14. № 1. P. 80–90.
72. Vrbáčký M., Kovalčíková J., Chawengsaksophak K., Beck I.M., Mráček T., Nůsková H., Sedmera D., Papoušek F., Kolář F., Sobol M., et al. // *Hum. Mol. Genet.* 2016. V. 25. № 21. P. 4674–4685.
73. Marković A., Tauchmannová K., Šimáková M., Mlejnek P., Kaplanová V., Pecina P., Pecinová A., Papoušek F., Liška F., Šilhavý J., et al. // *Biomedicines*. 2022. V. 10. № 2. P. 276.
74. Haraguchi M., Tsujimoto H., Fukushima M., Higuchi I., Kuribayashi H., Utsumi H., Nakayama A., Hashizume Y., Hirato J., Yoshida H., et al. // *Mol. Cell Biol.* 2002. V. 22. № 14. P. 5212–5221.
75. López L.C., Akman H.O., García-Cazorla Á., Dorado B., Martí R., Nishino I., Tadesse S., Pizzorno G., Shungu D., Bonilla E., et al. // *Hum. Mol. Genet.* 2009. V. 18. № 4. P. 714–722.
76. Graham B.H., Waymire K.G., Cottrell B., Trounce I.A., MacGregor G.R., Wallace D.C. // *Nat. Genet.* 1997. V. 16. № 3. P. 226–234.
77. Esposito L.A., Melov S., Panov A., Cottrell B.A., Wallace D.C. // *Proc. Natl. Acad. Sci. USA*. 1999. V. 96. № 9. P. 4820–4825.
78. Brower J.V., Rodic N., Seki T., Jorgensen M., Fliess N., Yachnis A.T., McCarrey J.R., Oh S.P., Terada N. // *J. Biol. Chem.* 2007. V. 282. № 40. P. 29658–29666.
79. Kokoszka J.E., Waymire K.G., Levy S.E., Sligh J.E., Cai J., Jones D.P., MacGregor G.R., Wallace D.C. // *Nature*. 2004. V. 427. № 6973. P. 461–465.
80. Tyynismaa H., Sembongi H., Bokori-Brown M., Granycome C., Ashley N., Poulton J., Jalanko A., Spelbrink J.N., Holt I.J., Suomalainen A. // *Hum. Mol. Genet.* 2004. V. 13. № 24. P. 3219–3227.
81. Tyynismaa H., Mjosund K.P., Wanrooij S., Lappalainen I., Ylikallio E., Jalanko A., Spelbrink J.N., Paetau A., Suomalainen A. // *Proc. Natl. Acad. Sci. USA*. 2005. V. 102. № 49. P. 17687–17692.
82. Tyynismaa H., Carroll C.J., Raimundo N., Ahola-Erkkilä S., Wenz T., Ruhanen H., Guse K., Hemminki A., Peltola-Mjosund K.E., Tulkki V., et al. // *Hum. Mol. Genet.* 2010. V. 19. № 20. P. 3948–3958.
83. Trifunovic A., Wredenberg A., Falkenberg M., Spelbrink J.N., Rovio A.T., Bruder C.E., Bohlooly-Y M., Gidlöf S., Oldfors A., Wibom R., et al. // *Nature*. 2004. V. 429. № 6990. P. 417–423.
84. Kujoth C.C., Hiona A., Pugh T.D., Someya S., Panzer K., Wohlgemuth S.E., Hofer T., Seo A.Y., Sullivan R., Jobling W.A., et al. // *Science*. 2005. V. 309. № 5733. P. 481–484.
85. Miller R.A. // *Science*. 2005. V. 310. № 5747. P. 441–443.
86. Hance N., Ekstrand M.I., Trifunovic A. // *Hum. Mol. Genet.* 2005. V. 14. № 13. P. 1775–1783.
87. Vermulst M., Wanagat J., Kujoth G.C., Bielas J.H., Rabino-vitch P.S., Prolla T.A., Loeb L.A. // *Nat. Genet.* 2008. V. 40. № 4. P. 392–394.
88. Ross J.M., Stewart J.B., Hagström E., Brené S., Mourier A., Coppotelli G., Freyer C., Lagouge M., Hoffer B.J., Olson L., et al. // *Nature*. 2013. V. 501. № 7467. P. 412–415.
89. Akman H.O., Dorado B., López L.C., García-Cazorla Á., Vilà M.R., Tanabe L.M., Dauer W.T., Bonilla E., Tanji K., Hirano M. // *Hum. Mol. Genet.* 2008. V. 17. № 16. P. 2433–2440.

90. Bartesaghi S., Betts-Henderson J., Cain K., Dinsdale D., Zhou X., Karlsson A., Salomoni P., Nicotera P. // *Hum. Mol. Genet.* 2010. V. 19. № 9. P. 1669–1677.
91. Zhou X., Curbo S., Zhao Q., Krishnan S., Kuiper R., Karlsson A. // *Hum. Mol. Genet.* 2019. V. 28. № 17. P. 2874–2884.
92. Viscomi C., Spinazzola A., Maggioni M., Fernandez-Vizarrá E., Massa V., Pagano C., Vettor R., Mora M., Zeviani M. // *Hum. Mol. Genet.* 2009. V. 18. № 1. P. 12–26.
93. Wang J., Wilhelmsson H., Graff C., Li H., Oldfors A., Rustin P., Brüning J.C., Kahn C.R., Clayton D.A., Barsh G.S., et al. // *Nat. Genet.* 1999. V. 21. № 1. P. 133–137.
94. Wredenberg A., Wibom R., Wilhelmsson H., Graff C., Wiener H.H., Burden S.J., Oldfors A., Westerblad H., Larsson N.G. // *Proc. Natl. Acad. Sci. USA.* 2002. V. 99. № 23. P. 15066–15071.
95. Aydin J., Andersson D.C., Hänninen S.L., Wredenberg A., Tavi P., Park C.B., Nils-Göran L., Bruton J.D., Westerblad H. // *Hum. Mol. Genet.* 2009. V. 18. № 2. P. 278–288.
96. Ekstrand M.I., Terzioglu M., Galter D., Zhu S., Hofstetter C., Lindqvist E., Thams S., Bergstrand A., Hansson F.S., Trifunovic A., et al. // *Proc. Natl. Acad. Sci. USA.* 2007. V. 104. № 4. P. 1325–1330.
97. Desdín-Micó G., Soto-Heredero G., Aranda J.F., Oller J., Carrasco E., Gabandé-Rodríguez E., Blanco E.M., Alfranca A., Cussó L., Desco M., et al. // *Science.* 2020. V. 368. № 6497. P. 1371–1376.
98. Silva J.P., Köhler M., Graff C., Oldfors A., Magnuson M.A., Berggren P.O., Larsson N.G. // *Nat. Genet.* 2000. V. 26. № 3. P. 336–340.
99. Sörensen L., Ekstrand M., Silva J.P., Lindqvist E., Xu B., Rustin P., Olson L., Larsson N.G. // *J. Neurosci.* 2001. V. 21. № 20. P. 8082–8090.
100. Ekstrand M.I., Falkenberg M., Rantanen A., Park C.B., Gaspari M., Hulthenby K., Rustin P., Gustafsson C.M., Larsson N.G. // *Hum. Mol. Genet.* 2004. V. 13. № 9. P. 935–944.
101. Pondarré C., Antiochos B.B., Campagna D.R., Clarke S.L., Greer E.L., Deck K.M., McDonald A., Han A.-P., Medlock A., Kutok J.L., et al. // *Hum. Mol. Genet.* 2006. V. 15. № 6. P. 953–964.
102. Cossée M., Puccio H., Gansmuller A., Koutnikova H., Dierich A., LeMeur M., Fischbeck K., Dollé P., Koenig M. // *Hum. Mol. Genet.* 2000. V. 9. № 8. P. 1219–1226.
103. Puccio H., Simon D., Cossée M., Criqui-Filipe P., Tiziano F., Melki J., Hindelang C., Matyas R., Rustin P., Koenig M. // *Nat. Genet.* 2001. V. 27. № 2. P. 181–186.
104. Seznec H., Simon D., Monassier L., Criqui-Filipe P., Gansmuller A., Rustin P., Koenig M., Puccio H. // *Hum. Mol. Genet.* 2004. V. 13. № 10. P. 1017–1024.
105. Thierbach R., Schulz T.J., Isken F., Voigt A., Mietzner B., Drewes G., von Kleist-Retzow J.-C., Wiesner R.J., Magnuson M.A., Puccio H., et al. // *Hum. Mol. Genet.* 2005. V. 14. № 24. P. 3857–3864.
106. Miranda C.J., Santos M.M., Ohshima K., Smith J., Li L., Bunting M., Cossée M., Koenig M., Sequeiros J., Kaplan J., et al. // *FEBS Lett.* 2002. V. 512. № 1–3. P. 291–297.
107. Clark R.M., De Biase I., Malykhina A.P., Al-Mahdawi S., Pook M., Bidichandani S.I. // *Hum. Genet.* 2007. V. 120. № 5. P. 633–640.
108. Coppola G., Marmolino D., Lu D., Wang Q., Cnop M., Rai M., Acquaviva F., Cocozza S., Pandolfo M., Geschwind D.H. // *Hum. Mol. Genet.* 2009. V. 18. № 13. P. 2452–2461.
109. Anderson P.R., Kirby K., Hilliker A.J., Phillips J.P. // *Hum. Mol. Genet.* 2005. V. 14. № 22. P. 3397–3405.
110. Anderson P.R., Kirby K., Orr W.C., Hilliker A.J., Phillips J.P. // *Proc. Natl. Acad. Sci. USA.* 2008. V. 105. № 2. P. 611–616.
111. Swarup V., Julien J.-P. // *Prog. Neuropsychopharmacol Biol. Psychiatry.* 2011. V. 35. № 2. P. 363–369.
112. Kreilau F., Guerra S., Masanetz R., Menne V., Yerbury J., Karl T. // *Genes Brain Behav.* 2020. V. 19. № 2. P. 1–14.
113. Riboldi G., Nizzardo M., Simone C., Falcone M., Bresolin N., Comi G.P., Corti S. // *Prog. Neurobiol.* 2011. V. 95. № 2. P. 133–148.
114. Elchuri S., Oberley T.D., Qi W., Eisenstein R.S., Roberts L.J., van Remmen H., Epstein C.J., Huang T.T. // *Oncogene.* 2005. V. 24. № 3. P. 367–380.
115. Hashizume K., Hirasawa M., Imamura Y., Noda S., Shimizu T., Shinoda K., Kurihara T., Noda K., Ozawa Y., Ishida S., et al. // *Am. J. Pathol.* 2008. V. 172. № 5. P. 1325–1331.
116. Lebovitz R.M., Zhang H., Vogel H., Cartwright J., Dionne L., Lu N., Huang S., Matzuk M.M. // *Proc. Natl. Acad. Sci. USA.* 1996. V. 93. № 18. P. 9782–9787.
117. Li Y., Huang T.T., Carlson E.J., Melov S., Ursell P.C., Olson J.L., Noble L.J., Yoshimura M.P., Berger C., Chan P.H., et al. // *Nat. Genet.* 1995. V. 11. № 4. P. 376–381.
118. Melov S., Coskun P., Patel M., Tuinstra R., Cottrell B., Jun A.S., Zastawny T.H., Dizdaroglu M., Goodman S.I., Huang T.T., et al. // *Proc. Natl. Acad. Sci. USA.* 1999. V. 96. № 3. P. 846–851.
119. Kokoszka J.E., Coskun P., Esposito L.A., Wallace D.C. // *Proc. Natl. Acad. Sci. USA.* 2001. V. 98. № 5. P. 2278–2283.
120. Esposito L.A., Kokoszka J.E., Waymire K.G., Cottrell B., MacGregor G.R., Wallace D.C. // *Free Radic. Biol. Med.* 2000. V. 28. № 5. P. 754–766.
121. Reddy V.N., Giblin F.J., Lin L.R., Dang L., Unakar N.J., Musch D.C., Boyle D.L., Takemoto L.J., Ho Y.S., Knoernschild T., et al. // *Invest. Ophthalmol. Vis. Sci.* 2001. V. 42. № 13. P. 3247–3255.
122. De Haan J.B., Bladier C., Griffiths P., Kelner M., O’Shea R.D., Cheung N.S., Bronson R.T., Silvestro M.J., Wild S., Zheng S.S., et al. // *J. Biol. Chem.* 1998. V. 273. № 35. P. 22528–22536.
123. Shiomi T., Tsutsui H., Matsusaka H., Murakami K., Hayashidani S., Ikeuchi M., Wen J., Kubota T., Utsumi H., Takeshita A. // *Circulation.* 2004. V. 109. № 4. P. 544–549.
124. Chen H., Detmer S.A., Ewald A.J., Griffin E.E., Fraser S.E., Chan D.C. // *J. Cell Biol.* 2003. V. 160. № 2. P. 189–200.
125. Chen H., McCaffery J.M., Chan D.C. // *Cell.* 2007. V. 130. № 3. P. 548–562.
126. Detmer S.A., Velde C. Vande, Cleveland D.W., Chan D.C. // *Hum. Mol. Genet.* 2008. V. 17. № 3. P. 367–375.
127. Alavi M.V., Bette S., Schimpf S., Schuettauf F., Schraermeyer U., Wehrl H.F., Ruttiger L., Beck S.C., Tonagel F., Pichler B.J., et al. // *Brain.* 2007. V. 130. № 4. P. 1029–1042.
128. Davies V.J., Hollins A.J., Piechota M.J., Yip W., Davies J.R., White K.E., Nicols P.P., Boulton M.E., Votruba M. // *Hum. Mol. Genet.* 2007. V. 16. № 11. P. 1307–1318.
129. Ishihara N., Nomura M., Jofuku A., Kato H., Suzuki S.O., Masuda K., Otera H., Nakanishi Y., Nonaka I., Goto Y.I., et al. // *Nat. Cell Biol.* 2009. V. 11. № 8. P. 958–966.
130. Gerber S., Charif M., Chevrollier A., Chaumette T., Angebault C., Kane M.S., Paris A., Alban J., Quiles M., Delettre C., et al. // *Brain.* 2017. V. 140. № 10. P. 2586–2596.
131. Oishi K., Hofmann S., Diaz G.A., Brown T., Manwani D., Ng L., Young R., Vlassara H., Ioannou Y.A., Forrest D., et al. // *Hum. Mol. Genet.* 2002. V. 11. № 23. P. 2951–2960.
132. Liberman M.C., Tartaglioni E., Fleming J.C., Neufeld E.J. // *J. Assoc. Res. Otolaryngol.* 2006. V. 7. № 3. P. 211–217.

Cooperation and Competition of RNA Secondary Structure and RNA–Protein Interactions in the Regulation of Alternative Splicing

M. A. Vorobeva¹, D. A. Skvortsov¹, D. D. Pervouchine^{2*}

¹M. V. Lomonosov Moscow State University, Moscow, 119192 Russian Federation

²Skolkovo Institute of Science and Technology, Moscow, 121205 Russian Federation

*E-mail: d.pervouchine@skoltech.ru

Received: October 16, 2023; in final form, October 31, 2023

DOI: 10.32607/actanaturae.26826

Copyright © 2023 National Research University Higher School of Economics. This is an open access article distributed under the Creative Commons Attribution License, which permits unrestricted use, distribution, and reproduction in any medium, provided the original work is properly cited.

ABSTRACT The regulation of alternative splicing in eukaryotic cells is carried out through the coordinated action of a large number of factors, including RNA-binding proteins and RNA structure. The RNA structure influences alternative splicing by blocking *cis*-regulatory elements, or bringing them closer or farther apart. In combination with RNA-binding proteins, it generates transcript conformations that help to achieve the necessary splicing outcome. However, the binding of regulatory proteins depends on RNA structure and, vice versa, the formation of RNA structure depends on the interaction with regulators. Therefore, RNA structure and RNA-binding proteins are inseparable components of common regulatory mechanisms. This review highlights examples of alternative splicing regulation by RNA-binding proteins, the regulation through local and long-range RNA structures, as well as how these elements work together, cooperate, and compete.

KEYWORDS RNA structure, long-range interactions, splicing, RNA-binding proteins, regulation.

ABBREVIATIONS AS – alternative splicing; RBP – RNA-binding protein; snRNA – small nuclear RNA; snRNP – small nuclear ribonucleoprotein; 5'ss – 5' splice site; 3'ss – 3' splice site; PPT – polypyrimidine tract; BPS – branch point sequence.

INTRODUCTION

During maturation, most eukaryotic transcripts undergo splicing, a process in which regions called introns are removed, and the remaining exons are joined to form the mature mRNA [1]. In most cases, splicing is catalyzed by a macromolecular complex called the spliceosome, which consists of small nuclear ribonucleoproteins (snRNPs), which in turn consist of small nuclear RNAs (snRNAs) and the associated proteins [2–4].

The spliceosome recognizes *cis*-regulatory elements in the pre-mRNA, of which the four main classes are the 5' splice site (5'ss), the 3' splice site (3'ss), the polypyrimidine tract (PPT), and the branch point sequence (BPS) [5]. However, processing of identical transcripts can occur differently due to the activation of different splice sites in them or due to their use in different combinations. Thus, many different mRNA isoforms can be found in living cells that are formed

due to alternative splicing (AS) of pre-mRNAs transcribed from the same gene.

Several main types of AS events can be distinguished, including cassette exon skipping, the use of an alternative 5'ss or 3'ss, intron retention, or mutually exclusive exon choice [6, 7]. According to the current estimates, at least 95% of human genes containing more than one exon are subject to alternative splicing [8, 9]. The coordinated changes in splicing of multiple pre-mRNAs are an integral part of the regulation of a number of cellular processes [10–12].

AS is regulated by a combination of RNA–protein, RNA–RNA, and protein–protein interactions that occur between *cis*-regulatory elements and *trans*-acting factors [13, 14]. In addition to the key elements described above (5'ss, 3'ss, PPT, BPS), AS is influenced by additional *cis*-regulatory elements, which can be located both in exons and introns, called exonic and intronic enhancers and silencers of splicing. The in-

teraction of enhancers and silencers with *trans*-acting factors stimulates or suppresses the splice site choice, respectively [15]. The outcome of splicing depends on the coordinated action of multiple enhancers and silencers [16].

In this review, we will briefly provide information about the most studied regulation of AS by RNA-binding proteins, discuss the regulation of AS by RNA secondary structure, and then describe the known facts on the joint action of proteins and RNA structure in the regulation of AS.

REGULATION OF AS BY RNA-BINDING PROTEINS

More than 1,500 RNA-binding proteins (RBPs) are involved in AS regulation [17]. They can be divided into several classes: heterogeneous nuclear ribonucleoproteins (hnRNP), serine/arginine-rich proteins (SR), and others, such as tissue-specific RNA-binding proteins (e.g., NOVA, neuronal PTB/hnRNP I, RBFOX family, etc.) [6]. Here, we will briefly describe examples related to the RNA structure, while more detailed information on AS regulation by various RBP classes can be found in other reviews [6, 18–20].

The ubiquitously expressed SR and hnRNP proteins are the best-studied mediators of splice site recognition [21–25]. SR proteins are involved in both constitutive and alternative splicing, making this RBP family unique compared to other RBPs [22]. SR proteins are generally considered to be positive splicing regulators; they promote exon inclusion by helping to recruit U1 snRNP to the 5'ss and U2 auxiliary factor (U2AF) to the 3'ss through protein–protein interactions during the early stages of spliceosome assembly [21, 26].

SR and hnRNP proteins are considered antagonists. The nature of this antagonism is not entirely clear, since high-affinity hnRNP binding sites do not often overlap with SR protein binding sites in exons. A potential mechanism involves cooperative binding of hnRNP oligomers that extend along the transcript to prevent SR proteins from binding to pre-mRNA [24]. The best characterized hnRNPs involved in splicing regulation are the negative regulators hnRNP A/B and the PPT binding protein PTB, also known as hnRNP I. The hnRNPA2/B1 factor is mainly a splicing inhibitor that interferes with the recognition of 5'ss and 3'ss, which often leads to the exclusion of alternative exons (the functions of hnRNP A/B are detailed in [27]). PTB binds to polypyrimidine tracts, like U2AF65 does, which promotes the binding of U2 snRNP to the 3'ss. This implies that PTB may interfere with functional recognition of 3'ss [28]. The mechanism and direction of action of proteins belonging to the hnRNP family depends on the location of their

binding sites: when binding upstream or inside the cassette exon, they usually act as repressors; when binding downstream, they act as activators of AS [19, 29, 30].

Besides SR and hnRNP proteins, several tissue-specific RNA-binding splicing regulators have been characterized. These include neuron-specific factors NOVA [31], PTBP2 (nPTB, brPTB) [32] and SRRM4 (nSR100) [33], as well as tissue-specific factors such as proteins of the RBFOX family [34], MBNL [35, 36], CELF [37], QKI [38], and TIA [39, 40]. They can exert their action through both tissue-specific expression and binding to pre-mRNA motifs that are enriched in genes expressed in a particular cell type or tissue. Tissue-specific regulators of AS are most often studied in relation with pathologies (e.g., neurodegenerative diseases or muscular dystrophy) [41–43].

The presence of RNA polymerase II is required for recruitment and proper distribution of splicing factors to their binding sites. Accordingly, transcription and splicing mutually influence each other through spatial and kinetic mechanisms [44]. RNA polymerase II has a C-terminal heptad repeat domain (CTD) that is used as a landing pad for accessible factors, allowing their concentration to increase near splice sites [45–48]. The rate of transcription elongation influences AS by determining how quickly splice sites become available for competitive binding with *trans*-acting factors, particularly due to the formation of secondary structure in pre-mRNA [49–53].

REGULATION OF AS BY PRE-mRNA SECONDARY STRUCTURE

Although most RNA molecules in a cell are single-stranded, their parts can adopt double-helical conformations, from which the secondary structure is formed. The secondary structure of RNA can be highly stable both *in vitro* and *in vivo*, and changes in its constituent elements are a well-known mechanism for the regulation of many cellular processes, including splicing [54–58].

Complementary base pairings forming RNA secondary structure can be classified as local and long-range interactions [59]. The simplest type of local RNA secondary structure is a hairpin (also known as stem-loop). Because pre-mRNA folding occurs cotranscriptionally, most of the *in vivo* RNA structure is generated through local interactions [60, 61]. In contrast, long-range interactions are formed between complementary sites separated by large fragments (more than 100 nt) of the primary sequence [62]. Long-range interactions share some features with the tertiary structure, yet they still represent the secondary level of organization, i.e., they deter-

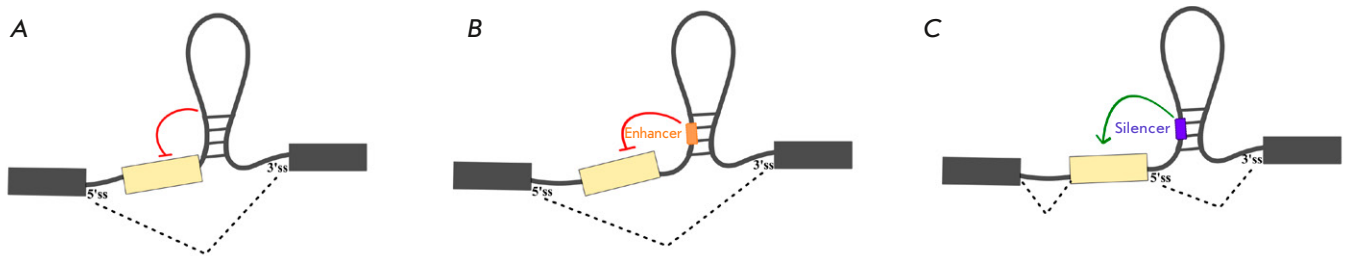


Fig. 1. Blockage of *cis*-regulatory splicing elements by RNA structure. (A) Blockage of a splice site; (B) blockage of an intronic splicing enhancer; (C) blockage of an intronic splicing silencer. Red and green lines indicate the activating and inhibitory effects on splicing, respectively

mine how the polynucleotide chain is folded due to base pairings [59].

LOCAL STRUCTURES IN PRE-mRNA

Extensive experimental evidence exists for AS regulation by local pre-mRNA structure, for example, by preventing spliceosome recognition of the 5'ss, 3'ss, or BPS sequence elements [63]. The simplest mechanism of AS regulation by local secondary structure is the blockage of splice sites (*Fig. 1A*) [64]. Thus, in the pre-mRNA of the human *tau* gene, a local secondary structure obstructs the 5'ss of exon 10, which prevents this exon from being included in the mature transcript [65]. The formation of a hairpin near the 5'ss splice can interfere with the interaction of pre-mRNA with the spliceosome, as it does in the case of exon 7 of the *SMN2* gene, where such a hairpin interferes with the binding of the 5'-ss to U1 snRNP, thus reducing the level of exon inclusion [66].

The pre-mRNA of the fibronectin gene (*FN1*) is the most striking example of the influence of the hairpin structure on the function of a splicing enhancer (*Fig. 1B*). One of the exons of *FN1*, known as the EDA exon, is highly structured and forms seven hairpins. The enhancer is located in the terminal loop of hairpin V and is recognized by *trans*-acting factors such as SRSF1. A change in the enhancer localization from a loop to a stem reduces its regulatory ability [67]. A similar mechanism of AS regulation involving an intronic splicing silencer is observed in the pre-mRNA of the human immunodeficiency virus (*Fig. 1C*) [68].

A non-canonical type of local secondary structure that influences AS is G-quadruplex (GQ). In a G-quadruplex, four guanines interact with each other through Hoogsteen hydrogen bonds and their stacks form a four-stranded helix [69]. GQs act as *cis*-elements in AS regulation, usually reside in intronic regions, and promote exon inclusion. For example, disruption of the ability to form GQ significantly reduces the inclusion of exon 8 in the *CD44* gene [70]. Several splicing regulators such as hnRNP H,

hnRNP F, SRSF1, SRSF9, hnRNP U, and U2AF65 can interact with GQ [71–73]. The formation of GQ in the pre-mRNA of the *TP53* gene in intron 3 regulates the splicing of intron 2, thus changing the ratio between the active and inactive isoforms [74]; intron retention leads to the generation of an inactive form of the protein, $\Delta 40p53$ [75].

Local secondary structures in pre-mRNA can also act as targets of small molecules. For example, 22 isoforms are generated as a result of AS of the transcript of the human telomerase reverse transcriptase gene (*hTERT*), of which only the full-length mRNA is translated into an active protein with reverse transcriptase activity [71]. The use of the GQ stabilizer reduces the level of active telomerase by eliminating exons 7 and 8. This leads to the synthesis of a truncated inactive protein called hTERT- β . Riboswitches are another important class of local RNA structures that influence AS and are targets of small molecules [76].

LONG-RANGE INTERACTIONS IN PRE-mRNA, RNA BRIDGES, AND LOOP-OUTS

Long-range interactions in pre-mRNAs have been documented in viruses such as the tobacco mosaic virus [77], human immunodeficiency virus [78], etc. [79, 80]. The most remarkable example in eukaryotes, the *Drosophila Dscam* gene, is discussed below; however, we note here that more and more data support the presence of long-range interactions in human pre-mRNAs and their impact on AS [81–86].

Long-range interactions can regulate AS by various mechanisms. First, like local RNA structures, they can block *cis*-regulatory elements [87]. Second, long-range interactions can act as “RNA bridges” that bring *cis*-regulatory elements closer together [34]. Third, long-range interactions can also move *cis*-regulatory elements away from each other. For instance, long-range interactions between neighboring introns can loop out an intermediate exon or a group of exons and promote their skipping. The example of long-range in-

teractions in the *Drosophila* *CG33298* and *Gug* genes, which function as RNA bridges and simultaneously block splice sites [87], demonstrates that these three mechanisms are not mutually exclusive.

RNA bridges can bring *cis*-regulatory elements closer together in space without the participation of auxiliary proteins (Fig. 2A). For example, long-range interactions in the pre-mRNA of the mammalian *SF1* gene bring the strong 5'ss of exon 9 closer to the weak 3'ss of exon 10, and the destruction of the secondary structure leads to the activation of the stronger 3'ss located 21 nts downstream [62]. RNA bridges can also bring intronic *cis*-regulatory elements closer to splice sites (Fig. 2B). For successful assembly of the spliceosome and splicing of the *ENAH* gene, it is necessary that the binding site of the RBFOX2 factor be close in space to an alternative exon, which is achieved through the interaction of distant regions in the pre-mRNA forming an RNA bridge [34]. Many cases have been described in which *cis*-regulatory elements are located at a considerable distance from the regulated exon, such as in the *Drosophila* *14-3-3ζ* gene [88], as well as the human *ENAH* and *KIF21A* genes [34]. Genome-wide maps of RNA-protein interactions also show that the majority of binding sites are located much further than 1,000 nts from their potential target exons [89].

Looping out a part of pre-mRNA by secondary structure, on the one hand, can bring the flanking *cis*-regulatory elements closer together, and on the other hand, place the intervening sequence in a loop, which is believed to promote the exclusion of the looped-out region (Fig. 3A) [90]. For example, complementary interactions between the introns flanking an alternative exon tend to increase the frequency of its skipping [91]. The secondary structure in the *Drosophila* *Nmnat* gene loops approximately 350 nt and leads to the exclusion of exon 5 and the poly(A) signal from the pre-mRNA. In this case, the structure brings the distal acceptor splicing site closer to the donor site, thereby promoting the exclusion of skipped terminal exon [87]. Exon loop-outs are also characteristic of long-range interactions in other mammalian genes, for example, the *CASK* and *PHF20L1* genes [92], the dystonin gene (*DST*), in which complementary regions presumably loop out a cluster of six exons [93], as well as the human telomerase gene (*hTERT*), in which long-range interactions between tandem repeats lead to skipping of two exons [94]. The example of the secondary structure in the pre-mRNA of proteolipid protein 1 (*PLP1*), the two alternative splice isoforms of which differ in the choice of an alternative 5'ss in the intron between exons 3 and 4, demonstrates that loop-outs not only

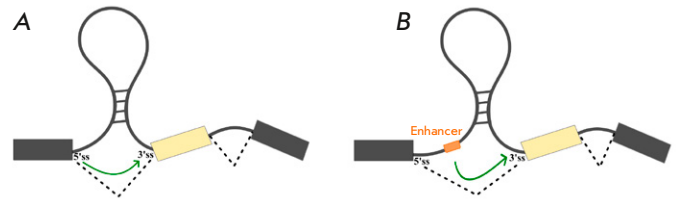


Fig. 2. Spatial segregation of *cis*-regulatory splicing elements by RNA structure (RNA "bridges"). (A) Bringing splice sites closer together. (B) Bringing a splicing enhancer closer to the splice site

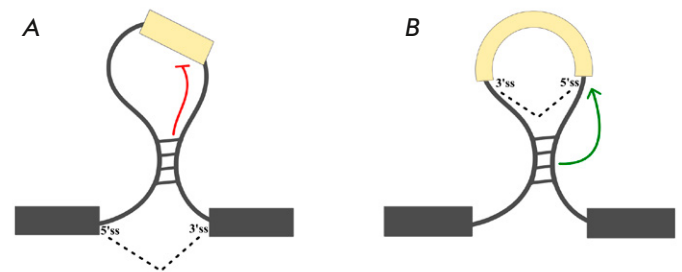


Fig. 3. Spatial separation of *cis*-regulatory splicing elements by the RNA structure (loop-outs). (A) Looping out a region containing one or more exons. (B) Back-splicing in an intron leading to the formation of a circular RNA. Red and green lines indicate the activating and inhibitory effects on splicing, respectively

of exons, but also of individual splice sites have a remarkable influence on splicing [95].

However, the most fascinating example of the influence of long-range interactions on AS is the *Drosophila* *Dscam* gene, in which complementary base pairings can occur at a distance of up to 12,000 nucleotides. A remarkable feature of the *Dscam* splicing mechanism is that complementary regions form a group of competing RNA structures that control the mutually exclusive choice of exons [96, 97]. The docker site located upstream of the exon 6 cluster can base-pair with only one of many selector sites located upstream of each of the alternative exons, thereby not only bringing together the distant 5'ss and 3'ss, but also looping out the intervening exons. The mutually exclusive mechanism of splicing is additionally controlled by *hrp36*, a factor that suppresses the ectopic inclusion of alternative exons promoted by SR proteins [98]. A similar mechanism was discovered in many other genes containing clusters of mutually exclusive exons (see review in [99]), e.g., example, *14-3-3ζ* [100], *Mhc* [88], *srp*, *RIC-3*, *MRP1* [101], *DNM1* [102], *TCF3*, *CD55* [103], and *ATE1* [52]. It has been

suggested that tandem duplications generating clusters of mutually exclusive exons inevitably lead to the formation of competing RNA structures and, consequently, to mutually exclusive AS [104].

However, placing a part of pre-mRNA in a loop does not prevent its binding to spliceosomal components and, on the contrary, can promote splicing. The example of circular RNAs shows that complementary interactions in introns, in particular the ones formed by Alu repeats, facilitate the so-called back-splicing that covalently links the 5'- and 3'-ends of RNA, resulting in the formation of circular transcripts (Fig. 3B) [105, 106]. In sum, it can be concluded that spatial segregation, spatial separation, and blockage of *cis*-regulatory elements by RNA structure are special cases of a more general molecular mechanism in which the splicing outcome is determined by transcript conformation, which, in turn, depends on long-range interactions in its secondary structure.

COOPERATION AND COMPETITION OF RNA SECONDARY STRUCTURE AND RNA-PROTEIN INTERACTIONS

Pre-mRNA forms local secondary structure co-transcriptionally simultaneously interacting with RBPs [107]. RBPs contain well-defined RNA-binding domains (RBDs), such as RNA recognition domain (RRM), hnRNP K homology domain (KH), zinc fingers (ZF), etc., which interact with specific sequences and/or structures in RNA [108]. Most RBDs recognize very short (3–7 nt) degenerate motifs, which are often organized in clusters. This increases the binding specificity of RBPs that contain multiple RBDs and also allows several RBPs to cooperate with each other [17]. For instance, high-affinity binding of the neuron-specific splicing factor NOVA is determined by the YCAY (Y = C/U) motif, which is usually found in clusters of several tetramers [109]. Some RBPs recognize spatially separated bipartite motifs that have a particular structural context [110]. However, RBPs recognizing similar motifs may have different binding profiles, and even high-affinity interactions may happen to be nonfunctional [111].

Multiple lines of evidence indicate that the most important factor influencing RBP binding is RNA structure [112]. RBP binding sites can be involved in various pre-mRNA structural elements [113]. It appears that ZF RBDs interact with RNA duplexes, as more than twenty ZF domain-containing RBPs selectively bind highly structured double-stranded microRNA precursors [108]. RBPs containing KH domains tend to prefer large hairpin loops. Given that most of these RBPs contain multiple RBDs, large hairpin loops allow simultaneous binding of multiple KH domains at once, as is the case with NOVA1 and

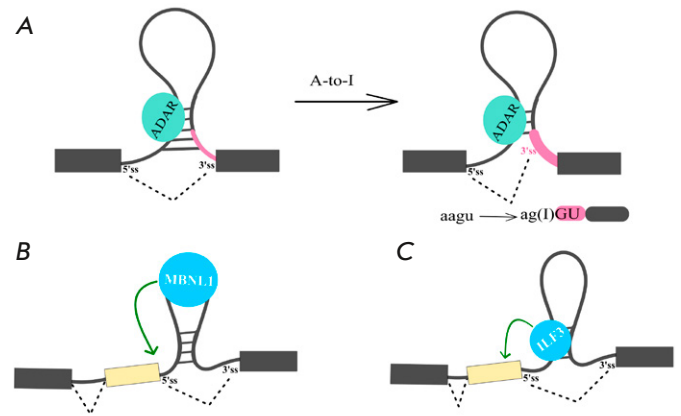


Fig. 4. The combined effect of RNA secondary structure and RNA-protein interactions. (A) Creation of a splice site through RNA editing (A-to-I RNA editing). (B) Binding of an RNA-binding protein to a stem-loop structure. (C) Binding of an RNA-binding protein to a double-stranded region

PCBP2 [109, 114–116]. It can be assumed that the outcome of AS should depend on the balance between RNA–RNA and RNA–protein interactions, with the competition between them depending on the repertoire of the RBPs that are expressed in a given cell type [111]. Moreover, RBPs themselves often function combinatorially by binding to sites and structural elements on common mRNA targets [117].

Changes in RNA structure and the consequent changes in AS can occur due to interaction with other nucleic acids (e.g., with microRNA [118]), as well as a result of post-transcriptional modifications of the pre-mRNA primary sequence [119]. Thus, A-to-I editing performed by ADAR proteins regulates AS by changing the nucleotide sequence of the main splicing *cis*-elements (Fig. 4A) [120–122]. Additionally, ADAR2 can bind to the double-stranded RNA formed by the GA-rich sequence and polypyrimidine tract, thereby preventing U2AF65 recruitment [123]. Methylated N6-adenosine (m⁶A) and the associated proteins can regulate AS [119, 124]. For example, m⁶A modification can promote hnRNP C binding by altering the structure of the target RNA and exposing a single-stranded splice site. The same mechanism is also characteristic of hnRNP G [125].

RNA structure can obstruct *cis*-regulatory splice elements and RBP binding sites, but this is not the only way it can affect AS. Splicing of exon 5 of the human cardiac troponin T (*cTNT*) gene requires binding of the MBNL1 protein at the 3' end of the upstream intron. MBNL1 binds to a part of the intron that forms a hairpin (Fig. 4B), whereas the splicing factor U2AF65 binds the same region when it is sin-

gle-stranded. Stabilization of the local RNA structure in the form of a hairpin blocks U2AF65 binding, which prevents U2 snRNP recruitment and leads to exon skipping [126]. Another remarkable example is binding of hnRNP F to a pre-mRNA containing G-quadruplexes, which stimulates the inclusion of a cassette exon in the *CD44* gene. Interestingly, another AS regulator, ESRP1, also stimulates the inclusion of the alternative exon in *CD44* independently of hnRNP F by binding to a GU-rich motif partially overlapping with GQ. This suggests that *CD44* pre-mRNA exists in equilibrium between linear and GQ forms, which allows to maintain the correct splice isoform ratio [70].

Regulation of AS can occur due to RBP-dependent stabilization or destabilization of RNA secondary structure [127]. For example, the ZFR (zinc-finger RNA-binding protein) and ILF3 proteins were shown to form heterodimeric duplexes with ILF2. The resulting complexes bind nonspecifically to double-stranded regions in the pre-mRNA, thereby affecting the accessibility of splice sites and the binding of *trans*-acting factors (Fig. 4C). The interaction of ILF3 and ZFR with RNA structure affects mutually exclusive choice of exons in the *ATE1* gene. It was suggested that ZFR and ILF3 are involved in stabilizing RNA duplexes during mutually exclusive splicing, although the precise mechanism of their action remains unknown.

Some RBPs regulate AS by changing the pre-mRNA tertiary structure. Unlike RNA bridges, in this case it is protein–protein rather than complementary interactions that induce pre-mRNA conformation that is necessary for AS. For example, homodimers of the hnRNPA1 protein interact with specific sites located in neighboring introns, bring them closer, and loop out the intervening exon, which leads to its skipping [90]. A similar mechanism is also characteristic of the hnRNP F/H proteins [128]. It was also shown that hnRNPA1 and hnRNP H can interact with each

other and with other hnRNP family members [129]. The influence of the NOVA protein on splicing is also explained by spatial segregation of distant pre-mRNA regions, because its binding sites are often located at the beginning of the intron and near the BPS, which suggests that NOVA binds to two sites at the ends of the intron and forms a loop that brings the 5'ss and BPS closer together [130]. Homotypic and heterotypic interactions between RBPs, which bring remote regions of the pre-mRNA closer to each other, may be a widespread mechanism of AS regulation.

CONCLUSION

AS regulation by RNA structure and AS regulation by RNA-binding proteins have been described previously as independent mechanisms. However, since binding of AS regulators may depend on RNA structure and, conversely, RNA structure formation may depend on interactions with regulators, multiple cross-talks between them exist. It is clear that the pre-mRNA structure is involved in the regulation of accessibility of splicing factor binding sites and contributes to the generation of conformations required for splicing through RNA bridges and loop-outs. Protein factors can participate in modifying the pre-mRNA sequence, organizing its secondary and tertiary structure, thereby influencing the splicing outcome. Therefore, the local and long-range interactions in the structure of pre-mRNA and protein factors must be considered as inseparable parts of common regulatory cascades. ●

The authors would like to thank Maria Vlasenok, Marina Petrova, and Olga Dontsova for critical comments.

This work was supported by the Ministry of Science and Education of the Russian Federation (grant No. 075-10-2021-116).

REFERENCES

- Gilbert W. // *Nature*. 1978. V. 271. № 5645. P. 501.
- Will C.L., Lührmann R. // *Cold Spring Harb. Perspect. Biol.* 2011. V. 3. № 7. P. a003707.
- Matera A.G., Wang Z. // *Nat. Rev. Mol. Cell. Biol.* 2014. V. 15. № 2. P. 108–121.
- Yan C., Wan R., Shi Y. // *Cold Spring Harb. Perspect. Biol.* 2019. V. 11. № 1. P. a032409.
- Shapiro M.B., Senapathy P. // *Nucl. Acids Res.* 1987. V. 15. № 17. P. 7155–7174.
- Wang Y., Liu J., Huang B.O., Xu Y.M., Li J., Huang L.F., Lin J., Zhang J., Min Q.H., Yang W.M., Wang X.Z. // *Biomed. Rep.* 2015. V. 3. № 2. P. 152–158.
- Nilsen T.W., Graveley B.R. // *Nature*. 2010. V. 463. № 7280. P. 457–463.
- Wang E.T., Sandberg R., Luo S., Khrebtkova I., Zhang L., Mayr C., Kingsmore S.F., Schroth G.P., Burge C.B. // *Nature*. 2008. V. 456. № 7221. P. 470–476.
- Pan Q., Shai O., Lee L.J., Frey B.J., Blencowe B.J. // *Nat. Genet.* 2008. V. 40. № 12. P. 1413–1415.
- Grabowski P.J. // *Cell*. 1998. V. 92. № 6. P. 709–712.
- Schwerk C., Schulze-Osthoff K. // *Mol. Cell*. 2005. V. 19. № 1. P. 1–13.
- Baralle F.E., Giudice J. // *Nat. Rev. Mol. Cell Biol.* 2017. V. 18. № 7. P. 437–451.
- Ule J., Blencowe B. // *Mol. Cell*. 2019. V. 76. № 2. P. 329–345.
- Wahl M.C., Will C.L., Lührmann R. // *Cell*. 2009. V. 136. № 4. P. 701–718.
- Wang Z., Burge C.B. // *RNA*. 2008. V. 14. № 5. P. 802–813.

16. Barash Y., Calarco J.A., Gao W., Pan Q., Wang X., Shai O., Blencowe B.J., Frey B.J. // *Nature*. 2010. V. 465. № 7294. P. 53–59.
17. Gerstberger S., Hafner M., Tuschl T. // *Nat. Rev. Genet.* 2014. V. 15. № 12. P. 829–845.
18. Li Q., Lee J.A., Black D.L. // *Nat. Rev. Neurosci.* 2007. V. 8. № 11. P. 819–831.
19. Fu X.D., Ares M. // *Nat. Rev. Genet.* 2014. V. 15. № 10. P. 689–701.
20. Dvinge H. // *FEBS Lett.* 2018. V. 592. № 17. P. 2987–3006.
21. Zhou Z., Fu X.D. // *Chromosoma*. 2013. V. 122. № 3. P. 191–207.
22. Long J.C., Caceres J.F. // *Biochem. J.* 2009. V. 417. № 1. P. 15–27.
23. Pandit S., Zhou Y., Shiue L., Coutinho-Mansfield G., Li H., Qiu J., Huang J., Yeo G.W., Ares M., Fu X.D. // *Mol. Cell*. 2013. V. 50. № 2. P. 223–235.
24. Martinez-Contreras R., Cloutier P., Shkreta L., Fiset J.F., Revil T., Chabot B. // *Adv. Exp. Med. Biol.* 2007. V. 623. P. 123–147.
25. Dreyfuss G., Matunis M.J., Piñol-Roma, S., Burd C.G. // *Annu. Rev. Biochem.* 1993. V. 62. P. 289–321.
26. Sahebi M., Hanafi M.M., van Wijnen A.J., Azizi P., Abiri R., Ashkani S., Taheri S. // *Gene*. 2016. V. 587. № 2. P. 107–119.
27. Liu Y., Shi S.L. // *Wiley Interdiscip. Rev. RNA*. 2021. V. 12. № 2. P. e1612.
28. Xue Y., Zhou Y., Wu T., Zhu T., Ji X., Kwon Y.S., Zhang C., Yeo G., Black D.L., Sun H., et al. // *Mol. Cell*. 2009. V. 36. № 6. P. 996–1006.
29. Schaub M.C., Lopez S.R., Caputi M. // *J. Biol. Chem.* 2007. V. 282. № 18. P. 13617–13626.
30. Caputi M., Zahler A.M. // *J. Biol. Chem.* 2001. V. 276. № 47. P. 43850–43859.
31. Zhang C., Frias M.A., Mele A., Ruggiu M., Eom T., Marney C.B., Wang H., Licatalosi D.D., Fak J.J., Darnell R.B. // *Science*. 2010. V. 329. № 5990. P. 439–443.
32. Markovtsov V., Nikolic J.M., Goldman J.A., Turck C.W., Chou M.Y., Black D.L. // *Mol. Cell Biol.* 2000. V. 20. № 20. P. 7463–7479.
33. Quesnel-Vallières M., Irimia M., Cordes S.P., Blencowe B.J. // *Genes Dev.* 2015. V. 29. № 7. P. 746–759.
34. Lovci M.T., Ghanem D., Marr H., Arnold J., Gee S., Parra M., Liang T.Y., Stark T.J., Gehman L.T., Hoon S., et al. // *Nat. Struct. Mol. Biol.* 2013. V. 20. № 12. P. 1434–1442.
35. Warf M.B., Berglund J.A. // *RNA*. 2007. V. 13. № 12. P. 2238–2251.
36. Wang E.T., Cody N.A., Jog S., Biancolella M., Wang T.T., Treacy D.J., Luo S., Schroth G.P., Housman D.E., Reddy S., et al. // *Cell*. 2012. V. 150. № 4. P. 710–724.
37. Ladd A.N., Charlet N., Cooper T.A. // *Mol. Cell Biol.* 2001. V. 21. № 4. P. 1285–1296.
38. Hall M.P., Nagel R.J., Fagg W.S., Shiue L., Cline M.S., Perriman R.J., Donohue J.P., Ares M. // *RNA*. 2013. V. 19. № 5. P. 627–638.
39. Wang Z., Kayikci M., Briese M., Zarnack K., Luscombe N.M., Rot G., Zupan B., Curk T., Ule J. // *PLoS Biol.* 2010. V. 8. № 10. P. e1000530.
40. Gal-Mark N., Schwartz S., Ram O., Eyraş E., Ast G. // *PLoS Genet.* 2009. V. 5. № 11. P. e1000717.
41. Berto S., Usui N., Konopka G., Fogel B.L. // *Hum. Mol. Genet.* 2016. V. 25. № 12. P. 2451–2464.
42. Zhou H., Mangelsdorf M., Liu J., Zhu L., Wu J.Y. // *Sci. China Life Sci.* 2014. V. 57. № 4. P. 432–444.
43. Prashad S., Gopal P.P. // *RNA Biol.* 2021. V. 18. № 7. P. 972–987.
44. Das R., Dufu K., Romney B., Feldt M., Elenko M., Reed R. // *Genes Dev.* 2006. V. 20. № 9. P. 1100–1109.
45. Bird G., Zorio D.A., Bentley D.L. // *Mol. Cell Biol.* 2004. V. 24. № 20. P. 8963–8969.
46. Saldi T., Cortazar M.A., Sheridan R.M., Bentley D.L. // *J. Mol. Biol.* 2016. V. 428. № 12. P. 2623–2635.
47. Yuryev A., Patturajan M., Litingtung Y., Joshi R.V., Gentile C., Gebara M., Corden J.L. // *Proc. Natl. Acad. Sci. USA*. 1996. V. 93. № 14. P. 6975–6980.
48. Misteli T., Spector D.L. // *Mol. Cell*. 1999. V. 3. № 6. P. 697–705.
49. Aslanzadeh V., Huang Y., Sanguinetti G., Beggs J.D. // *Genome Res.* 2018. V. 28. № 2. P. 203–213.
50. Dujardin G., Lafaille C., de la Mata M., Marasco L.E., Muñoz, M. J., Le Jossic-Corcós C., Corcos L., Kornblihtt A.R. // *Mol. Cell*. 2014. V. 54. № 4. P. 683–690.
51. Aitken S., Alexander R.D., Beggs J.D. // *PLoS Comput. Biol.* 2011. V. 7. № 10. P. e1002215.
52. Kalinina M., Skvortsov D., Kalmykova S., Ivanov T., Dontsova O., Pervouchine D.D. // *Nucl. Acids Res.* 2021. V. 49. № 1. P. 479–490.
53. Saldi T., Riemondy K., Erickson B., Bentley D.L. // *Mol. Cell*. 2021. V. 81. № 8. P. 1789–1801.
54. Baralle F.E., Singh R.N., Stamm S. // *Biochim. Biophys. Acta Gene Regul. Mech.* 2019. V. 1862. № 11–12. P. 194448.
55. Rieder L.E., Reenan R.A. // *Semin. Cell Dev. Biol.* 2012. V. 23. № 3. P. 281–288.
56. Xu B., Meng Y., Jin Y. // *Wiley Interdiscip. Rev. RNA*. 2021. V. 12. № 1. P. e1626.
57. Rubtsov P.M. // *Mol. Biol. (Moscow)*. 2016. V. 50. № 6. P. 935–943.
58. Herbert A., Hatfield A., Lackey L. // *Biosci. Rep.* 2023. V. 43. № 3. P. BSR20220149.
59. Pervouchine D.D. // *Genes (Basel)*. 2018. V. 9. № 6. P. 302.
60. Lai D., Proctor J.R., Meyer I.M. // *RNA*. 2013. V. 19. № 11. P. 1461–1473.
61. Fong N., Kim H., Zhou Y., Ji X., Qiu J., Saldi T., Diener K., Jones K., Fu X.D., Bentley D.L. // *Genes Dev.* 2014. V. 28. № 23. P. 2663–2676.
62. Pervouchine D.D., Khrameeva E.E., Pichugina M.Y., Nikolaienko O.V., Gelfand M.S., Rubtsov P.M., Mironov A.A. // *RNA*. 2012. V. 18. № 1. P. 1–15.
63. Buratti E., Baralle F.E. // *Mol. Cell Biol.* 2004. V. 24. № 24. P. 10505–10514.
64. Hiller M., Zhang Z., Backofen R., Stamm S. // *PLoS Genet.* 2007. V. 3. № 11. P. e204.
65. Hutton M., Lendon C.L., Rizzu P., Baker M., Froelich S., Houlden H., Pickering-Brown S., Chakraverty S., Isaacs A., Grover A., et al. // *Nature*. 1998. V. 393. № 6686. P. 702–705.
66. Singh N.N., Singh R.N. // *Biochim. Biophys. Acta Gene Regul. Mech.* 2019. V. 1862. № 11–12. P. 194403.
67. Muro A.F., Caputi M., Pariyarath R., Pagani F., Buratti E., Baralle F.E. // *Mol. Cell Biol.* 1999. V. 19. № 4. P. 2657–2671.
68. Damgaard C.K., Tange T.O., Kjems J. // *RNA*. 2002. V. 8. № 11. P. 1401–1415.
69. Rhodes D., Lipps H.J. // *Nucl. Acids Res.* 2015. V. 43. № 18. P. 8627–8637.
70. Huang H., Zhang J., Harvey S.E., Hu X., Cheng C. // *Genes Dev.* 2017. V. 31. № 22. P. 2296–2309.
71. Gomez D., Lemarteleur T., Lacroix L., Mailliet P,

- Mergny J.L., Riou J.F. // *Nucl. Acids Res.* 2004. V. 32. № 1. P. 371–379.
72. Didiot M.C., Tian Z., Schaeffer C., Subramanian M., Mandel J.L., Moine H. // *Nucl. Acids Res.* 2008. V. 36. № 15. P. 4902–4912.
73. Millevoi S., Moine H., Vagner S. // *Wiley Interdiscip. Rev. RNA.* 2012. V. 3. № 4. P. 495–507.
74. Marcel V., Tran P.L., Sagne C., Martel-Planche G., Vasselin L., Teulade-Fichou M.P., Hall J., Mergny J.L., Hainaut P., van Dyck E. // *Carcinogenesis.* 2011. V. 32. № 3. P. 271–278.
75. Courtois S., Verhaegh G., North S., Luciani M.G., Lassus P., Hibner U., Oren M., Hainaut P. // *Oncogene.* 2002. V. 21. № 44. P. 6722–6728.
76. Wachter A. // *RNA Biol.* 2010. V. 7. № 1. P. 67–76.
77. Archer E.J., Simpson M.A., Watts N.J., O’Kane R., Wang B., Erie D.A., McPherson A., Weeks K.M. // *Biochemistry.* 2013. V. 52. № 18. P. 3182–3190.
78. Jacquenet S., Ropers D., Bilodeau P.S., Damier L., Mouglin A., Stoltzfus C.M., Branlant C. // *Nucl. Acids Res.* 2001. V. 29. № 2. P. 464–478.
79. Nicholson B.L., White K.A. // *Nat. Rev. Microbiol.* 2014. V. 12. № 7. P. 493–504.
80. Miller W.A., White K.A. // *Annu. Rev. Phytopathol.* 2006. V. 44. P. 447–467.
81. Kalmykova S., Kalinina M., Denisov S., Mironov A., Skvortsov D., Guigó, R., Pervouchine D. // *Nat. Commun.* 2021. V. 12. № 1. P. 2300.
82. Cai Z., Cao C., Ji L., Ye R., Wang D., Xia C., Wang S., Du Z., Hu N., Yu X., et al. // *Nature.* 2020. V. 582. № 7812. P. 432–437.
83. Lu Z., Zhang Q.C., Lee B., Flynn R.A., Smith M.A., Robinson J.T., Davidovich C., Gooding A.R., Goodrich K.J., Mattick J.S., et al. // *Cell.* 2016. V. 165. № 5. P. 1267–1279.
84. Aw J.G., Shen Y., Wilm A., Sun M., Lim X.N., Boon K.L., Tapsin S., Chan Y.S., Tan C.P., Sim A.Y., et al. // *Mol. Cell.* 2016. V. 62. № 4. P. 603–617.
85. Sharma E., Sterne-Weiler T., O’Hanlon D., Blencowe B.J. // *Mol. Cell.* 2016. V. 62. № 4. P. 618–626.
86. Ziv O., Gabryelska M.M., Lun A.T.L., Gebert L.F.R., Sheu-Gruttadauria J., Meredith L.W., Liu Z.Y., Kwok C.K., Qin C.F., MacRae I.J., et al. // *Nat. Methods.* 2018. V. 15. № 10. P. 785–788.
87. Raker V.A., Mironov A.A., Gelfand M.S., Pervouchine D.D. // *Nucl. Acids Res.* 2009. V. 37. № 14. P. 4533–4544.
88. Yang Y., Zhan L., Zhang W., Sun F., Wang W., Tian N., Bi J., Wang H., Shi D., Jiang Y., et al. // *Nat. Struct. Mol. Biol.* 2011. V. 18. № 2. P. 159–168.
89. van Nostrand E.L., Freese P., Pratt G.A., Wang X., Wei X., Xiao R., Blue S.M., Chen J.Y., Cody N.A.L., Dominguez D., et al. // *Nature.* 2020. V. 583. № 7818. P. 711–719.
90. Nasim F.U., Hutchison S., Cordeau M., Chabot B. // *RNA.* 2002. V. 8. № 8. P. 1078–1089.
91. Miriami E., Margalit H., Sperling R. // *Nucl. Acids Res.* 2003. V. 31. № 7. P. 1974–1983.
92. Margasyuk S., Kalinina M., Petrova M., Skvortsov D., Cao C., Pervouchine D.D. // *RNA.* 2023. V. 29. № 9. P. 1423–1436.
93. Pervouchine D.D. // *RNA.* 2014. V. 20. № 10. P. 1519–1531.
94. Wong M.S., Shay J.W., Wright W.E. // *Nat. Commun.* 2014. V. 5. P. 3306.
95. Taube J.R., Sperle K., Banser L., Seeman P., Cavan B.C., Garbern J.Y., Hobson G.M. // *Hum. Mol. Genet.* 2014. V. 23. № 20. P. 5464–5478.
96. Graveley B.R. // *Cell.* 2005. V. 123. № 1. P. 65–73.
97. Wang X., Li G., Yang Y., Wang W., Zhang W., Pan H., Zhang P., Yue Y., Lin H., Liu B., et al. // *Nat. Commun.* 2012. V. 3. P. 1255.
98. Olson S., Blanchette M., Park J., Savva Y., Yeo G.W., Yeakley J.M., Rio D.C., Graveley B.R. // *Nat. Struct. Mol. Biol.* 2007. V. 14. № 12. P. 1134–1140.
99. Jin Y., Dong H., Shi Y., Bian L. // *Wiley Interdiscip. Rev. RNA.* 2018. V. 9. № 3. P. e1468.
100. Yang Y., Sun F., Wang X., Yue Y., Wang W., Zhang W., Zhan L., Tian N., Shi F., Jin Y. // *RNA Biol.* 2012. V. 9. № 5. P. 691–700.
101. Yue Y., Yang Y., Dai L., Cao G., Chen R., Hong W., Liu B., Shi Y., Meng Y., Shi F., et al. // *RNA.* 2016. V. 22. № 1. P. 96–110.
102. Suyama M. // *Bioinformatics.* 2013. V. 29. № 17. P. 2084–2087.
103. Hatje K., Rahman R.U., Vidal R.O., Simm D., Hammesfahr B., Bansal V., Rajput A., Mickael M.E., Sun T., Bonn S., Kollmar M. // *Mol. Syst. Biol.* 2017. V. 13. № 12. P. 959.
104. Ivanov T.M., Pervouchine D.D. // *Genes (Basel).* 2018. V. 9. № 7. P. 356.
105. Welden J.R., Stamm S. // *Biochim. Biophys. Acta Gene Regul. Mech.* 2019. V. 1862. № 11–12. P. 194410.
106. Pervouchine D.D. // *Biochim. Biophys. Acta Gene Regul. Mech.* 2019. V. 1862. № 11–12. P. 194384.
107. Eperon L.P., Graham I.R., Griffiths A.D., Eperon I.C. // *Cell.* 1988. V. 54. № 3. P. 393–401.
108. Lunde B.M., Moore C., Varani G. // *Nat. Rev. Mol. Cell. Biol.* 2007. V. 8. № 6. P. 479–490.
109. Jensen K.B., Musunuru K., Lewis H.A., Burley S.K., Darnell R.B. // *Proc. Natl. Acad. Sci. USA.* 2000. V. 97. № 11. P. 5740–5745.
110. Dominguez D., Freese P., Alexis M. S., Su A., Hochman M., Palden T., Bazile C., Lambert N.J., van Nostrand E.L., Pratt G.A., et al. // *Mol. Cell.* 2018. V. 70. № 5. P. 854–867.
111. Witten J.T., Ule J. // *Trends Genet.* 2011. V. 27. № 3. P. 89–97.
112. Taliaferro J.M., Lambert N.J., Sudmant P.H., Dominguez D., Merkin J.J., Alexis M.S., Bazile C., Burge C.B. // *Mol. Cell.* 2016. V. 64. № 2. P. 294–306.
113. Cusack S. // *Curr. Opin. Struct. Biol.* 1999. V. 9. № 1. P. 66–73.
114. Lewis H.A., Musunuru K., Jensen K.B., Edo C., Chen H., Darnell R.B., Burley S.K. // *Cell.* 2000. V. 100. № 3. P. 323–332.
115. Teplova M., Malinina L., Darnell J.C., Song J., Lu M., Abagyan R., Musunuru K., Teplov A., Burley S.K., Darnell R.B., Patel D.J. // *Structure.* 2011. V. 19. № 7. P. 930–944.
116. Du Z., Fenn S., Tjhen R., James T.L. // *J. Biol. Chem.* 2008. V. 283. № 42. P. 28757–28766.
117. Nag S., Goswami B., Das Mandal S., Ray P.S. // *Semin Cancer Biol.* 2022. V. 32. Pt 3. P. 286–297.
118. Schorr A.L., Mangone M. // *Int. J. Mol. Sci.* 2021. V. 22. № 21. P. 11618.
119. Hsiao Y.E., Bahn J.H., Yang Y., Lin X., Tran S., Yang E.W., Quinones-Valdez G., Xiao X. // *Genome Res.* 2018. V. 28. № 6. P. 812–823.
120. Rueter S.M., Dawson T.R., Emeson R.B. // *Nature.* 1999. V. 399. № 6731. P. 75–80.
121. Lev-Maor G., Sorek R., Levanon E.Y., Paz N., Eisenberg E., Ast G. // *Genome Biol.* 2007. V. 8. № 2. P. R29.
122. Solomon O., Oren S., Safran M., Deshet-Unger N., Akiava P., Jacob-Hirsch J., Cesarkas K., Kabesa R., Amariglio N., Unger R., et al. // *RNA.* 2013. V. 19. № 5. P. 591–604.

REVIEWS

123. Mazloomian A., Meyer I.M. // *RNA Biol.* 2015. V. 12. № 12. P. 1391–1401.
124. Xiao W., Adhikari S., Dahal U., Chen Y.S., Hao Y.J., Sun B.F., Sun H.Y., Li A., Ping X.L., Lai W.Y., et al. // *Mol. Cell.* 2016. V. 61. № 4. P. 507–519.
125. Liu N., Dai Q., Zheng G., He C., Parisien M., Pan T. // *Nature.* 2015. V. 518. № 7540. P. 560–564.
126. Warf M.B., Diegel J.V., von Hippel P.H., Berglund J.A. // *Proc. Natl. Acad. Sci. USA.* 2009. V. 106. № 23. P. 9203–9208.
127. Haque N., Will A., Cook A.G., Hogg J.R. // *Nucl. Acids Res.* 2023. V. 51. № 12. P. 6411–6429.
128. Martinez-Contreras R., Fiset J.F., Nasim F.U., Mad-den R., Cordeau M., Chabot B. // *PLoS Biol.* 2006. V. 4. № 2. P. e21.
129. Fiset J.F., Toutant J., Brisson S., Desgroseillers L., Chabot B. // *RNA.* 2010. V. 16. № 1. P. 228–238.
130. Ule J., Stefani G., Mele A., Ruggiu M., Wang X., Taneri B., Gaasterland T., Blencowe B.J., Darnell R.B. // *Nature.* 2006. V. 444. № 7119. P. 580–586.

Soft X-ray Microscopy in Cell Biology: Current Status, Contributions and Prospects

S. A. Golyshev¹, E. P. Kazakov¹, I. I. Kireev¹, D. G. Reunov², I. V. Malyshev²

¹Belozersky Institute of Physico-Chemical Biology, Lomonosov Moscow State University, Moscow, 119992 Russian Federation

²Institute of Physics of Microstructures RAS, Nizhny Novgorod, 603950 Russian Federation

E-mail: sergei.golyshev@belozersky.msu.ru

Received: September 30, 2023; in final form, November 27, 2023

DOI: 10.32607/actanaturae.26551

Copyright © 2023 National Research University Higher School of Economics. This is an open access article distributed under the Creative Commons Attribution License, which permits unrestricted use, distribution, and reproduction in any medium, provided the original work is properly cited.

ABSTRACT The recent advances achieved in microscopy technology have led to a significant breakthrough in biological research. Super-resolution fluorescent microscopy now allows us to visualize subcellular structures down to the pin-pointing of the single molecules in them, while modern electron microscopy has opened new possibilities in the study of protein complexes in their native, intracellular environment at near-atomic resolution. Nonetheless, both fluorescent and electron microscopy have remained beset by their principal shortcomings: the reliance on labeling procedures and severe sample volume limitations, respectively. Soft X-ray microscopy is a candidate method that can compensate for the shortcomings of both technologies by making possible observation of the entirety of the cellular interior without chemical fixation and labeling with an isotropic resolution of 40–70 nm. This will thus bridge the resolution gap between light and electron microscopy (although this gap is being narrowed, it still exists) and resolve the issue of compatibility with the former, and possibly in the near future, the latter methods. This review aims to assess the current state of soft X-ray microscopy and its impact on our understanding of the subcellular organization. It also attempts to look into the future of X-ray microscopy, particularly as relates to its seamless integration into the cell biology toolkit.

KEYWORDS X-ray microscopy, cell biology, soft X-ray, water window, cryotomography.

ABBREVIATIONS cryo-SXT – cryotomography in the soft X-ray range; SXM – soft X-ray microscopy; EM – electron microscopy (microscope), SMLM – single-molecule localization microscopy; STED – stimulated emission depletion; SIM/3D-SIM – structured illumination microscopy; ER – endoplasmic reticulum.

PRINCIPLES OF SXM AND HOW IT COMPARES WITH OTHER TYPES OF MICROSCOPY

The modern technologies used in microscopic research in biology make it possible to address a wide range of problems: from monitoring of the development of the whole embryos, through the localization of single molecules in a cell, to direct visualization of the structure of macromolecules in their native state [1–3]. The development of both light and electron microscopy is constantly expanding the range of possibilities for researchers; however, despite all the successes achieved so far, both approaches retain their fundamental limitations.

Light microscopy is developing towards improving fluorescent methods, whose main advantage is the high contrast of the resulting image, in combination with the highest selectivity and sensitivity of fluores-

cent labeling methods [4]. The exploitation of these features has made it possible to bypass the diffraction limit for the resolving power of light microscopes. In the widely used methods of super-resolution light microscopy, a resolution of about 30 nm is routinely achieved [1]. However, the advantages of fluorescence microscopy are also its limitations. While allowing the observation of labeled molecules and the structures formed by them, a fluorescent microscope does not show components that do not carry labels (*Fig. 1A,D*). It is difficult to use more than three or four fluorescent labels in one experiment, and “optical” contrast methods (phase-contrast and differential interference contrast microscopy) are significantly inferior to fluorescence in terms of resolving power (*Fig. 1A,D*). Resolution anisotropy is an important limitation of most fluorescent methods aimed at maximizing the

resolving power: in the axial direction, the resolving power is approximately two times worse than that in the focal plane.

A fundamental limitation of transmission electron microscopy is the mean free path of an electron in a substance, which at maximum does not exceed 300–500 nm; therefore, ultrathin sections of the object under study, with a thickness comparable to the mean free path of electrons, need to be prepared for TEM studies [5]. Chemical fixation is necessary for meeting this requirement, which alters the structure and composition of the sample [5, 6]. The need for examining a series of sections, sometimes up to hundreds of slices, makes it difficult to study the three-dimensional organization of a cell whose dimensions are two orders of magnitude greater than the allowable thickness of the sections. Various approaches are used to overcome this limitation, each being a compromise between the volume under study, resolving power, and labor costs [7].

There are even more limitations for cryo-electron tomography methods, whose main advantage is that the native structure and composition of the cell remain preserved. The peculiarities of sample preparation force researchers to focus on the naturally thin cell portions or prepare a single slice (a lamella 100–500 nm thick) from the cell using ion beam milling. Therefore, the main area of application of cryo-EM tomography is in the analysis of macromolecular complexes in their native environment [8].

The role of a method that to some extent allows one to overcome the aforementioned limitations is claimed by cryo soft X-ray tomography (cryo-SXT), which currently is the most advanced branch of biological soft X-ray microscopy (SXM) [9]. The characteristics of this method are as follows: (1) it provides resolution of ~ 50 nm, and (2) it can be used to examine objects approximately 10 μm in thickness without the need to prepare sections (3) in the near-native vitrified state and (4) without using additional contrast or selective labeling to identify a given set of subcellular structures.

The objectives of this review were to assess the principles of the method, the instrumental basis and contribution of soft X-ray microscopy to cell biology, identify the research areas for which the features of SXM are most suitable, and to discuss the prospects for further development and implementation of SXM in cell biology.

SXM uses X-ray radiation with a photon energy of ~ 500 eV (wavelengths from 2.3 to 4.4 nm), corresponding to the so-called “water transparency window.” In this energy range, oxygen atoms, and therefore water molecules, weakly absorb X-ray pho-

tons (depending on the wavelength, absorption ranges from 10 to 40% in a 1- μm thick layer of water). Therefore, a sample of up to 15 μm in thickness is suitable for research [10–12]. Under these conditions, atoms of carbon and other light elements become efficient generators of absorption contrast. Most modern synchrotrons can generate X-rays in this energy range with high luminous flux intensity [13].

An SXM station consists of a synchrotron source of X-ray photons, a monochromator, a focusing system that illuminates the output aperture (microscope light source), and the microscope *per se*, where either a zone plate or the so-called “capillary condenser” is used as a condenser. The condenser projects a reduced image of the synchrotron output aperture onto the sample. The sample is placed on a cryogenically cooled high-tilt stage with a precision positioning mechanism. A zone plate is used as an objective lens, projecting an enlarged image of the sample on the digital detector. The optical paths of such stations make it possible to generate images with a depth of focus of 1.5–10 μm , and the resolution of such installations can range from 30 to 70 nm [10, 13, 14]. Interchangeable zone plate lenses allow one to choose between depth of focus and resolving power [15].

With such a combination of the optical path parameters and thickness of the object, the image will therefore inevitably represent the sum of the projections of all intracellular structures, which is almost inaccessible for visual deciphering. Angular tomography becomes the most productive way to extract morphological data from such an image [16]. The high brightness of the synchrotron radiation source makes it possible to extract the necessary amount of data for tomographic reconstruction in a reasonable amount of time.

Meanwhile, soft X-ray photons do not propagate in air, which requires placing all optical elements of the installation and the specimen in vacuum [17]. Overcoming this technical difficulty was facilitated by advances in the instrumental base of cryo-electron microscopy: the advent of automated devices for cryofixation of biological objects via ultra-fast freezing by plunging them into liquid ethane. This way, water does not crystallize but becomes an amorphous solid: vitrifies (“vitrūm” from Latin “glass”) [18]. Such a sample, when its temperature is maintained at -180 – 100°C , is stable under vacuum and resists irradiation due to constant heat removal.

The second contribution of EM to the development of cryo-SXT was the creation of goniometric or tilting cryo-cooled sample holders for equipping cryo-EMs. These devices were adapted for use at some SXM stations intended for biological research, which consolidated the sample preparation procedure up to the

use of standardized “grids” for EM in SXM instruments, but also introduced limitations inherent in EM tomography: the progressive increase in the effective sample thickness with an increasing tilt angle and the fact that it becomes shaded by holder structures at high tilts [10–13]. A unique feature of the SXM station at the ALS synchrotron (USA) is a fully rotating capillary sample holder, manufactured specifically for this installation and allowing isotropic resolution to be achieved without the distortions caused by tilt angle limitations [10, 19]. Vitrification of a sample by immersion using an automated device is a quick process, although it requires a certain level of skill, and preparing a sample for cryo-SXT examination takes about four hours, even if the design of a sample holder device is particularly complex [19].

The image of a cell obtained using cryo-SXT is very similar to a low-magnification electron micrograph [9, 16, 20] (*Fig. 1*); therefore, software packages for working with EM are suitable for reconstructing the volume from tilt series, for segmentation, and for subsequent data analysis [12, 13, 20]. Specialized tools are also being developed for working with cryo-SXT data, performing image restoration, and increasing their information yield [21], thus lightening the most operator-dependent steps: segmentation of three-dimensional data, as well as isolation of the contours and surfaces of organoids from the array of “voxels” [22, 23].

Scanning transmission X-ray microscopes (STXM), operating in the soft X-ray range, are less commonly used by biologists. In these devices, the sample is placed on a scanning stage, which displaces it with respect to a finely focused beam, and the image is generated based on changes in the brightness of the passing beam from point to point, measured by a single-pixel detector [24, 25].

Hence, SXM, especially in the implementation of cryo-SXT, is a mature method (in terms of the development of its technical base) focused on solving biological tasks, operating on the cellular scale, and holding a special place at the intersection of the capabilities of light and electron microscopy (*Fig. 1*).

APPLICATIONS OF SX MICROSCOPY IN CELL BIOLOGY

Müller et al. [9] presented a catalog of images of intracellular structures recorded using cryo-SXT, such as the nuclear envelope, the nucleolus, mitochondria, lysosomes, ER, and other endomembranes. Cryo-fixed transformed mouse cells 6–12 μm thick were the study object. Electron microscopy images of the same structures were used as the controls. Müller et al. pointed out that membrane structures are clearly distinguishable and recognizable, since they are vis-

ually perceived in the same way as those recorded using EM, but protein components such as chromatin subdomains and nuclear bodies are much less distinguishable (which may be due to the choice of the wavelength for the image registration), not to mention ribosomes and cytoskeletal elements whose dimensions are near the limit of the instrument’s resolution. What progress has been made in the application of SXM in cell biology since this work has appeared and what results have been obtained?

A significant body of the published papers describes the application of the method to various types of cells: human and animal cells, normal or tumor cells, those infected with a virus or in contact with nanoparticles, etc. [22, 26–31], yeast [16, 26, 32], and bacteria [12] to test the suitability of the method or a specific SXM tool for solving problems related to the visualization of subcellular structures and compare SXM with light and electron microscopy. These studies, together with “proof of concept,” propose various improvements to or combinations of methods, such as correlating a fluorescent label with an SXM image [20, 28] or combining cryo-SXT with labeling of plasma membrane proteins with colloidal gold-labeled antibodies [29].

In parallel with the development of the methodology for correlation fluorescence and SXM analysis, Duke et al. [20] also studied the system of endosomes (vesicles involved in the intracellular digestion of substances absorbed from the outside) and autophagosomes encapsulating component cells subject to recycling. To identify autophagosomes, two fluorescent genetically encoded tags were applied and the entire endocytic compartment was labeled *in vivo* with colloidal gold-labeled antibodies captured by the cell by endocytosis. In the SXM image, endosomes are identified by gold particles inside and have transparent contents. Vesicles that fall into the zones of colocalization of fluorescent labels are distinguished by dense contents and a transparent halo, and they are correlated with autophagosomes. Using the correlation of fluorescent and SXM images, specialized zones of generation of numerous autophagosome precursors (omegasomes) in the ER were visualized for the first time. Simultaneously, it was confirmed that thin and long tubular connections between individual mitochondria appear in the mitochondrial system during starvation, which are used to initiate autophagy. This example of the analysis of systemic changes in a cell not only demonstrates the power of cryo-SXT in combination with light microscopy, but also generates new data and directly corroborates the results previously obtained using other methods.

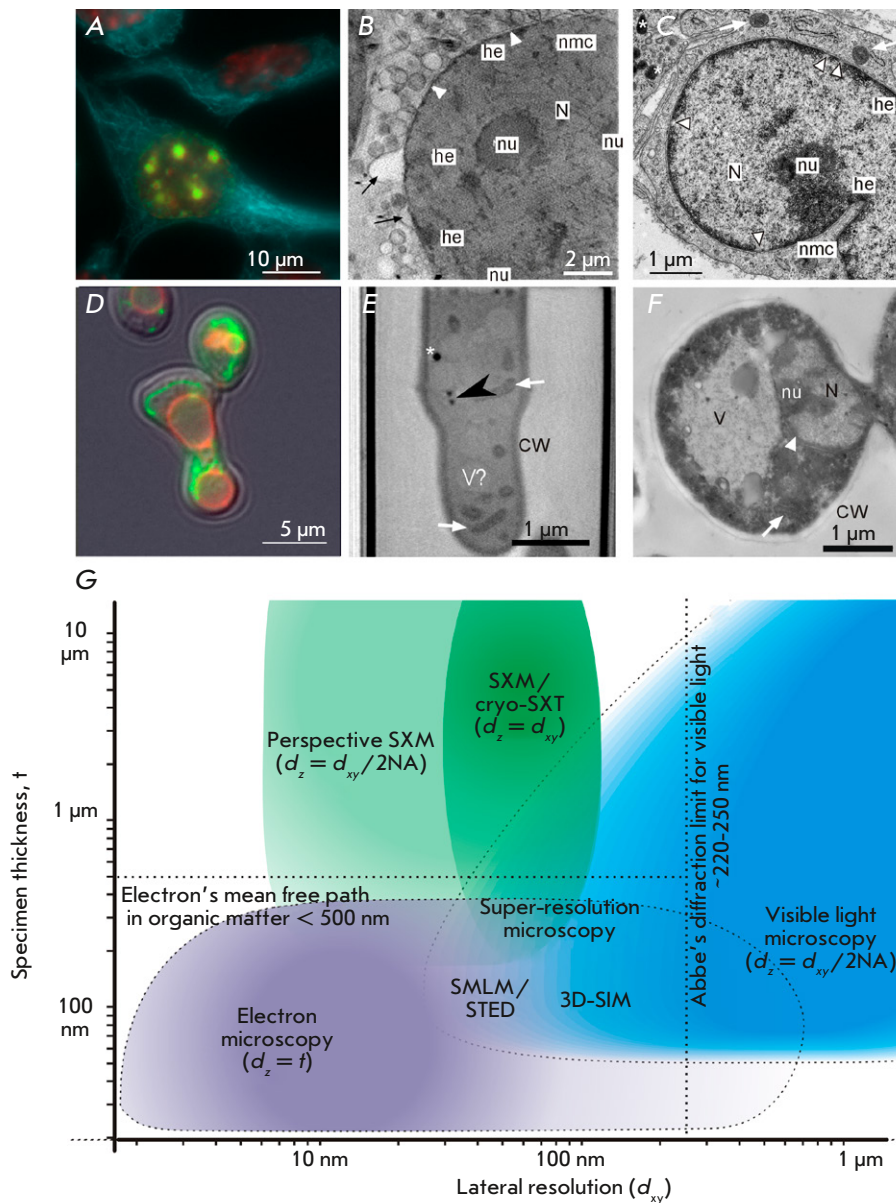


Fig. 1. Soft X-ray microscopy in comparison with visible light and electron microscopy. (A–C) – mammalian cells (mouse fibroblasts). (A) – fluorescent micrograph of whole chemically fixed mouse cells *in vitro*: blue – microtubules, fluorescent anti- α -tubulin antibodies; green – newly replicated DNA, click-reaction with ethynyl-deoxyuridine; red – nuclei, DNA-binding fluorescent dye DAPI. (B) – tomographic slice of cryofixed cell by cryo-SXT: N – nucleus, nu – nucleoli; he – heterochromatin, nmc – nuclear membrane channel, arrowheads – nuclear envelope, black arrows – outer nuclear membrane blebs (adapted with modifications from [11] CC 4.0 BY). (C) – EM micrograph of aldehyde-fixed heavy metal-stained cell: mouse connective tissue, ultrathin section: white arrow – mitochondria; * – lipid droplets. (D–F) – yeasts *S. cerevisiae*. (D) – fluorescent micrograph of a whole cell (zygote): green – mitochondria, chimeric mitochondrial protein Idh1-GFP; red – vacuolar membrane, FM4-64 fluorescent dye; cell outline – differential interference contrast (photo kindly provided by Knorre D.A.). (E) – tomographic slice of cryofixed cell by cryo-SXT: V – vacuole, CW – cell wall; black arrowhead – structure used for correlation of images, possibly – small lipid droplet, (adapted with modifications from [15] CC0 1.0). (F) – EM micrograph of aldehyde-fixed heavy metal-stained cell, ultrathin section. (G) – Soft X-ray, visible light and electron microscopy positions in a “resolution space.” Color intensity represents the scale in which each method is mostly demanded in the studies of the cellular structure and functions. NA – numeric aperture, the light-gathering capacity of the microscopes’ lens which, in combination with the wavelength (λ), is the determinant of the critical resolution: $d_{xy} = 0,61 \times \lambda/NA$ [4]. Photos A, C, F were taken by the authors of the review

The ability of cryo-SXT to allow one to visualize the entire cell volume, identify many subcellular systems, and measure organelle sizes without using contrast/labeling was employed to study the dynamics of the redistribution of mast cell secretory granules upon antigen stimulation [33] and the emptying of insulin vesicles in secretory pancreatic cells in response to glucose stimulation [34]. It was also used to visualize and quantify pre-apoptotic changes under the influence of the anticancer agent cisplatin, in combination with adjuvants to reduce its effective concentration [35], as well as to estimate the average volume of mitochondrial fragments in cancer cells after exposure to the free radicals generated by an iridium-based photosensitizer [36]. Finally, that capacity was used to measure the mitochondrial volume, the radius of lipid droplets and cytoplasmic vesicles when cells are infected with the SARS-CoV-2 virus [37], to analyze the redistribution of cytoplasmic vesicles and changes in the mitochondrial morphology under the influence of the herpes simplex virus [22], and to collect quantitative parameters on the response of endothelial cells to glucose stimulation (the *in vitro* model of vascular damage processes in diabetes) [38].

Along with the feasibility of carrying out morphometry at the whole-cell level, cryo-SXT allows one to capture new and often unexpected structural aspects of the studied phenomena, such as the formation of thin (at the threshold of the resolving power of CTMR), thread-like outgrowths of the ER cisterns that are formed in the contact areas between the ER and mitochondria [39]. Such areas are marked by clusters of the proteins involved in mitochondrial fission and are detected using fluorescent chimeric constructs.

Cryo-SXT was applied to visualize mitochondrial fragmentation, increase the number of lipid droplets, and cytoplasmic vacuolation in mammalian and yeast cells upon exposure to gold nanoparticles and gold ions [40, 41]. It has also been shown that a small fraction of gold nanoparticles taken up by the cell ends up in the cytoplasm rather than in the endosomal-lysosomal compartment. Their number is too small to be detected by their fluorescent signal and to be effectively detected in ultrathin sections by EM methods. In addition, some particles were detected in lipid droplets, which is unusual [40].

Biogenic gold nanoparticles, which are formed by yeast cells and are subsequently released into the periplasmic space, were also discovered and identified using cryo-SXT. The identification of these particles required the use of additional physical methods of measurement, and the localization of particles, includ-

ing in mitochondria (for the first time), was additionally confirmed by EM [41].

The existence of such structures and phenomena cannot be assumed *a priori*; they are not resolved by light microscopy, and their accidental detection by electron microscopy is extremely unlikely or can be ignored even if it had happened.

Sometimes changes in cell physiology (e.g., the development of a pathology at the cellular level) lead to the formation of new structures with dimensions that are comparable to the cell *per se*, thus significantly impeding their detailed analysis and topology identification by EM methods, while their fine organization lies beyond the resolution of light microscopy. An example of this is the transformation of the ER when cells are infected with the hepatitis C virus, when the endoplasmic reticulum is transformed into a spongy labyrinth of membrane channels that occupy almost the entire cytoplasm [42, 43]. A detailed analysis of the geometry of membrane channels during this transformation on a cell-wide scale was carried out by cryo-SXT [30]. Changes in the contacts of the ER with mitochondria, the cell's energy sources and important participants in lipid metabolism, which also change during viral infection, were studied simultaneously. Cryo-SXT allowed Pérez-Berná [30] to analyze the dynamics of ER transformation and show that the transformation begins locally but involves both the ER and mitochondria, starting from the onset [30].

Jamme et al. [44] used cryo-SXT to show that wild-type yeast cells and mutants producing only triacylglycerols form homogeneous lipid droplets that efficiently absorb soft X-ray photons, and, in cells producing sterol ethers only, lipid droplets have a transparent core that is surrounded by a highly absorbing shell. By combining the cryo-SXT data with the findings obtained using other non-invasive techniques, Jamme et al. confirmed the idea that lipid droplets have a layered structure with a triacylglycerol-based core and a shell formed by sterol ethers. This two-layer model was proposed based on studies of isolated lipid droplets, but the isolation procedure may have caused lipid redistribution, which did not make the result entirely convincing.

Not only organic matter density in organelles, but other factors, as well, can be an indicator of organelle composition. By varying the wavelength of soft X-ray photons, one can identify elements that have absorption peaks in the range of water transparency, estimate their concentration, and determine their state in crystalline particles and the zones of their specific concentration. This makes it possible to use SXM to study processes such as tissue mineralization, the formation of shells and spicules in invertebrates, and the

absorption and excretion of nanoparticles and other nanoconstructs from cells by using the features of their composition as an additional criterion for their identification.

Thus, nitrogen distribution and the carbon-to-nitrogen ratio in the cells of *Anabena* sp. were visualized using radiation with energies greater and lower than the nitrogen absorption edge (410 eV) [45]. Under nitrogen starvation conditions, these blue-green algae form specialized cells (heterocysts) that fix atmospheric nitrogen. Using the resolving power of SXM, Teramoto et al. [45] were able to identify vegetative cells and heterocysts and analyzed the studied parameter with respect to the cell type, which had not been done previously. In both cell types, elements are distributed unevenly, the carbon-to-nitrogen ratio increases from the cell periphery towards its center, but the peripheral zone of heterocysts had a nitrogen-rich layer, which is not observed in vegetative cells.

Research into the calcium accumulation pathways (absorption edges at 352.6 and 338.3 eV) in the cells of unicellular algae forming calcite inclusions and in the mesenchymal cells of sea urchin larvae forming spicules composed of calcium carbonate showed that, despite the difference in models, both algae and echinoderm larvae have specialized vesicles that concentrate calcium ions from seawater and act as an intermediate depot for this ion [46, 47]. In algae, it is a single, large “vacuole-like” cistern [46], and the cells of sea urchin larvae contain a population of vesicles ~ 100 nm in diameter, containing calcium ion at concentrations ranging from 1 M (lower limit of detection) to a concentration corresponding to anhydrous amorphous calcium carbonate, which the spicules are composed of. SXM made it possible to accurately count the number of calcium-containing vesicles [47].

When mammalian cells absorb hydroxyapatite nanoparticles, which stimulate bone tissue regeneration, fluorescent calcium sensors show that a population of calcium-containing vesicles appears in the cells, but electron microscopy does not allow them to be identified against the background of the general population of vesicles in cells [48]. The use of cryo-SXT and analysis of the linear absorption coefficients of organelles made it possible to isolate internalized nanoparticles and identify lipid droplets and a separate population of vesicles with intermediate absorption efficiency. This correlated with multivesicular bodies; their absorption coefficient was linked to the possibility of depositing calcium ions released during nanoparticle dissolution [48].

High density and, therefore, increased contrast in cryo-SXT images is a distinctive feature of some intracellular pathogens and symbionts. This fact is ef-

ficiently used by researchers investigating the life cycles of these organisms and their interactions with cells. When studying the formation of cowpox (*Vaccinia*) virions and the structures that appear in infected cells, it became possible to distinguish between mature and immature virion forms and discover “viral factories” in which replication of viral genomes occurs [49].

Kördel et al. [50] studied the transfer of a substance from the host cell to the virus during the development of an unidentified giant DNA virus (presumably Cedratvirus) infecting the amoeba *Acanthamoeba castellanii*. Updated data were obtained on the number of virions formed during viral replication. Based on measurements of the absorption coefficients, the earlier estimates of material transfer obtained by less accurate and indirect methods have been corrected. It has been shown that 6–12% of the host cell substance is converted into virions. A structure has been discovered which may potentially be a viral replication factory. It has been shown that the changes affect the contractile vacuole and phagosomes, but not the nucleus, which allows the cell to function until lysis, increasing the efficiency of virus production [50]. The linear dependence of absorption coefficients on the organic matter concentration, visualized in cryo-SXT images, combined with the ability to process the entire cell volume, makes cryo-SXT a preferred tool for conducting this type of research, compared to EM, which allows the detection of much smaller virions but imposes restrictions on sample volumes. Nevertheless, EM is a necessary additional tool for this kind of work, which is directly noted by the authors of the cited publications.

Semi-automatic image segmentation, followed by measurement of the volumes of bacterial cells, showed that each intracellular “inclusion” (a vacuole in which the human pathogenic bacteria *Chlamydia trachomatis* proliferate) contains a much wider range of cell forms than estimated previously [51], according to the EM analysis of serial sections (inclusion diameter being 10–15 μm). Counting the amount of chlamydia in the inclusions showed that the volume of individual bacterial cells, which is the main criterion used to separate infectious from proliferating forms of chlamydia, depends on their concentration rather than the absolute amount. The more densely a vacuole is populated, the less often large and abnormally large cells are found in it, which means that cell concentration can be a signal of a transition from a large reproducing form to a small infectious one, all combined with host cell lysis and the next cycle of infection.

Hale et al. [52], by using inhibition assay and stopping the release of the mature asexual cells (merozo-

ites) of *Plasmodium falciparum* from erythrocytes at various stages of this process, employed cryo-SXT as an auxiliary technique complementing both light and electron microscopy data. It was shown that the release of merozoites into the bloodstream with erythrocyte destruction, causing a fever attack in malaria, is strictly coordinated in time. Before the erythrocyte destruction, (1) disintegration of the vacuole membrane in which the merozoites are produced and release of mature merozoites into the erythrocyte cytoplasm occur, followed by (2) a collapse of the erythrocyte cytoskeleton, leading to the loss of their characteristic shape and formation of close contacts between the plasma membranes of the erythrocyte and merozoites, and (3) only then does a new generation of merozoites enter the blood. Here, cryo-SXT is a kind of control procedure supporting the light microscopy data with structural data characterized by a better resolution and allowing one to minimize interpretation errors associated with the features of sample preparation for EM.

A study of the changes at the level of individual organelles occurring in cells during the *Shigella flexneri* infection using a combination of fluorescence microscopy and cryo-SXT showed that mitochondrial fragmentation takes place in cells during the infection [53]. Correlation of light microscopy and cryo-SXT data made it possible to visualize a “trap” of septins (proteins involved in the remodeling of membranes, the cytoskeleton, and encapsulation of intracellular pathogens [54]) around *Shigella* cells, as well as its close connection with the autophagosome.

The study focusing on the coordination mechanisms of host and symbiont division in *Braarudosphaera bigelowii*, a unicellular alga whose cells obligately contain an endosymbiont, a cyanobacterium with a highly reduced genome that cannot exist independently but has a mechanism for nitrogen fixation, looks extremely interesting. This symbiosis may be an intermediate evolutionary phase of the symbiogenetic formation of a new organelle (a “nitroplast”), as once happened with mitochondria. The use of cryo-SXT as the main tool in this study seems quite justified, taking into account the sizes of the organism and symbiont (approximately $10 \times 5 \mu\text{m}$ and $4 \times 2 \mu\text{m}$, respectively) and the high contrast between the symbiont and the chloroplasts and mitochondria of the host cell [55].

It is noteworthy that in most of the studies discussed above, the researchers focused on an inherent limitation of lipid-rich organelles: lipid droplets, mitochondria, ER cisterns, etc. Meanwhile, very little attention has been paid to such an important area as research into the ultrastructure and functioning of the cell nucleus and the genetic apparatus. This was

because the efficiency of absorption of SX photons by lipids is high, making them stand out against the background of the cytoplasm [9, 11], and variations in the absorption coefficient inside the cell nucleus are insignificant; so, it becomes possible to distinguish only such large and dense formations as the nucleolus and heterochromatic blocks against the background of euchromatin [28, 56]. Meanwhile, the resolving power of the method is still insufficient in order to visualize chromatin substructures with dimensions around 100 nm or less [57]. The attempts at spectral separation of DNA, RNA, and proteins in SXM images of nuclei and chromosomes [25] offer hope for significant improvement in the contrast of nucleic acids, which will open up new opportunities in studying nuclear structures using the SXM methods. The late stages of compaction of individual chromosomes during the preparation of a eukaryotic cell for division, chromatid segregation before their distribution to daughter cells, and the initial stages of chromosome de-condensation during the formation of daughter nuclei are currently considered the most suitable for research using cryo-SXT.

SXM and super resolution fluorescence microscopy

Correlative light and electron microscopy, including cryo-format, are already a well-tested combination of methods [58–60]. Since cryo-SXT borrows many aspects of sample preparation from cryo-electron microscopy, it is understandable that the integration of conventional fluorescent methods and cryo-SXT has been implemented and is used to solve routine problems, primarily for localizing an object of interest with a fluorescence microscope integrated into a SXM-station before implementing cryo-SXT [11, 61]. Meanwhile, the current level of development of fluorescence microscopy in its super-resolution versions makes it possible to achieve a resolution of 100–150 nm for structured illumination microscopy and ~30 nm for SMLM and STED [1, 62], which is already comparable to the resolution of SXM.

It looks very promising to combine super-resolution light microscopy in the STED and SMLM variants with SXM. This combination of methods will potentially allow one not only to localize the molecular sources of the fluorescent signal with an accuracy of 20 nm, but also to correlate them with intracellular structures that do not carry a fluorescent label using SXM.

SMLM, combined with cryo-SXT, has been resorted to for localizing and studying the fine structure and dynamics of cholesterol crystals in a cellular model of atherosclerosis [63, 64]. Lipids have a high linear absorption coefficient in SXM [9]. So, lipid structures

offer the most contrast in SXM images, but it is impossible to identify cholesterol in an overall lipid context. SMLM makes it possible to fluorescently label cholesterol and perform high-resolution studies of its distribution, albeit without reference to specific sub-cellular structures. With this approach, the resolution of the light component is superior to that achieved using X-ray methods: Varsano et al. [63] claimed it to be 35 nm vs. 70 nm [63].

A combination of methods made it possible to correlate the fluorescent label with structures on the plasmalemma sharply outlined in the SXM image, as well as with the surface of lipid droplets in the cytoplasm [63], and to track the movement of the crystalline structures formed by cholesterol in the cell, identifying them against the background of other lipid structures [64]. However, this integration of methods is not flawless. SMLM requires many, sometimes tens of thousands, albeit short exposures, so image registration takes considerable time. Furthermore, artificial conditions are required for implementing the mechanisms of reversible quenching and return of fluorophore molecules to the “light” state [62]. Therefore, Schermelleh [62] performed SMLM on aldehyde-fixed cells using a standard microscope, and only after that was the specimen subjected to vitrification and cryo-SXT performed. The limitations in this case include not only the need to fix the cell to implement SMLM registration, but also the fact that the carriers of fluorescence are antibodies that penetrate membranes slowly and ineffectively, which forced the authors to focus on the plasmalemma, where the target was accessible to antibodies, and make do with a low signal intensity in the cytoplasm. The combination of SMLM and cryo-SXT is attractive due to its comparable resolving power in both modalities, but the combination of limitations may be critical for further development of this approach.

The second option is to use a limited super-resolution SIM system, in combination with cryo-SXT, both image registration procedures being implemented in the cryo format. SIM allows one to work with fluorescent proteins, and, therefore, it makes it possible to directly combine light and SXM images.

The cryo format makes the use of high-aperture immersion objectives extremely difficult, although not impossible [65, 66]. To solve this problem, a specialized cryo-SIM microscope was integrated into the SXM station, in which the 3D-SIM technology using a “dry” lens with a numerical aperture of 0.9 and a large working distance allow one to obtain images with a resolution of 210 nm (diffraction limit being ~ 340 nm) without transferring heat to a sample kept at cryogenic temperatures [67].

The combination of cryo-3D-SIM and cryo-SXT was used to study the dynamics of endosomes containing reovirus particles during infection [66]. Cryo-3D-SIM allowed the authors to visualize vesicles of various sizes and distinguish between vesicles carrying virus particles and vesicles from which the viral complex was released. The efficient rejection of out-of-focus luminescence and the better axial resolution of 3D-SIM compared to diffraction-limited microscopy [62] made it possible to accurately correlate the fluorescent signal from labeled vesicles with the structures observed in the cryo-SXT image. The key observation was that the egress of the virus does not disrupt the endosomes, leaving their shape round and their membranes intact. As suggested [62], virions can leave endosomes due to the formation of collapsible pores in the membranes.

3D-SIM was used to localize bundles of actin filaments in the SXM image. These filaments poorly absorb X-ray photons and are, therefore, virtually invisible; however, highly detailed fluorescent data allows one to accurately identify the zone where the actin structures are located and identify their intracellular environment using SXM [68].

To solve similar problems related to correlating fluorescence and X-ray images, a unique “laser scanning confocal cryo-tomograph” with an immersion lens was built using a full-rotating cryo-sample holder from a complementary cryo-SXT instrument [28]. The microscope was tested on a model of localization and visualization of the Barr body (inactivated X chromosome) in female mouse cells and became an essential part of the SXM station at the ALS synchrotron (USA) [39].

An obvious application of this combination of methods is the identification of X-ray images of intracellular structures that have either been poorly characterized or not characterized at all, for which protein markers are available, especially in connection with work focusing on creating “X-ray atlases” of cell morphology [9, 11]. Despite the general similarity of EM and SXM images, not all structures are displayed in the same way due to differences in sample preparation. All that is left to do is wait for the design of a cryo-3D-SIM installation with an immersion lens integrated into the SXM station.

PROSPECTS FOR SXM

A promising SXM tool

An alternative to the optical design with zone plates, which has become the industry standard in cryo-SXT, can be the use of normal-incidence mirror lenses optimized for the wavelengths of the water transparency window [69]. Calculations show that such a

microscope, with a completely achievable numerical aperture of 0.3 [70] (vs. ~ 0.05 – 0.06 for the zone plates) at a wavelength of 3.37 nm will allow for a lateral resolution of ~ 5 nm, which is an order of magnitude better than the standard achievable 40–70 nm in cryo-SXT and lies in the range previously accessible only by EM. This tool is currently a laboratory prototype and has not yet reached its design parameters; however, the functionality of all elements of the system has been demonstrated.

An inherent limitation of this instrument is the anisotropic resolution associated with stretching of the point spread function along the main optical axis of the device, like in a visible light microscope [71]. The same simple calculation shows that the axial resolution of such an instrument will approach 40 nm, which is somewhat better than when working on an EM in normal mode, where the axial resolution is equal to the thickness of the physical slice, very rarely reaching 50 nm (usually thicker) (Fig. 1). The shallow depth of focus of this SXM significantly complicates the implementation of angular tomography, so that for three-dimensional reconstruction, simpler algorithms for volume reconstruction from a series of optical sections (z-tomography) using deconvolution [72–74], like for widefield and confocal visible light microscopes, become optimal. Proper choice of the deconvolution algorithm and its parameters can partially compensate for the resolution anisotropy, but eliminating it completely will be impossible because of its fundamental nature.

Based on this optical scheme, a design for an SXM station was proposed [71] for the SKIF synchrotron source (“Siberian Circular Photon Source”) that is currently under construction. The project involves two operating modes: scanning using a lens with a numerical aperture of 0.3 to illuminate the sample with a beam focused onto a spot of diffraction dimensions, with registration of variations in the brightness of the passing beam with a single-pixel detector when scanning by displacing the sample relative to the beam, and a widefield mode in which a second lens builds an image sample on the matrix detector. It is planned that the instrument will be equipped with a cryo-stage for biological applications.

Potentially, due to its short focal distance and the small thickness of the optical section and high light-collecting ability, which in turn reduces the radiation dose required to obtain an image, this SXM in the widefield mode will allow one to observe dynamic processes in living cells isolated from vacuum in an enclosed fluidic microchamber. The question of the practical feasibility of such observations remains open.

Selective labels for SXM

Light microscopy offers a wide array of methods for highly selective labeling of subcellular structures and biomolecules (fluorescently labeled antibodies, constructs with fluorescent proteins, high-specificity fluorescent dyes, etc.) (Fig. 1A,D). In contrast, electron microscopy largely relies on morphological criteria, accumulated through the decades of EM development, for identifying the observed structures. Selective labeling techniques in EM are less varied and not as reliable as those in light microscopy. SXM in general and cryo-SXT, during its development, may turn out to be in the same situation.

To be compatible with cryofixation, selective imaging techniques should not affect cell viability when functioning *in vivo*. If any auxiliary action is required to visualize the labeled structure (e.g., fixation), the question immediately arises: is the “native state” of the cell preserved? Moreover, such a label must efficiently generate contrast when using radiation in which the biological matter is transparent and, therefore, must differ drastically from the “living matter” in terms of structure or composition. In the study by Kong et al. [75], a protein localization system developed for EM based on chimeric constructs with peroxidases and photoactivatable proteins that generate reactive oxygen species was adapted for SXM. Visualization of the label is achieved by oxidation of diaminobenzidine (DAB), facilitated by the labeled protein. DAB penetrates the plasmalemma of both fixed and living cells [76]. Its insoluble oxidized form is locally deposited and efficiently absorbs soft X-ray photons due to the high density of the DAB precipitate [75]. The technique involves aldehyde fixation before “developing” the label with a solution of DAB and hydrogen peroxide; however, unlike the EM version of this method, the SXM version does not require additional contrasting with OsO_4 [76]. The use of the free radical generator protein miniSOG, instead of peroxidase, does not require incubation with hydrogen peroxide; it is activated by irradiation with visible light [75]. Obviously, the protocol can be combined with other proposed labeling systems [20, 63].

CONCLUSION

With all its features and the relatively “young age” of the method, soft X-ray microscopy (primarily in the implementation of cryo-tomography) has productively been added to the toolkit of cell biology. The most promising direction for its further development seems to be closer integration of cryo-SXT imaging and super resolution light microscopy. The development of genetically encoded tags, especially “multimodal” ones, capable of generating both a fluorescent signal and

absorption contrast in SX, will add wholly new possibilities to this promising combination of methods, allowing researchers to switch from correlation and purely morphological criteria in ultrastructural analysis to direct consideration of the molecular aspects of the structure and dynamics of subcellular systems. We remain hopeful that the current technical challenges discussed above will be overcome and such a combined approach will become practically accessible.

It can be envisioned that in the future there will be a closer convergence of SXM with cryo-EM. For example, integration of a focused ion beam source into a cryo-SXT instrument will enable cryo-SXT navigation to produce lamellae for cryo-EM tomography including objects of interest. Ideally, this integration will result in a “seamless pipeline” that allows comprehensive interrogation of cell structure and function across a full range of scales and resolutions, leveraging the strengths of all the available microscopic techniques.

The main “infrastructural” problems of cryo-SXT that remain unresolved are the need for expensive equipment for sample cryofixation during its preparation and a limited number of SXM installations at large synchrotron sources, each of which is unique in its own way. These factors limit the affordability of the method. The construction of new X-ray sources, including SKIF installations with an already planned

X-ray microscopy station and RIF (“Russian Photon Source”) in the Russian Federation, will lead to a significantly deeper integration of SXM into research practice.

The emergence of sufficiently bright laser-plasma sources of soft X-ray photons has spurred attempts to create “laboratory-level” devices [31, 32, 77] to uncouple SXM instruments from the “mega-science” installations. So far, these efforts are of a design and exploratory nature, but the creation of a commercially distributed SXM, comparable in price and operating costs to biological EM, should make SXM methods as popular as light and electron microscopy. Designing a laboratory cryo-SXT microscope with high-aperture optics and a resolution of 5–7 nm can potentially dislodge EM from the position of the primary method of ultrastructural imaging, leaving it only as a segment of near-atomic resolution. ●

The authors would like to express their gratitude to D.A. Knorre for providing the images and authors who permit to use their works based on a Creative Commons license.

The work was carried out with the financial support of the Russian Science Foundation (grant No. 22-62-00068).

REFERENCES

- Schermelleh L., Ferrand A., Huser T., Eggeling C., Sauer M., Biehmaier O., Drummen G.P.C. // *Nat. Cell Biol.* 2019. V. 21. № 1. P. 72–84.
- Wu Y., Shroff H. // *Histochem. Cell. Biol.* 2022. V. 158. № 4. P. 301–323.
- Saibil H.R. // *Mol. Cell.* 2022. V. 82. № 2. P. 274–284.
- Murphy D., Davidson M. *Fundamentals of Light Microscopy and Electronic Imaging.* Wiley-Blackwell, 2013. 538 p.
- Knott G., Genoud C. // *J. Cell Sci.* 2013. V. 15. № 126(Pt 20). P. 4545–4552.
- Osumi M. // *J. Electron. Microsc. (Tokyo).* 2012. V. 61. № 6. P. 343–365.
- Peddie C.J., Genoud C., Kreshuk A., Meehan K., Micheva K.D., Narayan K., Pape C., Parton R.G., Schieber N.L., Schwab Y., et al. // *Nat. Rev. Meth. Primers.* 2022. V. 2. P. 51.
- Wagner J., Schaffer M., Fernández-Busnadiego R. // *FEBS Lett.* 2017. V. 591. № 17. P. 2520–2533.
- Müller W.G., Heymann J.B., Nagashima K., Guttman P., Werner S., Rehbein S., Schneider G., McNally J.G. // *J. Struct. Biol.* 2012. V. 177. № 2. P. 179–192.
- Le Gros M.A., McDermott G., Cinquin B.P., Smith E.A., Do M., Chao W.L., Naulleau P.P., Larabell C.A. // *J. Synchrotron Radiat.* 2014. V. 21. № 6. P. 1370–1377.
- Groen J., Conesa J.J., Valcárcel R., Pereiro E. // *Biophys. Rev.* 2019. V. 11. № 4. P. 611–619.
- Cossa A., Wien F., Turbant F., Kaczorowski T., Węgrzyn G., Arluison V., Pérez-Berná A.J., Trépout S., Pereiro E. // *Methods Mol. Biol.* 2022. V. 2538. P. 319–333.
- Carzaniga R., Domart M.C., Collinson L.M., Duke E. // *Protoplasma.* 2014. V. 251. № 2. P. 449–458.
- Loconte V., Chen J.H., Vanslebrouck B., Ekman A.A., McDermott G., Le Gros M.A., Larabell C.A. // *FASEB J.* 2023. V. 37. № 1. P. e22681.
- Weinhardt V., Chen J.H., Ekman A.A., Guo J., Remesh S.G., Hammel M., McDermott G., Chao W., Oh S., Le Gros M.A., Larabell C.A. // *PLoS One.* 2020. V. 15. № 1. P. e0227601.
- Liu J., Li F., Chen L., Guan Y., Tian L., Xiong Y., Liu G., Tian Y. // *J. Microsc.* 2018. V. 270. № 1. P. 64–70.
- Reinhard J., Kaleta S., Abell J.J., Wiesner F., Wünsche M., Seemann E., Westermann M., Weber T., Nathanael J., Iliou A., et al. // <https://doi.org/10.48550/arXiv.2304.14413>.
- Studer D., Humbel B.M., Chiquet M. // *Histochem. Cell. Biol.* 2008. V. 130. № 5. P. 877–889.
- Chen J.H., Vanslebrouck B., Loconte V., Ekman A., Cortese M., Bartenschlager R., McDermott G., Larabell C.A., Le Gros M.A., Weinhardt V. // *STAR Protoc.* 2022. V. 3. № 1. P. 101176.
- Duke E.M., Razi M., Weston A., Guttman P., Werner S., Henzler K., Schneider G., Tooze S.A., Collinson L.M. // *Ultramicroscopy.* 2014. V. 143. № 100. P. 77–87.
- Guzzi F., Gianoncelli A., Billè F., Carrato S., Kourousias G. // *Life (Basel).* 2023. V. 13. № 3. P. 629.

22. Nahas K.L., Fernandes J.F., Vyas N., Crump C., Graham S., Harkiolaki M. // *Biol. Imaging*. 2022. V. 2. P. e3.
23. Dyhr M.C.A., Sadeghi M., Moynova R., Knappe C., Kepsutlu Çakmak B., Werner S., Schneider G., McNally J., Noé F., Ewers H. // *Proc. Natl. Acad. Sci. USA*. 2023. V. 120. № 24. P. e2209938120.
24. Lühl L., Andrianov K., Dierks H., Haidl A., Dehlinger A., Heine M., Heeren J., Nisius T., Wilhein T., Kanngießner B. // *J. Synchrotron Radiat*. 2019. V. 26. № 2. P. 430–438.
25. Shinohara K., Toné S., Ejima T., Ohigashi T., Ito A. // *Cells*. 2019. V. 8. № 2. P. 164.
26. Larabell C.A., Nugent K.A. // *Curr. Opin. Struct. Biol*. 2010. V. 20. № 5. P. 623–631.
27. Chiappi M., Conesa J.J., Pereiro E., Sorzano C.O., Rodríguez M.J., Henzler K., Schneider G., Chichón F.J., Carrascosa J.L. // *J. Nanobiotechnol*. 2016. V. 14. P. 15.
28. Smith E.A., McDermott G., Do M., Leung K., Panning B., Le Gros M.A., Larabell C.A. // *Biophys. J*. 2014. V. 107. № 8. P. 1988–1996.
29. Niclis J.C., Murphy S.V., Parkinson D.Y., Zedan A., Sathananthan A.H., Cram D.S., Heraud P. // *J. R. Soc. Interface*. 2015. V. 12. № 108. P. 20150252.
30. Pérez-Berná A.J., Rodríguez M.J., Chichón F.J., Friesland M.F., Sorrentino A., Carrascosa J.L., Pereiro E., Gastaminza P. // *ACS Nano*. 2016. V. 10. № 7. P. 6597–6611.
31. Fahy K., Weinhardt V., Vihinen-Ranta M., Fletcher N., Skoko D., Pereiro E., Gastaminza P., Bartenschlager R., Scholz D., Ekman A., et al. // *J. Phys. Photonics*. 2021. V. 3. P. 031002.
32. Carlson D.B., Gelb J., Palshin V., Evans J.E. // *Microsc. Microanal.* 2013. V. 19. № 1. P. 22–29.
33. Chen H.Y., Chiang D.M., Lin Z.J., Hsieh C.C., Yin G.C., Weng I.C., Guttman P., Werner S., Henzler K., Schneider G., et al. // *Sci. Rep*. 2016. V. 6. P. 34879.
34. White K.L., Singla J., Loconte V., Chen J.H., Ekman A., Sun L., Zhang X., Francis J.P., Li A., Lin W., et al. // *Sci. Adv*. 2020. V. 6. № 50. P. eabc8262.
35. Gil S., Solano E., Martínez-Trucharte F., Martínez-Esaín J., Pérez-Berná A.J., Conesa J.J., Kamma-Lorger C., Alsina M., Sabés M. // *PLoS One*. 2020. V. 15. № 3. P. e0230022.
36. Bolitho E.M., Sanchez-Cano C., Huang H., Hands-Portman I., Spink M., Quinn P.D., Harkiolaki M., Sadler P.J. // *J. Biol. Inorg. Chem*. 2020. V. 25. № 2. P. 295–303.
37. Loconte V., Chen J.H., Cortese M., Ekman A., Le Gros M.A., Larabell C., Bartenschlager R., Weinhardt V. // *Cell. Rep. Methods*. 2021. V. 1. № 7. P. 100117.
38. Scrimieri R., Locatelli L., Cazzaniga A., Cazzola R., Malucelli E., Sorrentino A., Iotti S., Maier J.A. // *Sci. Rep*. 2023. V. 13. № 1. P. 15133.
39. Elgass K.D., Smith E.A., LeGros M.A., Larabell C.A., Ryan M.T. // *J. Cell Sci*. 2015. V. 128. № 15. P. 2795–2804.
40. Kepsutlu B., Wycisk V., Achazi K., Kapishnikov S., Pérez-Berná A.J., Guttman P., Cossmer A., Pereiro E., Ewers H., Ballauff M., et al. // *ACS Nano*. 2020. V. 14. № 2. P. 2248–2264.
41. Dang Z., Tao X.Y., Guan Y., Wu Z., Xiong Y., Liu G., Tian Y., Tian L.J. // *ACS Nano*. 2023. V. 17. № 10. P. 9069–9081.
42. Egger D., Wölk B., Gosert R., Bianchi L., Blum H.E., Moradpour D., Bienz K. // *J. Virol*. 2002. V. 76. № 12. P. 5974–5984.
43. Asselah T., Bièche I., Mansouri A., Laurendeau I., Cazals-Hatem D., Feldmann G., Bedossa P., Paradis V., Martinot-Peignoux M., Lebre C., et al. // *J. Pathol*. 2010. V. 221. № 3. P. 264–274.
44. Jamme F., Cinquin B., Gohon Y., Pereiro E., Réfrégiers M., Froissard M. // *J. Synchrotron Radiat*. 2020. V. 27. № 3. P. 772–778.
45. Teramoto T., Azai C., Terauchi K., Yoshimura M., Ohta T. // *Plant Physiol*. 2018. V. 177. № 1. P. 52–61.
46. Sviben S., Gal A., Hood M.A., Bertinetti L., Politi Y., Bennet M., Krishnamoorthy P., Schertel A., Wirth R., Sorrentino A., Pereiro E., Faivre D., Scheffel A. // *Nat. Commun*. 2016. V. 7. P. 11228.
47. Kahil K., Varsano N., Sorrentino A., Pereiro E., Rez P., Weiner S., Addadi L. // *Proc. Natl. Acad. Sci. USA*. 2020. V. 117. № 9. P. 30957–30965.
48. Bonany M., Pérez-Berná A.J., Dučić T., Pereiro E., Martín-Gómez H., Mas-Moruno C., van Rijt S., Zhao Z., Espanol M., Ginebra M.P. // *Biomater. Adv*. 2022. V. 142. P. 213148.
49. Chichón F.J., Rodríguez M.J., Pereiro E., Chiappi M., Perdiguero B., Guttman P., Werner S., Rehbein S., Schneider G., Esteban M., et al. // *J. Struct. Biol*. 2012. V. 177. № 2. P. 202–211.
50. Kördel M., Svenda M., Reddy H.K.N., Fogelqvist E., Arsana K.G.Y., Hamawandi B., Toprak M.S., Hertz H.M., Sellberg J.A. // *Sci. Rep*. 2021. V. 11. № 1. P. 5025.
51. Phillips P., Parkhurst J.M., Kounatidis I., Okolo C., Fish T.M., Naismith J.H., Walsh M.A., Harkiolaki M., Dumoux M. // *Life (Basel)*. 2021. V. 11. № 8. P. 842.
52. Hale V.L., Watermeyer J.M., Hackett F., Vizcay-Barrena G., van Ooij C., Thomas J.A., Spink M.C., Harkiolaki M., Duke E., Fleck R.A., et al. // *Proc. Natl. Acad. Sci. USA*. 2017. V. 114. № 13. P. 3439–3444.
53. Lobato-Márquez D., Conesa J.J., López-Jiménez A.T., Divine M.E., Pruneda J.N., Mostowy S. // *J. Cell Sci*. 2023. V. 136. № 7. P. jcs261139.
54. Weirich C.S., Erzberger J.P., Barral Y. // *Nat. Rev. Mol. Cell Biol*. 2008. V. 9. № 6. P. 478–489.
55. Turk-Kubo K.A., Loconte V., Vanslebrouck B., Mak W.K.E., Ekman A., Chen J.H., Takano Y., Horiguchi T., Nishimura T., Adachi M., et al. // *Microsc. Microanal*. 2023. V. 29. № 29 Suppl. 1. P. 1165.
56. Le Gros M.A., Clowney E.J., Magklara A., Yen A., Markenscoff-Papadimitriou E., Colquitt B., Myllys M., Kellis M., Lomvardas S., Larabell C.A. // *Cell Rep*. 2016. V. 17. № 8. P. 2125–2136.
57. Bian Q., Belmont A.S. // *Curr. Opin. Cell Biol*. 2012. V. 24. № 3. P. 359–366.
58. Polishchuk E.V., Polishchuk R.S., Luini A. // *Methods Mol. Biol*. 2013. P. 931. P. 413–422.
59. Hampton C.M., Strauss J.D., Ke Z., Dillard R.S., Hammonds J.E., Alonas E., Desai T.M., Marin M., Storms R.E., Leon F., et al. // *Nat. Protoc*. 2017. V. 12. № 1. P. 150–167.
60. Berger C., Premaraj N., Ravelli R.B.G., Knoops K., López-Iglesias C., Peters P.J. // *Nat. Methods*. 2023. V. 20. № 4. P. 499–511.
61. Schneider G., Guttman P., Rehbein S., Werner S., Follath R. // *J. Struct. Biol*. 2012. V. 177. № 2. P. 212–223.
62. Schermelleh L., Heintzmann R., Leonhardt H. // *J. Cell Biol*. 2010. V. 190. № 2. P. 165–175.
63. Varsano N., Dadosh T., Kapishnikov S., Pereiro E., Shimon E., Jin X., Kruth H.S., Leiserowitz L., Addadi L. // *J. Am. Chem. Soc*. 2016. V. 138. № 45. P. 14931–14940.
64. Varsano N., Beghi F., Elad N., Pereiro E., Dadosh T., Pinkas I., Perez-Berna A.J., Jin X., Kruth H.S., Leiserowitz L., Addadi L. // *Proc. Natl. Acad. Sci. USA*. 2018. V. 115. № 30. P. 7662–7669.

65. Faoro R., Bassu M., Mejia Y.X., Stephan T., Dudani N., Boeker C., Jakobs S., Burg T.P. // *Proc. Natl. Acad. Sci. USA*. 2018. V. 115. № 6. P. 1204–1209.
66. Kounatidis I., Stanifer M.L., Phillips M.A., Paul-Gilloteaux P., Heiligenstein X., Wang H., Okolo C.A., Fish T.M., Spink M.C., Stuart D.I., et al. // *Cell*. 2020. V. 182. № 2. P. 515–530.e17.
67. Phillips M.A., Harkiolaki M., Susano Pinto D.M., Parton R.M., Palanca A., Garcia-Moreno M., Kounatidis I., Sedat J.W., Stuart D.I., Castello A., et al. // *Optica*. 2020. V. 7. № 7. P. 802–812.
68. Koronfel M., Kounatidis I., Mwangangi D.M., Vyas N., Okolo C., Jadhav A., Fish T., Chotchuang P., Schulte A., Robinson R.C., et al. // *Acta Crystallogr. D Struct. Biol*. 2021. V. 77. № 12. P. 1479–1485.
69. Malyshev I.V., Reunov D.G., Chkhalo N.I., Toropov M.N., Pestov A.E., Polkovnikov V.N., Tsybin N.N., Lopatin A.Y., Chernyshev A.K., Mikhailenko M.S., et al. // *Opt. Express*. 2022. V. 30. № 26. P. 47567–47586.
70. Chkhalo N.I., Malyshev I.V., Pestov A.E., Polkovnikov V.N., Salashchenko N.N., Toropov M.N. // *Phys. Usp*. 2020. V. 190. № 1. P. 74–91.
71. Malyshev I.V., Pestov A.E., Polkovnikov V.N., Reunov D.G., Toropov M.N., Chkhalo N.I., Rakshun Ya.V. Khomiakov Yu.V., Chernov V.A., Shchelokov I.A. // *J. Surface Investigation, X-ray, Synchrotron and neutron tech*. 2023. V. 5. P. 3–15.
72. Shaw P. // *Histochem. J*. 1994. V. 26. № 9. P. 687–694.
73. Malyshev I.V., Chkhalo N.I. // *Ultramicroscopy*. 2019. V. 202. P. 76–86.
74. Gureyev T.E., Quiney H.M., Allen L.J. // *J. Opt. Soc. Am. A Opt. Image Sci. Vis*. 2022. V. 39. № 5. P. 936–947.
75. Kong H., Zhang J., Li J., Wang J., Shin H.J., Tai R., Yan Q., Xia K., Hu J., Wang L., et al. // *Natl. Sci. Rev*. 2020. V. 7. № 7. P. 1218–1227.
76. Ou H.D., Phan S., Deerinck T.J., Thor A., Ellisman M.H., O’Shea C.C. // *Science*. 2017. V. 357. № 6349. P. eaag0025.
77. Fogelqvist E., Kördel M., Carannante V., Önfelt B., Hertz H.M. // *Sci. Rep*. 2017. V. 7. № 1. P. 13433.

Muscarinic Cholinoreceptors in Skeletal Muscle: Localization and Functional Role

I. V. Kovyazina^{1,2*}, A. A. Khamidullina¹

¹Kazan State Medical University, Kazan, 420012 Russian Federation

²Kazan Institute of Biochemistry and Biophysics, FRC Kazan Scientific Center of RAS, Kazan, 420111 Russian Federation

*E-mail: irina.kovyazina@list.ru; i.kovyazina@kazangmu.ru

Received: July 20, 2023; in final form, September 24, 2023

DOI: 10.32607/actanaturae.25259

Copyright © 2023 National Research University Higher School of Economics. This is an open access article distributed under the Creative Commons Attribution License, which permits unrestricted use, distribution, and reproduction in any medium, provided the original work is properly cited.

ABSTRACT The review focuses on the modern concepts of the functions of muscarinic cholinoreceptors in skeletal muscles, particularly, in neuromuscular contacts, and that of the signaling pathways associated with the activation of various subtypes of muscarinic receptors in the skeletal muscles of cold-blooded and warm-blooded animals. Despite the long history of research into the involvement of muscarinic receptors in the modulation of neuromuscular transmission, many aspects of such regulation and the associated intracellular mechanisms remain unclear. Now it is obvious that the functions of muscarinic receptors in skeletal muscle are not limited to the autoregulation of neurosecretion from motor nerve endings but also extend to the development and morphological rearrangements of the synaptic apparatus, coordinating them with the degree of activity. The review discusses various approaches to the study of the functions of muscarinic receptors in motor synapses, as well as the problems arising when interpreting experimental data. The final part of the review is devoted to an analysis of some of the intracellular mechanisms and signaling pathways that mediate the effects of muscarinic agents on neuromuscular transmission.

KEYWORDS skeletal muscle, neuromuscular junction, acetylcholine, muscarinic cholinoreceptor, autoregulation.

ABBREVIATIONS ACh – acetylcholine; mAChR – muscarinic cholinoreceptor; NMJ – neuromuscular junction; EPP – endplate potential.

INTRODUCTION

Acetylcholine (ACh) is one of the main neurotransmitters and modulators of the nervous system. ACh receptors – nicotinic (ionotropic) and muscarinic (metabotropic) ones – are expressed in a variety of tissues, from neuromuscular junctions and the parasympathetic nervous system to the cortical areas involved in cognitive functions such as learning and memory. Cholinergic agents, including allosteric modulators, are actively used in the treatment of various pathologies [1–3].

The first studies that demonstrated the involvement of muscarinic cholinergic receptors (mAChRs) in the regulation of neuromuscular transmission go back to the 1960s [4, 5]. By now, all the five known mAChR subtypes (M1–M5) have been found in the vertebrate neuromuscular contacts, and the signal-

ing pathways triggered by the activation of these receptors are multiple, complex, and often inter-related.

The exact location of different mAChR subtypes in skeletal muscles is not entirely clear: some of these receptors can apparently be located not only on nerve endings, but also on the sarcolemma and Schwann cells [6–8]. Multiple signaling pathways are associated with the activation of different mAChR subtypes in the vertebrate skeletal muscles: some of them alter the concentration of intracellular Ca^{2+} by regulating its release from intracellular depots or modifying the functions of the calcium channels modulating, either directly or indirectly, the neurosecretion process (e.g., via enhancement of free radical production). Other mechanisms involve direct impact on the vesicle exocytosis machinery; e.g., via the regulation of protein

kinase A activity, phosphorylation of SNAP-25 protein, etc.

It is known today that the functions of mAChRs in the regulation of neuromuscular transmission are not confined to the control of neurosecretion intensity. A number of studies have revealed that these receptors are involved in the regulation of the timing of ACh release [9–11]. Muscarinic receptors, and the odd subtypes in particular, can reside on the sarcolemma and regulate the contractile activity of muscle fibers, as it has been shown for M5 mAChRs [12], or participate in the control of the resting membrane potential [13]. Relatively recently, the role of various mAChR subtypes in maintaining synaptic stability, growth, and development of motor synapses has been revealed [7]. That is, these receptors ensure the functionality of a tripartite synapse (nerve ending – muscle fiber – Schwann cell) and coordinate the development and morphological features of the synaptic machine with its activity level.

This review attempts to summarize the currently known data on the localization of mAChRs in vertebrate skeletal muscles, the effects of muscarinic agents on synaptic transmission parameters, and the signaling pathways coupled with the activation of different subtypes of mAChRs in the neuromuscular contacts.

PHARMACOLOGICAL AND GENETIC APPROACHES TO STUDYING THE mAChR FUNCTIONS

Five mAChR subtypes (M1–M5) are distinguished depending on the localization, molecular structure, nucleotide sequence, and functions. The conserved structure of the mAChR subtypes is the reason for the poor selectivity of most of the muscarinic agonists and antagonists used for pharmacological studies and the difficulties arising when interpreting the experimental data [2, 14]. Currently, the only highly selective mAChR antagonists available are the “muscarinic toxins” isolated from the mamba venom [15].

Allosteric modulations are another pharmacological approach to the study of muscarinic functions [16]. Muscarinic receptor subtypes exhibit high structural homology in the transmembrane domains where the orthosteric binding site is located, but the extramembrane domains are less conserved. Targeted synthesis of compounds that bind specifically to the allosteric domains makes it possible to achieve a highly advantageous selectivity in binding that is otherwise impossible with orthosteric ligands [17–19].

Recently, animals with mutations in the genes encoding various subtypes of these receptors have witnessed expanded use, in addition to the pharmacological analysis, in the study of the functional role of

mAChRs both in the whole organism and in individual cells. Thus, it has been found that in rats *Rattus norvegicus*, genes encoding various mAChR subtypes reside on chromosomes 1 (M1 subtype), 3 (M4 and M5 subtypes), 4 (M2 subtype), and 17 (M3 subtype) [20]. These data have made it possible to develop congenic and consomic animal strains that can be used to study the functions of different mAChR subtypes [20, 21]. Research into the synaptic transmission (including in peripheral synapses) in animals with mutations in genes encoding different mAChRs have shed light on the physiological role of different mAChR subtypes. Various cognitive and behavioral abnormalities, as well as changes in the morphology of synaptic contacts and in the pharmacological effects of cholinergic agents, have been observed in animals with mutations in mAChRs, viable and fertile [1, 21–23].

LOCALIZATION OF mAChRs IN SKELETAL MUSCLES

In the area of vertebrate neuromuscular contacts (NMJs), mAChRs can reside both on the membrane of nerve endings and the sarcolemma, as well as on Schwann cells [6–8]. These cholinergic receptors can be activated by vesicular ACh released from nerve endings either spontaneously (asynchronously) or synchronously during nervous activity, as well as by non-quantal ACh, which makes up a very significant part of the neurotransmitter in the synaptic contact area [13, 24, 25]. The presence of muscarinic receptors, and those of M1 subtype in particular, on the sarcolemma of the rat diaphragm was reported in [8]. Megan Wright et al. [7] showed that in mouse LAL muscle, M2 receptors are present exclusively in motor neurons, whereas M1, M3, and M5 mAChRs can be associated with Schwann cells and/or muscle fibers. Meanwhile, the presence of functional M1–M4 mAChRs was demonstrated by RT-PCR for a culture of Schwann cells obtained from the phrenic nerve of newborn rats, and the M2 subtype was predominant [26]. At the same time, the M4 mAChRs were expressed in the culture of Schwann cells at a very low level and the M5 subtype was not detected at all; similar results were obtained later for human Schwann cells [27].

M1–M4 mAChRs subtypes were shown to be present and functioning in the area of rat neuromuscular contact at all stages of postnatal ontogenesis [28, 29].

All the five mAChR subtypes were also discovered in the NMJs of cold-blooded animals. The presence and functional activity of M1–M5 subtypes were demonstrated by combining the immunohistochemistry and microelectrode recording of the endplate potentials (EPPs) in the synaptic area of the frog *m. cutaneous pectoris* [11]. The different effects of

muscarine in these NMJs could be associated with the heterogeneous localization of mAChRs, in particular, those of M3 subtype: some of these receptors can reside at the nerve ending and be activated by a small amount of the agonist, while the remaining part can be located at some distance from the secretion zone (e.g., on Schwann cells or on the sarcolemma). These remote receptors can be activated at high levels of secretion only or by an exogenous non-hydrolysable agonist such as muscarine or carbachol. The presence of mAChRs on perisynaptic Schwann cells in the frog NMJs is indirectly evidenced by the muscarine-induced increase in intracellular Ca^{2+} ions in this compartment of the neuromuscular contact [30]. The scheme of ACh secretion regulation triggered by M3 subtype mAChRs residing on the sarcolemma was proposed for the lizard motor synapses, involving the synthesis of endocannabinoids, and 2-AG in particular, from muscle membrane lipids [6].

The heterogeneous localization of mAChRs in the NMJ may partly explain the multiple and often ambiguous effects of muscarinic agents on the neuromuscular transmission.

FUNCTIONAL ROLE OF mAChRs IN SKELETAL MUSCLE

The possibility of autoregulation of ACh release from motor nerve endings on the feedback principle was first shown for nicotinic cholinergic receptors back in the 1960s. The muscarinic regulation was discovered later [4–5, 31].

Most of the early studies of neuromuscular transmission pointed to the facilitation of neurosecretion upon activation of nicotinic receptors, whereas the muscarinic receptors were believed to play the role of inhibitor of the ACh quantal release [31–33]. The discovery of different mAChR subtypes (including those that can facilitate neurosecretion) in the innervated areas of skeletal muscles, as well as the ambiguous results of studies performed under different experimental conditions, forced a rethink of this postulate [7, 34–36]. Thus, it was shown that methoctramine, the blocker of M2/M4 mAChRs, increases the EPP quantal content in the rat NMJ at a physiologically relevant Ca^{2+} level but inhibits the ACh release under reduced Ca^{2+} conditions (or when the amount of ACh in the synaptic cleft is diminished by adding the exogenous cholinesterase) [36]. One may assume that it is the increased activation of mAChRs, particularly of the M1 and M2 subtypes, that induces the alteration of the EPP quantal content upon the inhibition of synaptic acetylcholinesterase [35]. Although the experiments performed at reduced ambient Ca^{2+} do not unequivocally apportion the physiological role of mAChRs in the synapse, they demonstrate the pos-

sibility of switching from one signaling pathway to another and allow one to highlight the effects of the activation of certain mAChRs associated with the alteration of the intracellular Ca^{2+} level (and, therefore, manifest themselves more obviously when the Ca^{2+} level is initially lower).

The difference in the intensity of muscarinic effects on the spontaneous and evoked secretion in frog neuromuscular synapses at reduced and physiologically relevant Ca^{2+} was noted in a number of studies [11, 37]. Under reduced Ca^{2+} conditions, selective blockers of M1, M2/M4, and M3 mAChRs reduced the quantal release of ACh. At a “physiological” Ca^{2+} level, some muscarinic agents influenced the ACh quantal release only at a high-frequency pattern of motor nerve stimulation. Partially, this may happen due to time-delayed processes developing in motor nerve endings upon mAChRs activation. This assumption was indirectly confirmed by the estimation of the Ca^{2+} transient in the nerve ending; that is, the integral signal reflecting the Ca^{2+} metabolism in the cell over a fairly long period of time (several tens of ms) after the action potential arrival. In these experiments, activation of M2 mAChR in frog motor nerve endings led to a small but significant decrease in the amplitude of the Ca^{2+} transient [38].

In addition to the regulation of the amount of ACh secreted from the nerve endings, activation of mAChRs may also lead to changes in the timing of the release process. Along with the EPP quantal content, the timing of transmitter release is a factor ensuring synaptic plasticity [39, 40]. The degree of synchrony of neurosecretion in the NMJ depends on a number of factors such as temperature, the pattern of motor nerve firing, and the presence of physiologically active agents [40–42]. In frog motor synapses, inactivation of the M2 mAChRs not only modulates the EPP quantal content, but also desynchronizes the ACh release process [11, 43]. Further studies into muscarinic regulation of the timing of ACh secretion were conducted using animals with mutations in the genes encoding different subtypes of mAChRs [44]. M2 mAChR knockout mutants demonstrated, in contrast to wild-type mice, greater sensitivity to the experimental modifications of the Ca^{2+} level in the cytoplasm (variation of $[\text{Ca}^{2+}]$ in the bathing solution, addition of calcium buffers, etc.). In mutant mice, not only did these manipulations lead to changes in the EPP quantal content, but they also altered the timing of ACh secretion.

M1 receptors may also be involved in controlling the timing of ACh secretion [10, 45]. However, in frog NMJs, the involvement of these receptors in the regulation of secretion synchrony was obvious only under

conditions of high-frequency stimulation of the motor nerve. The blockade of these mAChRs prevented any increase in the duration of the EPP rise time which, in the case of unchanging temporal parameters of unquantal EPPs, could be regarded as indirect evidence of a shift in the synchrony of the ACh quanta secretion [10].

The synthesis of positive and negative allosteric modulators of M5 mAChR (compounds VU-023842 and ML-375 [17, 46]) allowed one to better understand the physiological role of M5 mAChRs in skeletal muscles. So, at positive modulation of M5 mAChR, the EPP quantal content and EPP rise time increased, whereas the synaptic depression (serial EPP amplitudes rundown) caused by high-frequency nerve firing was deepened [12].

The effects of mAChR activation or inactivation on motor synapses are not limited to the regulation of the quantal ACh secretion. In the presence of the positive M5 mAChR modulator, compound VU-0238429, the strength of muscle contractions decreased, both during indirect and direct stimulation. This observation supports the postsynaptic localization of M5 mAChRs and the possibility of direct regulation of muscle contractility by ACh [12]. The mechanisms driving such regulation of muscle properties remain unclear. For example, it was shown that the activation of all mAChRs expressed in a mouse fibroblast cell culture (NIH 3T3) can inhibit L-type Ca^{2+} channels via protein kinase C activation [47]. The question of co-localization of M5 receptors with Ca^{2+} channels in skeletal muscles and the possibility of their functional regulation remains open.

It was suggested that activation of M1 mAChR on the sarcolemma by ACh (presumably of non-quantal origin) protects skeletal muscle fibers from early post-denervation depolarization [13]. That is, M1 mAChR can mediate trophic, non-impulse regulation of the resting membrane potential in skeletal muscles. In the absence of nerve stimulation, endogenous activation of the M1 mAChR was detected, modulating the non-quantal release of ACh from the nerve ending, and these receptors apparently resided on muscle fibers; that is, the control of non-quantal secretion could be retrograde [48].

A number of studies have demonstrated the involvement of mAChRs in the structural rearrangements in the synapses. Thus, mAChRs located on the perisynaptic Schwann cell regulate the activity of the glial fibrillary acidic protein (GFAP), which maintains the cell shape and is involved in the regulation of cell proliferation and synaptic plasticity. This regulation is mediated via the alteration of $[Ca^{2+}]_i$ in perisynaptic Schwann cells. It is assumed that M2 mAChR in the

Schwann cells of warm-blooded animals is involved in the control of the proliferation, differentiation, and myelination of these cells [30, 49, 50]. In neuromuscular preparations of newborn rats, muscarinic autoreceptors of the M1, M2 and M4 subtypes can participate in the differentiation of “strong” and “weak” synapses in the case of polyinnervation of muscle fibers at early stages of synaptogenesis [51, 52].

The role of various mAChR subtypes in the maintenance of synaptic stability, growth, and development of mice motor synapses was studied in detail using pharmacological and genetic analysis [7]. Blockade of all five mAChR subtypes with atropine (subcutaneous injections for 7 days) had a pronounced effect, including the disappearance of some nerve endings and the spontaneous sprouting of others, as well as muscle atrophy. Blockade of only M2/M4 mAChR subtypes with methoctramine caused changes at the level of nerve endings, but it did not affect the muscle fibers. Injections of the M3 mAChR blocker 4-DAMP caused complete elimination of nerve endings, but it did not affect the Schwann cells. Similar morphological changes were observed in genetically modified mice: M2^{-/-} mutants were characterized by instability of nerve endings (elimination of nerve terminals accompanied by spontaneous sprouting), while M5 muscarinic receptor knockout mice were characterized by a small size of motor synapses and muscle fiber atrophy.

Thus, different mAChR subtypes ensure the functionality of the tripartite synapse (nerve ending – muscle fiber – Schwann cell) and coordinate the development and morphological properties of the synapse with its activity.

SIGNALING PATHWAYS ASSOCIATED WITH mAChR ACTIVATION IN THE NMJ

Muscarinic cholinoreceptors can activate numerous signaling pathways in the neuromuscular junction. The classical concept of neuromodulation mediated through odd (M1, M3, M5) and even (M2, M4) mAChR subtypes divides the signaling pathways associated with these subtypes into the activation of G_q and $G_{i/o}$ proteins. Traditionally, the facilitation of ACh secretion, mediated through the activation of “odd” mAChRs, has been associated with the activation of phospholipase C, leading to the synthesis of inositol-4,5-trisphosphate (IP_3) and diacylglycerol (DAG) [53]. IP_3 increases the secretion intensity by releasing Ca^{2+} from intracellular stores, and DAG can have a direct effect on the proteins of the exocytotic machinery. Regulation of the activity of protein kinase A through changes in the level of cAMP upon activation of $G_{i/o}$ proteins leads to the modulation of

Ca²⁺ channels, proteins of exocytotic machinery, and also controls the process of ACh loading into vesicles [54–57]. However, recent studies have shown that in the mouse NMJs, the M1 and M2 mAChR subtypes can use the same targets downstream of G protein activation [58]; that is, there is a reciprocal relationship between M1 and M2 mAChRs, which is implemented through the protein kinase A anchoring protein. Some effects associated with the activation of M2 mAChRs are observed only when the M1 receptors are active (e.g., reduced activity of the catalytic subunits of protein kinase A and elevated activity of regulatory subunits). Other changes may be caused by additional activation of M1 receptors (e.g., an increase in the level of the regulatory protein RIIβ and its release into the cytosol). Moreover, mAChRs may share the same signaling pathways with receptors for other neurotransmitters. For example, it has been shown that in rat NMJs, presynaptic adenosine A2 and muscarinic M1-receptors facilitate neurosecretion, and that these receptors share the same intracellular signaling pathway [59, 60]. Competition between receptors can occur through signal convergence to a common link via the activation of protein kinase A and Ca²⁺ entry through L-type Ca²⁺ channels. Later, it was shown that endogenous adenosine released during rhythmic nerve activity is involved in the fine-tuning of the presynaptic activity of M1 and M2 mAChRs [61]. The prevalence of autofacilitation associated with M1 mAChRs during rhythmic nerve stimulation occurs due to the accumulation of endogenous adenosine in the synapse area, which acts on A1 receptors and attenuates the effects associated with the activation of the M2 mAChRs. A similar phenomenon — the absence of any effect of M2 mAChR activation on spontaneous ACh secretion in frog synapses in response to the action of adenosine — was observed in frog synapses [62].

In the lizard NMJs, mAChR activation led to a two-phase modulation of neurosecretion: short-term (< 12 min) activation of M3 receptors by muscarine reduced the quantal release of ACh, while the longer term activation of M1 receptors, on the contrary, increased it, and both of these effects depended on the level of nitric oxide in the synaptic contact area [63]. The severity of the effects associated with the stimulation of M1 receptors was dependent on the cAMP level and protein kinase A activity. The decline in EPP quantal content upon activation of M3 receptors residing on the muscle cell is mediated via the rise of the synthesis of endocannabinoids, probably 2-AG [6]. In the synaptic cleft, endocannabinoids bind to the CB1-type receptors on presynaptic nerve endings, thus restricting Ca²⁺ entry and leading to a decrease

in ACh. Moreover, at least one link in this regulatory chain requires the production of nitric oxide (either in muscles or in Schwann cells).

It is worth noting that in the study performed in frog NMJs [64], activation of M3 mAChRs also reduced the EPP quantal content; however, this suppression of ACh secretion was associated solely with the activation of NO synthase and an increase in the nitric oxide level: it did not involve endocannabinoid production. This fact, however, does not rule out the presence and functional role of CB1 type cannabinoid receptors in the motor synapses of frog. The activity of NO synthase may be elevated due to an increase in the [Ca²⁺]_i upon activation of the G_q proteins associated with the M3 mAChR subtype. It is interesting to note that inhibition of phosphoinositide 3-kinase (PI3K) by wortmannin prevented the restoration of the original level of secretion after muscarine had been removed from the bathing solution; that is, the application of muscarine led to an imbalance between the synthesis of membrane phospholipids and their breakdown, which apparently could affect the properties of a number of signaling molecules associated with membranes and involved in the regulation of exocytosis.

Another mechanism of muscarinic regulation of ACh secretion in motor synapses is associated with the activity of G-protein-gated K⁺ channels (GIRK channels). The activation of GIRK channels by G_i proteins usually leads to hyperpolarization of the cell and reduces its excitability. One of the metabotropic receptors coupled to G_i proteins is the M2 mAChR subtype. Studies involving the fluorescent label FluxOR™ made it possible to visualize the opening of K⁺ channels upon activation of M2 mAChR in frog skeletal muscle [65]. These experiments directly showed that GIRK channels are functionally active in frog motor synapses and that they are coupled to M2 mAChRs. An analysis of EPPs and MEPPs recorded in the presence of an activator (ML-297) and a blocker (tertiapin-Q) of GIRK channels has revealed that these channels demonstrate an ambivalent behavior in frog NMJs. Depending on the level of extracellular Ca²⁺, M2 mAChRs can either inhibit or increase the level of evoked ACh secretion in frog NMJs [11]. One can conjecture that extracellular Ca²⁺ can serve as a switch between the stimulatory and inhibitory functions of M2 mAChRs; that is, that these receptors can both activate and inhibit GIRK channels, differentially modulating the evoked neurotransmitter release. The next link in this signaling circuit downstream the GIRK channel is the L-type Ca²⁺ channel. It is suggested that the suppression (due to hyperpolarization) of the asynchronous (spontaneous) activity of these

Ca²⁺ channels during interstimulus intervals can ensure that they successfully fire in response to the action potential.

Another signaling pathway associated with M2 mAChRs in the NMJs of both cold-blooded and warm-blooded animals is associated with the tonic block of the exocytotic machinery upon activation of these receptors and its elimination upon depolarization of the motor nerve ending [66]. It has been suggested that at rest, M2 mAChRs have an increased affinity for ACh and, when activated, switch the exocytotic machinery to the state of tonic block. When the presynaptic membrane is depolarized, the affinity of M2 mAChRs for ACh decreases, the ACh molecules dissociate, and the proteins of the exocytotic machinery can then interact with Ca²⁺, which ultimately leads to ACh release. Later, the dependence of the ACh dissociation constant on the resting membrane potential for M2 mAChRs was demonstrated directly on oocytes by K⁺ currents recording through GIRK channels and by assessing the degree of binding and unbinding of labeled ACh [67]. Using the “uncaged” carbachol, it was shown that in the case of rapid (within several ms) release of cholinergic in the area of a motor synapse, blockade of M2 mAChRs leads to a significant, dose-dependent decrease in the quantal release of ACh in wild-type mice, while in M2 (-/-) mutants carbachol has no effect on the intensity of secretion. This can be interpreted as the involvement of M2 mAChRs in the earliest phase of secretion, within a few ms after depolarization of the nerve ending [68].

In rat Schwann cells, M2 receptors, in addition to the canonical pathway associated with the G_i protein, also activate non-canonical pathways, including the PI3K/AKT/mTOR signaling pathway, which can modulate the proliferation and migration of these glial cells [50].

COMPARISON OF SIGNALING PATHWAYS ASSOCIATED WITH mAChR ACTIVATION AT CENTRAL AND MOTOR SYNAPSES

As a part of this review, it was interesting to compare some signaling pathways associated with mAChRs in motor and central synapses.

In the CNS, mAChRs are located in various brain regions innervated by cholinergic neurons, both on postsynaptic and presynaptic membranes, as well as in glial cells. mAChRs are involved in a variety of processes such as learning, concentration of attention, regulation of sleep-wake cycle, motor control, and others. mAChR activation is associated with effects such as postsynaptic excitation, postsynaptic inhibition, and presynaptic autoinhibition [69, 70].

One of the mechanisms responsible for postsynaptic excitation is the inhibition of the voltage-gated K⁺ channels (M-channels) associated with M1/M3/M5 subtypes, as a result of the activation of phospholipase C. M channels include some members of the Kv7 subfamily: mainly Kv7.2 and Kv7.3 [71, 72]. To stabilize them in the open state, a given density of phosphatidylinositol 4, 5-bisphosphate (PIP₂) in the cell membrane is required [73, 74]. Rapid hydrolysis of PIP₂ by phospholipase C leads to the inactivation of the K⁺ channel, which causes depolarization and enhanced excitability of the cell. This mechanism was first encountered in sympathetic neurons, but it is also typical of some central neurons (e.g., hippocampal pyramidal neurons, cortical pyramidal neurons). M channels are usually concentrated in the axon's initial segment, where they control the action potential threshold. An additional excitation mechanism associated with the activation of odd-numbered mAChRs and depletion of membrane lipids is the inhibition of some other K⁺ channels; for example, Ca²⁺-dependent K⁺ channels or leak K⁺ channels [75-78].

M channels (Kv7.2, Kv7.3 and Kv7.4) were found in striated muscles [79, 80]; they are credited with the role of regulators of skeletal muscle differentiation and maintenance of muscle tone [81-83]. Considering the presence of odd-numbered mAChRs on the sarcolemma, their possible co-localization with Kv7 channels and modulation of K⁺ channels functioning seems a very plausible idea that could explain some of the effects of muscarinic agents on muscles.

Postsynaptic inhibition occurs in the central nervous system as a result of the activation of inward rectifying K⁺ channels (GIRK channels) associated with the M2 mAChRs. This mechanism was first discovered in sympathetic and parasympathetic neurons [84], and later similar M2-mediated effects of ACh were detected in some central neurons [70, 85-87]. The slow inhibitory postsynaptic potential is a delayed hyperpolarization starting approximately 50 ms after the “nicotinic” EPP. This hyperpolarization closely resembles the myocardial response to vagal stimulation and results from the activation of the G_i-protein K⁺ inward rectifier channels (mainly Kir_{3.1} and Kir_{3.2}) following the activation of the M2 mAChRs. Coupling of M2 mAChRs with GIRK channels was shown for the neuromuscular synapse [65]. In motor synapses, GIRK channels are localized on the presynaptic membrane; it turns out that they can not only reduce cell excitability, but, under certain conditions, also facilitate ACh secretion due to the suppression of “calcium noise” during rest intervals. At vertebrate motor synapses, this signaling pathway is involved in the auto-regulation of neurosecretion.

As for autoregulation in the CNS, here presynaptic inhibition (autoinhibition) is typically associated with direct inactivation of voltage-dependent Ca^{2+} channels coupled with M2/M4 receptors. In sympathetic neurons, these two mAChR subtypes and their related G_i and G_o proteins and effector channels can form the functional microdomains or signalosomes [88], possibly with the participation of some auxiliary proteins [89].

Every year, new mechanisms responsible for signal transmission via metabotropic receptors are being discovered, and the already known ones are becoming more complex due to the identification of additional isoforms of the molecules involved in signal transmission, the recognition of new points of intersection of signaling pathways, and the identification of differences in signal transmission specific to different cells. It is traditionally believed that odd receptor subtypes (M1, M3 and M5) activate phospholipase C through pertussis toxin-insensitive G-proteins of the G_q family, and that receptors of the M2 and M4 subtypes regulate the activity of adenylate cyclase (using pertussis toxin-sensitive G-proteins of the G_i family) without PLC stimulation. However, this specificity is not absolute and “even” mAChRs can activate the α -subunit of the G_s and $G_{q/11}$ proteins, thus triggering numerous signaling pathways, depending on the nature and concentrations of the agonist [90–92].

NEUROMUSCULAR PATHOLOGIES ASSOCIATED WITH IMPAIRED MUSCARINIC REGULATION

An imbalance in the cholinergic system is the major cause behind the symptoms in many neurological diseases, including Alzheimer’s and Parkinson’s, schizophrenia, depression, and bipolar disorder [16]. However, there is currently scant data directly connecting any diseases with defects in the muscarinic regulation of skeletal muscles, and neuromuscular transmission in particular.

Violation of muscarinic adaptation may be one of the pathogenetic factors that lead to the development of amyotrophic lateral sclerosis. It is known that perisynaptic Schwann cells are involved in maintaining the stability and normal functioning of motor synapses, and that mAChRs play an important role in the implementation of these processes. One of the functions of Schwann cells is rapid removal of axonal debris after damage to peripheral nerve fibers [93]. An increase in the phagocytic activity of Schwann cells is associated with the expression of galectin-3, and the level of mAChR activation is a determining factor when a Schwann cell switches from the maintenance mode to the repair mode [94]. A mouse model of amyotrophic lateral sclerosis (SOD1 strain) exhibits

increased mAChR activation in Schwann cells during the pre-onset stage of the disease [95] and an inability to activate galectin-3 during nerve injury [96, 97].

In patients with chronic fatigue syndrome (myalgic encephalomyelitis) and Lambert–Eaton myasthenic syndrome, the enhanced production of autoantibodies to certain mAChR subtypes (M1, M3, M4) was detected, which is likely to aggravate the severity of some symptoms of these diseases, manifested as impaired motor activity [98, 99].

CONCLUSION

This review has attempted to summarize the currently known facts and hypotheses as they relate to the functions of muscarinic receptors in the skeletal muscles of cold- and warm-blooded animals. Basic information and assumptions about the localization, consequences of pharmacological and genetic influences and mAChR-related signaling cascades in the NMJ and vertebrate skeletal muscle are presented in *Table 1* and *Figures 1–3*.

Today, there is no doubt that all five (M1–M5) currently known mAChR subtypes are present in vertebrate skeletal muscles. The signaling pathways associated with the activation of various mAChR subtypes in vertebrate skeletal muscles are diverse, and the effects of the activation of these receptors vary in duration (from several ms to tens of minutes) and, apparently, retain the possibility of “switching” from one signaling pathway to another depending on factors of internal or external nature. Some of these intracellular mechanisms are associated, in one way or another, with changes in the level of intracellular Ca^{2+} (by regulating its release from intracellular stores or modifying the functions of Ca^{2+} channels). Other possible signaling pathways involve a direct effect on the exocytotic machinery; for example, through the regulation of protein kinase A activity, phosphorylation of the SNAP-25 protein, etc.

The functions of mAChRs in skeletal muscle are not limited to the autoregulation of ACh secretion. Muscarinic receptors of the M1 and M2 subtypes can be involved in the regulation of the timing of ACh release. Odd-numbered mAChRs can be located on the sarcolemma and regulate the contractility of muscle fibers or participate in the maintenance of the resting membrane potential.

It is worth noting that mAChRs *per se* are the targets of various endogenous factors, such as free radicals [100, 101]. In addition, they are voltage-sensitive (moreover, in the physiological range of shifts in the cell membrane potential) [102–104]. Therefore, we can envisage the possibility of a dynamic regulation of mAChRs properties at different patterns of synapse

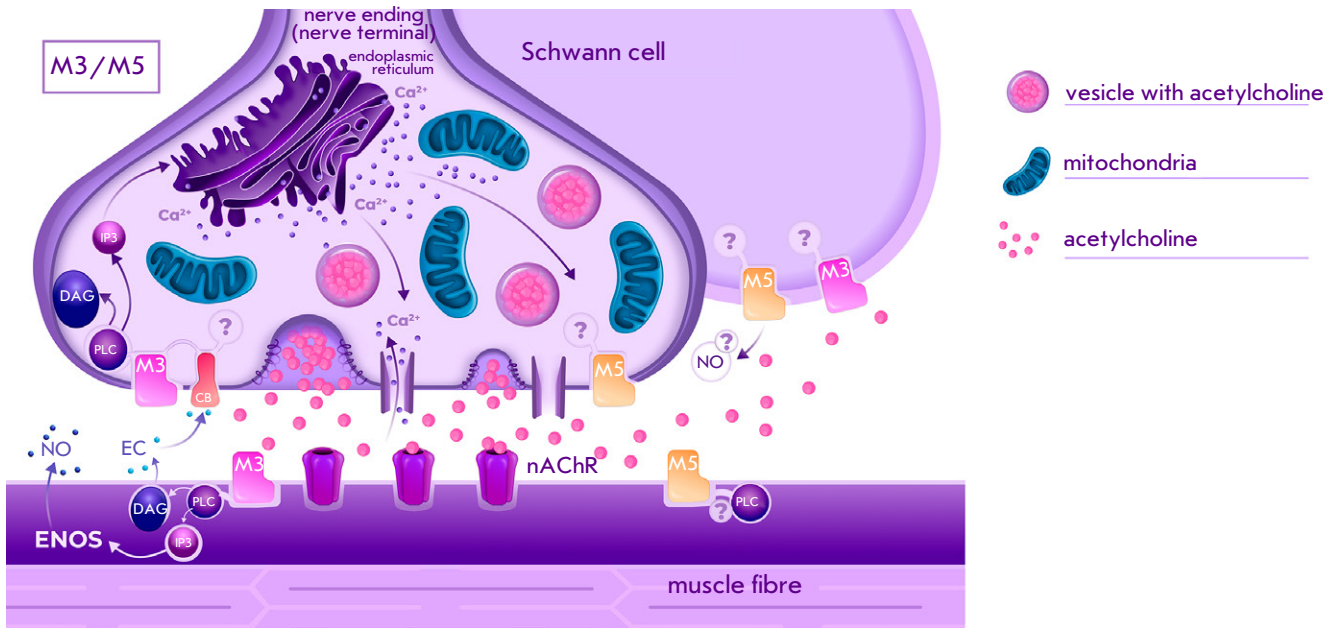


Fig. 3. Schematic representation of the localization of M3 and M5 subtypes muscarinic acetylcholine receptors and the associated signaling pathways in the neuromuscular synapse of vertebrates [7, 8, 29, 48, 52, 58]; nAChR, nicotinic acetylcholine receptor, PLC, phospholipase C, DAG, diacylglycerol, IP3, inositol triphosphate, NO, nitric oxide, ENOS, endothelial form of NO synthase, EC, endocannabinoid (presumably 2-AG), CB, endocannabinoid receptor

Table 1. Localization and functions of mAChRs in vertebrate skeletal muscles

Subtype	Localization	Effects associated with activation	Putative signaling pathways
M1	nerve ending [7, 11, 29]; sarcolemma [8]; Schwann cell [29]	augmentation of EPP quantal content [10, 11, 29, 31, 63]; regulation of non-quantal ACh release and muscle resting membrane potential [8, 13]; differentiation of “strong” and “weak” synapses at the early stages of synaptogenesis [51, 52]	activation of phospholipase C, [Ca ²⁺] _i elevation, regulation of the activities of protein kinases A and C [52, 58, 63]
M2	nerve ending, Schwann cell [7, 29, 30, 49, 50]	Ca ²⁺ -dependent regulation of EPP quantal content and the timing of ACh release [11, 29, 34, 43, 44, 65, 66]; regulation of Schwann cell differentiation and proliferation [30, 49, 50]; control of the development of motor nerve endings during the ontogenesis [7], differentiation of “strong” and “weak” synapses at the early stages of synaptogenesis [51, 52]	regulation of cAMP level and protein kinases A and C activities [52, 58]; tonic block of the exocytosis apparatus [66]; Ca ²⁺ -dependent regulation of K ⁺ channel (GIRK) and L-type Ca ²⁺ channel [65]; PI3K/AKT/mTOR signaling pathway [50]
M3	nerve ending [29]; sarcolemma [63]; Schwann cell [29]	Ca ²⁺ -dependent regulation of EPP quantal content [6, 11, 63, 64]; control of the development of motor nerve endings during ontogenesis [7]	activation of phospholipase C, elevation of endocannabinoids and nitric oxide production [6, 63, 64]
M4	nerve ending [7, 29]; Schwann cell [29]	regulation of EPP quantal content [6]; differentiation of “strong” and “weak” synapses at the early stages of synaptogenesis [51, 52]	no data
M5	sarcolemma [7]; nerve ending? Schwann cell?	control of muscle growth and synaptic contact formation during the ontogenesis [7], regulation of muscle contractility [12]; augmentation of EPP quantal content [12]	no data

operation (e.g., reduction of the probability of activation during the generation of an action potential or when the NMJ operates in a high-frequency mode).

mAChR ligands, including allosteric modulators, are actively used for treating various pathologies, and a targeted search for novel, highly selective muscarinic agents as potential therapeutic agents is currently underway [1, 2, 16]. The localization of all currently known mAChR subtypes in skeletal muscle and the diversity of the signaling cascades associated with

their activation should be taken into account when using muscarinic agents as medications. ●

This work was carried out under the State Assignment of the Kazan Institute of Biochemistry and Biophysics, Federal Research Center of the Kazan Scientific Center of the Russian Academy of Sciences.

The authors would like to thank A.R. Yunusova for technical assistance with graphical illustrations.

REFERENCES

- Eglen R.M. // *Handb. Exp. Pharmacol.* 2012. № 208. P. 3–28.
- Leach K., Simms J., Sexton P.M., Christopoulos A. // *Handb. Exp. Pharmacol.* 2012. № 208. P. 29–48.
- Matta J.A., Gu S., Davini W.B., Bredt D.S. // *Science*. 2021. V. 373. № 6556. P. eabg6539.
- Hubbard J.L., Wilson D.F. // *Experientia*. 1970. V. 26. № 11. P. 1234–1235.
- Adler M., Albuquerque E.X. // *J. Pharmacol. Exp. Ther.* 1976. V. 196. № 2. P. 360–372.
- Newman Z., Malik P., Wu T.-Y., Ochoa C., Watsa N., Lindgren C. // *Eur. J. Neurosci.* 2007. V. 25. № 6. P. 1619–1630.
- Wright M.C., Potluri S., Wang X., Dentcheva E., Gautam D., Tessler A., Wess J., Rich M.M., Son Y.-J. // *J. Neurosci.* 2009. V. 29. № 47. P. 14942–14955.
- Malomouzh A.I., Arkhipova S.S., Nikolsky E.E., Vyskočil F. // *Physiol. Res.* 2011. V. 60. № 1. P. 185–188.
- Slutsky I., Rashkovan G., Parnas H., Parnas I. // *J. Neurosci. Off. J. Soc. Neurosci.* 2002. V. 22. № 9. P. 3426–3433.
- Kovyazina I.V., Tsentsevitsky A.N., Nikolsky E.E. // *Dokl. Biol. Sci.* 2015. V. 460. P. 5–7.
- Tsentsevitsky A.N., Kovyazina I.V., Nurullin L.F., Nikolsky E.E. // *Neurosci. Lett.* 2017. V. 649. P. 62–69.
- Kovyazina I.V., Khamidullina A.A., Fedorov N.S., Malomouzh A.I. // *J. Evol. Biochem. Phys.* 2022. V. 108. № 1. P. 98–108.
- Urazaev A., Naumenko N., Malomouzh A., Nikolsky E., Vyskočil F. // *Neurosci. Res.* 2000. V. 37. № 4. P. 255–263.
- Birdsall N.J., Curtis C.A., Eveleigh P., Hulme E.C., Pender E.K., Poyner D., Wheatley M. // *Pharmacology*. 1988. V. 37. Suppl 1. P. 22–31.
- Servent D., Blanchet G., Mourier G., Marquer C., Marcion E., Fruchart-Gaillard C. // *Toxicol. Off. J. Int. Soc. Toxicology*. 2011. V. 58. № 6–7. P. 455–463.
- van der Westhuizen E.T., Choy K.H.C., Valant C., McKenzie-Nickson S., Bradley S.J., Tobin A.B., Sexton P.M., Christopoulos A. // *Front. Pharmacol.* 2021. V. 11. P. 606656.
- Bridges T.M., Kennedy J.P., Hopkins C.R., Conn P.J., Lindsley C.W. // *Bioorg. Med. Chem. Lett.* 2010. V. 20. № 19. P. 5617–5622.
- Korczyńska M., Clark M.J., Valant C., Xu J., Moo E.V., Albold S., Weiss D.R., Torosyan H., Huang W., Kruse A.C., et al. // *Proc. Natl. Acad. Sci. USA*. 2018. V. 115. № 10. P. E2419–E2428.
- Zhu L., Rossi M., Cohen A., Pham J., Zheng H., Dattaroy D., Mukaibo T., Melvin J.E., Langel J.L., Hattar S., et al. // *Proc. Natl. Acad. Sci. USA*. 2019. V. 116. № 37. P. 18684–18690.
- Tseng J., Erbe C.B., Kwitek A.E., Jacob H.J., Popper P., Wackym P.A. // *Hear. Res.* 2002. V. 174. № 1–2. P. 86–92.
- Wess J. // *Handb. Exp. Pharmacol.* 2012. № 208. P. 95–117.
- Tanahashi Y., Komori S., Matsuyama H., Kitazawa T., Unno T. // *Int. J. Mol. Sci.* 2021. V. 22. № 2. P. 926.
- Svoboda J., Popelíková A., Stuchlík A. // *Front. Psychiatry*. 2017. V. 8. P. 215.
- Grinnell A.D., Gundersen C.B., Meriney S.D., Young S.H. // *J. Physiol.* 1989. V. 419. P. 225–251.
- Vyskočil F., Malomouzh A.I., Nikolsky E.E. // *Physiol. Res.* 2009. V. 58. № 6. P. 763–784.
- Loreti S., Vilaró M.T., Visentin S., Rees H., Levey A.I., Tata A.M. // *J. Neurosci. Res.* 2006. V. 84. № 1. P. 97–105.
- Piovesana R., Faroni A., Tata A.M., Reid A.J. // *Int. J. Mol. Sci.* 2020. V. 21. № 18. P. 6666.
- Santafé M.M., Salon I., Garcia N., Lanuza M.A., Uchitel O.D., Tomàs J. // *Eur. J. Neurosci.* 2003. V. 17. № 1. P. 119–127.
- Garcia N., Santafé M.M., Salon I., Lanuza M.A., Tomàs J. // *Histol. Histopathol.* 2005. V. 20. № 3. P. 733–743.
- Ko C.-P., Robitaille R. // *Cold Spring Harb. Perspect. Biol.* 2015. V. 7. № 10. P. a020503.
- Re L. // *Acta Physiol. Pharmacol. Ther. Latinoam. Organo Asoc. Latinoam. Cienc. Fisiol. Asoc. Latinoam. Farmacol.* 1999. V. 49. № 4. P. 215–223.
- Wessler I., Halank M., Rasbach J., Kilbinger H. // *Naunyn-Schmiedeberg's Arch. Pharmacol.* 1986. V. 334. № 4. P. 365–372.
- Vizi E.S., Somogyi G.T. // *Br. J. Pharmacol.* 1989. V. 97. № 1. P. 65–70.
- Slutsky I., Parnas H., Parnas I. // *J. Physiol.* 1999. V. 514 (Pt 3). P. 769–782.
- Minic J., Molgó J., Karlsson E., Krejci E. // *Eur. J. Neurosci.* 2002. V. 15. № 3. P. 439–448.

36. Santafé M.M., Lanuza M.A., Garcia N., Tomàs M., Tomàs J. // *Neuroscience*. 2007. V. 148. № 2. P. 432–440.
37. Arenson M.S. // *Naunyn. Schmiedebergs Arch. Pharmacol.* 1991. V. 343. № 2. P. 128–133.
38. Samigullin D.V., Khaziev E.F., Kovyazina I.V., Bukharaeva E.A., Nikolsky E.E. // *Genes Cells*. 2014. V. 9. № 3. P. 242–247.
39. Nikolsky E.E., Vyskocil F., Bukharaeva E.A., Samigullin D., Magazanik L.G. // *J. Physiol.* 2004. V. 560 (Pt 1). P. 77–88.
40. Bukharaeva E.A., Skorinkin A.I., Samigullin D.V., Petrov A.M. // *Biomedicines*. 2022. V. 10. № 8. P. 1771.
41. Katz B., Miledi R. // *J. Physiol.* 1965. V. 181. № 3. P. 656–670.
42. Kovyazina I.V., Tsentsevitsky A.N., Nikolsky E.E., Bukharaeva E.A. // *Eur. J. Neurosci.* 2010. V. 32. № 9. P. 1480–1489.
43. Slutsky I., Silman I., Parnas I., Parnas H. // *J. Physiol.* 2001. V. 536 (Pt 3). P. 717–725.
44. Slutsky I., Wess J., Gomez J., Dudel J., Parnas I., Parnas H. // *J. Neurophysiol.* 2003. V. 89. № 4. P. 1954–1967.
45. Dudel J. // *Eur. J. Neurosci.* 2007. V. 26. № 8. P. 2160–2168.
46. Berizzi A.E., Gentry P.R., Rueda P., Den Hoedt S., Sexton P.M., Langmead C.J., Christopoulos A. // *Mol. Pharmacol.* 2016. V. 90. № 4. P. 427–436.
47. Pemberton K.E., Jones S.V. // *Pflugers Arch.* 1997. V. 433. № 4. P. 505–514.
48. Malomouzh A.I., Mukhtarov M.R., Nikolsky E.E., Vyskočil F. // *J. Neurochem.* 2007. V. 102. № 6. P. 2110–2117.
49. Bélair E.-L., Vallée J., Robitaille R. // *J. Physiol.* 2010. V. 588 (Pt 7). P. 1039–1056.
50. Botticelli E., Salazar Intriago M.S., Piovesana R., Tata A.M. // *Life Basel Switz.* 2022. V. 12. № 2. P. 211.
51. Santafé M.M., Salon I., Garcia N., Lanuza M.A., Uchitel O.D., Tomàs J. // *Neuroscience*. 2004. V. 123. № 1. P. 61–73.
52. Tomàs J., Lanuza M.A., Santafé M.M., Cilleros-Mañé V., Just-Borràs L., Balanya-Segura M., Polishchuk A., Nadal L., Tomàs M., Garcia N. // *Mol. Neurobiol.* 2023. V. 60. № 3. P. 1580–1593.
53. Dencker D., Thomsen M., Wörtwein G., Weikop P., Cui Y., Jeon J., Wess J., Fink-Jensen A. // *ACS Chem. Neurosci.* 2012. V. 3. № 2. P. 80–89.
54. Machado J.D., Morales A., Gomez J.F., Borges R. // *Mol. Pharmacol.* 2001. V. 60. № 3. P. 514–520.
55. Catterall W.A. // *Curr. Mol. Pharmacol.* 2015. V. 8. № 1. P. 12–21.
56. Gaydukov A., Bogacheva P., Tarasova E., Molchanova A., Miteva A., Pravdivceva E., Balezina O. // *Cells*. 2019. V. 8. № 7. P. 762.
57. Pallien T., Klusmann E. // *Biochem. Soc. Trans.* 2020. V. 48. № 1. P. 39–49.
58. Cilleros-Mañé V., Just-Borràs L., Tomàs M., Garcia N., Tomàs J.M., Lanuza M.A. // *FASEB J.* 2020. V. 34. № 4. P. 4934–4955.
59. Oliveira L., Correia-de-Sá P. // *Neurosignals*. 2005. V. 14. № 5. P. 262–272.
60. Oliveira L., Timóteo M.A., Correia-de-Sá P. // *Eur. J. Neurosci.* 2002. V. 15. № 11. P. 1728–1736.
61. Oliveira L., Timóteo M.A., Correia-de-Sá P. // *Neurosci. Lett.* 2009. V. 459. № 3. P. 127–131.
62. Shakirzyanova A.V., Bukharaeva E.A., Nikolsky E.E., Giniatullin R.A. // *Eur. J. Neurosci.* 2006. V. 24. № 1. P. 105–115.
63. Graves A.R., Lewin K.A., Lindgren C.A. // *J. Physiol.* 2004. V. 559 (Pt 2). P. 423–432.
64. Tsentsevitsky A.N., Zakyrjanova G.F., Petrov A.M., Kovyazina I.V. // *Biochem. Biophys. Res. Commun.* 2020. V. 524. № 3. P. 589–594.
65. Tsentsevitsky A.N., Khaziev E.F., Kovyazina I.V., Petrov A.M. // *Neuropharmacology*. 2022. V. 209. P. 109021.
66. Parnas H., Slutsky I., Rashkovan G., Silman I., Wess J., Parnas I. // *J. Neurophysiol.* 2005. V. 93. № 6. P. 3257–3269.
67. Ben Chaim Y., Bochnik S., Parnas I., Parnas H. // *PLoS One*. 2013. V. 8. № 9. P. e74354.
68. Kupchik Y.M., Barchad-Avitzur O., Wess J., Ben-Chaim Y., Parnas I., Parnas H. // *J. Cell Biol.* 2011. V. 192. № 1. P. 137–151.
69. Brown D.A. // *J. Mol. Neurosci.* 2010. V. 41. № 3. P. 340–346.
70. Brown D.A. // *Neuropharmacology*. 2018. V. 136 (Pt C). P. 383–400.
71. Petrovic M.M., Nowacki J., Olivo V., Tsaneva-Atanasova K., Randall A.D., Mellor J.R. // *PLoS One*. 2012. V. 7. № 2. P. e30402.
72. Gigout S., Jones G.A., Wierschke S., Davies C.H., Watson J.M., Deisz R.A. // *BMC Neurosci.* 2012. V. 13. P. 42.
73. Fürst O., Mondou B., D'Avanzo N. // *Front. Physiol.* 2014. V. 4. P. 404.
74. Hille B., Dickson E., Kruse M., Falkenburger B. // *Prog. Mol. Biol. Transl. Sci.* 2014. V. 123. P. 219–247.
75. Vaithianathan T., Schneider E.H., Bukiya A.N., Dopico A.M. // *Adv. Exp. Med. Biol.* 2023. V. 1422. P. 217–243.
76. Bista P., Meuth S.G., Kanyshkova T., Cerina M., Pawlowski M., Ehling P., Landgraf P., Borsotto M., Heurteaux C., Pape H.-C., et al. // *Pflugers Arch.* 2012. V. 463. № 1. P. 89–102.
77. Bista P., Pawlowski M., Cerina M., Ehling P., Leist M., Meuth P., Aissaoui A., Borsotto M., Heurteaux C., Decher N., et al. // *J. Physiol.* 2015. V. 593. № 1. P. 127–144.
78. Leist M., Rinné S., Datunashvili M., Aissaoui A., Pape H.-C., Decher N., Meuth S.G., Budde T. // *J. Physiol.* 2017. V. 595. № 17. P. 5875–5893.
79. Iannotti F.A., Panza E., Barrese V., Viggiano D., Soldovieri M.V., Tagliatalata M. // *J. Pharmacol. Exp. Ther.* 2010. V. 332. № 3. P. 811–820.
80. Iannotti F.A., Barrese V., Formisano L., Miceli F., Tagliatalata M. // *Mol. Biol. Cell.* 2013. V. 24. № 3. P. 274–284.
81. Iannotti F.A., Silvestri C., Mazarrella E., Martella A., Calvigioni D., Piscitelli F., Ambrosino P., Petrosino S., Czifra G., Bíró T., et al. // *Proc. Natl. Acad. Sci. USA*. 2014. V. 111. № 24. P. E2472–2481.
82. Zagorchev P., Apostolova E., Kokova V., Peychev L. // *Naunyn. Schmiedebergs Arch. Pharmacol.* 2016. V. 389. № 4. P. 439–446.
83. Dupont C., Denman K.S., Hawash A.A., Voss A.A., Rich M.M. // *Exp. Neurol.* 2019. V. 315. P. 52–59.
84. Kuba K., Koketsu K. // *Prog. Neurobiol.* 1978. V. 11. № 2. P. 77–169.
85. McCormick D.A., Prince D.A. // *J. Physiol.* 1986. V. 375. P. 169–194.
86. Egan T.M., North R.A. // *Nature*. 1986. V. 319. № 6052. P. 405–407.
87. Sugawara S., Nakaya Y., Matsumura S., Hirose K., Saito Y., Kaneko R., Kobayashi M. // *Neuroscience*. 2022. V. 506. P. 1–13.
88. Fernández-Fernández J.M., Abogadie F.C., Milligan G., Delmas P., Brown D.A. // *Eur. J. Neurosci.* 2001. V. 14. № 2. P. 283–292.

89. Borroto-Escuela D.O., Romero-Fernandez W., García-Negredo G., Correia P.A., Garriga P., Fuxe K., Ciruela F. // *Cell. Physiol. Biochem. Int. J. Exp. Cell. Physiol. Biochem. Pharmacol.* 2011. V. 28. № 5. P. 1009–1022.
90. Ashkenazi A., Winslow J.W., Peralta E.G., Peterson G.L., Schimerlik M.I., Capon D.J., Ramachandran J. // *Science.* 1987. V. 238. № 4827. P. 672–675.
91. Santiago L., Abrol R. // *Int. J. Mol. Sci.* 2019. V. 20. № 21. P. 5290.
92. Michal P., El-Fakahany E.E., Dolezal V. // *J. Pharmacol. Exp. Ther.* 2007. V. 320. № 2. P. 607–614.
93. Kang H., Tian L., Mikesch M., Lichtman J.W., Thompson W.J. // *J. Neurosci. Off. J. Soc. Neurosci.* 2014. V. 34. № 18. P. 6323–6333.
94. Perez-Gonzalez A.P., Provost F., Rousse I., Piovesana R., Benzina O., Darabid H., Lamoureux B., Wang Y.S., Arbour D., Robitaille R. // *Glia.* 2022. V. 70. № 9. P. 1605–1629.
95. Arbour D., Tremblay E., Martineau É., Julien J.-P., Robitaille R. // *J. Neurosci. Off. J. Soc. Neurosci.* 2015. V. 35. № 2. P. 688–706.
96. Martineau É., Di Polo A., Vande Velde C., Robitaille R. // *eLife.* 2018. V. 7. P. e41973.
97. Martineau É., Arbour D., Vallée J., Robitaille R. // *J. Neurosci. Off. J. Soc. Neurosci.* 2020. V. 40. № 40. P. 7759–7777.
98. Loebel M., Grabowski P., Heidecke H., Bauer S., Hanitsch L.G., Wittke K., Meisel C., Reinke P., Volk H.-D., Fluge Ø., et al. // *Brain. Behav. Immun.* 2016. V. 52. P. 32–39.
99. Suzuki S. // *Brain Nerve Shinkei Kenkyu No Shinpo.* 2010. V. 62. № 4. P. 419–426.
100. Moyano P., de Frias M., Lobo M., Anadon M.J., Sola E., Pelayo A., Díaz M.J., Frejo M.T., Del Pino J. // *Toxicology.* 2018. V. 394. P. 54–62.
101. de Jongh R., Haenen G.R.M.M., van Koeveeringe G.A., Dambros M., De Mey J.G.R., van Kerrebroeck P.E.V. // *Neurourol. Urodyn.* 2007. V. 26. № 2. P. 302–308.
102. Rinne A., Mobarec J.C., Mahaut-Smith M., Kolb P., Bünemann M. // *Sci. Signal.* 2015. V. 8. № 401. P. ra110.
103. Ben-Chaim Y., Broide C., Parnas H. // *PLoS One.* 2019. V. 14. № 10. P. e0224367.
104. David D., Bentulila Z., Tauber M., Ben-Chaim Y. // *Int. J. Mol. Sci.* 2022. V. 23. № 22. P. 13988.

The Potential and Application of iPSCs in Gene and Cell Therapy for Retinopathies and Optic Neuropathies

E. V. Lapshin*, Y. G. Gershovich, A. V. Karabelsky

Gene Therapy Department, Science Center for Translational Medicine, Sirius University of Science and Technology, Krasnodar Region, Sirius, 354340 Russian Federation

*E-mail: lapshin.ev@talantiuspeh.ru

Received September 8, 2023; in final form, October 5, 2023

DOI: 10.32607/actanaturae.25454

Copyright © 2023 National Research University Higher School of Economics. This is an open access article distributed under the Creative Commons Attribution License, which permits unrestricted use, distribution, and reproduction in any medium, provided the original work is properly cited.

ABSTRACT This review focuses on *in vitro* modeling of diseases and the development of therapeutic strategies using iPSCs for the two most common types of optical pathologies: hereditary neuropathies and retinopathies. Degeneration of retinal ganglion cells and the subsequent optic nerve atrophy leads to various types of neuropathies. Damage to photoreceptor cells or retinal pigment epithelium cells causes various retinopathies. Human iPSCs can be used as a model for studying the pathological foundations of diseases and for developing therapies to restore visual function. In recent years, significant progress has also been made in creating ganglionic and retinal organoids from iPSCs. Different research groups have published data pertaining to the potential of using iPSCs for the modeling of optic neuropathies such as glaucoma, Leber hereditary optic neuropathy, etc., including in the development of therapeutic approaches using gene editing tools.

KEYWORDS induced pluripotent stem cells, retinopathies, optic neuropathies, retinal ganglion cells, organoids, gene therapy, cell therapy.

ABBREVIATIONS CRISPR – clustered regularly interspaced short palindromic repeats; RGCs – retinal ganglion cells; POG – primary open-angle glaucoma; IOP – intraocular pressure; LHON – Leber hereditary optic neuropathy; DOA – autosomal dominant optic atrophy; AMD – age-related macular dystrophy; DR – diabetic retinopathy; RP – retinitis pigmentosa; ESCs – embryonic stem cells; iPSCs – induced pluripotent stem cells; hESCs – human embryonic stem cells; ERG – electroretinogram; ETC – electron transport chain; HDR – homology-directed repair; NHEJ – non-homologous end joining; ROS – reactive oxygen species; OCR – oxygen consumption rate; LCA – Leber congenital amaurosis.

INTRODUCTION

In 2007, Takahashi et al. demonstrated that the pluripotent status can be induced in mature somatic fibroblasts by reprogramming through the overexpression of four pluripotent transcription factors (the so-called Yamanaka factors): OCT3/4, SOX2, C-MYC, and KLF4 [1]. Induced pluripotent stem cells (iPSCs) share the morphology of human embryonic stem cells (ESCs) and express their genetic markers.

Overexpression of the transcription factor cocktail makes possible the reprogramming of a patient's somatic cells to iPSCs [1–3], which possess such essential characteristics as:

- an ability to differentiate into cells derived from all the germ layers (the ectoderm, the mesoderm, and the endoderm) and
- an unrestricted reproductive capacity while maintaining a normal karyotype, which enables continuous production of the cell material [4–6].

The advances achieved in the methods that are used to work with human iPSCs have yielded the “disease-in-a-dish” concept. Combining iPSCs and the genome editing technology, analysis of the regulation of metabolic pathways, and phenotype assessment before and after genome editing represent at the moment a powerful tool for studying the progression of optic diseases, including rare inherited retinal disorders, and makes it possible to elaborate methods for testing the efficacy of drugs and novel therapeutic approaches.

Gene therapy is often the only way to manage inherited disorders. Replacement therapy involving correction of the genetic defect by inserting a functional gene copy into a patient's cells is usually employed. The iPSCs derived from patients' primary cells are a relevant and convenient model both for *in vitro* screening and for the assessment of the efficacy of gene therapy agents and for predicting the potential

adverse effects of the therapy, as well as improving the safety profile of the product.

The genetic material is delivered using cationic polymers, lipid nanoparticles, and different viral vector platforms. Cationic polymers are capable of penetrating into the cell nucleus but can destroy the cell membrane, thus exhibiting a toxic effect on the cell [7]. Lipid nanoparticles encapsulating DNA in liposomes fuse with cell membranes and release genetic material into the cell [8]. The drawbacks of DNA delivery using lipid nanoparticles include low effectiveness, because of the degradation of liposome–DNA complexes by cellular lysosomes. The most commonly used vectors are viruses that, in the case of single administration, ensure efficient delivery and the expression of a therapeutic gene, thus eliciting a long-term response to therapy in patients with severe genetic disorders. The diversity of viral vectors allows one to vary the specificity of their delivery into cells [9]. However, when choosing a viral vector, one should take into account its potential immunogenicity, as well as the risks of insertional mutagenesis that are associated with the application of integrative viral vectors.

The advances achieved in genome editing and the generation of iPSCs have consolidated into the new branch of gene therapy in combination with cell therapy. The technique involving *in vitro* editing of a patient's pathogenic genotypes and inserting gene-corrected iPSCs for phenotype correction are devoid of the shortcomings of conventional gene therapy, since they ensure immunocompatibility with the recipient and allow one to check the quality of iPSCs prior to transplantation [10].

The main innovation in using iPSCs in gene therapy consists in the development of genome editing approaches employing the CRISPR/Cas9 system and its analogs, whereas there are virtually no studies that deal with gene replacement therapy. The data on the application of iPSCs as models will be presented below, mainly to assess the degree of efficiency in editing autosomal-dominant mutations.

This review focuses on the *in vitro* modeling of the two most common types of disorders of the visual system (hereditary neuropathies and retinopathies), as well as on the development of therapeutic strategies using iPSCs. It also discusses the translational advances in cell and gene therapy.

GENE AND CELL THERAPY FOR NEUROPATHIES WITH iPSCs

Optic neuropathies caused by retinal ganglion cell death and optic nerve axonal degeneration are the leading causes of vision loss and blindness worldwide

[11, 12]. Retinal ganglion cells (RGCs) are specialized neurons, whose axons form the optic nerve transmitting information from the eye to the brain [13]. Glaucoma – a progressive optic neuropathy characterized by structural changes in the optic nerve head (optic disc) and irreversible vision loss – is the most common pathology, diagnosed in more than 60 million people [14–19]. Other optic neuropathies such as Leber hereditary optic neuropathy (LHON) and autosomal dominant optic atrophy (DOA) manifest themselves at an earlier age and are caused by mitochondrial mutations.

Gene therapy for neuropathies

LHON is characterized by the loss of central vision, and it predominantly affects males. Most of the mutations in patients with this disease were uncovered in the mitochondrial genes coding for the proteins of complex I of the electron transport chain (ETC): *MT-ND4* (m.11778G>A), *MT-ND1* (m.3460G>A), and *MT-ND6* (m.14484T>C). The pathogenesis of LHON is associated with decreased ATP synthesis and the accumulation of reactive oxygen species (ROS), leading to retinal ganglion cell death, optic atrophy and, consequently, central vision loss initially in one eye and then in the second eye.

Australian researchers have derived iPSCs from a patient with homoplasmic double mtDNA mutations (m.4160T>C and m.14484T>C) in the *MT-ND1* and *MT-ND6* genes, respectively. Such a genotype causes the so-called “Lebers Hereditary Optic Neuropathy Plus” (LHON Plus) disease when additional neurological symptoms, compared to those for optic neuropathy (e.g., movement disorders), develop. Mitochondria in these iPSCs were replaced with non-mutated mitochondria using the cybrid technology. The levels of apoptosis and ROS in RGCs derived from the edited iPSCs were lower than those in the control mutation-carrying RGCs [20].

DOA is the disorder caused by mitochondrial dysfunction presenting as decreased visual acuity at an early age and blindness. RGCs and their axons forming the optic nerve are damaged in patients with DOA. Mutations leading to DOA reside in the *OPA1* gene encoding the inner mitochondrial membrane protein, whose dysfunction affects mitochondrial fusion, ATP synthesis, signaling of apoptosis-inducing factors, calcium metabolism, and maintenance of mitochondrial genome integrity [21].

In iPSCs derived from a patient with the 1334G>A (R445H) mutation in the *OPA1* gene, the mutation was corrected using CRISPR/Cas9 genome editing combined with homology-directed repair (HDR), with ssDNA used as a template. The oxygen consumption

rate (OCR) in the edited iPSCs was higher than that in the mutated cells, which were characterized by reduced mitochondrial fragmentation and a lower level of apoptosis signaling [21].

Cell therapy for neuropathies

Cell replacement therapy with iPSCs is a promising approach to the treatment of neuropathies and retinopathies, especially at later stages of the pathologic process, when a significant number of cells have been lost. It is also believed that, in some cases, trophic factors released by stem cells can contribute to regeneration during transplantation. The efficacy of iPSC-based cell therapy has been proved in animal models of optic neuropathy [22, 23]. Ganglion cells differentiated from iPSCs can become integrated and survive after transplantation into the retina of mice used as a disease model [22]. Furthermore, transplantation of iPSC-derived progenitor cells has been shown to promote healing of an optic nerve injury in rats, accompanied by significant prompted potential restoration [23].

Cell therapy for neuropathies can be used to obtain non-ganglion cells. Thus, Abu-Hassan et al. demonstrated that transplantation of iPSC-derived trabecular meshwork cells can restore the homeostatic function in an *ex vivo* human anterior segment perfusion culture model [24], thus opening an interesting novel approach to the treatment of glaucoma.

Currently, there are no reports on clinical trials of cell therapy for optic neuropathy, but clinical trials of replacement retinal pigment epithelium cells derived from iPSCs are being conducted [25, 26]. The Advanced Cell Technology stem cell company has recently reported that phase I/IIa clinical trials of a suspension of retinal pigment epithelium cells derived from ESCs transplanted to patients with age-related macular degeneration and Stargardt disease have been successfully completed [25, 26]. Vision was improved, and neither serious adverse events nor immune responses were observed after low-dose transplantation of cells differentiated from ESCs into one eye in 18 patients. No data on rejection of the transplanted cells, uncontrolled cell proliferation, or serious eye or systemic problems have been reported. Visual functions were improved in most patients, and the target safety endpoints were attained in the trials. Furthermore, the team led by Prof. Masayo Takahashi (Japan) is preparing to launch clinical trials using iPSC-derived retinal pigment epithelium to treat age-related macular degeneration [26]. These clinical trials will confirm the conceptual feasibility of using pluripotent stem cells to restore the functionality of affected tissues, thus offering a new option for effective

and safe treatment of blindness caused by different pathological processes.

GENE AND CELL THERAPY FOR RETINOPATHIES WITH iPSCs

Inherited retinopathy is defined as any genetic disorder leading to retinal damage and, therefore, visual impairment. The prevalence of diseases belonging to this group is approximately 3 out of 100 people. The most common symptoms of retinopathies include visual field defects, an inability to adapt to poorly illuminated environments, distortion of objects' shape and size, as well as altered color perception. The data on the molecular processes associated with these diseases have been mostly acquired from fibroblast models, since retinal samples cannot be obtained. The use of iPSCs for this purpose can yield a more relevant model of the disease.

According to their type, retinopathies can be macular or peripheral. The central part of the retina (the macula) is affected in patients with macular retinopathy (e.g., Stargardt and Best disease). Peripheral vision is impaired in patients with peripheral retinopathy. The most common diseases belonging to this group include retinitis pigmentosa and choroideremia [27].

Different types of Leber congenital amaurosis (LCA) causing vision loss at birth or soon after are believed to be the most severe and earliest forms of inherited retinal disorders. Patients with this disease may also develop light hypersensitivity, involuntary eye movements (nystagmus) and farsightedness. Mental retardation can be observed in rare cases.

Application of gene therapy approaches to the treatment of inherited retinopathies

There are at least 20 types of LCA that are caused by different mutations in various genes, as well as by phenotypic manifestations. The most common pathological mutations in patients with LCA include mutations in the *CEP290*, *CRB1*, *GUC2D*, and *RPE65* genes. The molecular genetic reasons for LCA have yet to be identified in ~ 30% of cases [28]. Thus, the protein encoded by the *CEP290* gene is involved in cell division, microtubule assembly, as well as the formation of centrosomes and cilia. Mutations in this gene cause the most severe form of LCA: LCA type 10 [29]. Up to 15% of all the *CEP290* mutations are represented by the IVS26 – 2991+1655 A>G mutation in intron 26, which leads to the insertion of exon carrying a stop codon (C998X). The truncated peptide resulting from this mutation ensures only partial activity of *CEP290*. The iPSC model derived from a patient with this genotype was edited using the CRISPR/Cas9 sys-

tem. Compared to mutations in the coding region of the gene requiring a recombination template, splice site mutations can be corrected through targeted deletion. Thus, genome editing in iPSCs involving deletion of the splice site in the IVS26 region increased the synthesis level of functional CEP290 in [29].

Gene therapy using non-coding RNA targeting the IVS26 mutation proved to be effective in a 3D retinal organoid model derived from a patient's iPSCs. A fully phosphorothioate-modified and 2'-O-methyl-modified RNA oligonucleotide (QR-110) corrected the CEP290 splicing defect and restored the wild-type mRNA. Dose-dependent restoration of photoreceptor cilia was demonstrated [30].

LCA type 4, caused by *AIPL1* mutations, is characterized by severe vision impairment during infancy and progressive photoreceptor atrophy. The retinal organoid derived from the iPSCs of a patient carrying the 834 G>A (Trp278X) mutation in the *AIPL1* gene was edited using the CRISPR/Cas9, combined with HDR approaches with a 30% effectiveness. *AIPL1* expression was restored after editing, and the cGMP and PDE6 levels in the cells increased [31].

LCA type 7, which constitutes about 2% of all LCAs, is characterized by early photoreceptor dysfunction caused by mutations in the *CRX* gene (encoding the cone-rod homeobox protein). NHEJ (non-homologous end joining)-mediated CRISPR/Cas9 editing of the 263A>C (K88Q) mutation in the *CRX* gene in the retinal organoid model contributed to the development and maturation of photoreceptor cells. Interestingly, the genome editing strategy involved the insertion of two double-strand breaks. One of them targeted the mutation, while the other one targeted the allele-specific SNPs between exons 2 and 4 of the *CRX* gene [32].

Retinitis pigmentosa (RP) is an inherited disease affecting the retina and characterized by progressive photoreceptor loss. Patients experience problems with night and peripheral vision, although total blindness is quite rare. The disease onset usually takes place in childhood. One of the possible causes of RP is a mutation in the rhodopsin (*RHO*) gene [33]. Rhodopsin, a visual pigment found in the retinal rods, is a transmembrane receptor bound to G proteins; its conformation changes upon absorption of light quanta. Rhodopsin activates the G protein transducin, which activates cGMP-dependent phosphodiesterase, further reducing the permeability of cGMP-dependent ion channels, membrane hyperpolarization, and the generation of a nerve impulse [34]. By using a helper-dependent adenoviral vector (HDAdV), the editing of the mutation in the iPSCs of a patient carrying the mutation causing E181K substitution in the rhodopsin molecule was

performed. The edited iPSCs differentiated into photoreceptor cells were characterized by a decreased level of autophagy due to the suppression of ER stress-induced apoptosis. HDAdV gene transfer was performed by homologous recombination without the insertion of DNA breaks [34].

The 68C>A (P23H) mutation in this gene was also successfully edited using the CRISPR/Cas9 system in the iPSC model. No nonspecific gene editing was observed in wild-type (control) cells, while in mutant cells editing resulted in frameshift and translation termination, causing the inactivation of the mutant allele [29].

X-linked retinitis pigmentosa affects males (with an incidence of 1 case for every 15,000 individuals) and manifests itself as impaired night vision followed by a loss of peripheral vision and total blindness by age 40. In this case, mutations reside in the *RPGR* gene encoding the retinitis pigmentosa GTPase regulator, which affects the development of photoreceptor cells, a component of the centrosome-cilium protein interaction landscape. Approximately 16% of RP cases are associated with mutations in the *RPGR* gene. By using the CRISPR/Cas9 and HDR approaches, gene editing of iPSCs derived from a patient carrying the 3070 G>T mutation in the *RPGR* gene, where the single-strand template was mutation-free, was performed. Although this gene is GC-rich and carries nucleotide repeats, the editing efficiency amounted to 13% [35]. Deletions in *RPGR* exon 14 resulting in frameshift and loss of the sequences encoded by exons 15–19 are known. Such mutations impair ciliogenesis; therefore, patients with this defect have shortened photoreceptor cilia. The iPSCs derived from patients with *RPGR* mutation variants (1685_1686delAT, 2234_2235delGA, and 2403_2404delAG) were edited with the CRISPR/Cas9 tool, combined with HDR. The resulting three-dimensional retinal organoids had normal morphology, expressed recoverin, and contained a larger number of rods and cones compared to the control [36].

X-linked juvenile retinoschisis characterized by degenerative neuropathy and retinal detachment is another X-linked disorder. Juvenile retinoschisis develops predominantly in males; its incidence is approximately 1 case for 10,000 individuals. This disease is caused by mutations in the *RS1* gene involved in the cellular organization of the retina and intercellular adhesion. The iPSC models were derived from patients carrying the 625C>T (R209C) and 488G>A (W163X) mutations. The editing efficiency for iPSCs edited using the CRISPR/Cas9-mediated HDR approach amounted to 50%, but insertions were also present. For the 625C>T mutation, the efficiency of

Cas9-ABE7.10-mediated base editing was comparable to that achieved using the HDR approach [37].

Mutations in the *PRPF* genes causing RP type 13 are autosomal dominant and are observed in ~ 15% of all retinitis pigmentosa cases. The protein encoded by the *PRPF8* gene plays a crucial role in pre-mRNA splicing. It is the major component of the U2-type or U12-type spliceosome, and it is responsible for spliceosome positioning on pre-mRNA. iPSCs carrying the 6901 C>T (P2301S) mutation in the *PRPF8* gene were edited using the CRISPR/Cas9-Gem (Cas9 endonuclease and hemin protein) system via HDR. The edited iPSCs differentiated into retinal epithelial cells and regained morphology and apical–basal polarity, as well as the ability to phagocytize photoreceptor outer segments. Cas9-Gem was used for system degradation during the G0/G1 phase to reduce the probability of NHEJ-mediated insertions [38].

CRISPR/Cas9 genome editing, combined with HDR, was used to edit iPSCs derived from a patient carrying the 1115_1125del11 mutation in the *PRPF31* gene encoding the component of the pre-mRNA spliceosome complex (retinitis pigmentosa type 11). This gene editing restored the molecular and cellular phenotypes of the induced retinal organoids [39].

The *MERTK* gene, whose mutations cause autosomal recessive retinitis pigmentosa, encodes receptor tyrosine kinase transmitting signals from the extracellular matrix to the cytoplasm. This enzyme is involved in cell differentiation, cell survival, and phagocytosis of apoptotic cells. The 992_993delCA mutation in the *MERTK* gene was corrected in patient-derived iPSCs using CRISPR/Cas9 genome editing, combined with HDR. The edited iPSCs differentiated into retinal pigment cells and restored *MERTK* expression and phagocyte functions, compared to those observed in mutant variants [40, 41].

The main cause of recessive retinitis pigmentosa in ethnic Jews is a 354-bp Alu insertion in the *MAK* gene encoding serine/threonine protein kinase that is involved in cell cycle regulation and is important for the regulation of the cilium length and photoreceptor cell survival. CRISPR/Cas9-mediated editing of iPSCs via the HDR approach involving Alu insertion restored the *MAK* transcript [29].

Enhanced S-cone syndrome is caused by a mutation in the *NR2E3* gene encoding the transcription factor activating rod development and suppressing cone development. Patients with this syndrome typically suffer from retinal atrophy, followed by loss of vision. S cones belong to one of the three types of eye cones that is the least abundant in a normal human retina. Mutations in the *NR2E3* gene result in differentiation defects, accompanied by the formation of

a large number of S cones and the absence of rods. CRISPR/Cas9- and NHEJ-mediated mutant allele knockout in iPSCs derived from a patient carrying the 166G>A (G56R) mutation in the *NR2E3* gene resulted in normal functioning and development of rod photoreceptors in differentiated retinal organoids [42].

Usher syndrome is a disease that causes a loss of vision in late stages (as a result of retinitis pigmentosa) and hearing loss in earlier stages; vestibular disorders are also possible. One of the causes of this disease is a mutation in the *MYO7A* gene encoding myosin, the retinal motor protein that is involved in the renewal of the photoreceptor outer segment discs, contributes to the distribution and migration of the melanosomes and phagosomes in retinal pigment epithelium, and is associated with the regulation of opsin transport in retinal photoreceptors. iPSCs derived from a patient with *MYO7A* mutations (c.1184 G>A and c.4118C>T) were subjected to CRISPR/Cas9 genome editing, combined with HDR. Morphological (as stereocilia adhesion) and functional (as restoration of membrane potential) recovery of differentiated edited hair cells was then observed [43]. The Usher syndrome is also associated with mutations in the *USH2A* gene encoding the usherin protein, which is involved in sound and light perception as a member of the USH2 complex. In retinal photoreceptors, the USH2 complex supports the periciliary membrane complex, which plays a role in the regulation of intracellular protein transport. Patient-derived iPSCs were subjected to CRISPR-eSpCas9 genome editing, combined with HDR, to correct the 2276G>T (C759F) and 2299delG (E767Serfs*21) mutations located 22 bp apart from *USH2A* exon 13. A 15% editing efficiency and restoration of *USH2A* gene expression was been achieved. Moreover, iPSCs retained their genomic stability and pluripotency [44, 45].

Cell therapy for retinopathies

The iPSC-based cell therapy has proved to be effective in animal models of retinopathies. Thus, the human iPSC-derived retina was transplanted into the subretinal space in monkeys with laser-induced retinal injury and in immunodeficient rats with retinitis pigmentosa. The transplanted cells were integrated into the rat retina to form synaptic connections with host bipolar cells. In the monkey model, the transplanted cells integrated into the host retina; improvement of electroretinogram (ERG) was also recorded [46]. In a similar manner, in the mouse model of retinitis pigmentosa, subretinal transplantation of iPSC-derived retinal spheroids delayed retinal thinning, increased the level of pigment epithelium-derived factor (PEDF), and reduced the number of ap-

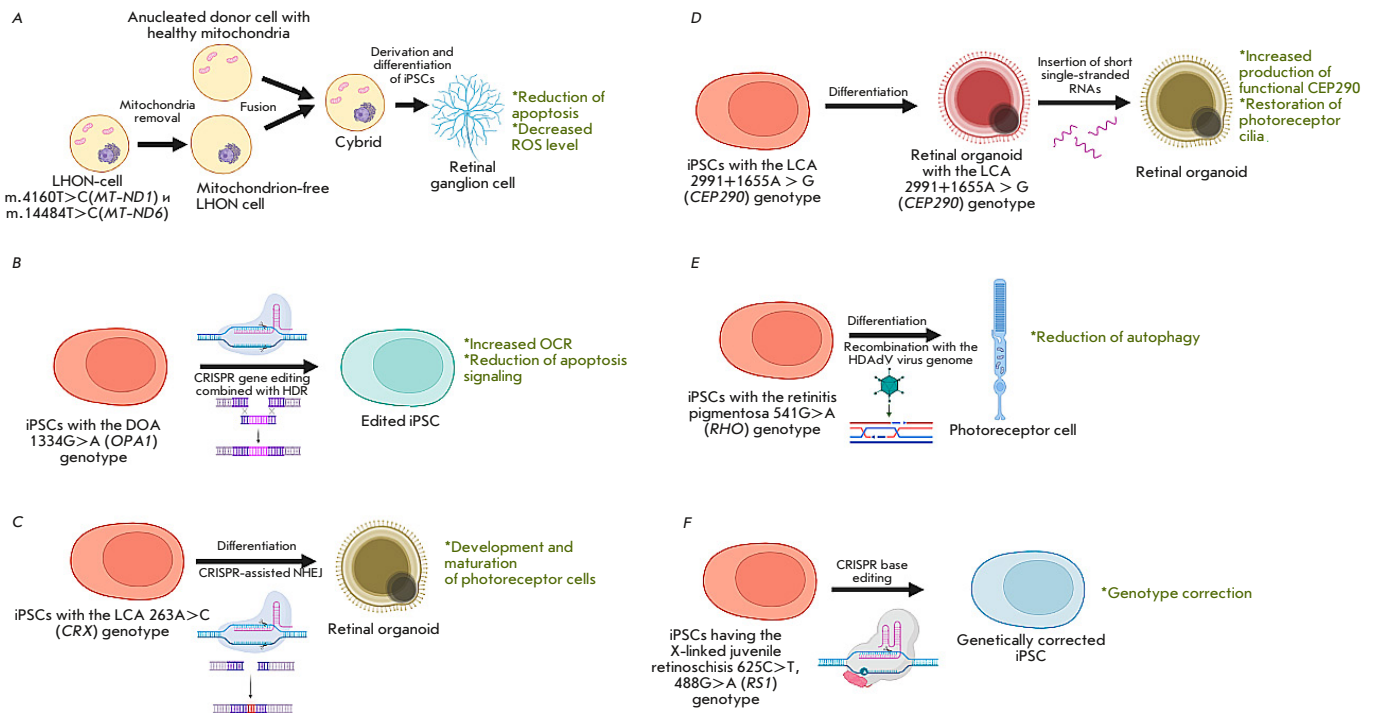


Fig. 1. Gene therapy approaches to the treatment of hereditary retinopathies/neuropathies in iPSC models. (A) – The mitochondrial replacement approach, creating cybrids in the LHON model. (B) – CRISPR editing combined with HDR in the DOA model. (C) – CRISPR editing with NHEJ in the LCA model. (D) – RNA interference in the LCA model. (E) – Recombination with the HDAdV genome in the retinitis pigmentosa model. (F) – CRISPR base editing using ABE7.10 in the model of X-linked juvenile retinoschisis

optic cells and the level of microglial infiltration into the retina [47]. In rats with an inherited mutation in the *MERTK* proto-oncogene tyrosine kinase (*MERTK*) gene as a model of retinal degeneration, subretinal transplantation of iPSC-derived RPE cells significantly restored the visual function as measured by thresholds in optokinetic tracking. None of the animals showed abnormal proliferation or teratoma formation [48]. Interestingly, co-transplantation of different types of retinal cells derived from iPSCs showed better results compared to the transplantation of individual cell types. This resulted in a better visual response and preservation of the outer nucleolar layer in the retinal degeneration rat model [49]. In the animal model of retinitis pigmentosa, subretinally transplanted iPSC-derived photoreceptor precursors expressing *CRX* were incorporated into the inner nuclear layer of cells. The transplanted cells expressed the marker arrestin 3, which was indicative of their further maturation [50].

In the preclinical study in rats and pigs, after differentiation into retinal cells, iPSCs derived from the CD34+ cells of patients with macular dystrophy inte-

grated and restored the retina. This study revealed that 10-fold fewer cells were required during monolayer transplantation to attain the therapeutic effect than when using a cell suspension. Meanwhile, retinal cells transplanted as a suspension failed to integrate into the retinal ganglion cell layer of the rat; the poly(lactic-co-glycolic acid) (PLGA)-based scaffold facilitated the integration of the transplanted cell layer into the Bruch's membrane of the rat [51].

CONCLUSIONS

Although the application of iPSCs in studies devoted to optic neuropathies and retinopathies is a relatively new approach, this technology undoubtedly has a high potential in terms of investigating the pathogenesis of diseases, as well as validating and optimizing gene therapy and genome editing technologies (Fig. 1, Table 1). Disease modeling using iPSCs allows one to study the main mechanisms causing loss of retinal ganglion cells; cell replacement therapy using iPSCs derived from the patient's own somatic cells presents a minimal risk of immune rejection after transplantation and exhibits high efficacy for different mod-

Table 1. Studying the potential of gene therapy approaches and gene editing of inherited retinopathies and optic neuropathies using the iPSCs models

Disease	Mutation	Inheritance type	Treatment approach	Main effects/outcome
LHON ^{*1}	m.4160T>C(<i>MT-ND1</i>) and m.14484T>C(<i>MT-ND6</i>)	Maternal, mitochondrial	mitochondrial replacement, cybrid generation	Reduction of apoptotic effects and ROS level ^{*2} in differentiated RGCs ^{*3} [20]
DOA ^{*4}	1334G>A (<i>OPA1</i>)	Autosomal dominant	CRISPR genome editing combined with HDR ^{*5}	Increased OCR ^{*6} in edited iPSCs ^{*7} and reduction of apoptotic signals [21]
LCA ^{*8}	2991+1655A > G (<i>CEP290</i>)	Autosomal recessive	CRISPR-assisted NHEJ ^{*9} , RNA interference	Increased production of functional CEP290. Restoration of photoreceptor cilia [29, 30]
	834G>A (<i>AIPL1</i>)	Autosomal recessive	CRISPR genome editing combined with HDR	Restoration of <i>AIPL1</i> gene expression, increased cGMP ^{*10} and PDE6 levels in retinal organoid cells [31]
	263A>C(<i>CRX</i>)	Autosomal recessive	CRISPR-assisted NHEJ	In the model of retinal organoids derived from patients' iPSCs, promoted the development and maturation of photoreceptor cells [32]
Retinitis pigmentosa	541 G>A (<i>RHO</i>)	Autosomal dominant	Recombination with the HDAdV genome	After gene editing, iPSCs differentiated to photoreceptor cells exhibited reduced autophagy [34]
	68C>A (<i>RHO</i>)	Autosomal dominant	CRISPR-assisted NHEJ	Inactivation of mutant allele [29]
	3070G>T (<i>RPGR</i>)	X-linked	CRISPR genome editing combined with HDR	Restoration of the nucleotide sequence [35]
	1685_1686delAT, 2234_2235delGA and 2403_2404delAG (<i>RPGR</i>)	X-linked	CRISPR genome editing combined with HDR	Retinal organoids had a normal morphology [36]
	6901C>T (<i>PRFP8</i>)	Autosomal dominant	CRISPR genome editing combined with HDR	The morphology and phagocytizing ability were restored in edited iPSCs differentiated into retinal epithelial cells [38]
	1115_1125del11 (<i>PRPF31</i>)	Autosomal dominant	CRISPR genome editing combined with HDR	Restoration of the molecular and cellular phenotypes in induced retinal organoids [39]
	992_993delCA (<i>MERTK</i>)	Autosomal recessive	CRISPR genome editing combined with HDR	Restoration of <i>MERTK</i> gene expression and phagocytic function [40, 41]
	354-bp Alu insertion (<i>MAK</i>)	Autosomal recessive	CRISPR genome editing combined with HDR	Restoration of <i>MAK</i> transcript [29]
X-linked juvenile retinoschisis	625C>T, 488G>A (<i>RS1</i>)	X-linked	CRISPR-mediated base editing using the ABE7.10 system	Restoration of the nucleotide sequence [37]
Enhanced S-cone syndrome	166G>A (<i>NR2E3</i>)	Autosomal recessive	CRISPR-assisted NHEJ	Normal functioning and development of rod photoreceptors in differentiated retinal organoids [42]
Usher syndrome	c.1184G>A and c.4118C>T (<i>MYO7A</i>)	Autosomal recessive	CRISPR genome editing combined with HDR	Morphological (stereocilia adhesion) and functional recovery (restoration of the membrane potential) [43]
	2276G>T (<i>USH2A</i>)	Autosomal recessive	CRISPR genome editing combined with HDR	Restoration of the nucleotide sequence [44, 45]

^{*1} – Leber hereditary optic neuropathy; ^{*2} – reactive oxygen species; ^{*3} – retinal ganglion cells; ^{*4} – autosomal dominant optic atrophy; ^{*5} – homology-directed repair; ^{*6} – oxygen consumption rate; ^{*7} – induced pluripotent stem cells; ^{*8} – Leber congenital amaurosis; ^{*9} – non-homologous end joining; ^{*10} – cyclic guanosine monophosphate.

els. Gene therapy, in combination with cell replacement therapy, can be used to correct genetic defects in iPSC-derived cells prior to transplantation.

iPSCs have a tremendous translational potential in a broad range of therapeutic areas. The development and improvement of protocols for enhancing the efficacy and purity of iPSC-derived retinal ganglion cells will be critical in elaborating a standardized meth-

odology for using iPSCs in disease modeling, drug screening, toxicology studies, cell and gene therapy, as well as regenerative medicine. ●

This work was supported by the Ministry of Science and Higher Education of the Russian Federation (Agreement No. 075-10-2021-093; Project No. GTH-RND-2112).

REFERENCES

- Takahashi K., Tanabe K., Ohnuki M., Narita M., Ichisaka T., Tomoda K., Yamanaka S. // *Cell*. 2007. V. 131. № 5. P. 861–872.
- Piao Y., Hung S.S., Lim S.Y., Wong R.C., Ko M.S. // *Stem Cells Transl. Med.* 2014. V. 3. № 7. P. 787–791.
- Hung S.S., Pebay A., Wong R.C. // *J. Vis. Exp.* 2015. V. 102. P. e53174.
- Evans M.J., Kaufman M.H. // *Nature*. 1981. V. 292. № 5819. P. 154–156.
- Martin G.R. // *Proc. Natl. Acad. Sci. USA*. 1981. V. 78. № 12. P. 7634–7638.
- Thomson J.A., Itskovitz-Eldor J., Shapiro S.S., Waknitz M.A., Swiergiel J.J., Marshall V.S., Jones J.M. // *Science*. 1998. V. 282. № 5391. P. 1145–1147.
- Giacca M., Zacchigna S. // *J. Control. Release*. 2012. V. 161. № 2. P. 377–388.
- Junquera E., Aicart E. // *Curr. Top. Med. Chem.* 2014. V. 14. № 5. P. 649–663.
- Eggermann K., Gess B., Häusler M., Weis J., Hahn A., Kurth I. // *Dtsch. Arztebl. Int.* 2018. V. 115. № 6. P. 91–97.
- Paolini Sguazzi G., Muto V., Tartaglia M., Bertini E., Compagnucci C. // *Int. J. Mol. Sci.* 2021. V. 22. № 24. P. 13674.
- Ghaffarieh A., Levin L.A. // *Int. Rev. Neurobiol.* 2012. V. 105. P. 1–17.
- Moore D.L., Goldberg J.L. // *J. Neuroophthalmol.* 2010. V. 30. № 4. P. 347–360.
- Yu D.Y., Cringle S.J., Balaratnasingam C., Morgan W.H., Yu P.K., Su E.N. // *Progr. Retinal Eye Res.* 2013. V. 36. P. 217–246.
- Cook C., Foster P. // *Can. J. Ophthalmol.* 2012. V. 47. № 3. P. 223–226.
- Quigley H.A., Broman A.T. // *Br. J. Ophthalmol.* 2006. V. 90. № 3. P. 262–267.
- Tham Y.C., Li X., Wong T.Y., Quigley H.A., Aung T., Cheng C.Y. // *Ophthalmology*. 2014. V. 121. № 11. P. 2081–2090.
- Garcia-Valenzuela E., Gorczyca W., Darzynkiewicz Z., Sharma S.C. // *J. Neurobiol.* 1994. V. 25. № 4. P. 431–438.
- Kerrigan L.A., Zack D.J., Quigley H.A., Smith S.D., Pease M.E. // *Arch. Ophthalmol.* 1997. V. 115. № 8. P. 1031–1035.
- Quigley H.A., Addicks E.M., Green W.R., Maumenee A.E. // *Arch. Ophthalmol.* 1981. V. 99. № 4. P. 635–649.
- Wong R.C.B., Lim S.Y., Hung S.S.C., Jackson S., Khan S., van Bergen N.J., De Smit E., Liang H.H., Kearns L.S., Clarke L., et al // *AGING-US*. 2017. V. 9. № 4. P. 1341–1350.
- Sladen P.E., Perdigão P.R.L., Salisbury G., Novoselova T., van der Spuy J., Chapple J.P., Yu-Wai-Man P., Cheetham M.E. // *Mol. Ther. Nucl. Acids*. 2021. V. 26. P. 432–443.
- Hambright D., Park K.Y., Brooks M., McKay R., Swaroop A., Nasonkin I.O. // *Mol. Vis.* 2012. V. 18. P. 920–936.
- Satarian L., Javan M., Kiani S., Hajkaram M., Mirnajafi-Zadeh J., Baharvand H. // *PLoS One*. 2013. V. 8. № 8. P. e71855.
- Abu-Hassan D.W., Li X., Ryan E.I., Acott T.S., Kelley M.J. // *Stem Cells*. 2015. V. 33. № 3. P. 751–761.
- Schwartz S.D., Hubschman J.P., Heilwell G., Franco-Cardenas V., Pan C.K., Ostrick R.M., Mickunas E., Gay R., Klimanskaya I., Lanza R. // *Lancet*. 2012. V. 379. № 9817. P. 713–720.
- Schwartz S.D., Regillo C.D., Lam B.L., Elliott D., Rosenfeld P.J., Gregori N.Z., Hubschman J.P., Davis J.L., Heilwell G., Spirn M., et al. // *Lancet*. 2015. V. 385. № 9967. P. 509–516.
- Hereditary retinal dystrophy. URL: <https://www.barranger.com/en/pathology/hereditary-retinal-dystrophy>.
- Leber congenital amaurosis. URL: <https://medlineplus.gov/genetics/condition/leber-congenital-amaurosis>.
- Burnight E.R., Giacalone J.C., Cooke J.A., Thompson J.R., Bohrer L.R., Chirco K.R., Drack A.V., Fingert J.H., Worthington K.S., Wiley L.A., et al. // *Mol. Ther.* 2017. V. 25. № 9. P. 1999–2013.
- Dulla K., Aguila M., Lane A., Jovanovic K., Parfitt D.A., Schulkens I., Chan H.L., Schmidt I., Beumer W., Vorthoren L., et al. // *Mol. Ther. Nucl. Acids*. 2018. V. 12. P. 730–740.
- Leung A., Sacristan-Reviriego A., Perdigão P.R.L., Sai H., Georgiou M., Kalitzeos A., Carr A.F., Coffey P.J., Michaelides M., Bainbridge J., et al. // *Stem Cell Repts.* 2022. V. 17. № 10. P. 2187–2202.
- Chirco K.R., Chew S., Moore A.T., Duncan J.L., Lamba D.A. // *Stem Cell Repts.* 2021. V. 16. № 11. P. 2690–2702.
- Rezaie T., Child A., Hitchings R., Brice G., Miller L., Coca-Prados M., Héon E., Krupin T., Ritch R., Kreutzer D., et al. // *Science*. 2002. V. 295. № 5557. P. 1077–1079.
- Yoshida T., Ozawa Y., Suzuki K., Yuki K., Ohyama M., Akamatsu W., Matsuzaki Y., Shimmura S., Mitani K., Tsubota K., et al. // *Mol. Brain*. 2014. V. 7. P. 45.
- Bassuk A.G., Zheng A., Li Y., Tsang S.H., Mahajan V.B. // *Sci. Rep.* 2016. V. 6. P. 19969.
- Deng W.L., Gao M.L., Lei X.L., Lv J.N., Zhao H., He K.W., Xia X.X., Li L.Y., Chen Y.C., Li Y.P., et al. // *Stem Cell Repts.* 2018. V. 10. № 4. P. 1267–1281.
- Huang K.C., Wang M.L., Chen S.J., Kuo J.C., Wang W.J., Nhi Nguyen P.N., Wahlin K.J., Lu J.F., Tran A.A., Shi M., et al. // *Stem Cell Repts.* 2019. V. 13. № 5. P. 906–923.
- Foltz L.P., Howden S.E., Thomson J.A., Clegg D.O. // *Int. J. Mol. Sci.* 2018. V. 19. № 12. P. 4127.
- Buskin A., Zhu L., Chichagova V., Basu B., Mozafari-Jovin S., Dolan D., Droop A., Collin J., Bronstein R., Mehrotra S., et al. // *Nat. Commun.* 2018. V. 9. № 1. P. 4234.

40. Artero-Castro A., Long K., Bassett A., Machuca C., León M., Ávila-Fernandez A., Cortón M., Vidal-Puig T., Ayuso C., Lukovic D., et al. // *Stem Cell Res.* 2019. V. 34. P. 101341.
41. Artero-Castro A., Long K., Bassett A., Ávila-Fernandez A., Cortón M., Vidal-Puig A., Jendelova P., Rodriguez-Jimenez F.J., Clemente E., Ayuso C., et al. // *Int. J. Mol. Sci.* 2021. V. 22. № 4. P. 2092.
42. Diakatou M., Dubois G., Erkilic N., Sanjurjo-Soriano C., Meunier I., Kalatzis V. // *Int. J. Mol. Sci.* 2021. V. 22. № 5. P. 2607.
43. Tang Z.H., Chen J.R., Zheng J., Shi H.S., Ding J., Qian X.D., Zhang C., Chen J.L., Wang C.C., Li L., et al. // *Stem Cells Transl. Med.* 2016. V. 5. № 5. P. 561–571.
44. Sanjurjo-Soriano C., Erkilic N., Baux D., Mamaeva D., Hamel C.P., Meunier I., Roux A.F., Kalatzis V. // *Mol. Ther. Methods Clin. Dev.* 2019. V. 17. P. 156–173.
45. Liu X., Lillywhite J., Zhu W., Huang Z., Clark A.M., Gosstola N., Maguire C.T., Dykxhoorn D., Chen Z.Y., Yang J. // *Genes (Basel)*. 2021. V. 12. № 6. P. 805.
46. Tu H.Y., Watanabe T., Shirai H., Yamasaki S., Kinoshita M., Matsushita K., Hashiguchi T., Onoe H., Matsuyama T., Kuwahara A., et al. // *EBioMedicine*. 2019. V. 39. P. 562–574.
47. Zhu D., Xie M., Gademann F., Cao J., Wang P., Guo Y., Zhang L., Su T., Zhang J., Chen J. // *Stem Cell Res. Ther.* 2020. V. 11. № 1. P. 98.
48. Surendran H., Nandakumar S., Reddy K.V.B., Stoddard J., Mohan K.V., Upadhyay P.K., McGill T.J., Pal R. // *Stem Cell Res. Ther.* 2021. V. 12. № 1. P. 70.
49. Salas A., Duarri A., Fontrodona L., Ramírez D.M., Badia A., Isla-Magrané H., Ferreira-de-Souza B., Zapata M.Á., Raya Á., Veiga A., et al. // *Mol. Ther. Methods Clin. Develop.* 2021. V. 20. P. 688–702.
50. Collin J., Zerti D., Queen R., Santos-Ferreira T., Bauer R., Coxhead J., Hussain R., Steel D., Mellough C., Ader M., et al. // *Stem Cells (Dayton, Ohio)*. 2019. V. 37. № 5. P. 609–622.
51. Sharma R., Khristov V., Rising A., Jha B.S., Dejene R., Hotaling N., Li Y., Stoddard J., Stankewicz C., Wan Q., et al. // *Sci. Transl. Med.* 2019. V. 11. № 475. P. eaat5580.

RIPK3 Expression in Fibroblasts in an *in vivo* and *in vitro* Skin Wound Model: A Controversial Result

I. S. Izumov¹, M. S. Shitova¹, M. S. Sabirov¹, S. A. Sheleg¹, O. L. Cherkashina¹, E. P. Kalabusheva¹, E. A. Vorotelyak^{1,2}, E. I. Morgun^{1*}

¹Koltzov Institute of Developmental Biology of Russian Academy of Sciences, Moscow, 119334 Russian Federation

²M.V. Lomonosov Moscow State University, Moscow, 119234 Russian Federation

*E-mail: lady.morgun2016@yandex.ru

Received: September 06, 2023; in final form, October 25, 2023

DOI: 10.32607/actanaturae.25452

Copyright © 2023 National Research University Higher School of Economics. This is an open access article distributed under the Creative Commons Attribution License, which permits unrestricted use, distribution, and reproduction in any medium, provided the original work is properly cited.

ABSTRACT One of the major problems of regenerative medicine is the development of hypertrophic scars and keloids. The protein kinase RIPK3 is involved in necroptosis; however, recent evidence indicates that it also has non-canonical functions, including its involvement in the development of renal fibrosis. The aim of our work was to study the expression of RIPK3 in mouse and human skin models of fibrotic processes. A subpopulation of RIPK3+Vim+ cells was found in both human keloid and a mouse wound, with the cell number being significantly greater in the mouse wound bed compared to healthy skin. Real-time polymerase chain reaction (RT-PCR) detected expression of the *Ripk3* and fibroblast biomarkers *Acta2*, *Fap*, *Col1a1*, and *Fn1* in the cells isolated from the wound bed, indicating that RIPK3 can be expressed by wound bed fibroblasts. An analysis of the human fibroblasts stained with anti-RIPK3 antibodies demonstrated an increase in the fluorescence intensity in the presence of lipopolysaccharide (LPS) at concentrations of 5, 10, 25, 50, and 100 ng/ml and TGF- β at concentrations of 0.1, 1, 2, and 5 ng/ml compared to the control. At the same time, the expression levels of RIPK3 and fibroblast activation markers in the presence of TGF- β and LPS did not differ significantly from the control. It is possible that RIPK3 expression in wound fibroblasts is not directly associated with fibrotic processes, and that kinase plays a different, yet unknown role in wound healing.

KEYWORDS scarring, keloid, skin, fibroblasts, cell culture, RIPK3.

ABBREVIATIONS RT-PCR – real-time polymerase chain reaction; ECM – extracellular matrix; RIPK3 – receptor-interacting serine/threonine-protein kinase 3; PFA – paraformaldehyde; DEG – differentially expressed gene; Vim – Vimentin; LPS – lipopolysaccharide; Fn – fibronectin; FAP – fibroblast activation protein- α ; Col1a1 – collagen type I alpha 1; UMAP – Uniform Manifold Approximation and Projection.

INTRODUCTION

Disorders of skin wound healing is a major medical problem. These disorders include pathologies associated with fibrotic processes, which are caused by enhanced proliferation of fibroblasts and excessive synthesis of the extracellular matrix (ECM), leading to hypertrophic and keloid scarring. There are approaches to the treatment of skin wounds [1]; however, the problem of regeneration anomalies, such as fibrosis, remains unresolved.

Protein kinase RIPK3 (Receptor-interacting serine/threonine-protein kinase 3) is an important member of necroptosis, the process of programmed cell death with morphological signs of necrosis. Protein kinases RIPK3

and RIPK1 are known to transmit a signal from receptors such as TNFR, FasR, TRAILR, TLR3, TLR4, and INFAR1 to MLKL, resulting in cell death [2, 3].

RIPK3 not only participates in necroptosis but also possesses non-canonical functions: it is involved in apoptosis and inflammation. RIPK3 promotes cytokine production in dendritic cells [4]. Recently, data has appeared on a possible involvement of RIPK3 in the development of fibrotic processes in kidneys and lungs [5, 6]. Previous experiments performed in our laboratory have demonstrated RIPK3 expression in mouse and human skin [7]. In this regard, the aim of our work is to study RIPK3 expression in mouse and human skin models of fibrotic processes.

EXPERIMENTAL

Biological sample

Thirty male C57Bl/6 mice were used in the study. Mice were housed at +23°C, with unlimited access to drinking water and food (according to GOST No. 33215-2014). All manipulations with the animals were carried out under general anesthesia, in accordance with “Regulations for studies using experimental animals” (Russia, 2010) and “International Guiding Principles (Ethical Codes) for Biomedical Research Involving Animals” (CIOMS and ICLAS, 2012), with the approval of the Bioethics Commission of the Institute of Developmental Biology of the Russian Academy of Sciences (protocols No. 51 of 09.09.2021 and No. 62 of 01.09.2022) and in strict compliance with the ethical principles established by the European Convention for the Protection of Vertebrate Animals used for Experimental and Other Scientific Purposes (Strasbourg, 2006).

In addition to the biological mouse sample, we used a keloid tissue sample and a normal human breast skin sample. Fragments of human skin were obtained by surgery, with the voluntary informed consent of the patient; experiments using cell cultures were carried out with the approval of the Bioethics Commission of the Institute of Developmental Biology of the Russian Academy of Sciences.

Cell isolation from wounds and intact mouse dermis

Biological samples were washed in Hank's Balanced Salt Solution supplemented with amphotericin B solution (Sintez OAO, Russia) and a gentamicin sulfate solution (BioPharmGarant, Russia). Tissues were minced and placed in 0.2% dispase solution (Gibco, catalog No. 17105-041). The samples were incubated in a thermal cycler at +37°C for 30 min. The epidermis was removed from tissue fragments in sterile conditions. The wound specimen was placed in a 0.2% collagenase I (Worthington Biochemical, catalog No. LS004197) and a IV solution (Gibco, catalog No. 1704-019). The skin was placed in a 0.2% collagenase IV solution (Gibco, catalog No. 1704-019). The resulting solution was centrifuged at +4°C and washed thrice with a sterile ice-cold DPBS solution; the sediment was then pipetted.

Mouse cell cultures

A suspension of cells isolated from normal mouse dermis was filtered through a strainer with a pore diameter of 100 µm. The cells isolated from the wound bed and normal dermis were resuspended in DMEM and DMEM Advanced, respectively. Both media were supplemented with 10% fetal bovine serum, 1% glu-

tamine, and 1% penicillin-streptomycin. Next, the cells were seeded in a 96-well plate. RNA was isolated from confluent cells.

Human cell cultures

Human fibroblasts were provided by the “Cell culture collection for biotechnological and biomedical research (general biological and biomedical areas)” center of the Institute of Developmental Biology n.a. N. K. Koltsov of the Russian Academy of Sciences.

Human fibroblasts from three different donors were cultured in 6-well plates containing a DMEM medium (PanEco) with 10% fetal calf serum, 1% glutamine, and 1% penicillin-streptomycin at 3×10^5 cells per well. A total of 24 h after cell seeding, the cell media was substituted with a Opti-MEM medium containing 1% fetal bovine serum [5]. After 60 min, the medium was changed to either a medium containing TGF-β at concentrations of 0.1, 1, 2, 5, and 10 ng/ml [5], lipopolysaccharide (LPS) at concentrations of 1, 5, 10, 25, 50, and 100 ng/ml [8], or a mixture of TGF-β (10 ng/ml) and LPS (100 ng/ml). After 24 h, the cells were fixed and stained with anti-RIPK3 antibodies using the standard laboratory protocol. The experiment was repeated with the exception that TGF-β was added at concentrations of 1 and 10 ng/ml, and LPS was added at concentrations of 10 and 100 ng/ml. Total RNA was isolated after 24 h using columns.

Mouse skin wound model

We used the approach presented in [9], which utilized a large (square wound, 1 cm² in area) and a small mouse wound (round wound with a diameter of 4 mm) model. We needed to simulate a small wound. However, it is impossible to isolate fibroblasts at the proliferation stage from a wound with a diameter of 4 mm due to its small size. For this reason, we used a wound with a diameter of 8 mm instead.

The mouse was anesthetized by intraperitoneal administration of Avertin. Veet depilatory cream (France) was used to remove hair in the surgical area. Five circles with a diameter of 8 mm were applied to the mouse back using a stencil; the tissue was excised within the boundaries of the applied circles. The resulting wounds were covered with a plaster (Tegadermtm). The mice were removed from the experiment on day 10 after surgery. Normal back skin of mice was used as a biological control.

Immunofluorescence staining

Skin wound specimens on slides and cell cultures in plastic plates were fixed using a 4% PFA solution for 10 min and then washed in phosphate-buffered saline (PBS, three times for 5 min each). The samples were

then coated with a blocking solution (5% donkey serum and 1% Triton in PBS) and incubated for 30 min in a humidified chamber at room temperature. The blocking solution was removed, and the primary antibody solution was added. The samples were incubated in a humid chamber at +4°C for at least 12 h.

The samples were washed in PBS, coated with a solution of secondary antibodies, and incubated in a humid chamber at room temperature for 1 h. The nuclei were counterstained with DAPI and mounted with a BrightMount/Plus medium (Abcam, UK).

We used primary antibodies to RIPK3 (Sigma, catalog No. HPA055087, dilution 1 : 500) and Vimentin (Abcam, catalog No. ab24525, dilution 1 : 500) and secondary antibodies AlexaFluor 488 (Abcam, Ab150173, dilution 1 : 500), AlexaFluor 594 (A21207, Invitrogen, dilution 1 : 500), and AlexaFluor 660 (A21074, Invitrogen, dilution 1 : 500). A lymph node was used as a positive control for the antibodies to RIPK3. Fibroblasts were used as a positive control for antibodies to Vimentin. The samples not stained with primary antibodies were used as a negative control.

Fluorescence microscopy

A Leica DMI6000 microscope was used for fluorescence microscopy and visualization of the preparations stained with antibodies. Photographs were processed and analyzed using the BZ-II Analyzer (Keyence), LAS X (Leica), ImageJ (FiJi), and STATISTICA (StatSoft) software.

RNA isolation, reverse transcription, PCR followed by gel electrophoresis and RT-PCR

RNA was isolated from the cells using columns (Biolabmix and Zymo Research) according to the manufacturer's instructions (USA, Russia). The samples were treated with DNase (ThermoFisher and Zymo Research); cDNA was synthesized using the MMLV RT kit (Eurogen) with an oligo(dT) primer according to the manufacturer's protocol. Real-time PCR was performed using the qPCRmix-HS SYBR PCR mixture (Evrogen), according to the manufacturer's instructions on a LightCycler 96 (Roche, Switzerland). Conventional PCR was carried out using the ScreenMix PCR mixture (Evrogen), according to the manufacturer's instructions on a T100 Thermal Cycler (Bio-Rad, USA). Horizontal gel electrophoresis was performed in a 2% agarose gel. The results were visualized on a ChemiDoc XRS+ System (Bio-Rad).

Primers were selected using PrimerBlast and PrimerSelect (Table 1). Gene expression levels were normalized to those of the housekeeping genes: beta-actin (*Actb*) and glyceraldehyde-3-phosphate dehydrogenase (*GAPDH*) in mouse and human samples, respectively.

Evaluation of the fluorescence intensity of the stained human fibroblast cells

The average fluorescence intensity was measured using the ImageJ software (FiJi). For a comparative analysis of the fluorescence intensity, same exposure

Table 1. Nucleotide sequences of PCR primers

Primer	Forward primer sequence	Reverse primer sequence
<i>hu FN1</i>	GCACCACCCAGACATTACT	CGGGACTCAGGTTATCAAAAGTG
<i>hu FAP</i>	ATGGGCTGGTGGATTCTTTGT	ATGTTTGTAGCCATCCTTGTCCT
<i>hu COL1A1</i>	CCCCTGGAAAGAATGGAGATGA	CAAACCACTGAAACCTCTGTGTC
<i>hu GAPDH</i>	GAAGGTCGGAGTCAACGGATTT	TTCTCAGCCTTGACGGTGC
<i>hu RIPK3</i>	ATGCTGCTGTCTCCACGGTAA	AAAGCCATCCATTTCTGTCCCTC
<i>mo Actb</i>	ACCCGCCACCAGTTTCG	AGCATCGTCGCCCGC
<i>mo Acta2</i>	CATTGGGATGGAGTCAGCGG	GACAGGACGTTGTTAGCATAGAGA
<i>mo Acta2</i>	CCCTGAAGAGCATCCGACAC	CAGAGTCCAGCACAATACCAGT
<i>mo Fn1</i>	GAGGAAGAAGACAGGACAGGAA	GTCAGAGTCGCACTGGTAGAA
<i>mo Fap</i>	AAGAAGCTCAAAGACGGGGG	TGCAAGGACCACCATACTT
<i>mo Ripk3</i>	ACACGGCACTCCTTGGTATC	CCTGAGGCAGTAGTTCTTGGTG
<i>mo Col1a1</i>	TGACTGGAAGAGCGGAGAGTA	GGCTGAGTAGGGAACACACA

of different samples of fibroblasts stained with the fluorescent antibodies was used. Measurements were taken at 30 points of 3–5 fields of view for the control and experimental groups. The results were analyzed using GraphPad Prism 8 (USA).

Analysis of *RIPK3* expression using RNA-seq data

Data collection. Three data sets were extracted from the NCBI GEO database (<https://www.ncbi.nlm.nih.gov/geo/>). The GSE113619 data set contains bulk RNA sequencing data for 27 samples of normal human skin (control) and 37 samples of keloid-prone skin, with biological replicates taken into account [10]. The GSE130973 data set includes RNA sequencing data on individual cells from five normal human skin samples [11]. The GSE163973 data set contains RNA sequencing data on individual cells from three human keloid scar samples [12].

Analysis of differential gene expression. Differential gene expression was analyzed using bulk RNA sequencing data and the EdgeR package (R version) [13].

Processing and analysis of individual cell RNA sequencing data. The Seurat v4.1.1 R package was used for data processing and analysis [14]. Fibroblasts from the datasets GSE113619 and GSE163973 were integrated using canonical correlation analysis (CCA). Data dimensionality reduction was performed using principal component analysis (PCA) of 3,000 highly variable genes (HVGs). The search for the nearest neighbors was performed using the *FindNeighbors* function for the first 30 PC's. Clustering was performed using the *FindClusters* function with the resolution parameter = 0.1.

Statistical analysis

The obtained data were analyzed using the Excel and GraphPad Prism 8 software (USA). Kruskal–Wallis one-way analysis of variance was used to compare multiple groups. The Mann–Whitney U test was used to compare two groups. Data were considered statistically significant at $P < 0.05$.

RESULTS AND DISCUSSION

RIPK3 expression in the scar tissue and normal human skin

Immunofluorescence staining of human keloid showed *RIPK3* expression in multiple Vimentin+ cells (Fig. 1A). Individual *RIPK3*+ cells were found in the dermis of normal skin (Fig. 1B).

In order to assess a change in the *RIPK3* expression in keloid scar fibroblasts *in vivo*, we analyzed the RNA sequencing data for human skin samples. We first used the bulk RNA sequencing data obtained by Onoufriadis et al. (GSE113619) in order to determine whether *RIPK3* belongs to differentially expressed genes (DEGs), compared to normal and keloid-prone skin [10]. The data set included 27 normal skin samples and 37 skin samples from keloid-prone individuals genetically susceptible to form keloids. A comparison of gene expression in normal and keloid-prone skin showed that *RIPK3* is not a DEG ($\log_{FC} = -0.07619307$, $P_{adjusted} = 1$). Figure 1G shows that the distribution of the gene counts in normal skin (light purple range diagram) does not differ from that of the skin in individuals with hereditary susceptibility to form keloids (light golden range diagram). The median count distribution is 1 in both cases.

The low level of *RIPK3* expression demonstrated in bulk RNA sequencing can potentially be due to the presence of a minor, specific cell population with an active gene. For this reason, we analyzed the results of the sequencing of RNA from individual cells of normal skin and keloid scar. Data on normal skin samples was used from the study by Solé-Boldo et al. (GSE130973) for a visual assessment of *RIPK3* expression in different cell types [11]. In normal skin, *RIPK3* expression, i.e. *RIPK3*+ cells, was detected at an insignificant level (Fig. 1C). Sequencing data for RNA from individual cells of the keloid scar were used from the study by Deng et al. (GSE163973) [12]. Visual evaluation of *RIPK3*+ cell representation demonstrates a significant number of these cells among endothelial cells and the fibroblasts of the keloid scar (Fig. 1D). The analyzed data were consolidated and integrated in order to perform a comparative analysis of fibroblasts from healthy skin and keloid scar. The object contained 11,710 cells. Of them, 5,948 and 5,762 cells were normal skin fibroblasts and keloid scar fibroblasts, respectively. We obtained four clusters of fibroblast cells and, similar to the study by Solé-Boldo et al., assessed the distribution of *RIPK3*+ cells between the clusters. As previously demonstrated using data sets containing all skin cell types (Fig. 1C,D), the number of *RIPK3*+ cells is increased among the fibroblasts of the keloid scar (Fig. 1E). Moreover, *RIPK3*+ fibroblasts do not form a separate cluster but instead are distributed randomly. We further compared genes with differential expression in normal skin and keloid scar cells. Similar to the results of bulk RNA sequencing (Fig. 1G), *RIPK3* cannot be considered a DEG, whose expression differs between normal skin and keloid scar fibroblasts. In addition, due to the small number

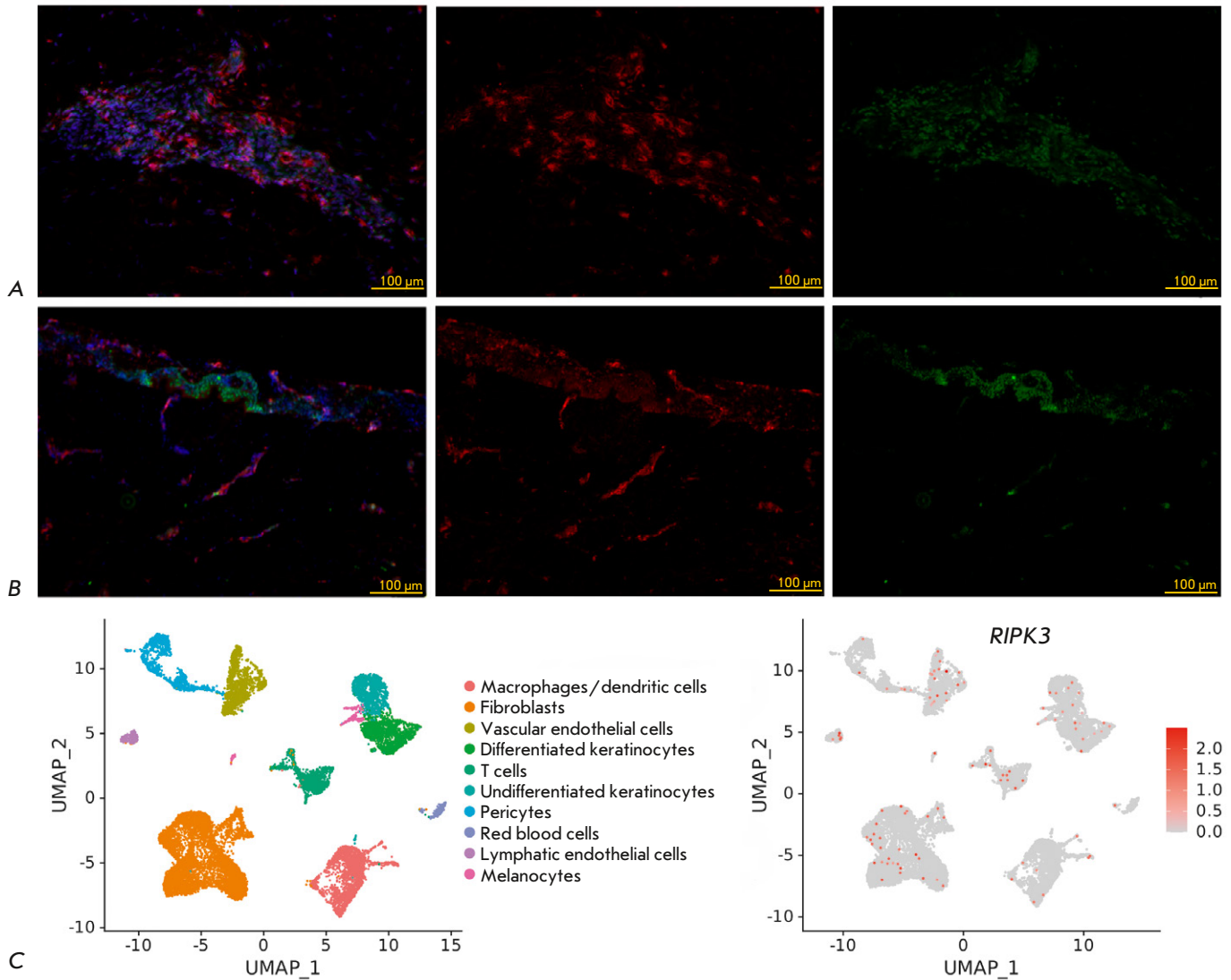


Fig. 1. Patterns of RIPK3 expression in human skin. Micropreparations of human keloid scar (A) and normal dermis (B), immunohistochemical staining with antibodies to Vim (red) and RIPK3 (green), nuclei stained with DAPI, 20× magnification. The UMAP plot of cell clusters with annotations for normal skin samples (left) and the distribution of *RIPK3*+ cells in these data (right) (C). The UMAP plot of cell clusters with annotations for normal scar and keloid scar samples (left) and the distribution of *RIPK3*+ cells in these data (right) (D). The UMAP plot for cell clusters in fibroblasts from normal skin and keloid scars (left) and the distribution of *RIPK3*+ cells in these data (right) (E). The percentage of *RIPK3*+ cells in fibroblasts from normal skin and keloid scars among the four obtained cell clusters (right) and the comparison of the proportions of *RIPK3*+ cells in all fibroblasts from normal skin and keloid scars (left), *** – P -value $< 2.2 \times 10^{-16}$ (Fisher's exact test) (F). The distribution of *RIPK3* raw gene counts in bulk RNA sequencing data on normal and keloid-prone human skin samples (G)

of cells expressing the gene, it was not included in the analysis.

Nevertheless, we see that the percentage of *RIPK3*+ cells in keloid scar fibroblasts is significantly greater than that in normal skin fibroblasts among all cell clusters (Fig. 1F, on the left). The difference in the number of *RIPK3*+ fibroblasts (28 out of 5,948 for normal skin cells and 318 out of 5,762 for keloid

cells) is statistically significant (Fisher's exact test, P -value < 0.001) (Fig. 1F, right). Thus, *RIPK3* expression in keloid scar fibroblasts is not elevated in *RIPK3*+ cells and corresponds to a physiological level similar to that in normal skin fibroblasts. Moreover, the significant (more than 10-fold) increase in the number of *RIPK3*-expressing cells may be associated with the transition of fibroblasts to an activated state.

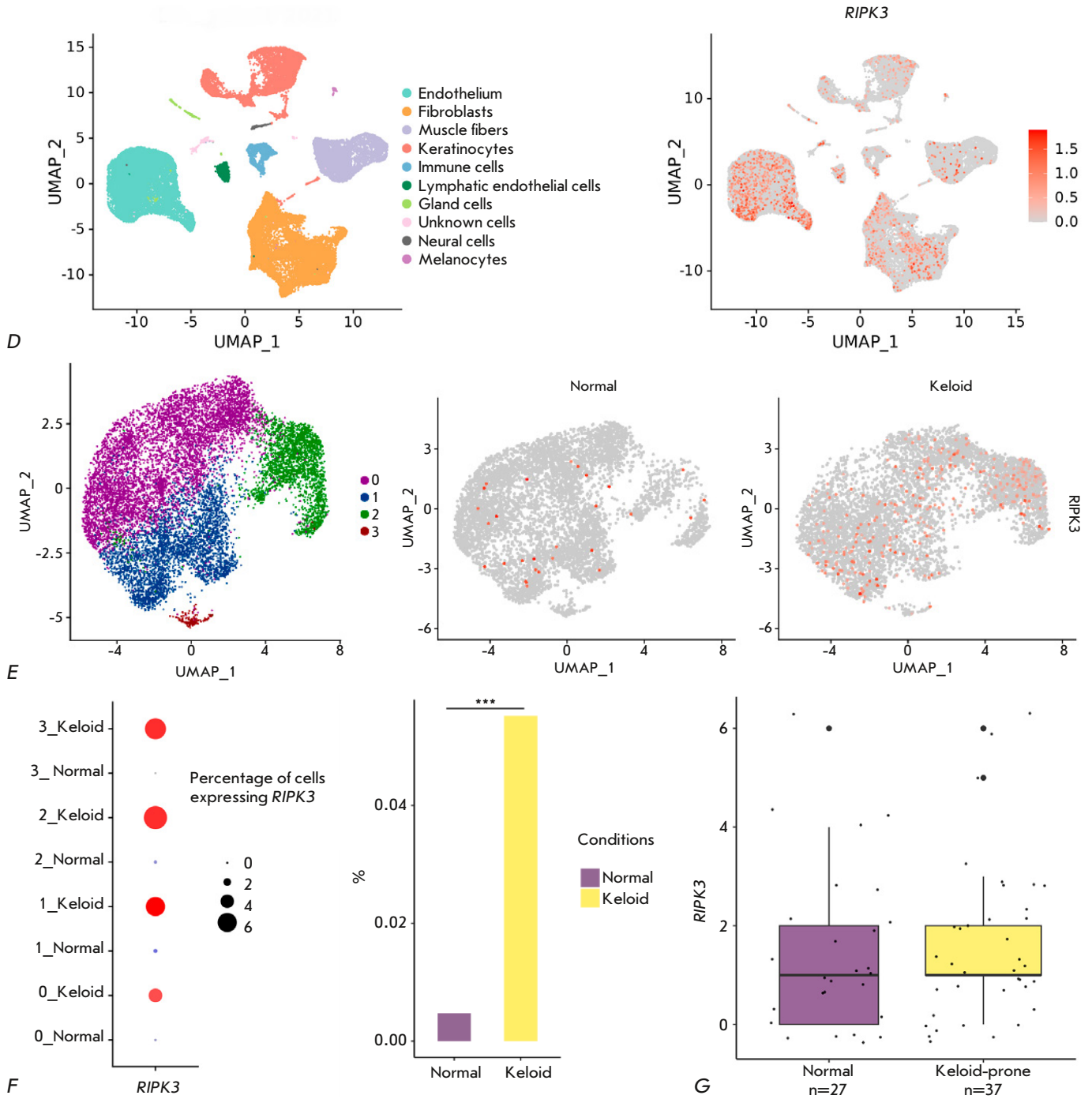


Fig. 1 (continued).

RIPK3 expression in wound and normal mouse tissue

Modeling of the fibrotic processes in the skin of laboratory mice does not imply a complete transfer of the processes that take place in the human body to the mouse due to the significant morphological and functional differences in the skin structure between

mice and humans [15]. For instance, mice are characterized by the presence of the *panniculus carnosus* muscle, which causes rapid wound regeneration by contraction, as well as wound-induced hair neogenesis, which is not characteristic of human skin. However, there exist papers on the study of fibrotic processes in mice. According to Lim et al. and Ito

et al., processes occurring in small and large wounds are accompanied by the activation of different signaling pathways and, therefore, have different outcomes [9, 16]. In the study by Lim et al., large wound ($\geq 1\text{cm}^2$) regeneration was accompanied by *Shh* upregulation resulting in wound-induced hair neogenesis in the wound bed and further complete structural and functional skin regeneration. During the healing of small wounds, an increase in *Shh* expression did not occur and, as a result, wound-induced hair neogenesis was not observed. Instead, regeneration outcome in fibrosis [9]. For this reason, we used the small wound mouse model. Considering that excessive scarring can occur due to an enhanced proliferation phase [17], and that the scar itself morphologically and functionally resembles a wound at the proliferation stage, we determined the time point in the regeneration of a mouse wound when it is at the proliferation stage: 10 days after wounding. At this time point, we observed wound closure with hyperproliferative epidermis, granulation tissue with a predominance of the cellular component over fibers, and the absence of hair follicles in mouse wound specimens, which can be considered an immature scar.

An immunofluorescent analysis confirmed the presence of RIPK3+Vim+, RIPK3-Vim+, RIPK3+Vim-, and RIPK3-Vim- cells in the mouse wound bed on regeneration day 10 and in normal skin (Fig. 2A). A subpopulation of RIPK3+Vim+ cells prevailed in the wound; the number of RIPK3+Vim+ cells was significantly greater in the wound bed compared to normal skin (Fig. 2A,C). The RIPK3-Vim+ cell subpopulation dominated in normal dermis; the number of cells was greater than that in the wound (Fig. 2B,C). This result indicates that there was a significantly greater number of RIPK3+ mesenchymal cells in the wound compared to normal dermis. However, not only fibroblasts but also endothelial cells and some inflammatory cells express vimentin. PCR followed by gel electrophoresis of primary cells isolated from the mouse wound bed showed expression of the markers of ECM synthesis and myofibroblast formation; i.e., the processes involved in fibrosis: *Acta2*, *Fap*, *Col1a1*, and *Fn1*, as well as *Ripk3* (Fig. 2D). In addition, the cells were defined morphologically as fibroblasts. Based on the obtained results, we concluded that the RIPK3+ cells of the mouse wound bed are fibroblasts. Nevertheless, RT-PCR did not show reliable differences in the expression of *Ripk3*, *Fap*, and *Fn1* between cultured wound bed cells and the cells isolated from normal dermis; this can be due to a change in the fibroblast phenotype during culture in plastic wells (Fig. 2E). It is possible that introduction of normal dermis fibroblasts in the cell culture and their attachment to the

plastic surface leads to their *de novo* activation. By that time, granulation tissue fibroblasts are already activated and continue to actively proliferate in the culture, which results in a decrease in the expression of the corresponding genes.

RIPK3 expression in human dermal fibroblasts in the presence of TGF- β 1 and LPS in an *in vitro* model

According to the data by Imamura, TGF- β causes a dose-dependent increase in RIPK3 expression in NIH 3T3 mouse embryo fibroblasts [5]. It was also shown that, after fibroblast exposure to TGF- β 1, RIPK3 can activate the serin/threonine protein kinase AKT. In turn, AKT phosphorylates the ATP citrate lyase ACL, which is involved in fibroblast activation [18–20].

Another mechanism of RIPK3-mediated regulation of fibrotic processes is possible. The study by Guo et al. suggests a role for TLR4/NF- κ B signaling in fibroblast activation, leading to the development of uterine fibroids. LPS induced the expression of collagen type I, TGF- β , and FAP in CD90+ fibroblasts [8]. LPS is also known to activate RIPK3 expression. Thus, we can assume the involvement of RIPK3 in LPS-induced activation of the TLR4/NF- κ B signaling pathway in fibroblasts [21].

An analysis of human dermal fibroblasts stained with antibodies to RIPK3 showed that addition of TGF- β at concentrations of 0.1, 1, 2, and 5 ng/ml (Fig. 3A) and LPS at concentrations 5, 10, 25, 50, and 100 ng/ml (Fig. 3B) results in a reliable increase in the fluorescence intensity. This indicates that RIPK3 expression can be regulated by TGF- β 1 and/or TLR4/NF- κ B signals. However, a comparison of real-time PCR results for *RIPK3* did not reveal significant differences between the control and analyzed cells (Fig. 3D). Real-time PCR analysis of markers of activated fibroblasts, namely *FAP*, *FN1*, and *COL1A1*, did not show significant differences between the experimental groups and the control. This result can be also due to the change in the cell phenotype in a 2D culture. The fibroblast phenotype is known to change depending on the substrate. Culturing of mouse lung fibroblasts in hydrogels with differing stiffness can lead to different cell phenotypes: with high expression levels of α -SMA (α -SMA Hi) and FAP (FAP Hi). A direct correlation of gene expression with the substrate stiffness is observed in α -SMA Hi, while a reverse correlation is noted in FAP Hi [22]. In addition, our study was performed in human and mouse primary dermal fibroblasts, which differ from the cells used in the studies with the methodology and concept we relied on. The study by Imamura was performed using NIH 3T3 mouse embryo fibroblasts

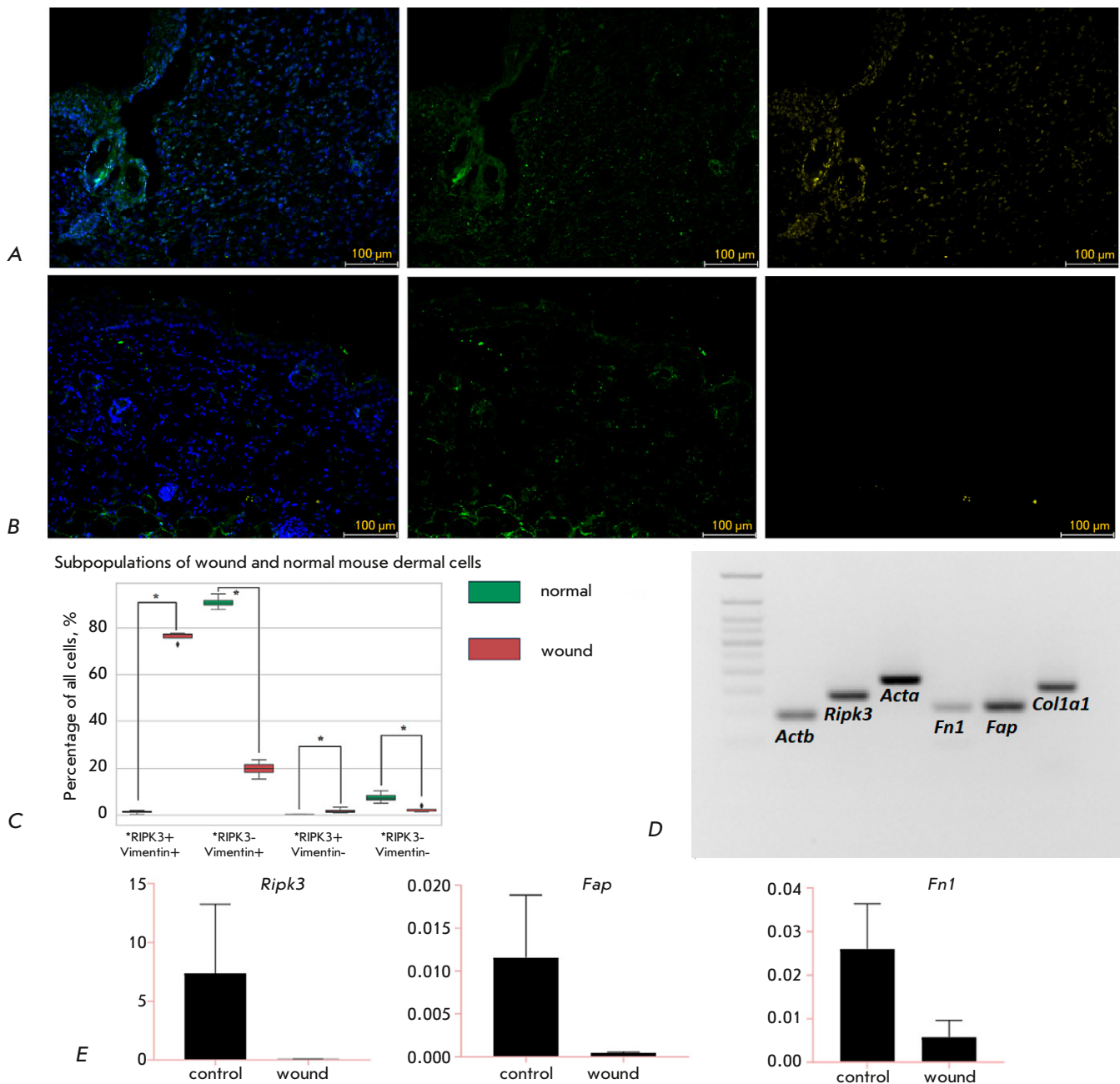


Fig. 2. RIPK3 expression patterns in mouse skin. Micropreparations of a wound at the proliferation stage (A) and normal mouse skin (B), immunohistochemical staining with antibodies to Vim (green) and RIPK3 (yellow), nuclei stained with DAPI, 20 \times magnification, scale bars 100 μ m. (C) – Statistical analysis of cell subpopulations in normal mouse dermis and wound bed, * $P < 0.05$ (Mann–Whitney U-test). Expression of ECM and *Ripk3* synthesis markers in mouse wound bed cells, PCR followed by gel electrophoresis (D); in cultured wound bed cells and intact dermis, RT-PCR, $P > 0.05$ (Mann–Whitney U test, gene expression data are presented as average values with a spread in the form of an average error) (E)

and human kidney fibroblasts; Guo et al. used human uterine fibroid cells [5, 8]. Thus, the *in vitro* model of fibrosis may not be the most suitable for studying the activation of human dermal fibroblasts and the role of RIPK3 in it. It is necessary to devel-

op another *in vitro* model to better grasp the role of RIPK3 in wound healing. Fibroblast cultures in collagen gel or organoids that preserve epithelial-mesenchymal interactions may be a promising approach in solving this riddle.

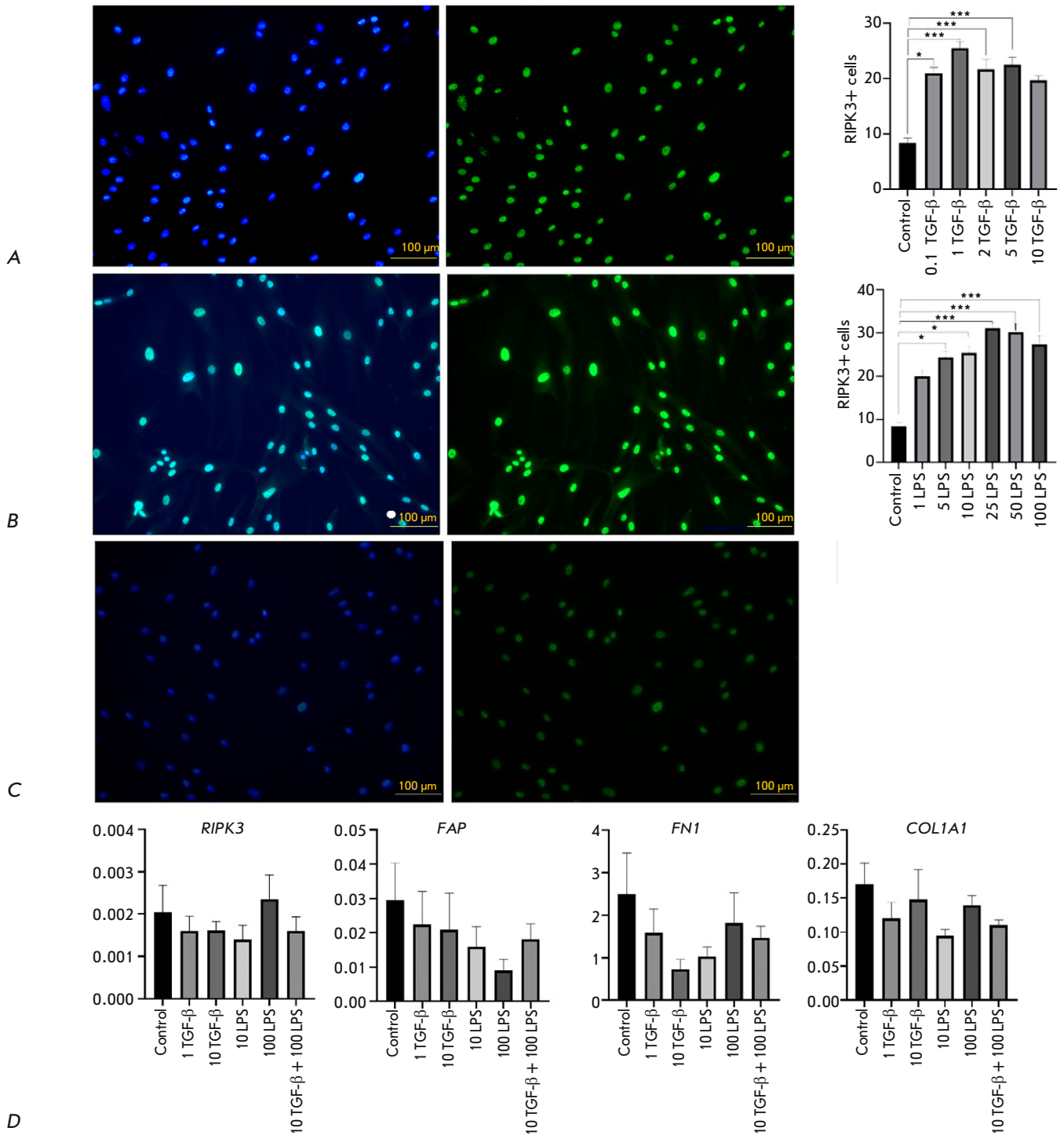


Fig. 3. Expression patterns of RIPK3 and ECM synthesis markers in human dermal fibroblasts. Human dermal fibroblasts cultured in medium containing TGF-β (A), LPS (B) and untreated (C), stained with antibodies to RIPK3, nuclei stained with DAPI, 20× magnification (left) scale bars 100 μm; statistical analysis of fluorescence intensity using the Kruskal–Wallis test, **P* < 0.05, ****P* < 0.001 the fluorescence intensity data are presented as averages with a spread in the form of an average error (right). Expression of ECM synthesis markers and RIPK3 in the presence of TGF-β and LPS in cultured human dermal fibroblasts, RT-PCR *P* > 0.05 (Mann–Whitney U test, gene expression data are presented as average values with a spread in the form of an average error (D)

CONCLUSION

A bioinformatics analysis of the data showed that human keloid scar tissue contains significantly more RIPK3+ fibroblasts compared to normal skin. RIPK3+Vim+ cells were found both in mouse wound bed and human keloid. The number of Vimentin+RIPK3+ cells during skin regeneration in mice was significantly higher compared to that in normal dermis. The expression of the *Ripk3* and ECM synthesis markers *Acta2*, *Fap*, *Col1a1*, and *Fn1* in cells isolated from a mouse wound bed indicates that these cells are fibroblasts. The fluorescence intensity was significantly higher after staining with antibodies to human RIPK3 fibroblasts treated with LPS at concentrations of 5, 10, 25, 50, and 100 ng/ml and TGF- β at concentrations of 0.1, 1, 2, and 5 ng/ml compared to the control. Real-time PCR revealed no significant differences in the expression level of the ECM synthesis genes *FAP*, *FN1*, *COL1A1*, and *RIPK3* between human

dermal fibroblasts treated with these substances and the control. This result is controversial and requires further research. It is possible that RIPK3 expression in wound fibroblasts is not directly associated with fibrotic processes, while RIPK3 plays another, yet unknown, role in wound healing. ●

The authors express their gratitude to the Center for Precision Genome Editing and Genetic Technologies for Biomedicine IGB RAS for the opportunity to perform bioinformatics analysis and L.Sh. Izmaylova and O.I. Sutyagina for consultations.

The work was performed as part of the project No. 21-74-30015 of the Russian Science Foundation.

The authors declare that there is no conflict of interest.

REFERENCES

- Meleshina A.V., Bystrova A.S., Rogovaya O.S., Vorotelyak E.A., Vasiliev A.V., Zagaynova E.V. // *Sovremennye tehnologii v medicine*. 2017. V. 9. No. 1. P. 198–220.
- Pasparakis M., Vandenabeele P. // *Nature*. 2015. V. 517. No. 7534. P. 311–320.
- Varfolomeev E., Vucic D. // *Cytokine*. 2018. V. 101. P. 26–32.
- Moriwaki K., Balaji S., McQuade T., Malhotra N., Kang J., Chan F.K.M. // *Immunity*. 2014. V. 41. No. 4. P. 567–578.
- Imamura M., Moon J.S., Chung K.P., Nakahira K., Muthukumar T., Shingarev R., Ryter S.W., Choi A.M., Choi M.E. // *JCI insight*. 2018. V. 3. No. 3. e94979.
- Mou F., Mou C. // *Med. Sci. Monitor: Int. Med. J. Exp. Clin. Res.* 2020. V. 26. e919739-1–e919739-9.
- Morgun E.I., Pozdniakova E.D., Vorotelyak E.A. // *Dokl. Biochem. Biophys.* 2020. V. 494. No. 1. P. 252–255.
- Guo J., Zheng L., Chen L., Luo N., Yang W., Qu X., Liu M., Cheng Z. // *Internat. J. Clin. Exp. Pathol.* 2015. V. 8. No. 9. P. 10014.
- Lim C.H., Sun Q., Ratti K., Lee S.H., Zheng Y., Takeo M., Lee W., Rabbani P., Plikus M.V., Cain J.E., et al. // *Nat. Commun.* 2018. V. 9. No. 1. P. 4903.
- Onoufriadis A., Hsu C.K., Ainali C., Ung C.Y., Rashidghamat E., Yang H.S., Huang H.Y., Niazi U., Tziotziou C., Yang J.C., et al. // *J. Investig. Dermatol.* 2018. V. 138. No. 12. P. 2690–2693.
- Solé-Boldo L., Raddatz G., Schütz S., Mallm J.P., Rippe K., Lonsdorf A.S., Rodríguez-Paredes M., Lyko F. // *Commun. Biol.* 2020. V. 3. No. 1. P. 188.
- Deng C.C., Hu Y.F., Zhu D.H., Cheng Q., Gu J.J., Feng Q.L., Zhang L.X., Xu Y.P., Wang D., Rong Z., et al. // *Nat. Commun.* 2021. V. 12. No. 1. P. 3709.
- Robinson M.D., McCarthy D.J., Smyth G.K. // *Bioinformatics*. 2010. V. 26. No. 1. P. 139–140.
- Hao Y., Hao S., Andersen-Nissen E., Mauck W.M. 3rd., Zheng S., Butler A., Lee M.J., Wilk A.J., Darby C., Zager M., et al. // *Cell*. 2021. V. 184. No. 13. P. 3573–3587. e29.
- Rippa A. L., Kalabusheva E. P., Vorotelyak E. A. // *Cells*. 2019. V. 8. No. 6. P. 607.
- Ito M., Yang Z., Andl T., Cui C., Kim N., Millar S.E., Cotsarelis G. // *Nature*. 2007. V. 447. No. 7142. P. 316–320.
- Gantwerker E.A., Hom D.B. // *Clinics in plastic surgery*. 2012. V. 39. No. 1. P. 85–97.
- Horowitz J.C., Lee D.Y., Waghray M., Keshamouni V.G., Thomas P.E., Zhang H., Cui Z., Thannickal V.J. // *J. Biol. Chem.* 2004. V. 279. No. 2. P. 1359–1367.
- Berwick D.C., Hers I., Heesom K.J., Moule S.K., Tavaré J.M. // *J. Biol. Chem.* 2002. V. 277. No. 37. P. 33895–33900.
- Zaidi N., Swinnen J.V., Smans K. // *Cancer Res.* 2012. V. 72. No. 15. P. 3709–3714.
- Yun M., Park S.H., Kang D.H., Kim J.W., Kim J.D., Ryu S., Lee J., Jeong H.M., Hwang H.R., Song K.S. // *J. Cell. Mol. Med.* 2022. V. 26. No. 21. P. 5506–5516.
- Avery D., Govindaraju P., Jacob M., Todd L., Monslow J., Puré E. // *Matrix Biology*. 2018. V. 67. P. 90–106.

Testing a Hypothesis of 12S rRNA Methylation by Putative METTL17 Methyltransferase

A. V. Mashkovskaia^{1*}, S. S. Mariasina^{2,3,4}, M. V. Serebryakova⁵, M. P. Rubtsova³,
O. A. Dontsova^{3,5,6,7}, P. V. Sergiev^{2,3,5,6}

¹Faculty of Bioengineering and Bioinformatics, Lomonosov Moscow State University, Moscow, 119192 Russian Federation

²Institute of functional genomics, Lomonosov Moscow State University, Moscow, 119192 Russian Federation

³Department of Chemistry, Lomonosov Moscow State University, Moscow, 119192 Russian Federation

⁴RUDN University, Moscow, 117198 Russian Federation

⁵Belozersky Institute of Physico-Chemical Biology, Lomonosov Moscow State University, Moscow, 119192 Russian Federation

⁶Center for Molecular and Cellular Biology, Skolkovo Institute of Science and Technology, Moscow, 119192 Russian Federation

⁷Shemyakin-Ovchinnikov Institute of Bioorganic Chemistry, Russian Academy of Sciences, Moscow, 117997 Russian Federation

*E-mail: mashkovskayaav@my.msu.ru

Received: August 28, 2023; in final form, October 26, 2023

DOI: 10.32607/actanaturae.25441

Copyright © 2023 National Research University Higher School of Economics. This is an open access article distributed under the Creative Commons Attribution License, which permits unrestricted use, distribution, and reproduction in any medium, provided the original work is properly cited.

ABSTRACT Mitochondrial ribosome assembly is a complex multi-step process involving many additional factors. Ribosome formation differs in various groups of organisms. However, there are universal steps of assembly and conservative factors that have been retained in evolutionarily distant taxa. METTL17, the object of the current study, is one of these conservative factors involved in mitochondrial ribosome assembly. It is present in both bacteria and the mitochondria of eukaryotes, in particular mice and humans. In this study, we tested a hypothesis of putative METTL17 methyltransferase activity. MALDI-TOF mass spectrometry was used to evaluate the methylation of a putative METTL17 target – a 12S rRNA region interacting with METTL17 during mitochondrial ribosome assembly. The investigation of METTL17 and other mitochondrial ribosome assembly factors is of both fundamental and practical significance, because defects in mitochondrial ribosome assembly are often associated with human mitochondrial diseases.

KEYWORDS mitochondrial ribosome, ribosome assembly factors, methyltransferases, RNA methylation, MALDI-TOF mass spectrometry.

INTRODUCTION

Mitochondrial ribosome assembly involves many factors that act in a strict hierarchy [1, 2]. Disruption of one of the assembly factors can significantly reduce the efficiency of ribosomal particle maturation. One of the conserved mitochondrial ribosome assembly factors, the METTL17 protein of class I SAM-dependent methyltransferases, harbors a mitochondrial localization signal and interacts with the small subunit of the mitochondrial ribosome during assembly [3–5].

The METTL17 factor plays an important role in mitoribosomal small subunit maturation; during ri-

bosome assembly, METTL17 interacts with several small subunit intermediates at the site where mRNA binding occurs in mature ribosomes [4, 5]. Binding of METTL17 leads to conformational changes in the small subunit's 12S rRNA region comprising helices 31–34 [4, 5]. In the absence of METTL17, mitochondrial ribosome assembly does not occur in correct fashion. A METTL17 knockout was shown to result in a decrease, not complete cessation, in the methylation level of two nucleotide residues in 12S rRNA [3], which is associated with disruption of the interaction with a mitoribosome assembly intermediate of known

RNA methyltransferases [6–9]. Errors in mitoribosome maturation in the absence of METTL17 lead to defects in mitochondrial translation and mitochondrial respiratory function [3–5]. At the level of the body, decreased METTL17 synthesis is associated with the development of Friedreich’s ataxia, one of the most common mitochondrial diseases [4].

Obviously, METTL17 is extremely important for correct mitoribosome assembly, but possible methyltransferase activity of this factor has not been studied. The fact is that METTL17 is assigned to the class I SAM-dependent methyltransferase family based on the sequence similarity and the presence of the methyltransferase domain and S-adenosylmethionine binding site in its structure. According to the human and trypanosome METTL17 structures, the METTL17 variants in these species can bind SAM, which is not true for the yeast homolog [4, 5]. These facts suggest that the METTL17 factor has the potential to exhibit methyltransferase activity.

We noticed that METTL17 interacts with a 12S rRNA region involving helices 31–34 [4, 5] during assembly and hypothesized that it might modify some nucleotide residue in this rRNA region. There are five known methylation sites in mitochondrial 12S rRNA, each of which is methylated by an appropriate methyltransferase [6–12]. However, we suspected that some modification might have been overlooked and decided to test a hypothesis that METTL17 methylates a mitochondrial 12S rRNA region comprising helices 31–34. The study flow chart and experiments performed to test the METTL17 target hypothesis are shown in Fig. 1.

EXPERIMENTAL

Mettl17 gene inactivation

The CRISPR-Cas9 system was used to inactivate the *Mettl17* gene in the NIH-3T3 cell line. The best-ranked guide RNA (5′-GACATTTACCTGTAGAGCCGG-3′) for cleaving the third exon of *Mettl17* was selected using the Benchling CRISPR designing tool (<https://benchling.com>). The genetic construct was generated using two DNA oligonucleotides containing the guide RNA sequence and adapters for ligation into the plasmid (the guide RNA sequence is shown in gray, the complementary sequence is shown in light gray):



Oligonucleotides were hybridized in T4-DNA ligase buffer (Thermo Scientific, USA): every oligonucleotide was added to a concentration of 1 μM ,

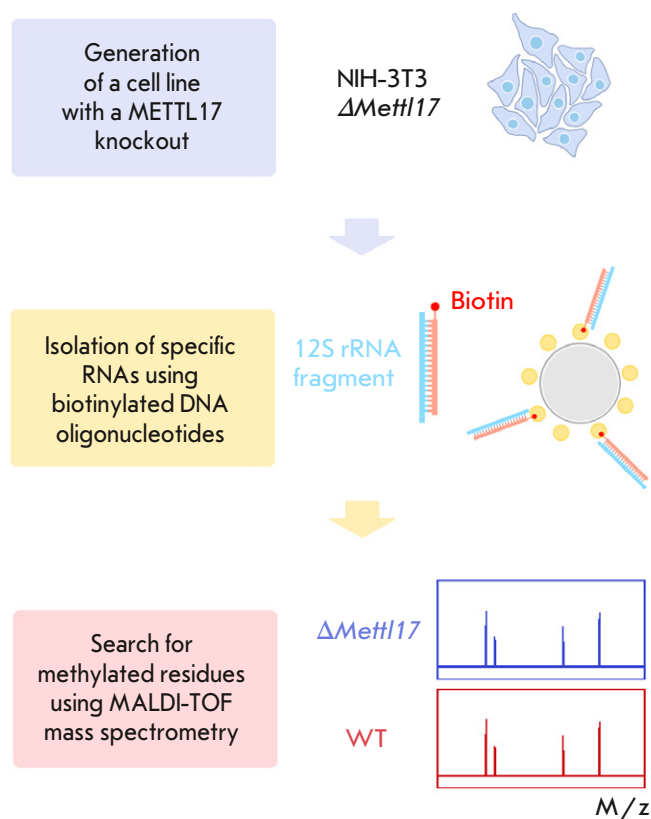


Fig. 1. Diagram of the search for the methylation target of the METTL17 mitochondrial factor

incubated at 95°C for 5 min, and left to cool to a temperature of 30°C in a closed thermostat. The resulting duplex solution (1 μL) was ligated into the pSpCas9(BB)-2A-GFP plasmid (PX458, Addgene #48138) cleaved at the BpI restriction endonuclease recognition sites [13]. Competent *Escherichia coli* cells (JM109 strain) were transformed with a ligase mixture, and colonies were grown on a plate supplemented with ampicillin (50 $\mu\text{g}/\text{mL}$). Plasmid DNA was isolated from overnight cultures using a Plasmid Miniprep reagent kit (Evrogen, Russia). The insert in the plasmid was confirmed by Sanger sequencing using a primer for the U6 promoter (5′-GACTATCATATGCTTACCGT-3′).

Wild-type NIH-3T3 cells were transfected with the guide RNA-containing plasmid using the Lipofectamine 3000 reagent (Thermo Scientific). For transfection, 100,000 cells, 500 ng of the plasmid, and 1.5 μL of lipofectamine were used. Twenty-four hours after transfection, cells were selected based on GFP fluorescence using a FACSaria III BD cell sorter; the signal was recorded at absorption/emission wavelengths of 488/530 nm. The selected cells were seeded

into a 96-well plate (200 μ L of medium per well) for monoclones. Individual monoclones were further cultured in the wells of a 24-well plate. To confirm the *Mettl17* knockout, total DNA was isolated from the cells using a QuickExtract DNA Extraction Solution (Lucigen). Next, the fragment comprising the cleaved region was amplified by PCR.

PCR primers:

Forward primer:

5'-GTGAGAAACTGCGGAAGGG-3'

Reverse primer:

5'-AGCCCTACCTTGTTCCTCAGG-3'.

The *Mettl17* mutation leading to gene inactivation was verified by Sanger sequencing of the amplified fragments.

Cultivation of cell lines

Wild-type NIH-3T3 and Δ *Mettl17* cells were cultured at 37°C and 5% CO₂ in DMEM/F12 (Gibco) supplemented with FBS to 10% volume and an antibiotic mixture (100 U/mL penicillin and 100 μ g/mL streptomycin) in a GlutaMAX (2 mM L-alanine-L-glutamine) solution. The cells were grown in tissue culture flasks (25 cm²) for adherent cells. At 90–100% confluency, the cells were subcultured: wild-type cells at a 1:10 dilution and Δ *Mettl17* cells at a 1:4 dilution. The cells were rinsed with PBS and detached with a 1 \times Trypsin-EDTA solution (Gibco) in PBS. The required number of cells was resuspended in a fresh medium.

For total RNA isolation, large cell volumes were grown in 150 mm Petri dishes. Before cell harvesting, most of the medium was first removed and cells were detached using a culture scraper. The medium with cells was centrifuged at +4°C and 1,000 rpm for 5 min, then the medium was removed, and the cell pellet was frozen and stored at –80°C until analysis.

Isolation of 12S rRNA fragments and MALDI-TOF mass spectrometry

Total RNA was isolated using an ExtractRNA reagent (Evrogen). Cell pellets were thawed on ice and homogenized in an ExtractRNA solution (1 mL per 100 mg of cells) in 15-mL tubes (Tissue grinding CKmix50_15ml) using a Precellys Evolution device. Disruption was performed at 6,000 rpm for 20 s; the procedure was run twice, and during the break, the solution was cooled on ice for 5 min. After cell disruption, total RNA was isolated according to the ExtractRNA reagent protocol; the resulting RNA samples were dissolved in miliQ water to a concentration of 5–7 mg/mL.

12S rRNA fragments were isolated using three biotinylated DNA oligonucleotides complementary to the 12S rRNA regions:

1. 5'-[biotin]GGTTTGCTGAAGATGGCGGTATAT-AGGCTGAATTAGCAAG-3'
2. 5'-[biotin]CCCATTTTCATTGGCTACACCTTGAC-CTAACGTTTTTATGT-3'
3. 5'-[biotin]GCAAGAGATGGTGAGGTAGAGCGGG-GTTTATCGATTATAGAACA-3'.

A solution of total RNA (2 mL, 2 mg/mL) and an oligonucleotide (100 pmol/mL) in 6 \times SSC buffer was incubated in a thermostat at 95°C for 5 min and then cooled in a closed thermostat to 40°C. After hybridization, the solution was treated with RNase T1 (Thermo Scientific) at a concentration of 1 U/mL at 37°C for 1.5 h. After incubation, DNA/RNA duplexes were isolated using Dynabeads M-280 Streptavidin beads (Thermo Scientific), 100 μ L of magnetic beads per sample. The magnetic beads were washed three times with 6 \times SSC buffer. Then, they were added to the solution and incubated at room temperature under stirring for 30 min. After incubation, the magnetic beads were washed successively with 3 \times SSC buffer (4 times), 1 \times buffer (3 times), and 0.1 \times buffer (3 times). Before the last wash, the beads were transferred to a clean tube. RNA was eluted using two techniques: elution with 100 μ L of 0.1 \times SSC buffer containing 6 M urea (70°C, shaking at 1,000 rpm for 5 min) and elution with DNase I (100 μ L of DNase solution in 1 \times DNase buffer, incubation at 37°C in a thermostat under regular stirring for 30 min). The eluate was collected on a magnetic stand and transferred to a clean tube. Then, isopropanol was added to 50%, NH₄OAc to 1 M, and 0.5 μ L of Glycoblue and left overnight at –20°C.

The next day, RNA was precipitated by centrifugation at the maximum speed (+4°C for 15 min). The pellet was washed with cold 80% ethanol and dried in a thermostat at 42°C. The RNA pellet was dissolved in 1 \times RNA Loading Dye (Thermo Scientific) and loaded onto a 12% polyacrylamide gel containing 7 M urea. The gel was stained with an ethidium bromide solution. Bands of RNA fragments were cut from the gel, chopped, washed twice with a solution of 25 mM ammonium citrate and 50% acetonitrile, and then dried in 100% acetonitrile. For MALDI-TOF mass spectrometry, the gel chops were air-dried and treated with an RNase T1 solution in 50 mM ammonium citrate at 37°C for 3 h. A 2,5-dihydroxybenzoic acid solution (50 mg/mL) containing 0.5% TFA and 30% acetonitrile was used as a matrix for MALDI mass spectrometry. An amount of 1.5 μ L of the matrix was added to 0.5 μ L of a citrate solution containing RNA oligonucleotides, and the mixture was applied to the target and

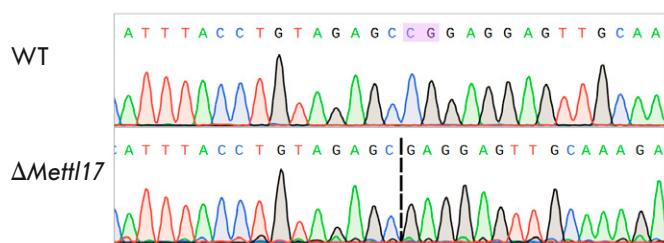


Fig. 2. Comparison of the METTL17 protein gene sequence in wild-type (WT) NIH-3T3 and knockout (Δ Mettl17) lines, Sanger sequencing

dried. The analysis was performed on an Ultraflex III BRUKER instrument equipped with a UV laser (Nd, 335 nm) using positive ion detection.

Software

The Mongo Oligo Mass Calculator freeware [14] was used to generate a mass-ordered list of all oligonucleotides produced by RNase T1 digestion of the mitochondrial 12S rRNA regions. This list was calculated using the sequence from the NCBI Public Sequence Bank (<https://www.ncbi.nlm.nih.gov/>). The house mouse (*Mus musculus*) mitochondrial 12S rRNA sequence was derived from the mitochondrial genome reference sequence (NC_005089).

RESULTS AND DISCUSSION

In this study, we tested the hypothesis holding that the METTL17 factor methylates a 12S rRNA region with which it interacts during mitochondrial ribosome assembly. First, we generated a cell line with a METTL17 knockout to compare the methylation of the 12S rRNA region under normal and METTL17 depletion conditions. A technique of specific RNA isolation with biotinylated DNA oligonucleotides was used to confirm 12S rRNA methylation. RNA fragments were isolated from wild-type and METTL17 knockout cells. The isolated and purified RNA samples were analyzed using MALDI-TOF mass spectrometry. Comparison of RNA masses from wild-type and knockout cells with pre-calculated theoretical masses allowed us to test the hypothesis of rRNA methylation by the METTL17 factor.

Generation of the NIH-3T3 Δ Mettl17 cell line

In this study, we used the NIH-3T3 cell line, which is a line of adherent fibroblast-like cells obtained from mouse embryonic tissue. The *Mettl17* gene was inactivated using a derivative of the plasmid pX458 [13], which encodes components of the CRISPR/Cas9 system (Cas9 protein gene and guide RNA sequence).

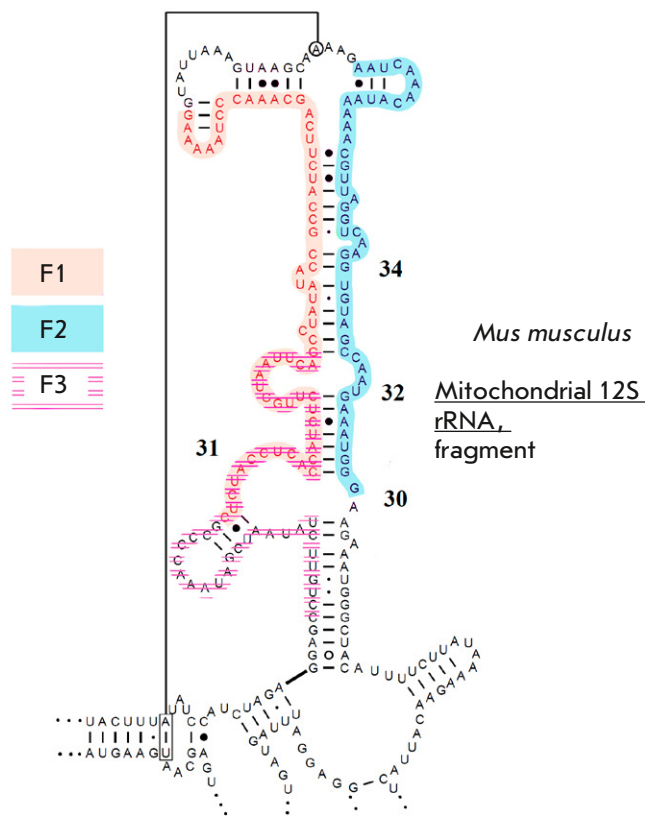


Fig. 3. Mouse 12S rRNA fragments analyzed using mass spectrometry (F1, F2, F3). Two fragments (F1, F3) partially overlap. Image adapted from [15]

The guide RNA was selected in such a way as to make a cut at the beginning of exon 3 of the *Mettl17* gene.

A cell line with a 2 bp deletion in exon 3 of the *Mettl17* gene was produced. This deletion resulted in a frameshift and the inactivation of the gene. A mutation in the gene was verified using Sanger sequencing (Fig. 2).

Methylation analysis of 12S rRNA fragments

To confirm methylation, we selected a 12S rRNA region comprising helices 31–34, with which METTL17 interacts. This is a large structured RNA region harboring double-stranded fragments (Fig. 3). Owing to this, we decided to divide this region into three fragments (Fig. 3). Each fragment was identified and analyzed separately.

Specific 12S rRNA fragments were isolated using a previously published approach [9, 16, 17], with minor modifications at the elution step. The experiment design is presented in Fig. 4. Specific rRNA fragments were isolated using biotinylated DNA oligonucleotides

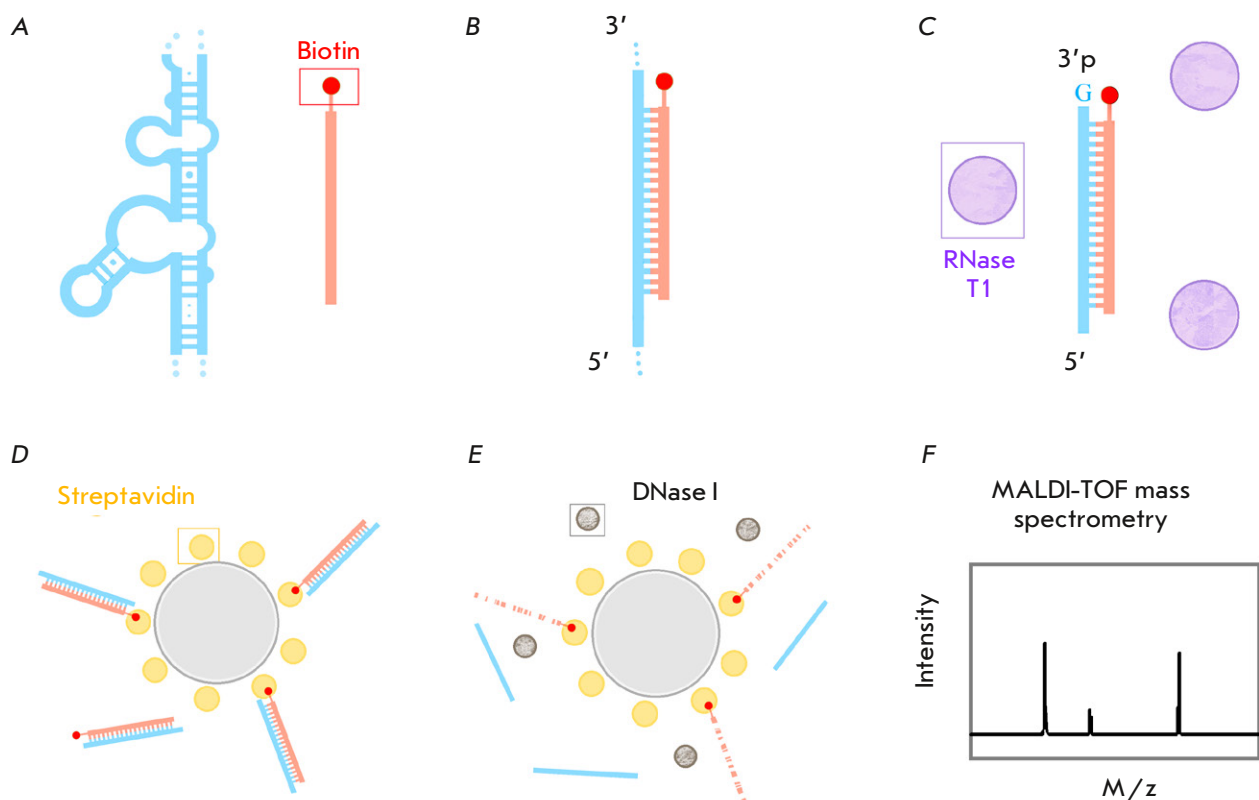


Fig. 4. Diagram for isolating RNA fragments using biotinylated oligonucleotides. (A) – a 12S rRNA region (blue) and a biotinylated oligonucleotide (coral, biotin – red). (B) – after annealing, the secondary structure of rRNA melts, and the rRNA region hybridizes with the oligonucleotide. (C) – after treatment with RNase T1, a DNA–RNA duplex remains; RNase T1 cuts ssRNA after guanylic acid residues, leaving a 3'-phosphate. (D) – DNA–RNA duplexes bind to magnetic beads through biotin–streptavidin interactions. (E) – after treatment with DNase I, DNA is destroyed and RNA occurs in solution. (F) – analysis of isolated RNA fragments using MALDI-TOF mass spectrometry

complementary to the 40–50-nt rRNA fragments of interest. After hybridization and the formation of DNA–RNA duplexes, the solution was treated with RNase T1 that excised ssRNA after guanyl residues. Thus, the DNA–RNA duplexes remained in solution, while all ssRNA was destroyed.

The DNA–RNA duplexes were isolated from the solution using streptavidin magnetic beads. RNA was eluted and separated in polyacrylamide gel to identify fragments of the required length (Fig. 5). We tried to elute RNA using a urea solution under heating, in accordance with a previously reported technique [9], as well as using a DNase solution (Fig. 5). During elution with urea, not only RNA fragments of interest, but also biotinylated DNA oligonucleotides entered the solution. Treatment with DNase enabled not only eluting RNA but also avoiding DNA in the solution.

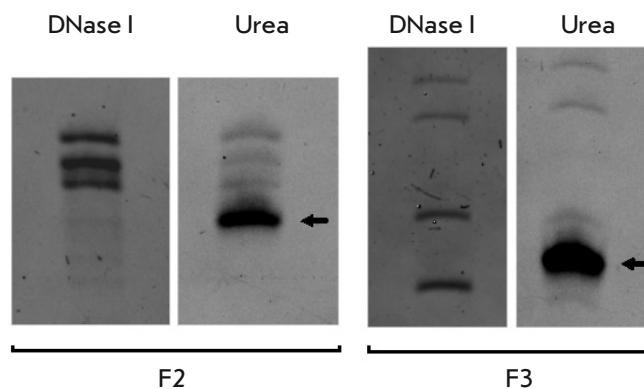


Fig. 5. Isolation of RNA fragments (F2, F3) on gel. Elution is performed using urea and DNase I. The DNA oligonucleotide eluted with urea is shown by an arrow

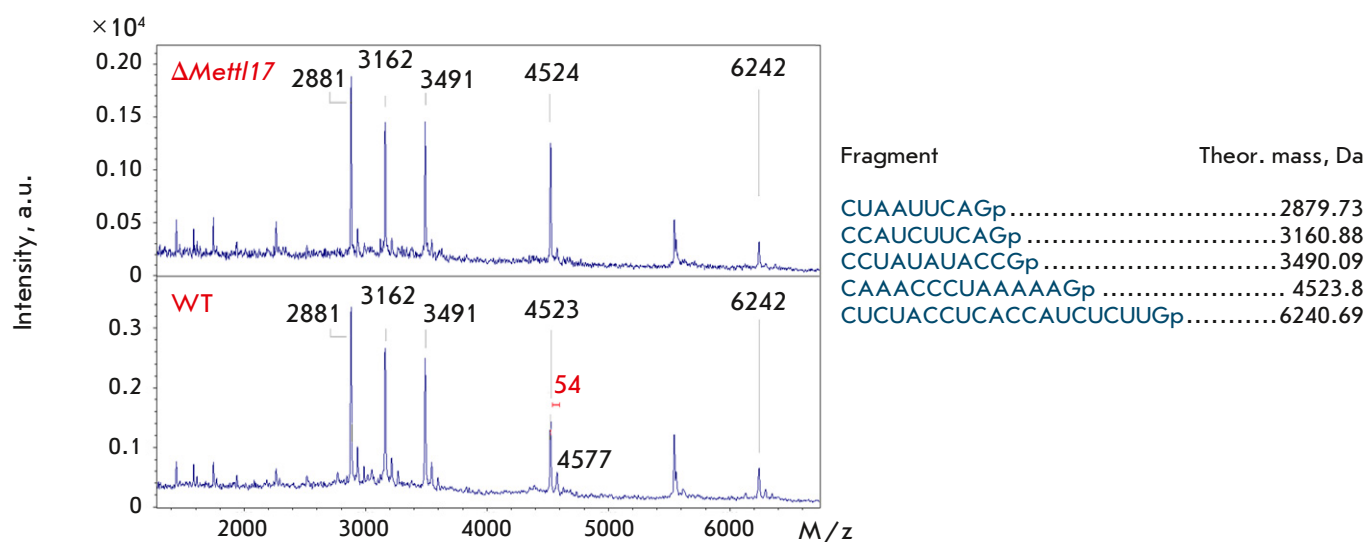


Fig. 6. Mass spectra of fragment 1 (peaks of RNA from the *METTL17* knockout are shown at the top, those from the wild-type line are shown at the bottom). Mass spectra were acquired in linear mode. Theoretically calculated peaks for fragment 1 are labeled

Loading the eluate on gel provided separation of RNA fragments from DNase molecules: so, the use of enzymatic elution did not complicate the mass spectrometric analysis.

Before the mass spectrometric analysis, bands of RNA fragments were cut from the gel and additionally treated with RNase T1 to digest the RNA into smaller fragments. The maximum fragment weight was 6.2 kDa, and the fragment length was up to 20 nucleotide residues. The theoretical masses of all the fragments were pre-calculated using an online tool [14].

We measured the mass spectra of the hydrolysates of three 12S rRNA fragments from wild-type and Δ *Mettl17* cells to determine whether an additional methyl group, absent in Δ *Mettl17* cells, is present in the RNA of wild-type cells. An additional CH_3 group increases the weight of a fragment by 14 Da. *Figures 6–8* show the mass spectra of three fragments; the result for knockout cells is shown on top, and that for wild-type cells is shown at the bottom. Based on the results of the mass spectrometric analysis, we found that the 12S rRNA region interacting with METTL17 was not methylated in wild-type cells, and that fragment masses were not affected by the *METTL17* knockout.

The resulting mass spectra contained all fragments with the predicted masses, with the exception of two short fragments (1–2 nucleotide residues) in the chro-

matogram of fragment 2 (*Fig. 7*) and a 4-nt fragment in the chromatogram of fragment 3 (*Fig. 8*). In the former case, the fragment mass is too small to be detected. In the latter case, we suggest that the CCUGp fragment was not present in the solution, because it was cleaved off by RNase T1. This region is located at the end of the analyzed fragment and may be cleaved by RNase due to the short length of the double-stranded region. Despite this fact, the entire 12S rRNA region that is in close contact with METTL17 was tested in the experiment. This indicates that METTL17 does not methylate the 12S rRNA region comprising helices 31–34, which leads to a conformational change in this rRNA region.

Therefore, we contend that METTL17 plays a primarily structural role in small mitoribosomal subunit assembly, a role which is not related to methylation. This supports the suggestion [2, 3] that METTL17 is a mitoribosome assembly factor that originates from methyltransferases and retains the characteristic folding and ability to bind SAM at least in some groups of organisms. It probably lost its methyltransferase activity and acts as a structural factor of mitoribosomal small subunit assembly, instead.

CONCLUSION

In this paper, we tested the hypothesis of methyltransferase activity of the METTL17 protein, a mitochondrial small subunit assembly factor. METTL17

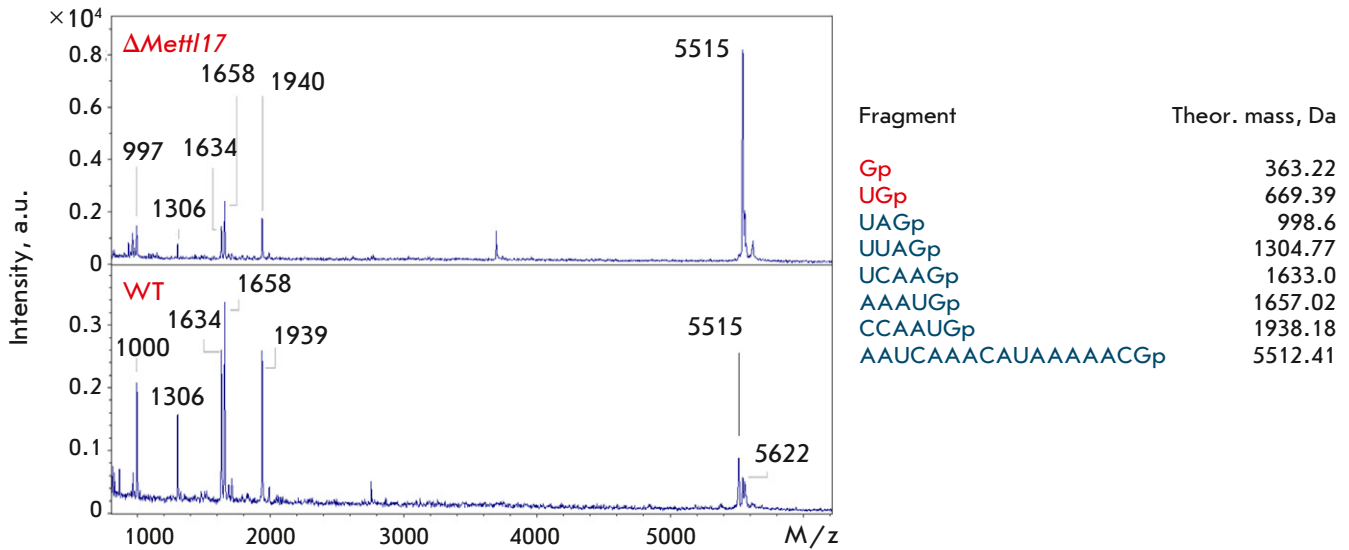


Fig. 7. Mass spectra of fragment 2 (peaks of RNA from the *METTL17* knockout are shown at the top, those from the wild-type line are shown at the bottom). Mass spectra were acquired in linear mode. Theoretically calculated peaks for fragment 2 are labeled

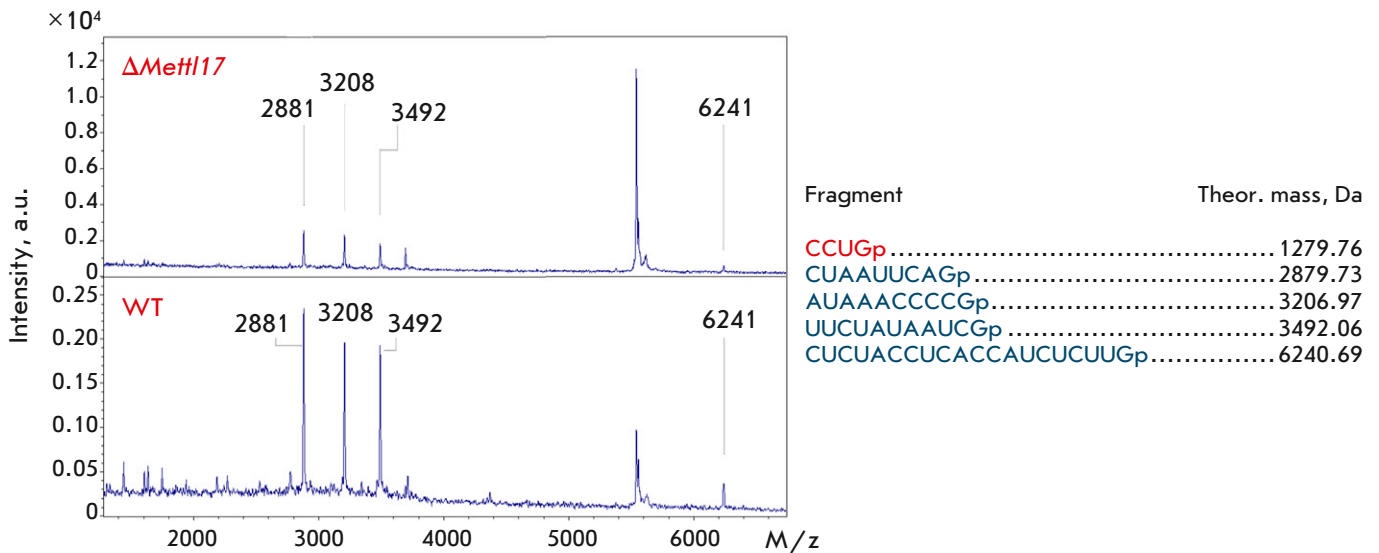


Fig. 8. Mass spectra of fragment 3 (peaks of RNA from the *METTL17* knockout are shown at the top, those from the wild-type line are shown at the bottom). Mass spectra were acquired in linear mode. Theoretically calculated peaks for fragment 3 are labeled

was shown not to methylate the 12S rRNA region, with which it comes into contact during assembly, despite the fact that this factor retains the features typical of class I SAM-dependent methyltransferases. We suggest that the *METTL17* factor has lost its original function during the evolutionary process and that it

instead plays a structural role in mitochondrial ribosome assembly. ●

*This study was supported
by a grant of the Russian Science Foundation
(No. 17-75-30027).*

REFERENCES

1. Bogenhagen D.F., Ostermeyer-Fay A.G., Haley J.D., Garcia-Diaz M. // *Cell Reports*. 2018. V. 22. № 7. P. 1935–1944.
2. Lopez Sanchez M., Krüger A., Shiriaev D.I., Liu Y., Rorbach J. // *Int. J. Mol. Sci.* 2021. V. 22. № 8. P. 3827.
3. Shi Z., Xu S., Xing S., Yao K., Zhang L., Xue L., Zhou P., Wang M., Yan G., Yang P., et al. // *FASEB J.* 2019. V. 33. № 11. P. 13040–13050.
4. Ast T., Itoh Y., Sadre S., McCoy J.G., Namkoong G., Chicherin I., Joshi P.R., Kamenski P., Suess D.L.M., Amunts A., et al. // *bioRxiv*. 2022. <https://doi.org/10.1101/2022.11.24.517765>
5. Harper N.J., Burnside C., Klinge S. // *Nature*. 2023. V. 614. № 7946. P. 175–181.
6. Metodiev M.D., Spåhr H., Loguercio Polosa P., Meharg C., Becker C., Altmueller J., Habermann B., Larsson N.G., Ruzzenente B. // *PLoS Genet.* 2014. V. 10. № 2. P. e1004110.
7. van Haute L., Hendrick A.G., D'Souza A.R., Powell C.A., Rebelo-Guioamar P., Harbour M.E., Ding S., Fearnley I.M., Andrews B., Minczuk M. // *Nucl. Acids Res.* 2019. V. 47. № 19. P. 10267–10281.
8. Chen H., Shi Z., Guo J., Chang K.J., Chen Q., Yao C.H., Haigis M.C., Shi Y. // *J. Biol. Chem.* 2020. V. 295. № 25. P. 8505–8513.
9. Laptev I., Shvetsova E., Levitskii S., Serebryakova M., Rubtsova M., Zgoda V., Bogdanov A., Kamenski P., Sergiev P., Dontsova O. // *Nucl. Acids Res.* 2020. V. 48. № 14. P. 8022–8034.
10. Boehringer D., O'Farrell H.C., Rife J.P., Ban N. // *J. Biol. Chem.* 2012. V. 287. № 13. P. 10453–10459.
11. Laptev I., Shvetsova E., Levitskii S., Serebryakova M., Rubtsova M., Bogdanov A., Kamenski P., Sergiev P., Dontsova O. // *RNA Biol.* 2020. V. 17. № 4. P. 441–450.
12. Powell C.A., Minczuk M. // *RNA Biol.* 2020. V. 17. № 4. P. 451–462.
13. Ran F.A., Hsu P.D., Wright J., Agarwala V., Scott D.A., Zhang F. // *Nat. Protoc.* 2013. V. 8. P. 2281–2308.
14. <http://rna.rega.kuleuven.be/masspec/mongo.htm>
15. Cannone J.J., Subramanian S., Schnare M.N., Collett J.R., D'Souza L.M., Du Y., Feng B., Lin N., Madabusi L.V., Müller K.M., et al. // *BMC Bioinformatics.* 2002. V. 3. P. 2.
16. Golovina A., Dzama M., Osterman I., Sergiev P., Serebryakova M., Bogdanov A., Dontsova O. // *RNA.* 2012. V. 18. № 9. P. 1725–1734.
17. Golovina A., Sergiev P., Golovin A., Serebryakova M., Demina I., Govorun V., Dontsova O. // *RNA.* 2009. V. 15. № 6. P. 1134–1141.

In Vitro Antiviral Activity of a New Indol-3-carboxylic Acid Derivative Against SARS-CoV-2

A. N. Narovlyansky^{1*}, M. V. Filimonova², N. G. Tsyshkova², A. V. Pronin¹, T. V. Grebennikova¹, E. V. Karamov¹, V. F. Larichev¹, G. V. Kornilayeva¹, I. T. Fedyakina¹, I. V. Dolzhikova¹, M. V. Mezentseva¹, E. I. Isaeva¹, V. V. Poloskov¹, L. S. Koval², V. P. Marinchenko², V. I. Surinova², A. S. Filimonov², A. A. Shitova², O. V. Soldatova², A. V. Sanin¹, I. K. Zubashev¹, A. V. Ponomarev¹, V. V. Veselovsky³, V. V. Kozlov¹, A. V. Stepanov³, A. V. Khomich⁴, V. S. Kozlov¹, S. A. Ivanov², P. V. Shegai², A. D. Kaprin², F. I. Ershov¹, A. L. Gintsburg¹

¹National Research Centre for Epidemiology and Microbiology named after the honorary academician N.F. Gamaleya, Ministry of Health of the Russian Federation, Moscow, 123098 Russian Federation

²National Medical Research Center for Radiology, Ministry of Health of the Russian Federation, Obninsk, 249036 Russian Federation

³N.D. Zelinsky Institute of Organic Chemistry, Russian Academy of Sciences, Moscow, 119991 Russian Federation

⁴Gamasintez LLC, Moscow, 123098 Russian Federation

*E-mail: narovl@yandex.ru

Received October 3, 2023; in final form, October 26, 2023

DOI: 10.32607/actanaturae.26623

Copyright © 2023 National Research University Higher School of Economics. This is an open access article distributed under the Creative Commons Attribution License, which permits unrestricted use, distribution, and reproduction in any medium, provided the original work is properly cited.

ABSTRACT The coronavirus disease (COVID-19) pandemic has brought into sharp relief the threat posed by coronaviruses and laid the foundation for a fundamental analysis of this viral family, as well as a search for effective anti-COVID drugs. Work is underway to update existent vaccines against COVID-19, and screening for low-molecular-weight anti-COVID drug candidates for outpatient medicine continues. The opportunities and ways to accelerate the development of antiviral drugs against other pathogens are being discussed in the context of preparing for the next pandemic. In 2012–2015, Tsyshkova et al. synthesized a group of water-soluble low-molecular-weight compounds exhibiting an antiviral activity, whose chemical structure was similar to that of arbidol. Among those, there were a number of water-soluble compounds based on 5-methoxyindole-3-carboxylic acid aminoalkyl esters. Only one member of this rather extensive group of compounds, dihydrochloride of 6-bromo-5-methoxy-1-methyl-2-(1-piperidinomethyl)-3-(2-diethylaminoethoxy)carbonylindole, exhibited a reliable antiviral effect against SARS-CoV-2 *in vitro*. At a concentration of 52.0 μM, this compound completely inhibited the replication of the SARS-CoV-2 virus with an infectious activity of 10⁶ TCID₅₀/mL. The concentration curves of the analyzed compound indicate the specificity of its action. Interferon-inducing activity, as well as suppression of syncytium formation induced by the spike protein (S-glycoprotein) of SARS-CoV-2 by 89%, were also revealed. In view of its synthetic accessibility – high activity (IC₅₀ = 1.06 μg/mL) and high selectivity index (SI = 78.6) – this compound appears to meet the requirements for the development of antiviral drugs for COVID-19 prevention and treatment.

KEYWORDS SARS-CoV-2, indole-3 carboxylic acid derivative, antiviral activity, cell culture.

ABBREVIATIONS WHO – World Health Organization; EMCV – encephalomyocarditis virus; IFN – interferon; IR – infrared spectrum; MS – mass spectrum; TCID₅₀ – 50% tissue culture infectious dose; CPE – cytopathic effect; T_m – melting point; FCS – fetal calf serum; ¹H NMR – proton nuclear magnetic resonance; CC₅₀ – 50% cytotoxic concentration of the compound; COVID-19 – coronavirus disease 2019; DMEM – Dulbecco's Modified Eagle Medium; GFP – green fluorescent protein; IC₅₀ – half-maximal inhibitory concentration; S glycoprotein – spike protein of the SARS-CoV-2 virus; SARS-CoV-2 – severe acute respiratory syndrome caused by CoV-2 – Coronaviridae: Coronavirinae: Betacoronavirus: Sarbecovirus; SI – selectivity index calculated as a ratio of CC₅₀ to IC₅₀ (SI = CC₅₀/IC₅₀).

INTRODUCTION

On May 5, 2023, the World Health Organization (WHO) declared “an end to COVID-19 as a public health emergency” [1]. Just like that, the pandemic that lasted 3 years 1 month and 24 days was over. According to the WHO, globally, as of July 12, 2023, there had been 767,972,961 confirmed cases of COVID-19, including 6,950,655 deaths. A total of 22,967,718 confirmed cases of COVID-19 and 399,715 deaths have been documented in Russia [2]. However, even according to WHO estimates, the number of COVID-19 deaths exceeds 20 million people [3].

Although the end of the pandemic and decline in the total number of infection cases have been proclaimed, the COVID-19 epidemic cannot be considered to have completely subsided. New subvariants of the virus (XBB.1.16 and XBB.2.3) have emerged; that is why research that aims to update existing COVID-19 vaccines and search for small-molecule anti-COVID-19 drug candidates for outpatient use continues to this day. Furthermore, approximately 65 million patients have been identified as suffering from long-term sequelae of the SARS-CoV-2 infection. These cases are referred to as “post COVID-19 conditions” or “long COVID” [4].

The pandemic of the COVID-19 coronavirus disease has given us a new appreciation of the threat posed by coronaviruses and has spurred a fundamental analysis of this viral family, as well as a search for effective anti-COVID drugs. Obviously, efficient therapeutic strategies for COVID-19 are still needed. A number of antiviral drugs such as remdesivir, nucleoside inhibitors (AT-527 and molnupiravir), the main protease (Mpro) inhibitor nirmatrelvir, the nirmatrelvir–ritonavir combination and molnupiravir, and immunotropic drugs (baricitinib, tocilizumab, and corticosteroids, etc.) were tested during the pandemic phase [5]. However, almost no effective small-molecule oral antivirals have been developed for outpatient therapy [6].

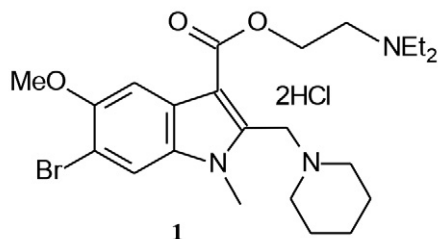


Fig. 1. 6-Bromo-1-methyl-5-methoxy-2-(1-piperidinomethyl)-3-(2-diethylaminoethoxy)carbonylindole dihydrochloride (compound **1**)

In 2012–2015, Tsyshkova et al. synthesized a group of water-soluble low-molecular-weight compounds exhibiting an antiviral activity, whose chemical structure was similar to that of arbidol. Among those, there are a number of compounds based on 5-methoxyindole-3-carboxylic acid aminoalkyl esters [7]. Only one member of this rather extensive group of compounds exhibited a reliable antiviral effect against SARS-CoV-2 *in vitro*; this compound was investigated in this study.

EXPERIMENTAL

The study compound, dihydrochloride of 6-bromo-5-methoxy-1-methyl-2-(1-piperidinomethyl)-3-(2-diethylaminoethoxy)carbonylindole (**1**) (Fig. 1), was synthesized [7] at the National Medical Research Center for Radiology of the Ministry of Health of the Russian Federation.

Compound **1** was obtained via multistep synthesis (the scheme is shown in Fig. 2).

The solvents and reagents used in this study, including ethyl-5-hydroxy-1,2-dimethyl-1*H*-indole-3-carboxylate, were purchased from Acros Organics. The melting points were measured using a Kofler heating bench. The IR spectra were recorded on a Bruker ALPHA T FT-IR spectrometer. The ¹H NMR spectrum of the solution in DMSO-*d*₆ was recorded on a Bruker AC-200 spectrometer at 298 K. The mass spectrum (EI) was recorded on a SHIMADZU LCMS-8040 mass spectrometer using a direct-insertion probe in the positive ion scanning mode (Q3+Scan).

1,2-Dimethyl-5-methoxy-3-(ethoxycarbonyl)indole (**3**)

A NaOH solution (10%, 40.0 mL) was added to a solution of 4.66 g (0.02 mol) of compound **2** in 40.0 mL of dioxane at 20°C; then 4.0 mL of dimethyl sulfate (0.042 mol) was added dropwise. The reaction mixture was stirred for 2 h, diluted with water, and cooled (to 4°C). The precipitate was filtered off, washed with water, and vacuum-dried (2 torr) over P₂O₅. Compound **3** (4.65 g, 94%) was obtained in the form of crystals with *T*_m = 113°C (in the literature, *T*_m = 117.5–118°C [8]).

6-Bromo-1,2-dimethyl-5-methoxy-3-(ethoxycarbonyl)indole (**4**)

A mixture of 4.65 g (0.0188 mol) of compound **3** and 3.36 g (0.0188 mol) of N-bromosuccinimide in 75.0 mL of CCl₄ was heated for 5 h upon boiling. The precipitate (succinimide) was filtered off from the hot reaction mixture. The filtrate was concentrated (by 1/3) by boiling away the solvent and cooling. The precipitate

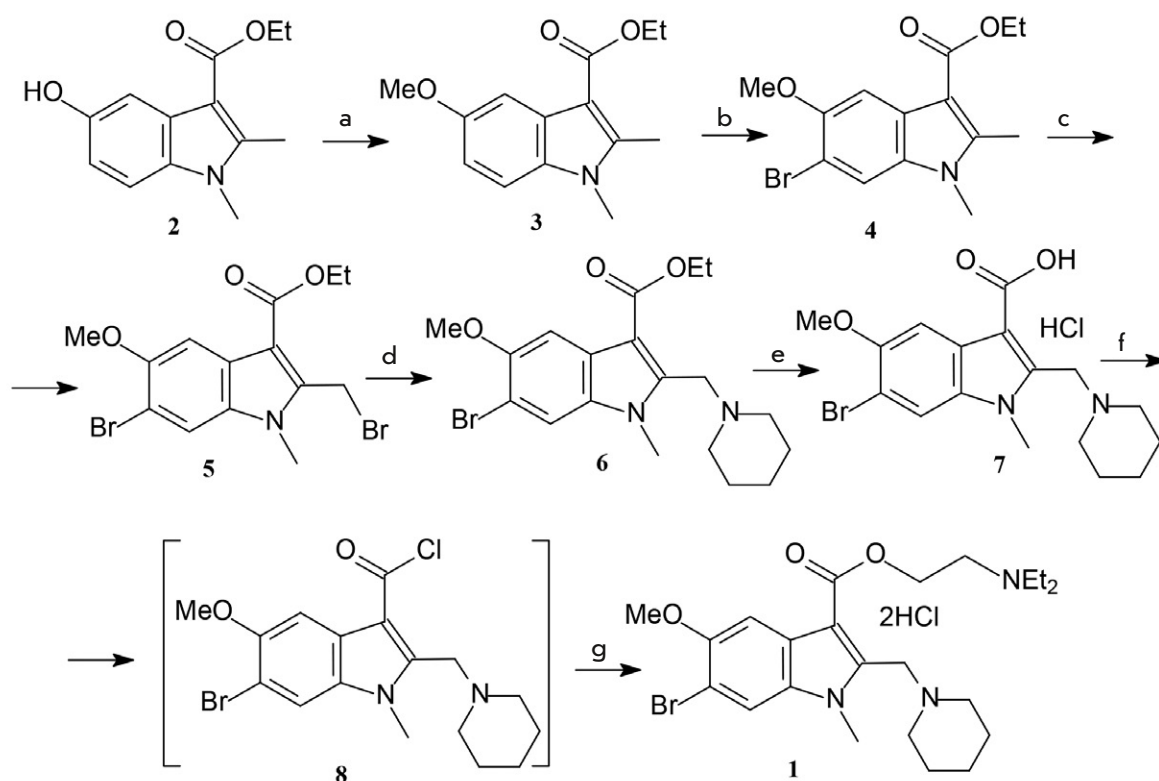


Fig. 2. Reagents and conditions: a. (1) aq. NaOH, dioxane; (2) Me₂SO₄, 20°C; b. N-bromosuccinimide, CCl₄, boiling; c. N-bromosuccinimide, (PhCOO)₂, CCl₄, irradiation (100 W bulb), boiling; d. piperidine, PhH, 20°C; e. (1) aq. NaOH, EtOH, boiling; (2) HCl (conc.); f. SOCl₂, dioxane, DMFA (cat.), 60°C; g. (1) Et₂NCH₂CH₂OH, Et₃N, PhH, boil.; (2) HCl, Et₂O, acetone, 20°C

was filtered off, washed with CCl₄ on a filter, and vacuum-dried (2 torr). Compound **4** (3.3 g, 54%) was obtained in the form of crystals with $T_m = 156^\circ\text{C}$ (in the literature, $T_m = 164\text{--}165^\circ\text{C}$ [8]).

6-Bromo-2-bromomethyl-5-methoxy-1-methyl-3-(ethoxycarbonyl)indole (**5**)

A mixture of 3.3 g (0.0101 mol) of compound **4**, 1.81 g (0.0101 mol) of N-bromosuccinimide, and 0.1 g of benzoyl peroxide in 30.0 mL of CCl₄ was boiled under illumination with a 100 W bulb during 5 h. After the succinimide solution had been filtered off from the hot mixture and the filtrate had cooled (to 20°C), the precipitate was filtered off, washed with CCl₄ on a filter, and vacuum-dried (2 torr). A total of 3.16 g (78%) of compound **5** was obtained in the form of crystals with $T_m = 142^\circ\text{C}$ (in the literature, $T_m = 141\text{--}142^\circ\text{C}$ [8]).

6-Bromo-5-methoxy-1-methyl-2-(1-piperidinomethyl)-3-(ethoxycarbonyl)indole (**6**)

A solution of 4.0 g (0.01 mol) of compound **5** and 1.7 g (0.02 mol) of piperidine in 50.0 mL of benzene was

left to rest at room temperature for 12 h. The precipitate (piperidine bromohydrate) was filtered off; the filtrate was concentrated to dryness under vacuum. Crystallization of the precipitate from ethanol yielded 1.7 g (82.9%) of compound **6** as crystals with $T_m = 124\text{--}125^\circ\text{C}$ (in the literature, $T_m = 124\text{--}125^\circ\text{C}$ [8]). Anal. Calcd. for C₁₉H₂₅BrN₂O₃: C, 55.75; H, 6.16; N, 6.84. Found: C, 55.72; H, 6.20; N, 7.02.

Hydrochloride of 6-Bromo-5-methoxy-1-methyl-2-(1-piperidinomethyl)-indole-3-carboxylic acid (**7**)

A solution of 6.0 g (0.15 mol) NaOH and 4.1 g (0.01 mol) of compound **6** in 60.0 mL of ethanol and 3.0 mL of water was boiled for 3 h. The reaction mixture was cooled down, diluted with water (10 mL), and acidified with concentrated hydrochloric acid. The precipitate was filtered off, washed with water on a filter, and vacuum-dried (2 torr) over P₂O₅. A total of 4.10 g (98%) of compound **7** in the form of crystals with $T_m = 236\text{--}238^\circ\text{C}$ was obtained. Anal. Calcd. for C₁₇H₂₂BrClN₂O₃: C, 48.88; H, 5.31; N, 6.71. Found: C, 48.68; H, 5.32; N, 6.65.

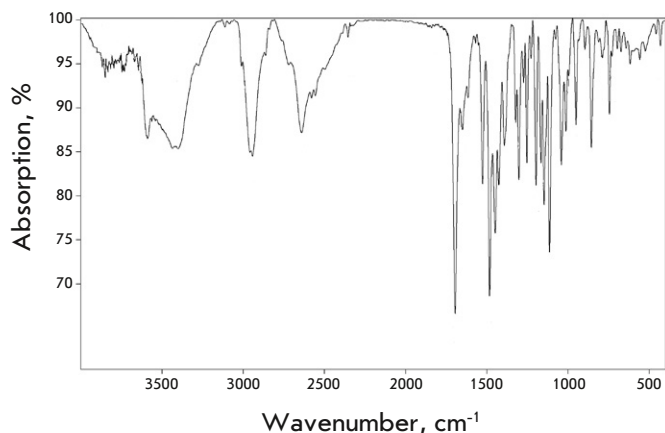


Fig. 3. IR spectrum of compound **1**

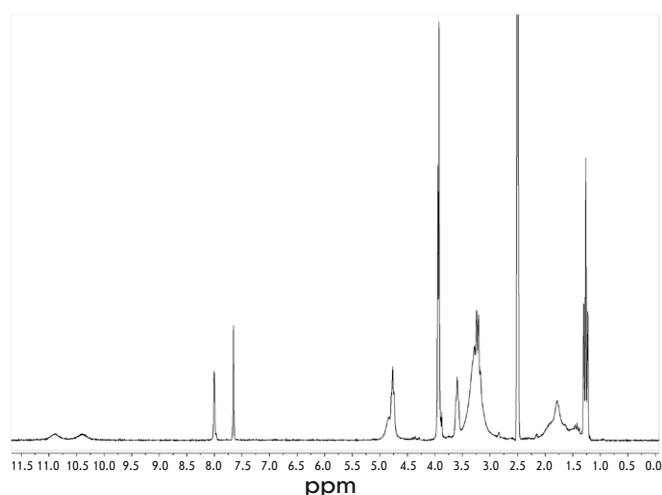


Fig. 4. ¹H NMR spectrum of compound **1**

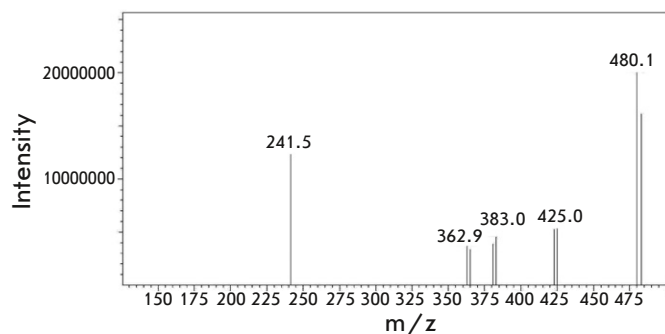


Fig. 5. Mass spectrum of compound **1**

Dihydrochloride of 6-bromo-5-methoxy-1-methyl-2-(1-piperidinomethyl)-3-(2-diethylaminoethoxy)carbonylindole (**1**)

Thionyl chloride (3.0 mL, 0.041 mol) and 2 droplets of dimethylformamide were added to a solution of 1.67 g (0.004 mol) of hydrochloride **7** in 30.0 mL of dioxane

under stirring. The reaction mixture was heated to 60°C during 3 h, concentrated to dryness under vacuum, and the remaining mixture was washed with diethyl ether. The resulting powdered chloroanhydride **8** was dissolved in 25 mL of benzene without additional purification and treated with a mixture of 1.2 mL (0.008 mol) of *N*-diethylaminoethanol and 1.12 mL (0.008 mol) of triethylamine. The reaction mixture was heated to 80°C during 2 h and cooled down. The precipitate (triethylamine hydrochloride) was filtered off and washed with hot benzene. The pooled filtrate was concentrated to dryness under vacuum; the remaining mixture was washed with hexane and vacuum-dried. A diethyl ether solution of hydrogen chloride (~30%, 2 mL) was added to the solution of the resulting product in 10 mL of acetone. The reaction mixture was concentrated to dryness under vacuum; the remaining mixture was crystallized from 2-propanol. Compound **1** (1.9 g, 85.2%) with $T_m = 237\text{--}240^\circ\text{C}$ was obtained. Its physicochemical characteristics are described below.

IR (KBr, ν , cm^{-1})

859, 1041, 1114, 1148, 1197, 1303, 1393, 1426, 1449, 1483, 1650, 1694 (C=O), 2354–2700, 2942, 3397, 3588 (Fig. 3).

¹H NMR spectrum (200 MHz, DMSO)

δ 10.76 (br s, 1H), 10.23 (br s, 1H), 8.03 (s, 1H), 7.65 (s, 1H), 4.87 (d, $J = 4.8$ Hz, 2H), 4.76 (t, $J = 5.1$ Hz, 2H), 3.95 (s, 3H), 3.93 (s, 3H), 3.61 (m, 2H), 3.50–3.06 (m, 8H), 2.15–1.33 (m, 6H), 1.26 (t, $J = 7.2$ Hz, 6H) (Fig. 4).

Mass spectrum

HRMS (ESI): Found m/z 480.1860 [M+H]; Anal. Calcd. for $\text{C}_{23}\text{H}_{35}\text{BrN}_3\text{O}_3$ + 480.1862 (Fig. 5).

Elemental analysis

Found: C, 49.89; H, 6.76; N, 7.48; Anal. Calcd.: C, 49.92; H, 6.56; N, 7.59; $\text{C}_{23}\text{H}_{36}\text{BrCl}_2\text{N}_3\text{O}_3$.

The solubility of compound **1** was determined in accordance with the General Pharmacopoeia Monograph (GPM.1.2.1.0005.15) [9]; it was inferred that 6-bromo-1-methyl-5-methoxy-2-(1-piperidinomethyl)-3-(2-diethylaminoethoxy)carbonylindole dihydrochloride **1** is an easily soluble compound.

Cells

A continuous kidney cell line of African green monkey (*Chlorocebus aethiops*) Vero E6 and a 293T cell line (a subclone of the transformed HEK 293 human embryonic kidney cell line, which is easily transfectable and maintains high levels of viral protein expression), as well as the L-929 mouse fibroblast cell line,

were used in the experiment. All the cell lines were provided by the All-Russian Cell Culture Collection of the N.F. Gamaleya National Research Center for Epidemiology and Microbiology of the Ministry of Health of the Russian Federation.

Animals

Male outbred white mice (weight, 12.0–14.0 g) were procured from the animal husbandry of NEO Market OJSC (Veterinary Certificate No. 250 N0679392). The experiments were conducted in compliance with the rules outlined in the European Convention for the Protection of Vertebrate Animals used for Experimental and other Scientific Purposes [10].

The animals were allocated into groups (intact and four study groups, with three mice per group) by random sampling with allowance for body weight. Housing, feeding, and care for the animals, as well as termination of the experiments involving them, were performed in compliance with the rules of Laboratory Practice accepted in the Russian Federation [11]. Study Protocol No. 43 dated May 3, 2023 was reviewed and approved by the Ethics Committee of the study site.

Viruses

The pandemic strain of human coronavirus SARS-CoV-2 with infective activity of 10^6 TCID₅₀/mL for Vero E6 cells (clinical isolate: hCoV-19/Russia/Moscow-PMVL-12/2020 (EPI_ISL_572398)) and the murine encephalomyocarditis virus (EMCV), Columbia SK-Col-SK strain with a titer of 10^7 TCID₅₀/mL, were used. The viruses were procured from the State Collection of Viruses of the D.I. Ivanovsky Institute of Virology, N.F. Gamaleya National Research Center for Epidemiology and Microbiology, Ministry of Health of the Russian Federation.

Quantification of the cytotoxicity of compound (1)

The Vero E6 cell culture in Gibco DMEM (Thermo FS) supplemented with 5 vol.% FCS, L-glutamine (2 mM) and a mixture of antibiotics (150 U/mL penicillin and 150 U/mL streptomycin) were inoculated into assay plates in the presence and in the absence of compound **1** and incubated at $37 \pm 0.5^\circ\text{C}$ for 96 h in an atmosphere of 5% CO₂. The monolayer confluence and cell viability were assessed daily. The culture medium was then removed from the plates, and 100 μL of the PC medium (DMEM medium supplemented with 2% Gibco FCS (Thermo FS)) and 20 μL of the CellTiter 96® Aqueous One Solution Cell Proliferation Assay (MTS) (Promega, G3582) were added to the monolayer cell culture in each well [12]. The plates were incubated at $37 \pm 0.5^\circ\text{C}$ for 3 h; the results

were recorded using a BIO-RAD automated reader at 490 nm using a 630 nm reference filter. The concentration of the solution of compound **1** reducing the optical density at $\lambda = 490$ nm by 50% compared to the control was regarded as the 50% cytotoxic dose (CC₅₀).

Conducting the antiviral activity determination experiment

A 24-hr monolayer cell culture prewashed with the PC medium and treated with non-toxic concentrations of compound **1** (i.e., concentrations lower than the CC₅₀ value) was used. Vero E6 cells were infected with the SARS-CoV-2 virus 60 min after addition of compound **1**. The following controls were used: positive control – cell culture infected with SARS-CoV-2 at different dilutions (from 10^{-1} to 10^{-7}) without compound **1**; negative control 1 – non-infected cell culture without compound **1**; negative control 2 – non-infected cell culture with 100 μL of the solutions of compound **1** at different concentrations. Each concentration of compound **1** was tested in four parallel runs. The assay plates were incubated at $37 \pm 0.5^\circ\text{C}$ for 96 h in an atmosphere of 5% CO₂ until the CPE of the virus was completely manifested in the viral control within the expected range. The antiviral activity of compound **1** was determined visually under a microscope 96 h post-infection by inhibition of the CPE of the virus in the Vero E6 cell culture. The inverse of the final dilution at which CPE had developed was regarded as the viral titer. TCID₅₀ was calculated using the Reed–Muench method for each concentration of the analyzed compound and control virus titer. The result was evaluated according to $\Delta\lg_{\text{max}}$ (the maximum decrease in the infective dose of the virus in the experiment compared to the control, expressed as decimal logarithms). The concentration of compound **1** reducing the virus titer by at least 1.5 lg was considered the minimum inhibitory concentration. The experiments were performed in three replicates to ensure statistically significant results.

Quantification of the efficiency of inhibition of syncytium formation

293T cells were co-transfected with a plasmid containing full-length S glycoprotein (pVAX-1-S-glycoprotein; Evrogen, Russia) and a GFP-encoding plasmid (pUCHR-IRES-GFP) using the Transporter™ 5 transfection reagent during 48 h. Next, compound **1** was added to the Vero E6 cell monolayer grown in 96-well plates at different concentrations and a suspension of 293T/S/GFP effector cells (3 : 1 cell ratio) was added to the wells. After 2 h, the number of syncytia formed was evaluated by fluorescence microscopy. The efficiency of inhibition of the cell–cell fusion

induced by S glycoprotein SARS-CoV-2 compared to that in the control (without compound **1**) was assessed using the GraphPadPrism 5.0 software and presented as a percentage.

Quantification of IFN-inducing activity

Blood samples were collected from the decapitated animals into tubes without anticoagulants 2, 24, 48, and 72 h after a single intraperitoneal injection of compound **1** at a dose of 121.2 $\mu\text{mol}/\text{mouse}$ (70 $\mu\text{g}/\text{mouse}$) or 0.2 mL of distilled water (placebo, control without compound **1**). The IFN activity in mouse serum was quantified for the L-929 mouse fibroblast cell line. A three-day-old monolayer of a passaged L-929 cell line grown on medium 199 and DMEM (1 : 1) supplemented with 7% FCS, L-glutamine and antibiotics (150 U/mL penicillin and 150 U/mL streptomycin) was used. The serum IFN level was determined by titrating samples in the L-929 mouse fibroblast culture using the mouse EMCV as a viral indicator: the final IFN dilution protecting 50% of the cells against the cytopathic effect of 100 TCID₅₀ of the virus was determined.

Statistical analysis

The half-maximal cytotoxic (CC_{50}) and inhibitory concentrations (IC_{50}) were calculated with the methods generally used in biological studies using the Microsoft Excel 5.0 and GraphPad Prism 6.01 software packages. The four-parameter logistic regression equation (menu items “Nonlinear regression” – “Sigmoidal dose-response (variable slope)”) was used as a working model for analyzing CC_{50} . The four-parameter logistic regression equation (menu items “Nonlinear regression” – “log (inhibitor) vs. response (variable slope)”) was used for analyzing IC_{50} . The selectivity index (SI) was calculated based on the data obtained according to the equation $\text{SI} = \text{CC}_{50}/\text{IC}_{50}$.

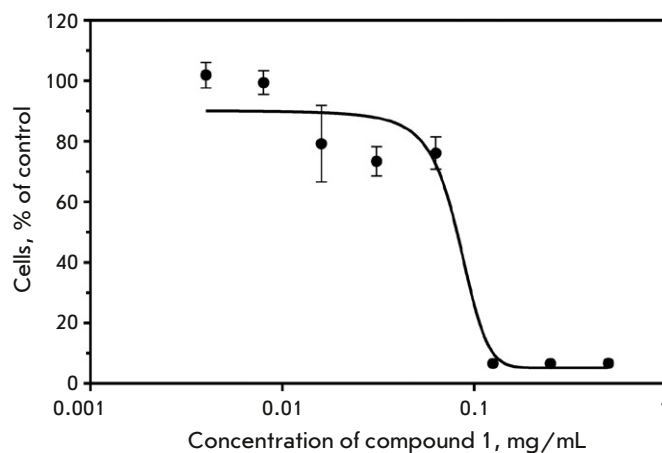


Fig. 6. Determining the cytotoxic effect of compound **1** 96 h after its addition to the Vero E6 cell culture (using MTS vital dye). $\text{CC}_{50} = 83.32 \mu\text{g}/\text{mL}$

RESULTS

Quantification of the cytotoxicity of compound **1**

The data obtained by studying the cytotoxic effect of compound **1** on the Vero E6 cell culture using a MTS vital dye were used to plot an analytical curve. Using this curve, we determined the SS_{50} value for compound **1**. The concentration reducing the optical density value by 50% compared to the control was 83.32 $\mu\text{g}/\text{mL}$ (144.30 μM) (Fig. 6).

Quantification of the antiviral activity of compound **1**

The antiviral activity of compound **1** was determined according to the decline in the infectious virus titer (TCID₅₀/mL) in the Vero E6 cell culture (Table 1).

Table 1 demonstrates that the analyzed compound exhibits a reliable dose-dependent antiviral activity

Table 1. The effect of compound **1** on the replication of SARS-CoV-2

Concentration of compound 1 , μM ($\mu\text{g}/\text{mL}$)	TCID ₅₀	Virus control	$\Delta\lg_{\text{max}}$ the maximum reduction of the infective dose of the virus in the experiment compared to control (expressed as the decimal logarithm)
52.0 (30.0)	10 ⁰	10 ⁶	6
26.0 (15.0)	10 ¹	10 ⁶	5
13.0 (7.5)	10 ³	10 ⁶	3

Note: TCID₅₀ – 50% tissue culture infectious dose.

Table 2. IFN activity in mouse serum

Time after injecting compound 1 or placebo to mice, h	IFN titer (U/mL)	
	Compound 1 (70 µg/mouse)	Placebo (control without compound 1)
2	40	< 4
24	20	
48	20	
72	20	

in vitro, which is indicative of its specific action, and completely suppresses the replication of the SARS-CoV-2 virus at a concentration of 52.0 µM (30 µg/mL) (i.e. by 6 lgTCID₅₀). In virological studies, the antiviral effect of drugs is usually considered satisfactory if Δlg TCID₅₀ is ≥ 2.0 [13].

The IC₅₀ value for the analyzed compound calculated using the GraphPadPrism 6.01 software was 1.84 µM (1.06 µg/mL). The selectivity index (SI) calculated as the ratio of CC₅₀ to IC₅₀ (SI = CC₅₀/IC₅₀) was 78.6.

Studies focusing on the efficiency of inhibition of the syncytium formation induced by the SARS-CoV-2 spike protein (S glycoprotein)

Additional studies were performed for syncytium formation mediated by the SARS-CoV-2 spike protein (S glycoprotein). Syncytium formation induced by the SARS-CoV-2 spike protein (S glycoprotein) was found to be inhibited by 89%.

Quantification of interferon (IFN)-inducing activity of compound 1

The titration data are listed in Table 2.

Compound 1, administered intraperitoneally at a single dose of 121.2 µmol/mouse (70 µg/mouse), was shown to exhibit an IFN-inducing activity.

DISCUSSION

Discovered and described in the 1960s, the coronavirus failed to draw much attention, because it caused acute respiratory infections with a mild course [14, 15]. However, the COVID-19 coronavirus pandemic has changed our attitude towards coronaviruses and initiated a search for antiviral agents that would be effective against SARS-CoV-2. The search and development of drugs for controlling the pandemic coronavirus infection are tightly related to the point of

application to viral replication and its effects during the treatment of patients. According to recent publications, the course of SARS-CoV-2 infection is divided into four stages associated with different requirements to drugs [16–18]. Thus, the pre-exposure stage is preferred for prophylactic immunization, use of neutralizing antibodies, and prophylactic antiviral drugs. Antibodies and intravenous and/or oral antiviral medications are effective during the next stage, after an individual has already been infected and viral replication is taking place. It has been established that a therapeutic effect is observed if anti-SARS-CoV-2 antibodies are administered within 10 days after the onset of symptoms [19, 20]; oral antiviral drugs can have an effect within 3–5 days after the onset of symptoms [17, 21]. The replication rate of the SARS-CoV-2 virus is known to increase approximately 3–5 days after the onset of clinical symptoms and then decrease within two or three days. The subsequent clinical events are associated with disruption of the immune response to SARS-CoV-2 [22]. However, in some patients, a recurrence of COVID-19 symptoms and presence of the virus were detected much later, indicating that the virus persisted and successfully continued to replicate in individual compartments during the later phase [23]. Therefore, it became clear that an oral antiviral and immunomodulatory small-molecule drug, which can be used during infection reactivation, is also needed to suppress viral reactivation during the late phases of the disease.

An extensive search across preclinical and clinical studies has identified a large number of compounds that exhibit anti-SARS-CoV-2 activity (low-molecular-weight compounds, monoclonal antibodies, peptide inhibitors, macromolecular inhibitors, as well as RNA- and cell-based therapeutics) [24–26].

Unlike vaccines, the available antiviral chemotherapeutic agents inhibiting viral replication (including

unusual nucleosides, and inhibitors of virus-specific proteins and enzymes) are generally effective against a broader range of pathogenic viruses. However, adverse effects are likely to develop during their use and resistant virus strains emerge thus leading to disease recurrence and exacerbation [27, 28].

Umifenovir (arbidol, the international name Umifenovirum) [29] is one of the commonly used antiviral drugs in Russia. It is included in the COVID-19 prevention and treatment guidelines [18]. According to Leneva et al. [30], umifenovir exhibits an antiviral activity and inhibits fusion of the viral envelope with cell membranes. Therefore, the virus cannot penetrate into the cell and its replication is suppressed. Umifenovir was shown to inhibit SARS-CoV-2 replication in Vero E6 cells [31, 32]. However, because of its low bioavailability and water insolubility, the therapeutic efficacy of arbidol is limited; so, it failed to assume a leading position among anti-COVID medications [33, 34].

The proposed drug candidate based on 6-bromo-1-methyl-5-methoxy-2-(1-piperidinomethyl)-3-(2-diethylaminoethoxy)carbonylindole dihydrochloride will most probably preferentially be aimed at preventing the infection and inhibiting SARS-CoV-2 replication. At this very stage, viral replication and reproduction in the adjacent cells needs to be suppressed and the innate immunity has to be stimulated by receptor activation and induction of the interferon system. The ability of compound **1**, used at a concentration of 52.0 μM , to completely stop the replication of the

SARS-CoV-2 virus in cells and the discovered effective mechanism of inhibition of syncytium formation induced by the spike protein (S glycoprotein) of the SARS-CoV-2 virus may apparently contribute to it. The revealed interferon-inducing ability of compound **1** may be indicative of its potential to activate the interferon system and the innate immunity, which also allows one to use the investigational drug to suppress the consecutive stages of immune dysfunction occurring in patients with COVID-19.

CONCLUSIONS

Our findings demonstrate that the synthesized compound **1** exhibits an antiviral effect against SARS-CoV-2 in *in vitro* studies. At a concentration of 52.0 μM , this compound completely inhibited the replication of the SARS-CoV-2 virus, with an infectious activity of 10^6 TCID₅₀/mL. The concentration curves indicate the specificity of the action of the analyzed compound and show that the developed compound is rather promising and can be further studied *in vitro* in experimental animals. Due to its synthetic accessibility, high activity (IC₅₀ = 1.06 $\mu\text{g}/\text{mL}$), and high selectivity index (SI = 78.6), compound **1** meets the requirements for developing antiviral drugs for COVID-19 prevention and treatment. ●

This work was conducted under State Assignment of the Ministry of Health of the Russian Federation (Topic No. 056-00119-21-00).

REFERENCES

- WHO has announced the end of the coronavirus pandemic. <https://www.rbc.ru/society/05/05/2023/645503499a79477d05bf2bb4https://www.rbc.ru/society/05/05/2023/645503499a79477d05bf2bb4>
- WHO Coronavirus (COVID-19) Dashboard (WHO, accessed 12.06.2023); <https://covid19.who.int/>
- LIVE: Media briefing on COVID-19 and global health issues. World Health Organization (WHO). <https://www.youtube.com/watch?v=B0oBevft4bs>
- Crook H., Raza S., Nowell J., Young M., Edison P. // *BMJ*. 2021. V. 374. № 1648. P. 1–18.
- Coopersmith C.M., Antonelli M., Bauer S.R., Deutschman C.S., Evans L.E., Ferrer R., Hellman J., Jog S., Kesecioglu J., Kissoon N., et al. // *Crit. Care Med*. 2021. V. 49. № 4. P. 598–622.
- Good S.S., Westover J., Jung K.H., Zhou X.J., Moussa A., La Colla P., Collu G., Canard B., Sommadossi J.P. // *Antimicrob. Agents Chemother*. 2021. V. 65. № 4. P. e02479–20.
- Filimonova M.V., Tsyshkova N.G., Narovlyansky A.N., Marinchenko V.P., Koval L.S., Parfenova T.M., Izmestyeva A.V., Ershov F.I. Patent RU 2552422 C2. Russian Federation. IPC C07D209/42(2006.01); A61K31/404(2006.01); A61P31/12(2006.01). 2015.
- Trofimov F.A., Tsyshkova N.G., Grinev A.N. // *Chem. Heterocycl. Compd*. 1973. V. 9. P. 282–285.
- OFS.1.2.1.0005.15 Solubility. GF RF 14 ed. V. 1. M., 2015. <https://pharmacopoeia.ru/ofs-1-2-1-0005-15-rastvorimost/>
- European Convention for the Protection of Vertebrate Animals Used for Experimental and other Scientific Purposes (ETS 123). // Strasbourg, 1986. 11 p.
- GOST “Guidelines for the maintenance and care of laboratory animals. Rules of equipment of premises and organization of procedures”; Guidelines for accommodation and care of animals. Environment, housing and management. ISS 13.020.01. Date of introduction 2016-07-01. <https://docs.cntd.ru/document/1200127789>
- CellTiter 96® AQueous One Solution Cell Proliferation Assay (MTS) («Promega», G3582). Instructions for use of products G3580, G3581 and G3582. Technical Bulletin.
- Guidelines for conducting preclinical studies of medicines. // ed. Mironova A.N. Part 1. M.: Grif and K, 2012. P. 527–551.
- Tyrrell D.A.J., Bynoe M.L. // *Br. Med. J*. 1965. V. 1. P. 1467–1470.
- Almeida J.D., Berry D., Cunningham C., Hamre D., Hofstad M.S., Mallucci L., McIntosh K., Tyrrell D.A.J. // *Nature*. 1968. V. 220. № 16. P. 650.

16. Cascella M., Rajnik M., Aleem A., Dulebohn S.C., Di Napoli R. Features, Evaluation and Treatment Coronavirus (COVID-19). // StatPearls [Internet]. Treasure Island (FL): StatPearls Publ., 2023.
17. Toussi S.S., Hammond J.L., Gerstenberger B.S., Andersen A.S. // Nat. Microbiol. 2023. V. 8. P. 771–786.
18. Temporary methodological recommendations. “Prevention, diagnosis and treatment of new coronavirus infection (COVID-19). Version 17 (09.12.2022)”.
19. Fact Sheet for Health Care Providers Emergency Use Authorization (EUA) of Bamlanivimab and Etesevimab. Eli Lilly and Company, 2022.
20. Fact Sheet for Health Care Providers Emergency Use Authorization (EUA) of REGEN-COV (Casirivimab and Imdevimab). Regeneron, 2022.
21. Petty L.A., Malani P.N. // JAMA. 2022. V. 327. № 24. P. 2464.
22. Vetter P., Eberhardt C.S., Meyer B., Murillo M., Torriani G., Pigny F., Lemeille S., Cordey S., Laubscher F., Vu D.L. et al. // mSphere. 2020. V. 5. № 6. P. e00827–20.
23. Deo R., Choudhary M.C., Moser C., Ritz J., Daar E.S., Wohl D.A., Greninger A.L., Eron J.J., Currier J.S., Hughes M.D., et al. // Ann. Intern. Med. 2023. V. 176. № 3. P. 348–354.
24. Li G., Hilgenfeld R., Whitley R., De Clercq E. // Nat. Rev. Drug Discov. 2023. V. 22. № 6. P. 449–475.
25. Zaki M.M., Lesha E., Said K., Kiaee K., Robinson-McCarthy L., George H., Hanna A., Appleton E., Liu S., Ng A.H.M., et al. // Sci. Adv. 2021. V. 7. № 33. P. eabg5995.
26. Meganck R.M., Baric R.S. // Nat. Med. 2021. V. 27. № 3. P. 401–410.
27. Samson M., Pizzorno A., Abed Y., Boivin G. // Antiviral Res. 2013. V. 98. № 2. P. 174–185.
28. Wyles D.L. // J. Infect. Dis. 2013. V. 207. № 1. P. 33–39.
29. WHO Collaborating Centre for Drug Statistics Methodology. J05 Antivirals for systemic use. J05AX Other antivirals. https://www.whocc.no/atc_ddd_index/?code=-J05AX.
30. Leneva I.A., Russell R.J., Boriskin Y.S., Hay A.J. // Antiviral Res. 2009. V. 81. № 2. P. 132–140.
31. Leneva I., Kartashova N., Poromov A., Gracheva A., Korchevaya E., Glubokova E., Borisova O., Shtro A., Logonova S., Shchukina V., et al. // Viruses. 2021. V. 13. № 8. P. 1665.
32. Ge Y., Tian T., Huang S., Wan F., Li J., Li S., Wang X., Yang H., Hong L., Wu N., et al. // Signal Transduct. Target Ther. 2021. V. 6. № 1. P. 165.
33. Chen C., Zhang Y., Huang J., Yin P., Cheng Z., Wu J., Chen S., Zhang Y., Chen B., Lu M., et al. // Front. Pharmacol. 2021. V. 12. P. 683296.
34. Archakov A.I., Guseva M.K., Uchaykin V.F., Ipatova O.M., Doschitsin Yu.F., Tikhonova E.G., Medvedeva N.V., Prozorovsky V.N., Strekalova O.S., Shironin A.V. Patent PCT/WO2010128889A1, RF. IPC A61K9/19. 2010.

BODIPY Dye Derivative for Irreversible Fluorescent Labeling of Eukaryotic Cells and Their Simultaneous Cytometric Analysis

A. Yu. Frolova, S. V. Kutyaikov, V. I. Martynov, S. M. Deyev, A. A. Pakhomov*

M.M. Shemyakin and Yu.A. Ovchinnikov Institute of Bioorganic Chemistry of the Russian Academy of Sciences, Moscow, 117997 Russian Federation

*E-mail: alpah@mail.ru

Received: October 19, 2023; in final form, November 03, 2023

DOI: 10.32607/actanaturae.26879

Copyright © 2023 National Research University Higher School of Economics. This is an open access article distributed under the Creative Commons Attribution License, which permits unrestricted use, distribution, and reproduction in any medium, provided the original work is properly cited.

ABSTRACT In this work, we synthesized a green fluorescent dye derivative, 1,3,5,7-tetramethyl-BODIPY, with a heptyl substituent at the 8-position. The obtained highly hydrophobic compound was able to rapidly and irreversibly bind to eukaryotic cells. Incubation of cells with the dye over different periods of time or at different concentrations allowed us to control the degree of cell labeling and the level of fluorescence. This made it possible to modulate the fluorescence level of different eukaryotic cell cultures and then distinguish them by their level of fluorescence signal in the green channel in cytometric experiments. The labeled cells can be combined and further analyzed in the same test tube under identical conditions using the channels in which the dye does not fluoresce. This approach has been tested on a number of tumor cell cultures containing the HER2 receptor on their surface. The representation of the receptor in these cells was analyzed in one test tube in one run using a HER2-specific ligand based on the hybrid protein DARPIn9_29-mCherry, which fluoresces in the red region of the spectrum.

KEYWORDS fluorescence, chromophore, cytometry, flow cytometry, BODIPY, cell labeling, cell analysis.

ABBREVIATIONS BDP-C7 – 8-heptyl-1,3,5,7-tetramethyl-BODIPY; BODIPY – 4,4-difluoro-4-bora-3a,4a-diaza-s-indacene; DARPIn – Designed Ankyrin Repeat Protein; HER2 – human epidermal growth factor receptor 2.

INTRODUCTION

Flow cytometry is a technique widely used for studying the functioning of living systems, developing new drugs, and in medicine for sample analysis and selection of treatment strategies. The method is based on the labeling of cells with fluorescent dyes, often conjugated with proteins targeted to various surface markers (e.g., antibodies), which allows one to phenotype the cells in a population [1, 2]. It is often necessary to compare cell cultures with each other during analysis, for example, to compare cell parameters with control samples. In this case, the samples are analyzed in parallel under identical conditions. However, it is impossible to provide completely identical conditions when preparing cell samples from experiment to experiment because of the inherent errors in the sample preparation due to pipetting, as well as the potential influence of the human factor.

In this study, we elaborated an approach that allows one to simultaneously analyze several cell cul-

tures in one test tube, even when they initially do not differ in the parameters detected cytometrically. For this purpose, different cell samples are pre-stained with a nonspecific dye so that each analyzed culture has a different fluorescence intensity in one of the detection channels of the cytometer. This is possible by treating the cells with a lipophilic dye that binds nonspecifically to cell membrane structures at different times or different concentrations.

EXPERIMENTAL

Synthesis of 8-heptyl-4,4-difluoro-1,3,5,7-tetramethyl-4-bora-3a,4a-diazaindacene (BDP-C7)

Octanoyl chloride (1 mL, 10 mmol) and 2,4-dimethylpyrrole (650 mg, 4 mmol) were successively dissolved in dry dichloromethane (50 mL) pre-flushed with argon. The mixture was stirred for 3 h at room temperature under argon atmosphere. Triethylamine (3 mL, 22 mmol) was then added, and after 15 min

at 0°C, boron trifluoride etherate (3 mL, 24 mmol) was added portion-wise (as three portions). The mixture was further stirred at 0°C for 3 h. After completion of the reaction, the resulting mixture was passed through a short column filled with a silica gel using toluene as an eluent. The solvent was evaporated, and the reaction product was separated by column chromatography on a silica gel using toluene as an eluent. The yield was 558 mg. ¹H-NMR (400 MHz, CDCl₃): δ 0.89 (t, 3H, CH₃CH₂), 1.31 (m, 6H, CH₃CH₂CH₂CH₂), 1.48 (m, 2H, CCH₂CH₂CH₂), 1.63 (m, 2H, CCH₂CH₂), 2.41 (s, 6H, CH₃), 2.51 (s, 6H, CH₃), 2.92 (t, 2H, CCH₂), 6.05 (s, 2H, CH). ¹³C-NMR (101 MHz, CDCl₃): δ 14.0, 14.4, 16.3, 22.6, 28.5, 29.0, 30.4, 31.7, 31.9, 76.7, 77.0, 77.3, 121.5, 131.4, 140.3, 146.7, 153.7. ¹⁹F-NMR (376 MHz, CDCl₃): δ 146.66 (q, J ¹⁹F-¹¹B = 32.3 Hz).

Spectrophotometry

The absorption and fluorescence emission spectra were measured using a Cary50 Bio spectrophotometer (Varian) and a Cary Eclipse spectrofluorometer (Varian), respectively. The fluorescence quantum yield was measured using a homologous derivative of BODIPY, 8-decene-1,3,5,7-tetramethyl-BODIPY [3–5], as a standard (the quantum yield of the standard in DMSO was considered to be 0.99).

Cell culture

SKBR3 human breast adenocarcinoma cells overexpressing the HER2 tumor marker [6], modified EMT6/P mouse mammary carcinoma cells overexpressing HER2 (EMT-HER2) [7], and HeLa human cervical cancer cells with a normal HER2 expression level [8] were cultured in DMEM (Gibco, Thermo Fisher Scientific, Inc, USA) supplemented with 10% fetal bovine serum (FBS, Gibco, Thermo Fisher Scientific, Inc.), 100 units/mL penicillin, 0.1 mg/mL streptomycin, and 0.25 µg/mL amphotericin (Gibco, Thermo Fisher Scientific, Inc.) at 37°C and 5% CO₂ in a humidified atmosphere. The growth medium was renewed every 2 days. The Versene solution (PBS and 0.02% EDTA) was used during culturing.

Flow cytometry

SKBR3, EMT-HER2, and HeLa cells were harvested with the Versene solution and precipitated at 125 g for 5 min; the supernatant was removed, and PBS containing 10% FBS was added to the cells to a concentration of 5 × 10³ cells/µL. Then, 100 µL of a solution of the **BDP-C7** dye at a given concentration in PBS containing 1% DMSO was added to 3 µL of cell suspension. The cells were incubated at room temperature for the specified time, sedimented at 500 g for 30 s, and the supernatant was removed. Next, either

100 µL of PBS was added to the cells and cytometric analysis was performed, or a PBS solution containing the 1 µM DARPIn-mCherry protein was added, incubated for 5 min and after sedimentation, removal of the protein solution and addition of 100 µL of PBS, a cytometric analysis was performed. A Novocyte 3000 VYB flow cytometer (ACEA Biosciences, USA) was used for the cell analysis. Green detection channel (FITC): laser excitation at 488 nm, emission detection through a 530/30 nm light filter; red detection channel (PE-Texas-Red): laser excitation at 561 nm, emission detection through a 615/20 nm light filter. Before analyzing the fluorescence level of the cells, events corresponding to living cells were first selected (gating in A-FSC / A-SSC channels), and then events corresponding to non-aggregated cells were selected (gating in A-FSC / H-FSC channels) [9].

Cell viability study

HeLa cells cultured in complete DMEM were seeded in a 96-well plate (10⁴ cells/well) and grown overnight. Prior to testing, the culture medium was removed and 100 µL of a fresh medium containing **BDP-C7** at the specified concentration and 1% DMSO was added. The **BDP-C7** substance was tested in concentrations ranging from 33 nM to 20 µM in three repeats. Sample solutions were prepared by serial 2.5-fold dilution of the concentrated sample. The culture medium containing 1% DMSO was added to the control cells. After overnight incubation, liquid was withdrawn, and 100 µL of 3-(4,5-dimethylthiazol-2-yl)-2,5-diphenyltetrazolium bromide (MTT) solution at a concentration of 5 mg/mL in a serum-free culture medium was added to each well and the cells were further incubated at 37°C for 3 h. The supernatant was then removed, and 100 µL of DMSO was added to dissolve the formazan crystals. The optical density was measured at 570 and 640 nm using an Infinite M1000 Pro plate reader (Tecan, Austria).

RESULTS AND DISCUSSION

A derivative of 1,3,5,7-tetramethyl-BODIPY containing a heptyl substituent at the position 8 (**BDP-C7**, Fig. 1A) was chosen as a dye to demonstrate the applicability of the proposed approach. BODIPY derivatives are characterized by high brightness and photostability; they possess narrow fluorescence excitation and emission bands, allowing them to minimally “interfere” with other dyes [10–14]. Examples of the use of BODIPY, including in cytometric tasks, have been described [15–17]. The methyl groups in **BDP-C7** protect the chromophore from interactions with the external environment, while the heptyl substituent increases the hydrophobicity of the dye and facilitates

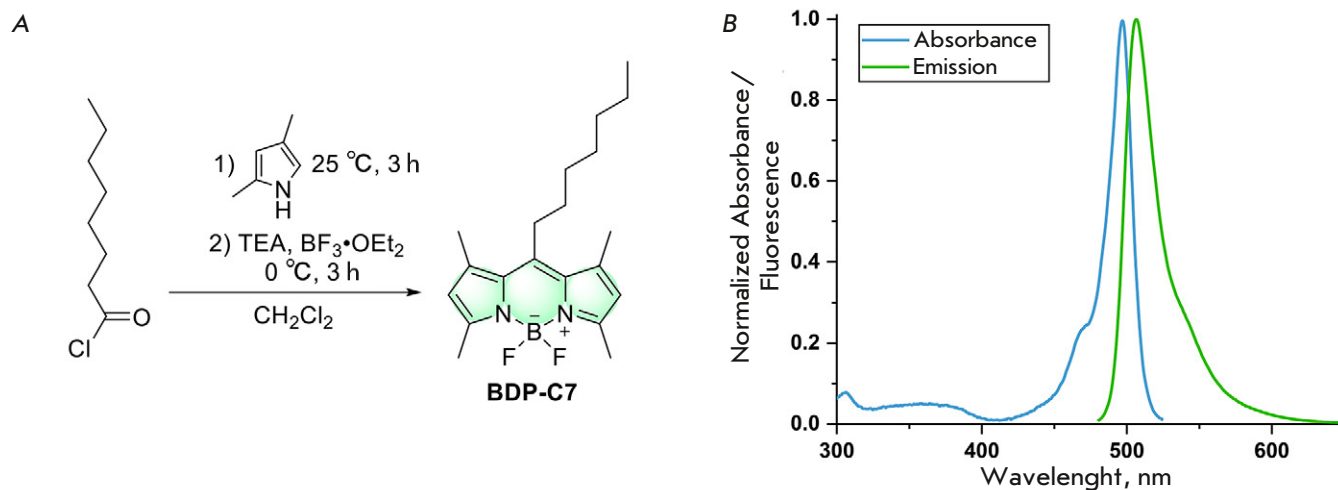


Fig. 1. Synthesis of the **BDP-C7** dye (A) and its absorption and fluorescence emission spectra in DMSO (B)

its irreversible binding to cell membrane structures. **BDP-C7** was synthesized starting from octanoyl chloride according to the protocol used previously for homologous compounds [3, 18, 19] (*Fig. 1A*).

When dissolved in DMSO, the dye exhibited narrow excitation and fluorescence emission bands, with the maxima of light absorption and fluorescence emission at 497 and 507 nm, respectively (*Fig. 1B*). The extinction coefficient was $87300 \text{ M}^{-1}\text{cm}^{-1}$, and the fluorescence quantum yield was 99%. Thus, **BDP-C7** is a bright fluorescent dye and is ideally suited for detection in the green channel of most fluorimetric instruments with laser excitation at 488 nm and detection in the 495–525 nm range.

To test the staining of eukaryotic cells with the **BDP-C7** dye, we used the HeLa cell culture, which is widely used in routine cell experiments. First, the cells were stained at different concentrations of **BDP-C7** for a short period of time. The cells were incubated for 2 min in PBS containing **BDP-C7** at a given concentration and 1% DMSO. After incubation, the unbound dye was washed off, and the cells were analyzed on a flow cytometer (*Fig. 2A,B*). *Figure 2A* indicates that the concentration of 1 nM is sufficient to distinguish the treated cells from the control, untreated cells. At 1 μM of the dye, there is probably almost maximum saturation of the cell with the dye; treatment with higher concentrations increases the fluorescence level only slightly. One can see that the samples treated with 1, 10, 100 nM, and 10 μM of the **BDP-C7** dye are well distinguishable from each other and from the control. Thus, by staining HeLa cells with the **BDP-C7** dye, we successfully obtained five populations that were well distinguishable in one detection channel. The number

of such populations can be increased to at least six due to the region around 10 nM.

Treatment of the cells with the **BDP-C7** dye at the same concentration but during different time periods (*Fig. 2B,D*) also yielded cells with different levels of green fluorescence, but this effect was not so significant. *Figure 2B* demonstrates that the level of cell fluorescence rises by less than an order of magnitude as the incubation time is increased from 1 to 10 min, while broadening of the peak due to the shoulder in the low-intensity region is observed upon incubation for 10 min. As the incubation time is increased to 15 and 20 min, in addition to peak broadening, the median cell fluorescence decreases. This is most likely to be caused by changes in cell morphology during the 10–20 min of incubation under suboptimal conditions (1% DMSO in PBS). At other concentrations of **BDP-C7**, the effect was similar (data not shown). Therefore, incubation of cells with the dye for more than 5 min makes no practical sense because of the changes occurring in the cells under unfavorable conditions and the resulting broadening of peaks; moreover, treatment with the dye at different concentrations for a short time period allows one to achieve a difference in the fluorescence signal of the cells of several orders of magnitude (*Fig. 2A,B*).

Next, we tested whether dye washout and fluorescence signal changes occur after **BDP-C7** binding to the cells. For this purpose, after washing off the unbound dye, the cells were incubated in PBS in different time intervals and then analyzed on a flow cytometer (*Fig. 3A*). In all the samples tested, the level of the fluorescent signal remained virtually unchanged with time (*Fig. 3*). We did not test times longer than 30 min, since this time period is usually

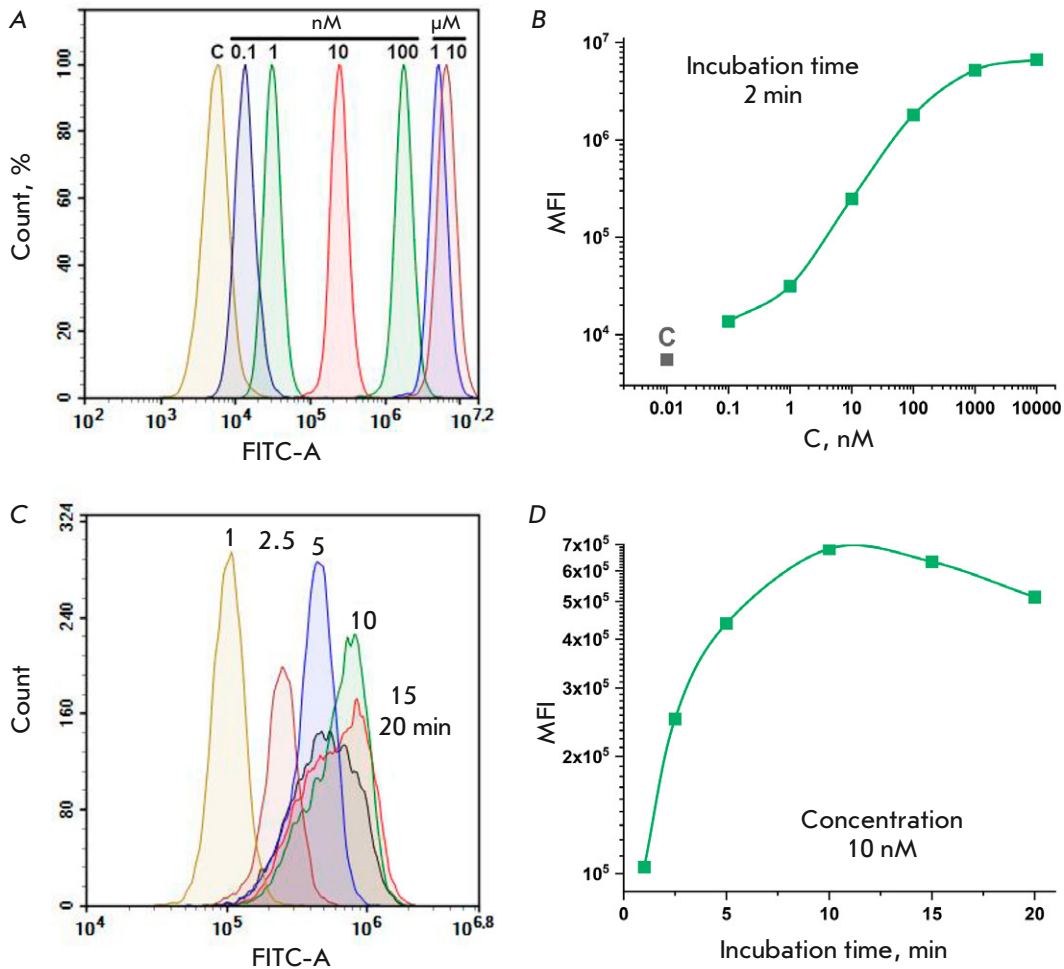


Fig. 2. Cytometric analysis of HeLa cells exposed to the **BDP-C7** dye for 2 min at concentrations ranging from 0.1 nM to 10 μM (A, B) and at 10 nM for 1–20 min (C, D). C – control cells not subjected to dye treatment. The histograms of the intensities in the green fluorescence channel with excitation at 488 nm and emission detection at 530/30 nm (A, C) and the median fluorescence intensity (MFI) values of the cell populations (B, D) are shown

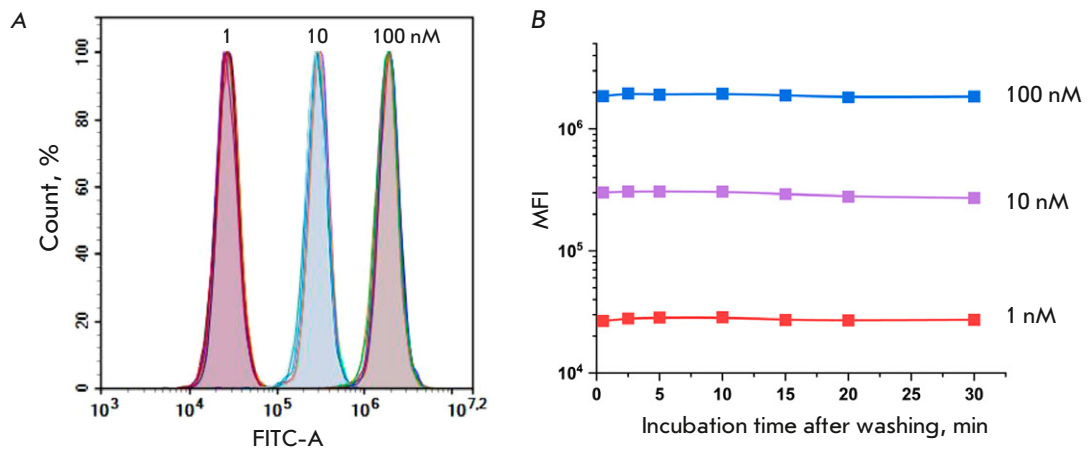


Fig. 3. Analysis of the **BDP-C7** dye washout from the cells. Cytometric analysis of HeLa cells exposed to the dye for 2 min at concentrations of 1, 10 and 100 nM. Cells after washing to remove the unbound dye and incubation in PBS buffer for a given time. Histograms of the intensities in the green fluorescence channel (A) and the median fluorescence intensity (MFI) of the cell population (B) at different incubation times after washing are shown

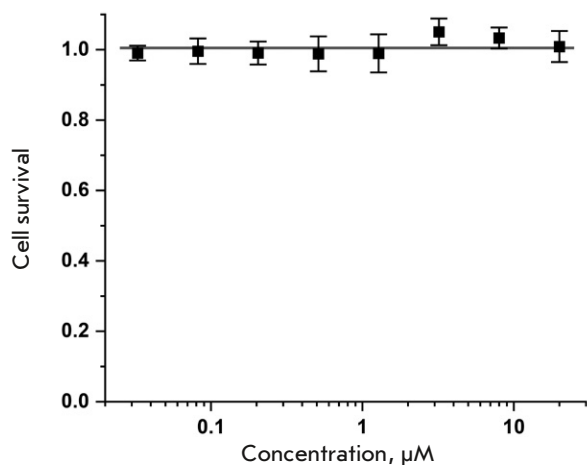


Fig. 4. Cytotoxicity of the **BDP-C7** dye as measured by MTT assay on HeLa cells

sufficient for the manipulations required for a cytofluorimetric analysis.

We also tested whether the dye could exhibit cytotoxicity at the concentrations used. Cytotoxicity was tested using the standard MTT assay at dye concentrations of up to 20 μM (Fig. 4). **BDP-C7** showed no toxicity in the entire tested concentrations range.

The applicability of the approach consisting in labeling cell cultures by staining with the green fluorescent dye **BDP-C7** at different concentrations was tested on HeLa, SKBR3, and EMT-HER2 cell cultures. These cells differ from each other in the expression level of the surface tumor marker, human epidermal growth factor receptor 2 (HER2). It is estimated that HeLa cells contain a small (normal) amount of HER2 on the surface [8], whereas the receptor is overexpressed in SKBR3 [6] and artificially derived EMT-HER2 [7]. The representativity of the receptor on the cell surface can be tested using HER2-targeted fluorescent antibodies [20, 21], as well as ligands based on designed ankyrin repeat proteins (DARPin)s. We used the fusion protein DARPin9_29-mCherry [22], where DARPin9_29 is a targeting protein that efficiently binds to HER2, and mCherry is a red fluorescent protein that provides fluorescence of the construct in the red region of the visible spectrum.

We first stained the cell cultures separately with the **BDP-C7** dye and DARPin9_29-mCherry to estimate the level of HER2 representation on different cultures. In order to distinguish the cell cultures from each other in the green channel, the SKBR3, HeLa, and EMT-HER2 cells were treated for 2 min with a PBS solution containing 1% DMSO and **BDP-C7** at concentrations of 1, 10 and 100 nM, respectively

(Fig. 5). One can see from the overlay of cell fluorescence histograms in the green channel that, after staining with **BDP-C7**, the cultures are fairly well differentiated from each other in terms of the fluorescence signal (Fig. 5B). After staining of the cells with the DARPin9_29-mCherry protein for the HER2 tumor marker (Fig. 5C), the HeLa culture differed well from EMT-HER2 in the red channel, whereas the SKBR3 cells used by us had an intermediate fluorescence value.

To compare the representation of the HER2 tumor marker on the analyzed cultures under identical conditions, we mixed SKBR3, HeLa, and EMT-HER2 cells in one test tube and then treated them with the DARPin9_29-mCherry protein (Fig. 6). One can see that when the cells were not pretreated with **BDP-C7**, after staining, the HeLa culture containing a small amount of HER2 on its surface is partially separated from the cells that overexpress the receptor, but it is impossible to distinguish SKBR3 and EMT-HER2 from each other (Fig. 6A,B).

If the cells are labeled with **BDP-C7** before mixing (Fig. 6C), then after staining with the DARPin9_29-mCherry protein, three clearly distinguishable cell populations can be observed in the dot plot showing the level of cell fluorescence in the green and red channels (Fig. 6D). By gating these cell populations, one can determine their belonging to a particular culture according to the level of the fluorescent signal in the green channel (Fig. 6E), since each culture was labeled with a green fluorescent dye at different concentrations. In the red channel, the fluorescence level of each population can be quantified to assess the representation of the HER2 tumor marker.

We compared the results of the analysis of the HER2 representation in the tested cultures according to the data obtained in three experiments for each cell culture separately and the data obtained in one test tube after labeling the cells with **BDP-C7** (Table 1). The results were found to almost fully match. According to the data obtained, in the SKBR3 cell line, the HER2 tumor marker was an order of magnitude more abundant than in HeLa, and HER2 representation in EMT-HER2 cells was additionally 3.5-fold higher.

The developed approach allows one to mix several cell populations in one sample and analyze them in a single test tube under completely identical conditions. Therefore, the potential artifacts associated with a variation of the concentrations of the substances acting on the cell, caused by pipetting errors during sample preparation or carelessness by the experimenter, are minimized. In addition, this approach allows one to reduce the consumption of ligands to the

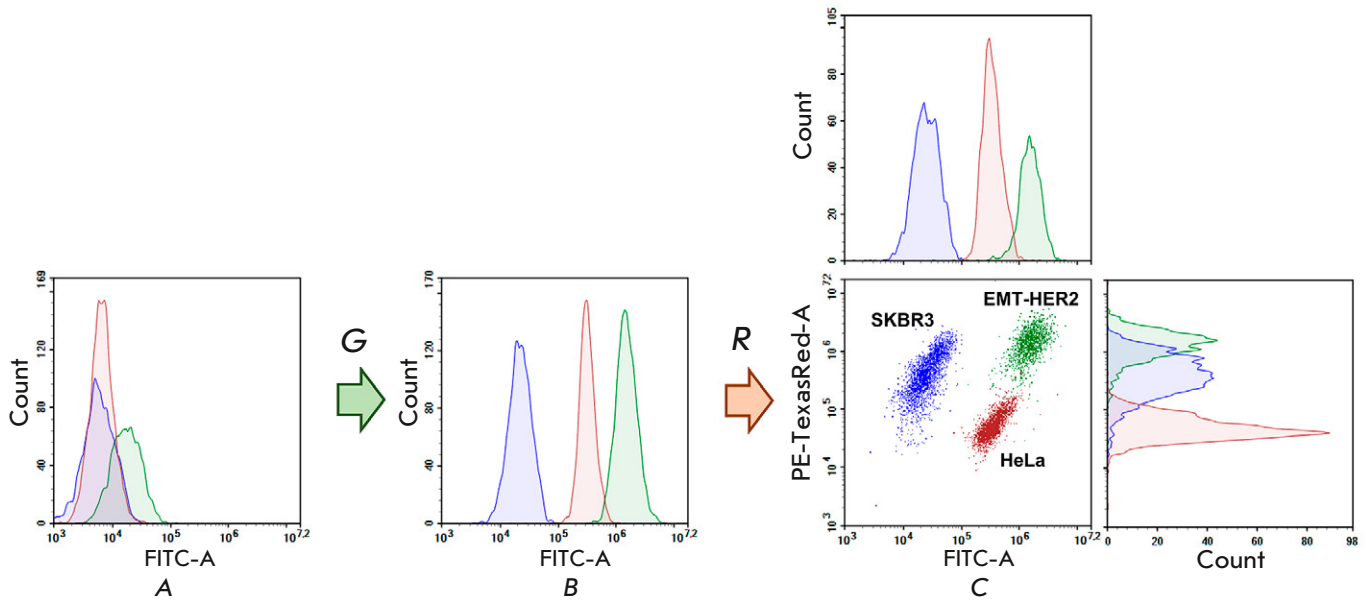


Fig. 5. Cytometric analysis of the SKBR3, HeLa, and EMT-HER2 cells, untreated (A), treated separately first with the green **BDP-C7** dye at concentrations of 1, 10, and 100 nM, respectively (B), then with red ligand to the HER2 tumor marker (DARPin9_29-mCherry, C). An overlay of the results obtained for each cell line in parallel experiments. Data for HeLa are shown in red; for SKBR3, in blue; and for EMT-HER2, in green

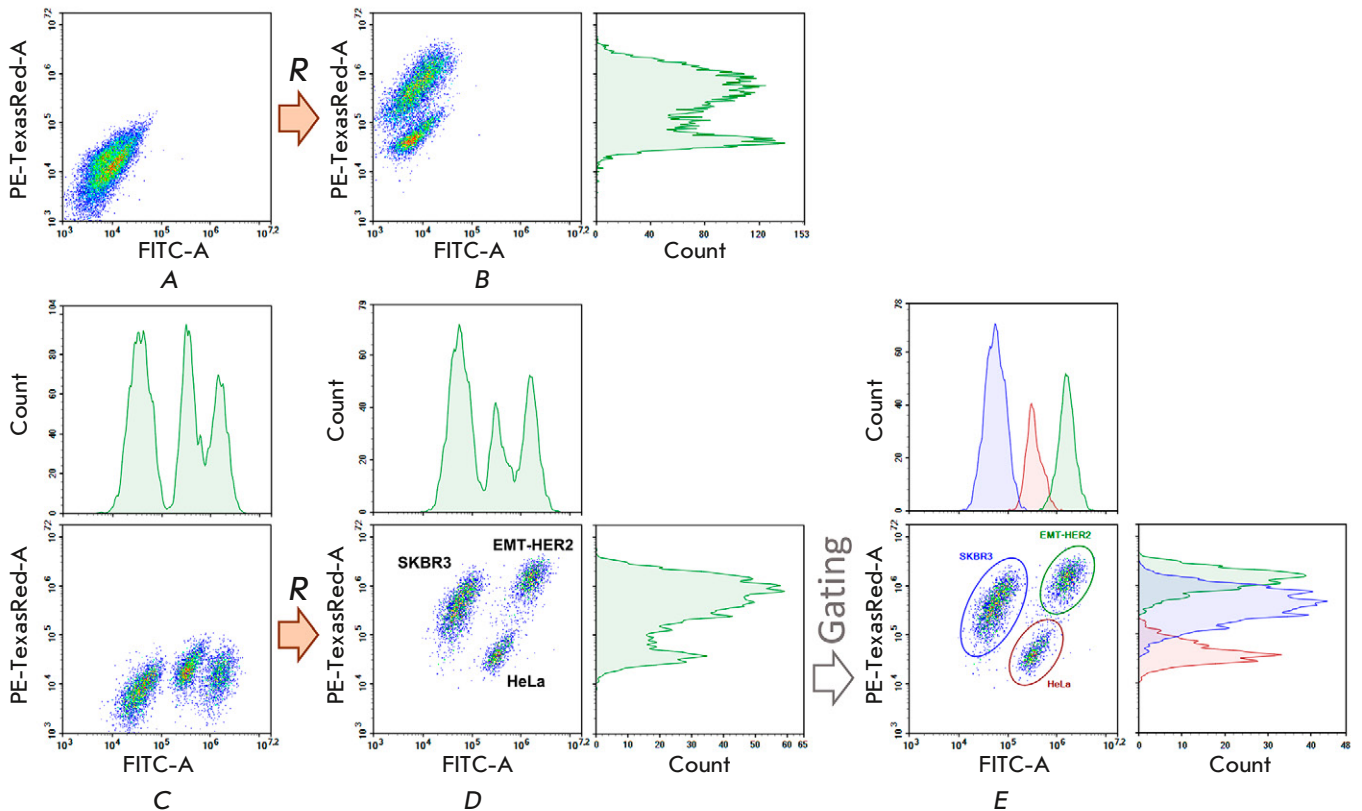


Fig. 6. Cytometric analysis of the HeLa, SKBR3, and EMT-HER2 cells mixed together before staining (A) and then treated with a red ligand to the HER2 tumor marker (DARPin9_29-mCherry, B). In (C), the cells were pre-stained with the green dye **BDP-C7** at different concentrations, washed and mixed in a single test tube, and then treated with DARPin9_29-mCherry (D). (E) – identification of individual cell populations and analysis of their fluorescence in the green (FITC) and red (PE-Texas Red) channels

analyzed cell receptors, since the assay is performed in a single test tube rather than in different ones for each cell culture. This may be relevant if the ligand is commercially unavailable or the quality of the ligand varies between batches. Our approach allows one to save time, since multiple samples can be analyzed in a single run. However, time must first be spent to fluorescently label the cells with the dye at different concentrations and adjust the concentrations, so that the cells become clearly distinguishable in the fluorescence channel of the dye. In addition, using extra dye “takes” one channel of detection.

CONCLUSION

In the present work, we have described an approach that allows one to perform a cytometric analysis of different cell cultures in a single test tube: i.e., under completely identical conditions. In this case, it is possible to analyze cells that do not initially differ in any “marker” receptors. Using the **BDP-C7** dye, the cells can be labeled in the green channel and the level of the fluorescent signal desired in each individual experiment can be adjusted.

Instead of the **BDP-C7** used in this work, other fluorescent dyes can theoretically be used. But it should be kept in mind that the dye needs to be chemically stable and bright enough to provide good contrast, be highly hydrophobic to nonspecifically bind well to the cells, and be nontoxic at the concentrations used. **BDP-C7** perfectly meets all of these requirements, while dyes containing double bonds and extended aromatic systems can be easily oxidized in cells and undergo spectral transformations due to this fact. Many

Table 1. Comparison of the results of the cytometric analysis of HER2 representation on the EMT-HER2, SKBR3 and HeLa tumor cells obtained in three independent experiments, as well as in an experiment with cell cultures pre-labeled with the **BDP-C7** dye and mixed in a single test tube

Cell culture	Parallel experiments		In a single test tube	
	MFI*	HPCV**	MFI*	HPCV**
EMT-HER2	1 410 051	61.08%	1 380 511	61.64%
SKBR3	411 140	86.96%	410 552	100.83%
HeLa	46 678	123.57%	39 616	38.15%

*MFI – median fluorescence intensity in the red channel (PE–Texas Red).

**HPCV – half-peak coefficient of variation.

$HPCV = FWHM / (2.36 \times X) \times 100\%$,

where FWHM is the full width at half maximum, X is the mean of the dataset.

polar dyes cannot accumulate well in the membrane structures of the cell and can be eliminated from the cell over time. ●

This work was supported by the Ministry of Science and Higher Education of the Russian Federation (Agreement No. 075-15-2021-1049).

REFERENCES

- Manohar S.M., Shah P., Nair A. // *Bioanalysis*. 2021. V. 13. № 3. P. 181–198.
- McKinnon K.M. // *Curr. Protoc. Immunol.* 2018. V. 120. № 1. P. 5.1.1–5.1.11.
- Pakhomov A.A., Mironiuk V.B., Kononevich Y.N., Korlyukov A.A., Volodin A.D., Pryakhina T.A., Martynov V.I., Muzafarov A.M. // *Mendeleev Commun.* 2017. V. 27. № 4. P. 363–365.
- Pakhomov A.A., Kim E.E., Kononevich Y.N., Ionov D.S., Maksimova M.A., Khalchenia V.B., Maksimov E.G., Anisimov A.A., Shchegolikhina O.I., Martynov V.I., et al. // *Dyes Pigments*. 2022. V. 203. P. 110371.
- Semenov A.N., Gvozdev D.A., Zlenko D.V., Protasova E.A., Khashimova A.R., Parshina E.Yu., Baizhumanov A.A., Lotosh N.Yu., Kim E.E., Kononevich Y.N., et al. // *Membranes*. 2022. V. 12. № 10. P. 905.
- Jost C., Schilling J., Tamaskovic R., Schwill M., Honegger A., Plückthun A. // *Structure*. 2013. V. 21. № 11. P. 1979–1991.
- Shipunova V.O., Komedchikova E.N., Kotelnikova P.A., Nikitin M.P., Deyev S.M. // *Pharmaceutics*. 2023. V. 15. № 3. P. 833.
- Tang Q., Onitsuka M., Tabata A., Tomoyasu T., Nagamune H. // *Anticancer Res.* 2018. V. 38. № 7. P. 4319–4325.
- Shipunova V.O., Komedchikova E.N., Kotelnikova P.A., Zelepukin I.V., Schulga A.A., Proshkina G.M., Shramova E.I., Kutscher H.L., Telegin G.B., Kabashin A.V., et al. // *ACS Nano*. 2020. V. 14. № 10. P. 12781–12795.
- Loudet A., Burgess K. // *Chem. Rev.* 2007. V. 107. № 11. P. 4891–4932.
- Marfin Y.S., Solomonov A.V., Timin A.S., Rummyantsev E.V. // *Curr. Med. Chem.* 2017. V. 24. № 25. P. 2745–2772.
- Martynov V.I., Pakhomov A.A. // *Russ. Chem. Rev.* 2021. V. 90. № 10. P. 1213–1262.
- Pakhomov A.A., Efremova A.V., Kononevich Y.N., Ionov D.S., Maksimova M.A., Volodin A.D., Korlyukov A.A., Dubinets N.O., Martynov V.I., Ivanov A.A., et al. // *ChemPhotoChem*. 2023. V. 7. № 5. P. e202200324.

14. Pakhomov A.A., Efremova A.V., Maksimova M.A., Kononevich Yu.N., Ionov D.S., Dubinets N.O., Martynov V.I., Muzafarov A.M., Alfimov M.V. // *High Energy Chem.* 2023. V. 57. № 3. P. 192–199.
15. Qiu B., Simon M. // *Bio-Protoc.* 2016. V. 6. № 17. P. e1912.
16. Pakhomov A.A., Deyev I.E., Ratnikova N.M., Chumakov S.P., Mironiuk V.B., Kononevich Y.N., Muzafarov A.M., Martynov V.I. // *BioTechniques.* 2017. V. 63. № 2. P. 77–80.
17. Zhu J., Tan N.K., Kikuchi K., Kaur A., New E.J. // *Anal. Sens.* 2023. P. e202300049. doi.org/10.1002/anse.202300049.
18. Pakhomov A.A., Kononevich Y.N., Stukalova M.V., Svidchenko E.A., Surin N.M., Cherkaev G.V., Shchegolikhina O.I., Martynov V.I., Muzafarov A.M. // *Tetrahedron Lett.* 2016. V. 57. № 9. P. 979–982.
19. Pakhomov A.A., Kononevich Y.N., Korlyukov A.A., Martynov V.I., Muzafarov A.M. // *Mendeleev Commun.* 2016. V. 26. № 3. P. 196–198.
20. Kuo W.-Y., Lin J.-J., Hsu H.-J., Chen H.-S., Yang A.-S., Wu C.-Y. // *Sci. Rep.* 2018. V. 8. № 1. P. 13735.
21. Swain S.M., Shastry M., Hamilton E. // *Nat. Rev. Drug Discov.* 2023. V. 22. № 2. P. 101–126.
22. Mironova K.E., Chernykh O.N., Ryabova A.V., Stremovskiy O.A., Proshkina G.M., Deyev S.M. // *Biochem. Mosc.* 2014. V. 79. № 12. P. 1391–1396.

System for Self-excited Targeted Photodynamic Therapy Based on the Multimodal Protein DARP-NanoLuc-SOPP3

E. I. Shramova¹, A. Yu. Frolova¹, V. P. Filimonova¹, S. M. Deyev^{1,2,3}, G. M. Proshkina^{1*}

¹Shemyakin-Ovchinnikov Institute of Bioorganic Chemistry, Moscow, Russian Academy of science, Moscow, 117997 Russian Federation

²"Biomarker" Research Laboratory, Institute of Fundamental Medicine and Biology, Kazan Federal University, Kazan, 420008 Russian Federation

³Sechenov First Moscow State Medical University (Sechenov University), Moscow, 119991 Russian Federation

*E-mail: gmb@ibch.ru

Received: November 20, 2023; in final form, November 28, 2023

DOI: 10.32607/actanaturae.27331

Copyright © 2023 National Research University Higher School of Economics. This is an open access article distributed under the Creative Commons Attribution License, which permits unrestricted use, distribution, and reproduction in any medium, provided the original work is properly cited.

ABSTRACT Despite the significant potential of photodynamic therapy (PDT) as a minimally invasive treatment modality, the use of this method in oncology has remained limited due to two serious problems: 1) limited penetration of the excitation light in tissues, which makes it impossible to affect deep-seated tumors and 2) use of chemical photosensitizers that slowly degrade in the body and cause photodermatoses and hyperthermia in patients. To solve these problems, we propose a fully biocompatible targeted system for PDT that does not require an external light source. The proposed system is based on bioluminescent resonance energy transfer (BRET) from the oxidized form of the luciferase substrate to the photosensitizing protein SOPP3. The BRET-activated system is composed of the multimodal protein DARP-NanoLuc-SOPP3, which contains a BRET pair NanoLuc-SOPP3 and a targeting module DARPIn. The latter provides the interaction of the multimodal protein with tumors overexpressing tumor-associated antigen HER2 (human epidermal growth factor receptor type II). *In vitro* experiments in a 2D monolayer cell culture and a 3D spheroid model have confirmed HER2-specific photo-induced cytotoxicity of the system without the use of an external light source; in addition, experiments in animals with subcutaneous HER2-positive tumors have shown selective accumulation of DARP-NanoLuc-SOPP3 on the tumor site. The fully biocompatible system for targeted BRET-induced therapy proposed in this work makes it possible to overcome the following limitations: 1) the need to use an external light source and 2) the side phototoxic effect from aberrant accumulation of chemical photosensitizers. The obtained results demonstrate that the fully protein-based self-excited BRET system has a high potential for targeted PDT.

KEYWORDS bioluminescent resonance energy transfer, targeted photodynamic therapy.

ABBREVIATIONS BRET – bioluminescent resonance energy transfer; HER2 – human epidermal growth factor receptor type II; PDT – photodynamic therapy; PS – photosensitizer.

INTRODUCTION

To date, photodynamic therapy (PDT) is widely used in oncology to treat inoperable tumors, skin and retinal cancer, as well as to irradiate the surface epithelium of organs accessible to catheters and endoscopes [1–3]. The key components of PDT are a photosensitizer (PS), excitation light of a certain wavelength, and molecular oxygen. PS photoexcitation in the presence of molecular oxygen generates singlet oxygen and/or free radicals, causing oxidative stress, followed by cell

apoptosis/necrosis [4]. The obvious advantages of PDT compared to other oncology methods include low general toxicity, minimal invasiveness, and high selectivity. Low invasiveness and high selectivity are achieved by a combination of two factors: 1) the photosensitizer is activated only by light of a certain wavelength, and 2) reactive oxygen species (ROS), which have a short lifetime and thus limited diffusion in the cell, are generated in the immediate proximity to the excited PS, resulting in localized cell death. That is the

reason why PDT is considered one of the most attractive photon-based methods for tumor therapy. While effectively treating the tumor, PDT remains a gentle approach in terms of its general effects on the body.

However, PDT has two significant limitations: 1) limited penetration depth (1–2 mm) of the excitation visible/near-infrared light (400–900 nm) in tissues due to light scattering by cellular structures [5], and 2) daylight-induced phototoxicity of chemical PS due to their slow biodegradation in the human body and accumulation in the skin. PS based on tetrapyrrole drugs (porphyrins and chlorins) and aminolevulinic acid approved for clinical use are known to accumulate in a patient's tissues, causing sunlight-induced photodermatoses and hyperthermia [6, 7].

In order to address the problem of limited penetration of excitation light into the body, approaches based on the use of self-excited PDT systems are actively being developed in experimental oncology [8]. These systems are based on bioluminescence resonance energy transfer (BRET) from an oxidized form of the luciferase substrate (donor) to a PS (acceptor). A number of systems for BRET-activated PDT based on chemical PS conjugates with luciferase that demonstrated their effectiveness in *in vivo* studies have been developed over the past ten years [9–14].

A new area of BRET-activated PDT is the development of systems based on biocompatible materials such as the ones using genetic hybrids of luciferases and protein phototoxins. Currently, only three systems demonstrating a possibility to use biomaterials for BRET-activated PDT are available.

In 2020, Kim E. et al. developed BRET-induced systems based on hybrids of RLuc luciferase and phototoxin proteins (KillerRed and miniSOG) [15]. A specific effect of the BRET-induced system on cancer cells is due to the presence of the lead peptide WLEAAYQRFL, which is specific to the integrin b1 receptor (ITGb1), in the luciferase-phototoxin protein molecule. In the absence of an external light source, the specific BRET-induced effect of this system was demonstrated in both primary tumor cells obtained from breast cancer patients and mouse xenograft tumor models.

In 2022, we proposed a fully genetically encoded BRET-induced system for PDT of deep-seated tumors [16]. The genetically engineered luciferase NanoLuc [17], used as an internal light source, and the phototoxic flavoprotein miniSOG [18], which acts as a ROS generator, were combined into one genetic construct. Using pseudotyped lentiviruses specific to the HER2 tumor marker, we have demonstrated the possibility of targeted delivery of the developed genetic construct directly inside tumor cells in the animal. We

managed to inhibit the growth of both the primary tumor site and metastases. Being genetically encoded, this construct can be delivered to tumors located at any depth in the body. Later, using the phototoxic protein SOPP3 [19] (a miniSOG analogue, characterized by a high quantum yield of singlet oxygen generation), we developed a targeted system for delivery of the BRET-activated protein pair NanoLuc–SOPP3 as part of HER2-specific liposomes. We demonstrated the effectiveness of this system in both subcutaneous xenograft tumor and deep-seated disseminated intraperitoneal tumor models [20].

Apparently, the development of BRET-induced systems based on fully biocompatible and biodegradable materials allows for overcoming the problem of both excitation light delivery into deep tissues and chemical PS toxicity.

In this work, we propose the use of the multimodal targeting protein DARP–NanoLuc–SOPP3, which contains, in addition to the BRET pair NanoLuc–SOPP3, the targeting module DARPIn. The latter ensures protein tropism for tumor-associated antigens of human breast and ovarian cancers. Using a 3D spheroid model, we showed that DARP–NanoLuc–SOPP3 can be used for targeted BRET-induced PDT. The experimental scheme is presented in *Fig. 1*.

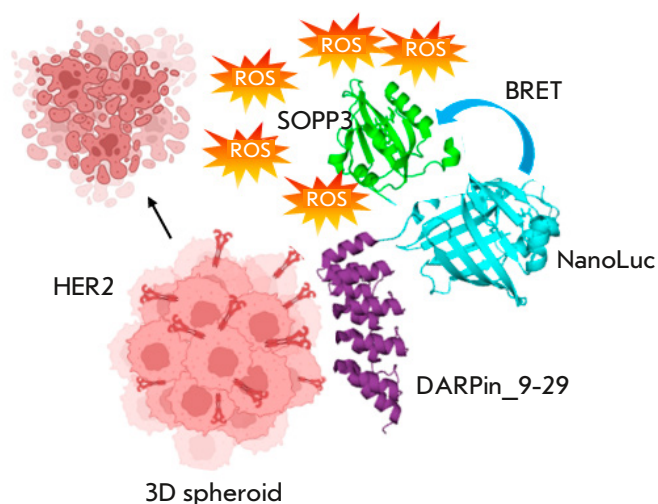


Fig. 1. System based on the multimodal protein DARP–NanoLuc–SOPP3 for targeted BRET-induced PDT. DARPIn provides binding of the NanoLuc–SOPP3 BRET pair to the HER2 receptors on the surface of cancer cells in the spheroid. Non-radiative energy transfer (BRET) from the oxidized substrate to the photosensitizing protein SOPP3 takes place in the presence of a luciferase substrate. Part of the energy is utilized for the production of reactive oxygen species (ROS), leading to cancer cell death. The illustration was generated using BioRender.com (<https://www.biorender.com>)

EXPERIMENTAL

Cloning of *DARP-NanoLuc-SOPP3*

The cloning sequence of *DARPin*₉₋₂₉ was amplified from the plasmid pET22-DARP-mCherry [21] using a set of specific primers T7 forward (5'-TAA TAC GAC TCA CTA TAG GG-3') and Dp-nano-rev (5'-GTG AAG AAG ACC ATC ATC GCG GCG CCA CCA CCA CTG CTC CCG GG-3'). The coding sequence of the NanoLuc luciferase gene was amplified from the plasmid pNL1.1.CMV (Promega) using a set of specific primers Dp-nano-dir (5'-GT GGT GGC GCG ATG GTC TTC ACA CTC GAA GAT-3') and Nano-G4S-Bam-rev (5'-GTA CGG ATC CGC TCC CTC CGC CAC CCG CCA GAA TGC GTT CGC ACA G-3'). The 5'-regions of primers Dp-nano-dir and Dp-nano-rev are mutually complementary, which allows for ligation of *DARPin*₉₋₂₉ and NanoLuc coding sequences during amplification. The PCR fragment encoding *DARP-NanoLuc* was treated with the restriction enzymes NdeI/BamHI and cloned into the pET24 vector, pretreated with the same restriction enzymes. The *SOPP3* coding sequence was amplified from the plasmid pET24-SOPP3 (kindly provided by A.A. Pakhomov, Institute of Bioorganic Chemistry of the Russian Academy of Sciences) using the specific primers mS-Bam-dir (5'-CAT CAC GGA TCC GAA AAG AGC TTT GTG ATT ACC-3') and mS-Hind-rev (5'-GTA CAA GCT TGC CAT CAA CCT GCA CAC CAA T-3'). The resulting PCR fragment was treated with the restriction enzymes BamHI/HindIII and ligated to vector pET24-DARP-NanoLuc, pretreated with the same set of restriction enzymes. The correct sequence of the resulting final construct was confirmed by sequencing. The coding sequence of *DARP-NanoLuc-SOPP3* corresponds to the protein with the following primary structure:

```
MDLGKKLLEAARAGQDDEVRLMANGAD
VNAHDFYGITPLHLAANFGHLEIVEVLLKH
GADVNAFDYDNTPLHLAADAGHLEIVEVL
LKYGADVNASDRDGHTPLHLAAREGHLEI
VEVLLKNGADVNAQDKFGKTAFDISIDNG
NEDLAEILQEFKPKSTPPGSSGGAMVFTLE
DFVGDWRQTAGYNLDQVLEQGGVSSLFQN
LGVSVTPIQRIVLSGENGLKIDIHVIIPYEG
SGDQMGQIEKIFKVVPVDDHHFKVILHY
GTLVIDGVTPNMIDYFGRPYEGIAVFDGKK
ITVTGTLWNGNKIIDERLINPDGSLFRVTI
NGVTGWRLCERILAGGGGSGSEKSFVITDP
RLPDNPIIFASDGFLLELTEYSREEILGRNGR
FLQGPETDQATVQKIRDAIRDQREITVQLIN
YTKSGKKFLNLLNLQPIRDQKGELQAFIGV
QVDGKLAAALEHHHHHHH.
```

***DARP-NanoLuc-SOPP3* expression**

The target protein gene was expressed in the Rosetta(DE3) *Escherichia coli* strain, transformed with plasmid pET24-DARP-NLuc-SOPP3. Transformants were grown in a liquid LB medium in the presence of kanamycin and chloramphenicol (30 and 34 µg/ml, respectively) at 37°C with aeration until the culture reached an optical density OD600 of 0.6–0.8. Gene expression was induced by adding isopropyl-β-D-1-thiogalactopyranoside (IPTG) to a final concentration of 0.4 mM. After addition of IPTG, the cells were grown at 37°C for 4 h and then incubated at 18°C overnight. The cell suspension was pelleted by centrifugation at 4,000 *g* for 10 min at room temperature. The resulting pellets were stored at -20°C. To isolate the protein, the cells were thawed and re-suspended in wash buffer (50 mM Tris-HCl, 500 mM NaCl, and 10 mM imidazole; pH 8.0). The cells were disrupted by sonication in an ultrasonic disintegrator Sonopuls HD 3100 (Bandeline, Germany) using the following mode: ultrasonic treatment for 10 seconds and cooling for 10 seconds; 5 cycles in total. The clarified cell lysate was obtained by centrifugation at 20,000 *g* and 4°C for 30 min. The supernatant was applied to a Ni-NTA Agarose column (Qiagen) pre-equilibrated with the wash buffer. The column was washed with a 5-fold volume of wash buffer, and the protein was eluted with a buffer containing 50 mM Tris-HCl, 500 mM NaCl, and 500 mM imidazole (pH 8.0).

Assessment of bioluminescence resonance energy transfer

In order to evaluate the effectiveness of BRET from the donor to the acceptor in the *DARP-NanoLuc-SOPP3* system, we measured the luminescence spectra of the *DARP-NanoLuc-SOPP3* and NanoLuc proteins in the presence of 10 µM furimazine. Measurements were conducted using an Infinite M1000 Pro plate reader (Tecan, Austria) in the wavelength range of 400–600 nm with a step of 2 nm and an integral time of 10 ms. The BRET value was calculated as the ratio of the energy emitted by the acceptor (*DARP-NanoLuc-SOPP3*) to that of the donor (NanoLuc). Due to the overlap of the emission spectra of the donor and acceptor, determination of the energy transfer efficiency requires the subtraction of signals resulting from emission of the donor in the absence of the acceptor [22–25]. Thus, the efficiency of energy transfer is the ratio of the donor-acceptor system (*DARP-NanoLuc-miniSOG* protein) emission at the wavelength of the acceptor emission maximum to the emission of the system at the wavelength of the donor emission maximum, with subtraction of the

same ratio by detecting the emission spectrum of a free donor (NanoLuc protein).

$$BRET\ VALUE = \frac{E_{DARP-NanoLuc-SOPP3(\lambda_{max\ acceptor})}}{E_{DARP-NanoLuc-SOPP3(\lambda_{max\ donor})}} - \frac{E_{NanoLuc(\lambda_{max\ acceptor})}}{E_{NanoLuc(\lambda_{max\ donor})}}$$

Cell cultures

The following cells were used in the study: HEK293T (cells that are easy to transfect) expressing the SV40 T-antigen derived from human embryonic kidney cells, SKOV3 (human ovarian carcinoma), SKOV3.ip1-Kat (cells stably expressing the far-red fluorescent protein TurboFP635), the original parental line SKOV3.ip1 (cell line isolated from intraperitoneal ascites of immunodeficient mice that were intraperitoneally injected with human ovarian adenocarcinoma SKOV3 cells), EA.hy926 (hybrid cells based on primary human umbilical vein cells and human lung adenocarcinoma A549 cells), BJ-5TA (immortalized hTERT fibroblasts derived from human foreskin cells), and HeLa (cervical carcinoma) cells. The cells were cultured under standard conditions (in a humidified atmosphere with 5% CO₂ at 37°C) in either a RPMI 1640 or DMEM medium (PanEco, Russia) supplemented with 2 mM L-glutamine (PanEco), 10% fetal bovine serum (Gibco), and an antibiotic (10 U/ml penicillin, 10 µg/ml streptomycin; PanEco).

Production of cells stably expressing GFP

A day before transfection, HEK293T cells were seeded into a 6-well plate at a concentration of 0.6×10^6 cells/ml in a complete growth medium without the antibiotic. On the day of transfection, the growth medium was replaced with a serum- and antibiotic-free medium. The third-generation lentiviral plasmids pMDLg/pPRE, pRSV-Rev, and pCMV-VSV-G, as well as the reporter plasmid pWPT-GFP, were mixed at a ratio of 2:1:0.4:2 in a serum- and antibiotic-free medium. A total of 2 µg of pMDLg/pPRE, 1 µg of pRSV-Rev, 0.4 µg of pCMV-VSV-G, and 2 µg of pWPT-GFP were added per well of a 6-well plate. The TransIntro® PL Transfection reagent (TransGen Biotech, China) was added to the DNA solution at a volume of 20 µl, mixed gently, and incubated at room temperature for 15 min. DNA-liposome complexes were added to the cells. The cells were incubated for 4–6 h. The medium was replaced with a complete culture medium. Viral particles were collected after 24, 48, and 72 h, pooled and centrifuged (10 min; 500 g). Viruses were added to ~70% monolayer EA.hy926 and BJ-5TA cells. The cells were centrifuged (in plates) for 90 min at 1,200 g in the presence of 8 µg/ml polybrene. The me-

dium containing lentiviral particles was replaced with a fresh complete growth medium after 7 h. GFP fluorescence was assessed using an Axiovert 200M fluorescence microscope (Carl Zeiss, Germany) and flow cytometry after 72 h.

Conjugation of DARP-NanoLuc-SOPP3 with fluorescent dyes

SOPP3 is a weak fluorophore. In order to visualize DARP-NanoLuc-SOPP3 by flow cytometry and confocal microscopy, it was conjugated with N-hydroxysuccinimide esters of dyes (AF488 and Cy5.5; Lumiprobe, Russia). Conjugation was conducted in 20 mM phosphate buffer (pH 8.0) in the presence of a 10-fold molar dye excess. The reaction was carried out for 1 h at room temperature. The protein-dye conjugate was purified from the unreacted dye by gel permeation chromatography on a Sephadex G25 column (Cytiva).

Flow cytometry analysis

GFP expression in EA.hy926 and BJ-5TA cells after lentiviral transduction and functional activity of the HER2-specific module in the DARP-NanoLuc-SOPP3 protein were determined using flow cytometry on a NovoCyte 3000 Flow Cytometer (AceaBio, USA). For this, the cells (EA.hy926, EA.hy926-GFP, BJ-5TA, BJ-5TA-GFP, and SKOV3.ip1-Kat) were removed from the plates using Versene solution (PanEco), washed with phosphate-buffered saline, and analyzed.

To assess the ability of DARP-NanoLuc-SOPP3 to bind the HER2 receptor, the cells (HER2-positive SKOV3.ip1-Kat cells, cervical cancer HeLa cells with normal HER2 expression levels, endothelial EA.hy926 cells, and stromal BJ-5TA cells) were incubated with a 300 nM DARP-NanoLuc-SOPP3-AF488 conjugate in a complete growth medium for 10 min at 37°C. The cells were washed thrice with phosphate-buffered saline and analyzed on a NovoCyte 3000 Flow Cytometer.

GFP and AF488 fluorescence was excited by a 488 nm laser and detected in the 530 ± 30 nm channel (FITC channel).

Confocal microscopy

The binding of the targeting module in DARP-NanoLuc-SOPP3 to the HER2 receptor on the surface of SKOV3.ip1 cells, which are characterized by overexpression of this receptor, was studied using confocal microscopy. Approximately 3,500 SKOV3.ip1 cells were seeded into 96-well glass bottom plates (Eppendorf) and cultured overnight. The 250 nM DARP-NanoLuc-SOPP3-Cy5.5 conjugate (based on the dye concentration) was added to the cells on the

next day. The cells were incubated with the conjugate for 20 min and 180 min. Nuclei were stained with 10 nM Hoechst 33342 at 37°C for 10 min. The cells were washed thrice with phosphate-buffered saline, supplemented with a FluoroBrite medium (Gibco), and analyzed using an LSM 980 confocal microscope (Carl Zeiss) and a 63× Plan Apochromat oil immersion lens. A 405-nm laser was used to excite Hoechst 33342; the dye fluorescence was detected at 410–520 nm. Cy5.5 was excited with a 639-nm laser and detected at 642–755 nm.

Spheroids were analyzed using a LSM 980 confocal microscope and a ×10 dry objective in the Z-stack mode. TurboFP635 was excited with a 543-nm laser and detected in the 642- to 755-nm range. GFP was excited with a 488-nm laser and detected at 497–562 nm.

Generation of 3D spheroids

The 3D spheroids were grown using an anti-adhesive agarose substrate as described in [26], with modifications. In short, 81-well agarose molds were prepared from 1% of the agarose melted in phosphate-buffered saline and placed into 12-well plates. SKOV3.ip1-Kat, EA.hy926, and BJ-5TA cells were removed from the wells, washed in the culture medium, and counted. To obtain spheroids from a single cell type, 150 µl of the cell suspension containing 10⁶ SKOV3.ip1-Kat cells were layered into each agarose mold. To obtain spheroids consisting of different cell types (epithelial, endothelial, and stromal cells), 150 µl of a suspension containing 5 × 10⁵ SKOV3.ip1-Kat cells, 2.5 × 10⁵ EA.hy926 cells, and 2.5 × 10⁵ BJ-5TA cells was layered into each agarose gel well. A complete culture medium was added to the agarose molds. The plates were centrifuged at 100 *g* for 1 min to sediment the cells to the bottom of the agarose mold. The period of spheroid formation was two days.

Analysis of the BRET-induced cytotoxicity of DARP-NanoLuc-SOPP3 in the monolayer (2D) cell culture and spheroids (3D culture)

To assess the BRET-induced cytotoxicity of DARP-NanoLuc-SOPP3 in the SKOV3.ip1-Kat, EA.hy926, and BJ-5TA monolayers, the cells were seeded in 96-well plates at a density of 35,000 cells/ml (SKOV3.ip1-Kat) and 25,000 cells/ml (EA.hy926 and BJ-5TA). The cells were cultured overnight under standard conditions. Different concentrations of DARP-NanoLuc-SOPP3 were added to the cells (0–1.8 µM). The cells were incubated with the protein for 20 min, and a luciferase substrate solution (30 µM) was added to the wells. The cells were incubated for 72 h under standard conditions. Cytotoxicity was an-

alyzed using the MTT assay. The assay is based on the ability of mitochondrial dehydrogenases to convert the water-soluble tetrazolium dye 3-(4,5-dimethylthiazol-2-yl)-2,5-diphenyltetrazolium bromide into formazan, which crystallizes in cells and has a purple color [27]. The culture medium was removed from the wells of a 96-well plate, and 100 µl (0.5 g/l) of a MTT solution (PanEco) was added to each well. The plates were incubated at 37°C for 1 h; the medium was removed, and the resulting formazan crystals were dissolved in DMSO (100 µl/well).

Spheroids grown for two days were used to assess the BRET-induced cytotoxicity of DARP-NanoLuc-SOPP3 in the 3D culture. On the day of the experiment, different concentrations of DARP-NanoLuc-SOPP3 (0–20 µM) were added to the cells. After 2 h of incubation, 30 µM furimazine was added into each well and the cells were incubated for 72 h under standard conditions. For cytotoxicity evaluation, each spheroid in a 10 µl agarose mold volume was placed into a well of the 96-well plate. A total of 90 µL of the MTT solution were added per well to a final concentration of 0.5 g/L. The plates were incubated at 37°C for 1 h. After the end of the incubation, the MTT solution was carefully removed using a pipette and formazan crystals were dissolved in DMSO (100 µL/well).

The absorbance of the formazan solution was measured at 570 nm using an Infinite M100 Pro plate reader (Tecan). Relative cell viability was calculated based on the ratio of absorption in experimental and control wells. The well with cells treated with 30 µM of the luciferase substrate solution was used as the control well. The DARP-NanoLuc-SOPP3 concentration causing growth inhibition of 50% of the cells in the population (IC₅₀) was calculated using the GraphPad Prism software (version 9.4.0; California, USA).

Analysis of DARP-NanoLuc-SOPP3 accumulation in HER2-positive xenograft tumor *in vivo*

The experiment on the animals was approved by the Commission of Animal Control and Welfare of the Shemyakin–Ovchinnikov Institute of Bioorganic Chemistry of the Russian Academy of Sciences (protocol 368/2022; December 19, 2022). Female Balb/c Nude mice (eight weeks old) were purchased from the Pushchino Nursery, which supplies specific pathogen-free (SPF) animals. The animals were kept in sterile conditions with unlimited access to sterile food and water.

To obtain a HER2-positive subcutaneous xenograft model, a suspension of SKOV3 cells (2 × 10⁶ cells) in a 30% Matrigel growth substrate

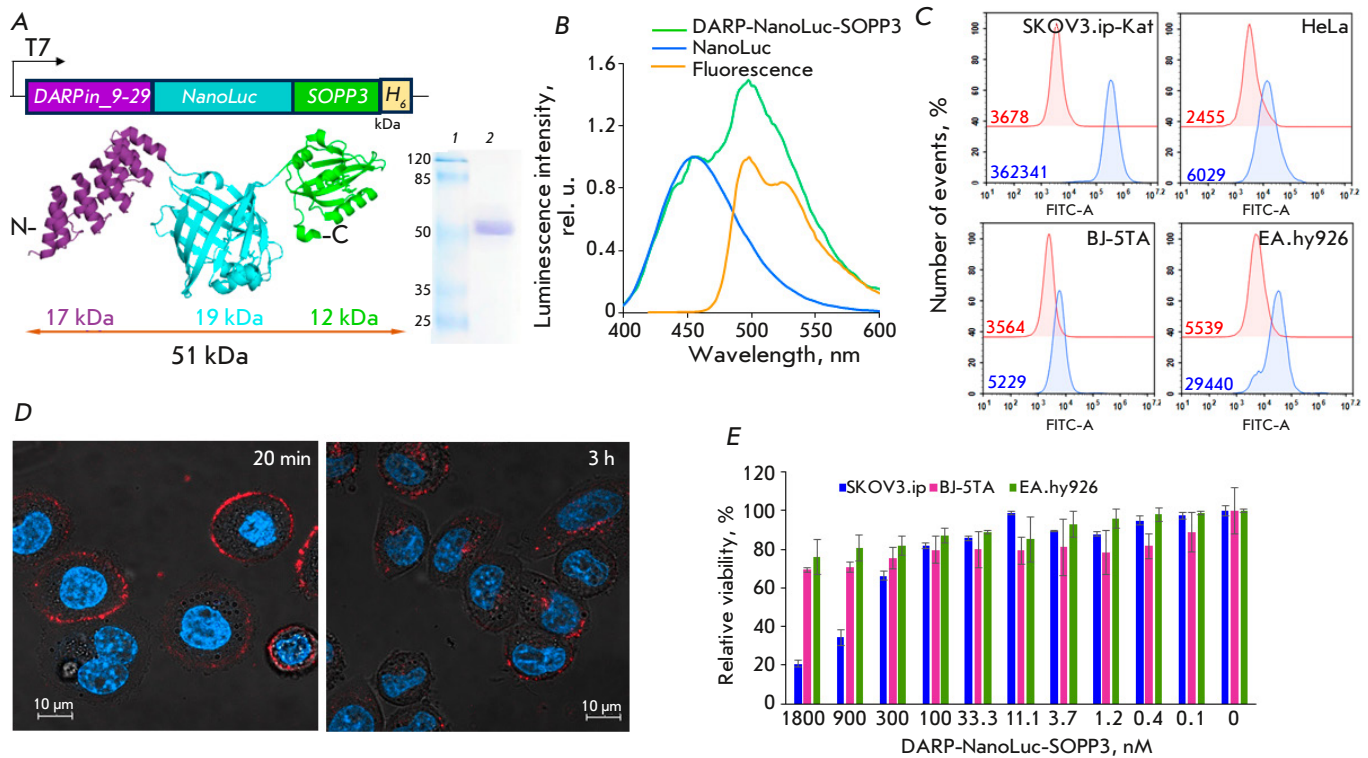


Fig. 2. System based on the multimodular protein DARP-NanoLuc-SOPP3 for targeted BRET-induced PDT: *in vitro* characterization. (A) – Schematic presentation of genetic and protein DARP-NanoLuc-SOPP3 constructs. An electropherogram of a purified protein is presented to the right of the diagram. Lane 1 is a molecular weight standard; lane 2 is DARP-NanoLuc-SOPP3. (B) – Normalized luminescence spectra of NanoLuc (blue curve) and DARP-NanoLuc-SOPP3 (green curve) in the presence of 10 μ M furimazine. The orange curve corresponds to the normalized fluorescence spectrum of DARP-NanoLuc-SOPP3-FITC under 460-nm laser excitation. (C) – receptor-specific interaction of DARP-NanoLuc-SOPP3-FITC with cells expressing the HER2 receptor at different levels. Flow cytometry data for the fluorescein 5-isothiocyanate (FITC, λ_{ex} = 488 nm, λ_{em} = 530 \pm 30 nm) fluorescence channel is presented. Red lines in the pictograms correspond to fluorescently unlabeled cells (control); blue lines correspond to cells treated with DARP-NanoLuc-SOPP3-FITC. Figures in the pictograms correspond to the median fluorescence intensity. (D) – merged confocal images of SKOV3.ip1 cells in the blue and red fluorescence channels after incubation with DARP-NanoLuc-SOPP3-Cy5.5 for 20 minutes and 3 h. Nuclei are stained with Hoechst 33342. (E) – *in vitro* BRET-induced cytotoxicity of DARP-NanoLuc-SOPP3 in the presence of 30 μ M furimazine. Data are presented for SKOV3.ip1, EA.hy926, and BJ-5TA cells. The scale bar in confocal images corresponds to 10 μ m

(Corning) was inoculated subcutaneously into the right flank of mice. DARP-NanoLuc-SOPP3 biodistribution in the animal body was studied once the tumor reached 200 mm³ in volume. Approximately three weeks after tumor inoculation, 100 μ l of a 40 μ M DARP-NanoLuc-SOPP3-Cy5.5 conjugate (based on the dye concentration) were injected into the retro-orbital sinus. The distribution of DARP-NanoLuc-SOPP3-Cy5.5 in the animal was assessed using the IVIS Spectrum In Vivo Imaging System (PerkinElmer, USA). The excitation/emission parameters for imaging were as follows: 640/680, 640/700, 640/720, 640/740, 640/760, 640/780, 675/720,

675/740, 675/760, 675/780, 710 /760, and 710/700 nm. Separation of the spectral image data was carried out using the IVIS Spectrum software.

RESULTS AND DISCUSSION

Production of the DARP-NanoLuc-SOPP3 protein for targeted BRET-induced PDT and its functional characterization in the 2D culture

To develop a targeted, fully protein-based BRET-induced system, we obtained a genetic construct encoding a targeting module specific to the HER2 tumor marker, a NanoLuc luciferase gene, and the phototoxic

protein SOPP3 gene within one reading frame (*Fig. 2*). The HER2-specific protein of non-immunoglobulin scaffold DARPin_9-29, which has high affinity for the HER2 receptor (1 nM) [28], was used as a targeting molecule. HER2 is a tumor-associated antigen whose overexpression is characteristic of numerous human tumors: breast, lung, gastric, ovarian, and prostate cancers [29, 30].

The genetic construct coding DARPin-NanoLuc-SOPP3 was obtained as described in the Experimental Section (*Fig. 2A*). DARPin-NanoLuc-SOPP3 was purified by metal-chelate affinity chromatography. A denaturing polyacrylamide gel electrophoresis shows that the isolated protein has the corresponding molecular weight: 51 kDa (*Fig. 2A*). The functional activity of the phototoxic module SOPP3 in the DARPin-NanoLuc-SOPP3 hybrid construct was assessed based on the fluorescence spectrum, which fully corresponds to the published data [19] (*Fig. 2B*). BRET effectiveness of the DARPin-NanoLuc-SOPP3 system was determined based on the luminescent spectra of the proteins DARPin-NanoLuc-SOPP3 and NanoLuc obtained in the presence of the luciferase substrate furimazine (*Fig. 2B*). The resulting BRET value is 1.14, which is consistent with our previous data for NanoLuc-SOPP3 [20].

The functional activity of the DARPin targeting module in the hybrid protein was assessed based on DARPin-NanoLuc-SOPP3's ability to interact with HER2 on the cancer cell surface. For this, DARPin-NanoLuc-SOPP3 was conjugated to a fluorescent dye (as described in the Experimental Section). Binding of the fluorescent conjugate to HER2 was studied using flow cytometry and confocal microscopy. *Figure 2C* shows that DARPin-NanoLuc-SOPP3 exhibits highly specific binding to SKOV3.ip-Kat cells characterized by HER2 overexpression, which is evidenced by a ~100-fold shift in the median fluorescence of conjugate-treated cells compared to the control. On the contrary, only a slight shift in the median fluorescence (2.5–5-fold) is observed in both epithelial HeLa cells, which are characterized by a normal HER2 expression level, and HER2-negative stromal cells (EA.hy926 and BJ5-TA) (*Fig. 2C*). Confocal microscopy showed that DARPin-NanoLuc-SOPP3-Cy5.5 effectively binds to the SKOV3.ip1 cell membrane surface during 30 min (*Fig. 2D*). Further incubation leads to DARPin-NanoLuc-SOPP3 internalization. The entire protein is internalized in the cells after three hours of incubation, as evidenced by the presence of red pixels in the cytoplasmic region in the images (*Fig. 2D*). An analysis of BRET-induced cytotoxicity in the monolayer (2D) culture of HER2-positive SKOV3.ip1 cells demonstrated that DARPin-NanoLuc-SOPP3

causes a phototoxic effect in the presence of furimazine with an IC_{50} of 588.6 nM, as calculated using the GraphPad Prism software.

Functional characterization of DARPin-NanoLuc-SOPP3 in the 3D culture

The 2D models are not the optimal system for assessing drug cytotoxicity, since they do not take into account many characteristics of the tumor in the body. This is because the tumor has a three-dimensional structure; hence, such parameters as the molecular oxygen gradient, nutrients and metabolites, the presence of intercellular contacts with the cell matrix and stromal cells cannot be taken into consideration in a 2D model. It is the specific tumor microenvironment that eventually determines the metabolism heterogeneity, gene expression pattern, and, thus, the resistance of cancer cells to therapeutic drugs. Human cancer 3D models, or spheroids, provide a better platform for studying drug efficacy compared to the conventional 2D culture by reproducing important aspects of the tumor microenvironment that are the closest to *in vivo* models. This is the reason why we assessed the BRET-induced cytotoxicity of DARPin-NanoLuc-SOPP3 in a culture of spheroids composed of ovarian cancer cells (SKOV3.ip1) and stroma cells presented by modified human umbilical vein EA.hy926 cells and modified fibroblast BJ-5TA cells.

In order to analyze the spheroid structure by confocal microscopy, EA.hy926 and BJ-5TA cells stably expressing *GFP* were generated using lentiviral transduction. The transduction efficiency was evaluated using flow cytometry. *Figure 3A* shows that the *GFP* transduction level in EA.hy926 and BJ-5TA cells was 98.33 and 75.87%, respectively.

Cell viability in the spheroids was determined by estimating the number of dead cells in the culture using propidium iodide staining and flow cytometry. SKOV3.ip1-Kat, EA.hy926-GFP, and BJ-5TA-GFP cell spheroids were used in the experiment. The original cell lines were used as controls. Spheroids were lysed using trypsin on day 5 of growth and then stained with propidium iodide. Fluorescence was measured in the propidium iodide channel. *Figure 3B* demonstrates that the number of dead cells in the spheroids is similar to that of dead cells in the original cell cultures on the corresponding day of cultivation with the same number of analyzed cells.

The spheroids were formed as described in the Experimental Section. *Figure 3C* shows that the resulting structures have the morphology of spheroids with a developed stromal network (green strands). Spheroids significantly increase in volume during cul-

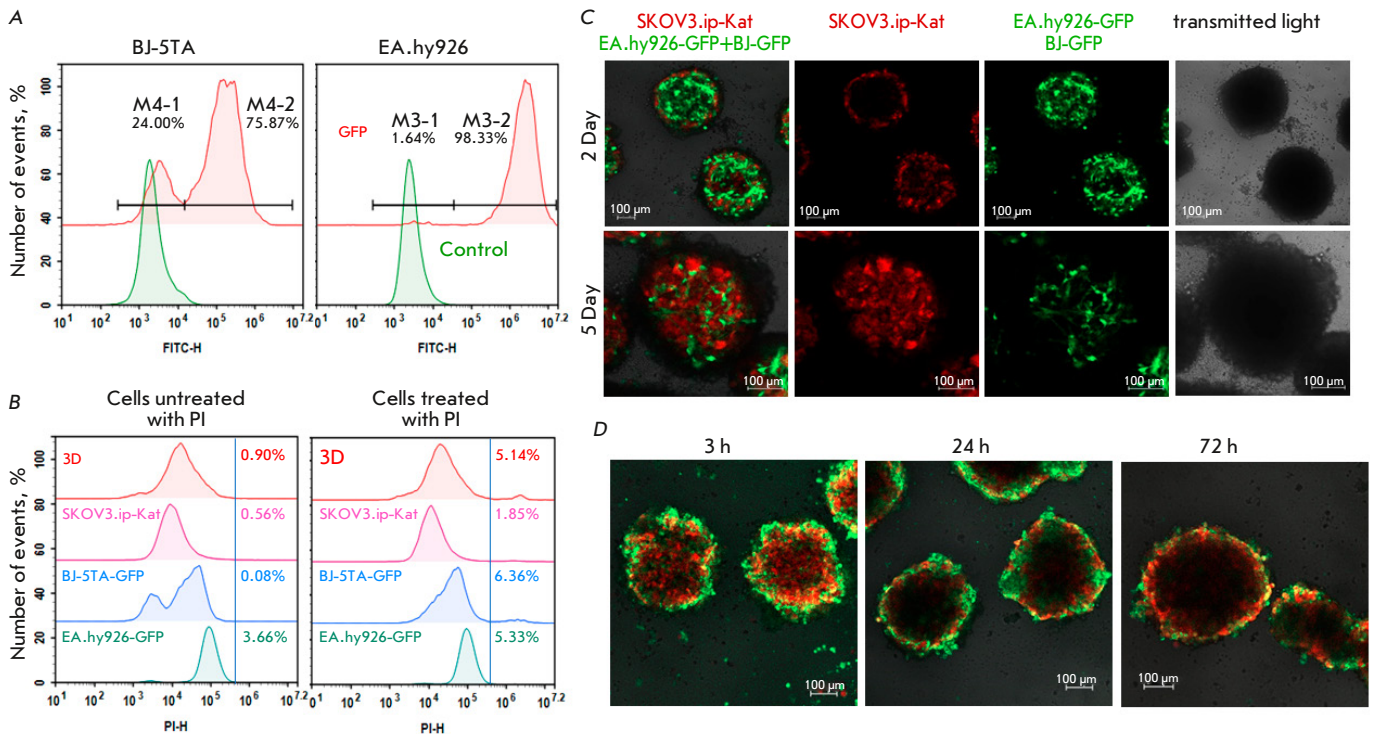


Fig. 3. Functional characterization of DARP-NanoLuc-SOPP3 in the 3D culture. (A) – Efficiency of the lentiviral transduction of BJ-5TA and EA.hy926 cells with the *GFP* gene estimated by flow cytometry. Green curves correspond to non-transduced cells (autofluorescence control), red curves correspond to transduced cells. Figures correspond to the fluorescence intensity in the FITC channel ($\lambda_{ex} = 488 \text{ nm}$, $\lambda_{em} = 530 \pm 30 \text{ nm}$) for transduced cells. (B) – Viability of spheroids on day 5 of cultivation. Flow cytometry data are presented for monolayer cultures (indicated in pictograms) and spheroids (3D) stained with propidium iodide (PI) (PI channel: $\lambda_{ex} = 488 \text{ nm}$, $\lambda_{em} = 615 \pm 20 \text{ nm}$). The left pictogram shows unstained cells (autofluorescence control); the right pictogram shows cells after incubation with PI. Figures correspond to the number of PI-stained cells expressed as a percentage of the total number of events. (C) – Confocal images of spheroids composed of SKOV3.ip-Kat, EA.hy926-GFP, and BJ-5TA-GFP cells. Merged images of spheroids in the red and green fluorescence channels (left column) and separate spheroid images in the red and green fluorescence channels on days 2 and 5 of cultivation are shown. The right column corresponds to the image of the spheroids in the transmitted light. (D) – DARP-NanoLuc-SOPP3-FITC interaction with the spheroids of SKOV3.ip-Kat, EA.hy926, and BJ-5TA cells. Confocal images of the spheroids after incubation with DARP-NanoLuc-SOPP3-FITC ($0.5 \mu\text{M}$, based on the dye concentration) for 3, 24, and 72 h, respectively, are presented. The scale bar in the confocal images corresponds to $100 \mu\text{m}$

tivation; by day five of cultivation, stromal cells are almost completely covered by ovarian adenocarcinoma cells, which is in complete agreement with the previously published data on spheroids of a similar composition [31].

To study the interaction of DARP-NanoLuc-SOPP3 with spheroids, we obtained the spheroids of fluorescent SKOV3.ip-Kat cells, as well as EA.hy926 and BJ-5TA cells not modified with GFP. To visualize the interaction of DARP-NanoLuc-SOPP3 with the HER2 receptor on the spheroid surface, the

DARP-NanoLuc-SOPP3-FITC conjugate was used. *Figure 3D* shows that DARP-NanoLuc-SOPP3-FITC effectively interacts with the spheroids, as indicated by the presence of the green “crown” around the spheroid. The green fluorescent signal on the spheroid surface decreases with time, indicating that DARP-NanoLuc-SOPP3 has penetrated into the spheroid.

The BRET-induced phototoxicity of DARP-NanoLuc-SOPP3 was studied in the spheroids of SKOV3.ip-Kat, EA.hy926-GFP, and BJ-5TA-GFP

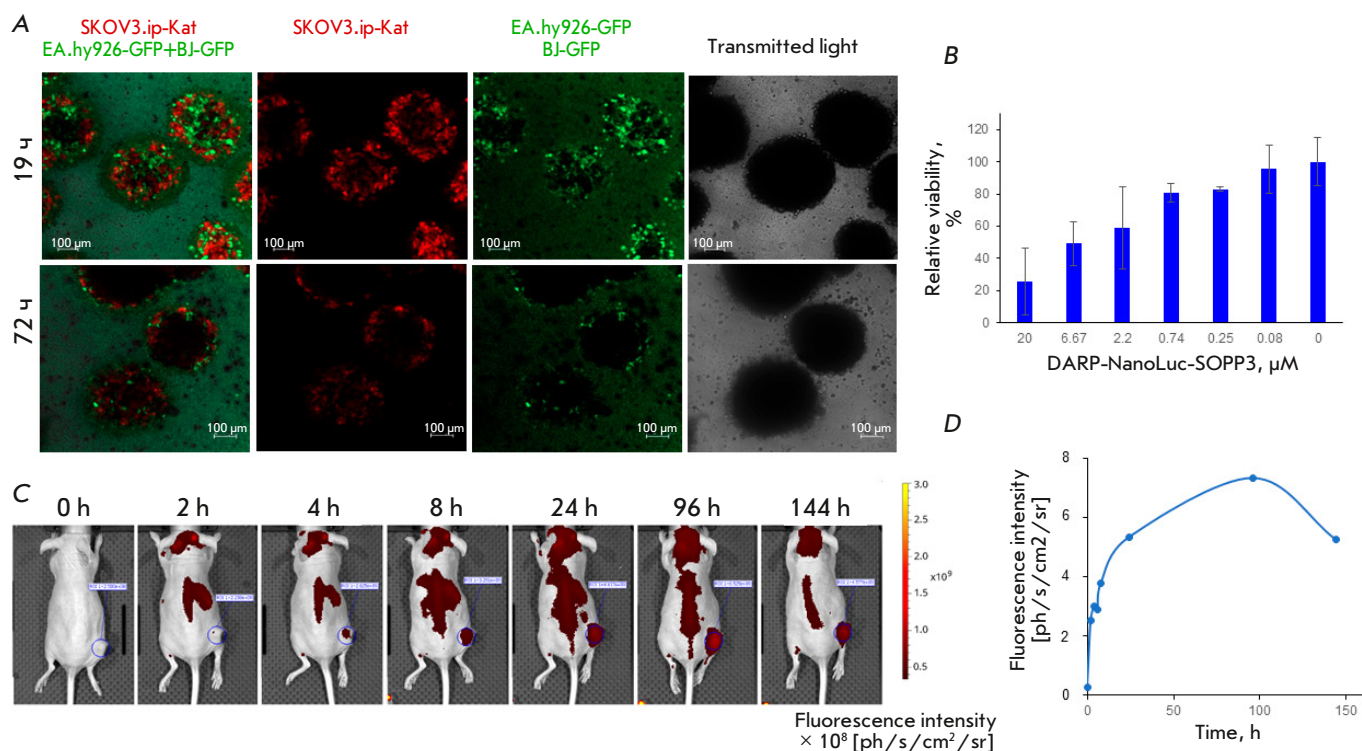


Fig. 4. DARP-NanoLuc-SOPP3 BRET-induced cytotoxicity in the 3D culture and biodistribution *in vivo*. (A) – Confocal images of spheroids (SKOV3.ip-Kat, EA.hy926-GFP, and BJ-5TA-GFP cells) after incubation with DARP-NanoLuc-SOPP3 (300 μ M) for 19 and 72 h. (B) – BRET-induced cytotoxicity of DARP-NanoLuc-SOPP3 in spheroids composed of ovarian cancer adenocarcinoma and stromal cells. (C) – Distribution of DARP-NanoLuc-SOPP3-Cy5.5 in a mouse with subcutaneous HER2-positive SKOV3 tumor (encircled by a blue dotted line). (D) – Dependence of the fluorescence intensity (expressed in photons per second per cm² per steradian) on time. The graph is based on data corresponding to the average brightness of the tumor area in Fig. C (blue dotted line) at a certain time point

cells. Figure 4A demonstrates a change in the spheroid structure morphology over time under the effect of DARP-NanoLuc-SOPP3 in the presence of furimazine. We would like to note that, in the interval of 19–72 h, the fluorescent signal decreases for both HER2-positive SKOV3.ip-Kat adenocarcinoma and stromal cells. The BRET-induced cytotoxicity of DARP-NanoLuc-SOPP3 in the presence of furimazine was ~10 times lower in the 3D culture compared to the 2D culture: the IC₅₀ was 6.58 μ M, as calculated using the GraphPad Prism v. 10.1.0 software (Fig. 4B).

To study the role of the DARPIn targeting module in the selective accumulation of DARP-NanoLuc-SOPP3 in HER2-positive animal tumors, the pattern of the DARP-NanoLuc-SOPP3–Cyanine 5.5 conjugate accumulation was studied in the tumor. For this, we used mice with subcutaneous xenograft tumors based on SKOV3 cells. The IVIS Spectrum In Vivo Imaging System was used for imaging. The fluorescent sig-

nal is first detected in the tumor two hours after intravenous injection of a 40- μ M DARP-NanoLuc-SOPP3-Cy5.5 solution (based on the dye concentration) to the animals. The signal gradually increases, reaching its maximum after 96 h (Fig. 4C,D), and then decreases. The obtained results indicate that the DARPIn targeting module in the NanoLuc-SOPP3 BRET pair not only allows for rapid (within the first 2–4 h after injection) accumulation of the drug in the tumor, but also makes it possible to avoid its accumulation in vital organs.

CONCLUSION

Conventional PDT is a very promising approach in cancer treatment given its spatial and temporal selectivity, as well as minimal invasiveness of healthy cells. However, the limited depth of light penetration required for PS activation, as well as aberrant accumulation of chemical PS in skin cells leading to undesira-

ble light-induced side effects, hinders the widespread clinical use of PDT [5, 32]. The development of BRET-activated systems based on completely biocompatible components can help solve these problems.

In this work, we developed a system for targeted HER2-specific BRET-activated PDT based on the multimodal protein DARP-NanoLuc-SOPP3, which consists of a HER2-specific targeting module and a NanoLuc-SOPP3 protein pair for BRET-induced PDT. *In vitro* experiments and experiments in the 3D spheroid model confirmed the photo-induced cytotoxicity of the system in HER2-positive human ovarian adenocarcinoma cells without the need for an external light source. Moreover, experiments in animals carrying subcutaneous HER2-positive tumors demonstrated selective accumulation of DARP-NanoLuc-SOPP3 at the tumor site. Considering the available data on the half-life of the luminescent signal in the NanoLuc-furimazine system, which is > 2 h [17], as well as our data on the BRET-induced phototoxicity of NanoLuc-SOPP3 [20], we believe that the multimodal protein DARP-NanoLuc-SOPP3 can be used for *in vivo* therapy. The regimen for ad-

ministration of the protein and luciferase substrate furimazine, which ensures long-term, simultaneous, and high maintenance of these components in the tumor, which are key for BRET-induced PDT, is proposed.

Our results show that there is great potential in the developed protein targeted self-exciting BRET system for PDT.

Based on the conducted experiments, we can conclude that the fully biocompatible system for targeted BRET-induced therapy using DARP-NanoLuc-SOPP3 makes it possible to overcome the two major limitations of conventional PDT: 1) the side phototoxic effect from the aberrant accumulation of chemical PS that results in light-activated responses, and 2) the need to use an external light source, which can often be achieved only by using expensive high-tech devices. ●

This work was financially supported by the Russian Science Foundation Grant No. 21-74-30016 “Organotypic tumor models using microfluidic technologies.”

REFERENCES

- Li X., Lovell J.F., Yoon J., Chen X. // *Nat. Rev. Clin. Oncol.* 2020. V. 17. № 11. P. 657–674.
- Dolmans D.E., Fukumura D., Jain R.K. // *Nat. Rev. Cancer.* 2003. V. 3. № 5. P. 380–387.
- Shramova E.I., Kotlyar A.B., Lebedenko E.N., Deyev S.M., Proshkina G.M. // *Acta Naturae.* 2020. V. 12. № 3. P. 102–113.
- Li X., Kwon N., Guo T., Liu Z., Yoon J. // *Angew. Chem. Int. Ed. Engl.* 2018. V. 57. № 36. P. 11522–11531.
- Fan W., Huang P., Chen X. // *Chem. Soc. Rev.* 2016. V. 45. № 23. P. 6488–6519.
- Borgia F., Giuffrida R., Caradonna E., Vaccaro M., Guarneri F., Cannavo S.P. // *Biomedicines.* 2018. V. 6. № 1. P. 1–12.
- Pallet N., Karras A., Thervet E., Gouya L., Karim Z., Puy H. // *Clin. Kidney J.* 2018. V. 11. № 2. P. 191–197.
- An Y., Xu D., Wen X., Chen C., Liu G., Lu Z. // *Adv. Hlth. Mater.* 2023. P. e2301326.
- Hsu C.Y., Chen C.W., Yu H.P., Lin Y.F., Lai P.S. // *Biomaterials.* 2013. V. 34. № 4. P. 1204–1212.
- Kim S., Jo H., Jeon M., Choi M.G., Hahn S.K., Yun S.H. // *Chem. Commun. (Camb.).* 2017. V. 53. № 33. P. 4569–4572.
- Kim Y.R., Kim S., Choi J.W., Choi S.Y., Lee S.H., Kim H., Hahn S.K., Koh G.Y., Yun S.H. // *Theranostics.* 2015. V. 5. № 8. P. 805–817.
- Yang Y., Hou W., Liu S., Sun K., Li M., Wu C. // *Biomacromolecules.* 2018. V. 19. № 1. P. 201–208.
- Al-Ani A.W., Zhang L., Ferreira L., Turyanska L., Bradshaw T.D., Thomas N.R. // *Nanomedicine.* 2019. V. 20. P. 102005.
- Yan H., Forward S., Kim K.H., Wu Y., Hui J., Kashiparekh A., Yun S.H. // *Biomaterials.* 2023. V. 296. P. 122079.
- Kim E.H., Park S., Kim Y.K., Moon M., Park J., Lee K.J., Lee S., Kim Y.P. // *Sci. Adv.* 2020. V. 6. № 37. P. eaba3009.
- Shramova E.I., Chumakov S.P., Shipunova V.O., Ryabova A.V., Telegin G.B., Kabashin A.V., Deyev S.M., Proshkina G.M. // *Light Sci. Appl.* 2022. V. 11. № 1. P. 38–50.
- Hall M.P., Unch J., Binkowski B.F., Valley M.P., Butler B.L., Wood M.G., Otto P., Zimmerman K., Vidugiris G., Machleidt T., et al. // *ACS Chem. Biol.* 2012. V. 7. № 11. P. 1848–1857.
- Shu X., Lev-Ram V., Deerinck T.J., Qi Y., Ramko E.B., Davidson M.W., Jin Y., Ellisman M.H., Tsien R.Y. // *PLoS Biol.* 2011. V. 9. № 4. P. e1001041.
- Westberg M., Bregnhøj M., Etzerodt M., Ogilby P.R. // *J. Phys. Chem. B.* 2017. V. 121. № 40. P. 9366–9371.
- Shramova E.I., Filimonova V.P., Frolova A.Yu., Pichkur E.N., Fedotov V.R., Konevega A.L., Deyev S.M., Proshkina G.M. // *Eur. J. Pharm. Biopharm.* 2023. V. 193. P. 208–217.
- Mironova K.E., Chernykh O.N., Ryabova A.V., Stremovskiy O.A., Proshkina G.M., Deyev S.M. // *Biochemistry (Moscow).* 2014. V. 79. № 12. P. 1391–1396.
- Pfleger K.D., Eidne K.A. // *Nat. Methods.* 2006. V. 3. № 3. P. 165–174.
- Proshkina G.M., Shramova E.I., Shilova O.N., Ryabova A.V., Deyev S.M. // *J. Photochem. Photobiol. B.* 2018. V. 188. P. 107–115.
- Shramova E.I., Proshkina G.M., Deyev S.M., Petrov R.V. // *Dokl. Biochem. Biophys.* 2018. V. 482. № 1. P. 288–291.
- Shramova E.I., Proshkina G.M., Deyev S.M., Petrov R.V. // *Dokl. Biochem. Biophys.* 2017. V. 474. № 1. P. 228–230.

26. Sogomonyan A.S., Shipunova V.O., Soloviev V.D., Lari-
onov V.I., Kotelnikova P.A., Deyev S.M. // *Acta Naturae*.
2022. V. 14. № 1. P. 92–100.
27. Mosmann T. // *J. Immunol. Methods*. 1983. V. 65. № 1–2.
P. 55–63.
28. Pluckthun A. // *Annu. Rev. Pharmacol. Toxicol.* 2015.
V. 55. P. 489–511.
29. Yarden Y. // *Oncology*. 2001. V. 61 Suppl 2. P. 1–13.
30. Yan M., Schwaederle M., Arguello D., Millis S.Z., Gatal-
ica Z., Kurzrock R. // *Cancer Metastasis Rev.* 2015. V. 34.
№ 1. P. 157–164.
31. Swaminathan S., Ngo O., Basehore S., Clyne A.M. //
ACS Biomater. Sci. Eng. 2017. V. 3. № 11. P. 2999–3006.
32. Mallidi S., Anbil S., Bulin A.L., Obaid G., Ichikawa M.,
Hasan T. // *Theranostics*. 2016. V. 6. № 13. P. 2458–2487.

Membrane Partitioning of TEMPO Discriminates Human Lung Cancer from Neighboring Normal Cells

O. K. Gasymov^{1*}, M. J. Bakhishova¹, R. B. Aslanov¹, L. A. Melikova^{1,2}, J. A. Aliyev²

¹Institute of Biophysics, Ministry of Science and Education Republic of Azerbaijan, Baku, AZ1171 Azerbaijan

²National Center of Oncology, Azerbaijan Republic Ministry of Health, Baku, AZ1012 Azerbaijan

*E-mail: oktaygasimov@gmail.com

Received: May 05, 2023; in final form, October 12, 2023

DOI:

Copyright © 2023 National Research University Higher School of Economics. This is an open access article distributed under the Creative Commons Attribution License, which permits unrestricted use, distribution, and reproduction in any medium, provided the original work is properly cited.

ABSTRACT The plasma membranes of normal and cancer cells of the lung, breast, and colon tissues show considerably different lipid compositions that greatly influence their physicochemical properties. Partitioning of the spin probe 2,2,6,6-tetramethylpiperidine-1-oxyl (TEMPO) into the membranes of human lung normal and carcinoma cells was assessed by EPR spectroscopy to estimate the impact of the lipid compositions. The goal was to reveal potential strategies for cancer therapy attributable to the membrane properties. The study was conducted at pH values of 7.3 and 6.2, relevant to the microenvironments of normal and cancer cells, respectively. The TEMPO partitioning was examined in the temperature interval of 283–317K to reveal the efficacy of local hyperthermia used in chemotherapy. Results indicate that the TEMPO partitioning coefficient for the membranes of human lung carcinoma cells is significantly higher compared with that of neighboring normal cells. Increased partition coefficients were observed at relatively higher temperatures in both normal and cancer cells. However, compared to the normal cells, the cancer cells demonstrated higher partition coefficients in the studied temperature range. The data obtained with C12SL (spin-labeled analog of lauric acid) indicate that increased membrane dynamics of the cancer cells is a possible mechanism for enhanced partitioning of TEMPO. Free energy values for partitioning estimated for pH values of 6.2 and 7.3 show that TEMPO partitioning requires 30% less energy in the cancer cells at pH 7.3. TEMPO and its derivatives have previously been considered as theranostic agents in cancer research. Data suggest that TEMPO derivatives could be used to test if complementary alkalization therapy is effective for cancer patients receiving standard chemotherapy with local hyperthermia.

KEYWORDS electron paramagnetic resonance, TEMPO partitioning, lung carcinoma, cell membrane lipid composition, cell membrane sensitivity.

ABBREVIATIONS NSCLC – non-small cell lung cancer; FAS – fatty acid synthase; SCD1 – stearoyl-CoA desaturase 1; EPR – Electron Paramagnetic Resonance.

INTRODUCTION

Cancer cells, even within the same tumor mass, show heterogeneity in both the phenotypic and functional levels. The heterogeneity of the cancer cell population is dynamic and susceptible to significant modifications by various factors during cancer development [1, 2]. In the course of development, cancer cells acquire new capabilities, such as evading apoptosis, self-sufficiency in growth signals, insensitivity to anti-growth signals, tissue invasion and metastasis, limitless replicative potential, and sustained angiogenesis. It is contended that these capabilities are shared in all types of human tumors [3]. Metastasis of cancer cells is the major cause of mortality in cancer patients. Epithelial-mesenchymal transition in cancer cells (carcinomas) is

critical for the development of metastasis capability. Several steps are involved in metastatic progression, during which cancer cells lose their polarity, cell-to-cell adhesion, etc. All these changes are manifested in the cell membranes that play a fundamental role in cell functioning [3, 4].

One of the main components of a cell membrane is a lipid bilayer that contains various lipids, such as asymmetrically arranged phospholipids, sphingolipids, glycolipids, cholesterol, etc. [5–7]. A wide variety of proteins, called transmembrane proteins, are embedded in the cell membranes and protrude on one or both sides. There are also peripheral membrane proteins that temporarily associate with the membranes of the cells to perform various functions. Both

membrane-embedded and -associated proteins and peptides play a critical role in cell functioning, particularly in cellular signal transduction. Often, for the cells to execute specific functions, the actions of these proteins need to be regulated in an orchestrated manner [4, 8–10]. Most studies related to cell membrane functions are devoted to investigating the proteins involved in various signaling pathways [11]. However, the lipid compositions provide not only specific hydrophobic environments for the proper folding of the membrane proteins, but also modulate their functions and participate in the maintenance of cell architecture [5–7]. Yet, relatively little attention has been paid to the functional role of lipids and lipid domains in the cell membrane.

A large body of evidence has been accumulated that supports the critical role of lipid compositions in healthy cell membranes and their significant alterations in various diseases, including cancer [12–14].

Lipid compositions play a pivotal role in cell functioning. Based on this observation, modulation of cell membrane components and/or properties has been proposed as a new therapeutic strategy for cancer therapy [13]. Lateral arrangements of the lipids in the membranes of the cells are heterogeneous and described as membrane lipid domains [15–18]. The lipid domains composed of various types of lipids are functional as lipids but indirectly can also influence and/or modulate membrane function. The specific composition of each lipid domain determines its distinct physicochemical properties [12, 14]. The lipid compositions of the membranes of cancer cells are significantly altered compared to those of healthy controls [13, 14, 19]. These findings provide the basis to characterize cancer cells by studying the lipid micro-environment of the membranes.

Lipid reprogramming of cancer cells and their possible mechanisms of action have also been investigated for lung cancer, particularly in non-small cell lung cancer (NSCLC). Lipid composition is also pivotal for NSCLC cell migration. It has been shown that migration of these cells can be inhibited considerably by cholesterol depletion in lipid rafts [20]. Progression of many types of cancer cells, including NSCLC, requires altered and enhanced fatty acid metabolism to support cell division and growth. In preclinical models, inhibition of acetyl-CoA carboxylase, the enzyme that regulates *de-novo* fatty acid synthesis, represses tumor growth in NSCLC [21, 22].

Overexpression of fatty acid synthase (FAS), a lipogenic enzyme, is observed in various types of cancer, including lung, colon, and prostate cancers. FAS provides a *de-novo* fatty acid synthesis that modifies the lipid compositions of cancer cells [23]. Stearoyl-CoA

desaturase 1 (SCD1) is another protein involved in lipid metabolism that plays an essential role in the malignant transformation of lung cancer cells [24, 25]. Desaturation and prolongation of fatty acids have been shown for lung cancer cells. In the desaturation event, each double bond in the *cis* configuration creates a twist in the acyl chain that, in turn, increases the membrane fluidity. Increased membrane fluidity induced by desaturation stimulates cancer metastasis and is associated with poor prognosis in lung cancer patients.

Electron Paramagnetic Resonance spectroscopy (EPR) with the use of various nitroxide probes has been developed as a powerful tool to characterize the lipid micro-environment of the cell membranes. Characterization of the lipid micro-environments of the cell membranes of healthy and cancer tissues is important to understand the functional changes in the cancer cell membranes associated with lipid components. The sensitivity of cancer cell membranes to relevant environmental conditions is an important attribute in developing a method for preferential drug delivery to cancer cells using the differences in the properties of the lipid domains. Previously, to segregate the contribution of only lipid components of the cell membranes, we investigated the properties of liposomes fabricated using lipids extracted from human lung cancer and normal cells [26, 27]. The liposomes composed of the cancer cell lipids showed significantly enhanced partitioning of spin probe 2,2,6,6-tetramethylpiperidine-1-oxyl (TEMPO) compared to those fabricated using normal cell lipids. In the current study, the partitioning of TEMPO into the membranes of live cells of human lung normal and carcinoma tissues was examined. A wide assortment of nitroxide spin probes can be used to characterize different regions of the cell membrane. TEMPO, used in this study, does not show any affinity to the membrane proteins and, therefore, provides a characterization of the lipid phase of the membrane as a separate component. However, unlike the studies performed in liposomes, the lipid phase of the membrane is modified by the presence of membrane proteins. The experiments were performed in a temperature interval of 283–317 K, the highest value of which matches the condition used in local hyperthermia [28, 29]. The experiments at pH 6.2 mimic the acidic environment created in cancer development [30–32]. The study revealed differences in parameters (polarity, micro-viscosity, and the energy required to transfer TEMPO from the aqueous to the membrane environment) between the membranes of cancer and healthy cells. Compared with previous works on liposomes [26, 27], the results obtained in this study indicate that pro-

teins embedded in the cell membranes significantly alter the dynamics of the lipid fraction, making them more dynamic and permeable to small molecules. The determined temperature and pH sensitivities of the cell membranes may help to choose or create the appropriate conditions for cancer therapy.

MATERIAL AND METHODS

Human lung tissue collection

Human lung tissues were collected immediately after the surgery on lung carcinoma patients in accordance with the tenets of the Declaration of Helsinki and approved by the review board of the Azerbaijan National Center of Oncology. Informed consent was obtained from each donor. Lung carcinoma patients were selected after computed tomography. The cancer diagnosis for individuals was confirmed after biopsy and subsequent histopathological grade (aggressiveness) evaluations. Experiments were performed on five individuals. However, due to similar findings, here we report, as an example, a case of a 52-year-old male who did not receive chemo- or radiation therapy before the surgery. The results for this case were more characteristic and, therefore, analyzed thoroughly. The pathology findings on the surgical lung tissue were consistent with Stage II, pT2bN0Mx, non-small cell lung cancer. Bulk lung tissue was segregated into cancer (carcinoma) and neighboring normal (also referred to as healthy) tissues by the pathologist. Normal and cancer cells in the investigated lung tissue are indicated in *Fig. 1*. Experiments with spin-labeled lauric acid (C12SL) were performed with the surgical tissue of the patient with the following pathology findings: 53-years-old male, lung adenocarcinoma, Stage II, pT-3N0Mx.ICD-O: 8260/3, invasive.

Preparation of epithelial cell suspension from lung tissue

The fresh lung tissue (about 2-3 h after the surgery) was washed thoroughly with PBS buffer to remove blood. Afterward, the tissue was cut into small pieces and then homogenized in PBS buffer using a glass homogenizer. The homogenized lung tissue was washed three times with PBS solution and then centrifuged (Eppendorf 5418) to remove the cell debris. Obtained cell suspension was used for the experiments. The intactness of the cells was assessed by Zeta-potential measurements as shown previously [33].

EPR spectroscopy

EPR measurements were performed using a Bruker ELEXSYS E580 spectrometer at X-band frequency with variable temperature accessory. The aqueous

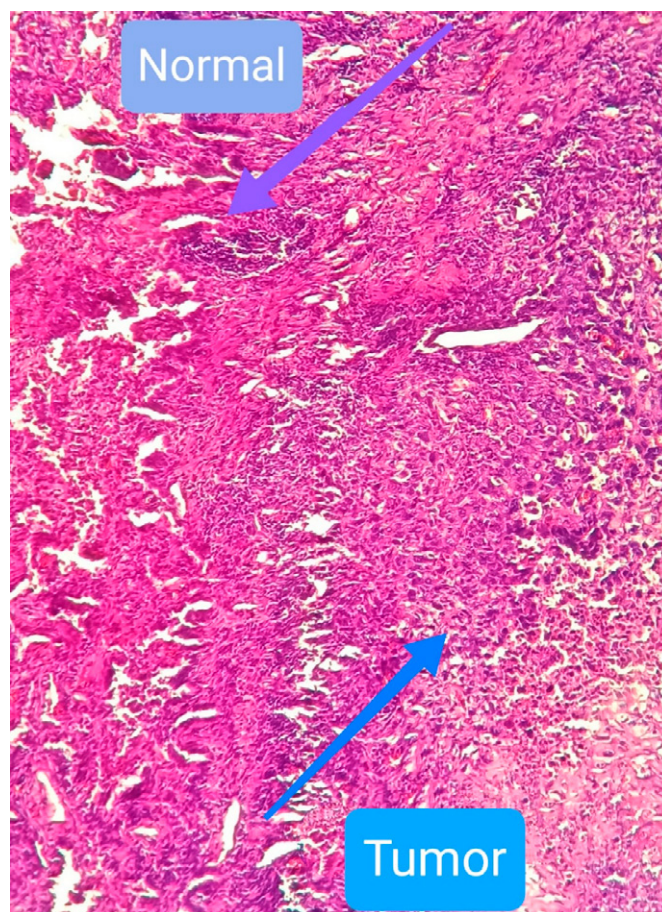


Fig. 1. Normal and cancer cells in lung tissue

suspension of lung carcinoma and neighboring normal cells with TEMPO were placed into Pyrex capillary tubes with an I.D. of 0.6 mm. EPR spectra were recorded with the following instrument parameters: scan width: 100 Gauss; sweep time: 40 s; modulation amplitude: 1 Gauss; modulation frequency: 100 kHz; microwave power: 0.47 mW; and time constant: 0.1 s. Before the measurements, the samples were kept for 5 minutes at each temperature to ensure that the sample temperature matched the set temperatures.

Partitioning of TEMPO in the membranes of human lung normal and carcinoma cells

TEMPO dissolved in an aqueous solution displays a well-known EPR spectrum with three components resulting from nitrogen hyperfine interactions. However, TEMPO incubated in the cell environment shows a composite EPR spectrum, the third component (located in a high magnetic field) of which is partially resolved. The difference in the nitrogen splitting constant of TEMPO in hydrophobic (cell membrane) and hydrophilic (aqueous) environments is the reason for the split of the third component. Consequently,

the EPR spectra of TEMPO incubated with cells in an aqueous environment reflect the partitioning of TEMPO in the lipid fraction of the cell membrane and aqueous environments. To resolve the spectral components, the EPR spectra of TEMPO were analyzed using the LabVIEW program developed by Christian Altenbach (<https://sites.google.com/site/altenbach/>), using the spectral simulation code written in FORTRAN [34]. Along with computer simulations, rotational correlation times of TEMPO were also calculated using the following formula that uses the peak heights and line widths of the first derivative EPR spectra [35]:

$$\tau_c = 6.5 \times 10^{-10} W_0 [(h_0/h_{-1})^{1/2} - 1],$$

where W_0 is the width (in Gauss) of the central component, while h_0 and h_{-1} are the heights of the central and high-magnetic field components of the first derivative EPR spectrum. As mentioned above, the EPR spectra resulting from the partitioning of TEMPO in the system are composite and consist of two components. Therefore, the formula above was applied after the decomposition of the EPR spectra into lipophilic and hydrophilic components. Because of the close similarity of the correlation times obtained from the software and the formula, data are shown only as deduced from the software.

Double integrals of the EPR spectral components (I_{mbr} and I_{aq} represent TEMPO confined in the membrane and aqueous environments, respectively) were employed to calculate partition coefficients with the following formula: $K = I_{mbr}/(I_{mbr} + I_{aq})$. To characterize the EPR spectral components, the membrane and aqueous environments were described as lipophilic and hydrophilic, respectively. Apparently, a partition coefficient depends on both the concentration of the lipid fractions and the number of lung cells in the aqueous system [36]. For an accurate comparison of the data related to the partition coefficients, the same amount (by weight) of cancer and normal cell suspensions were used. Both cancer and normal cell suspensions were incubated with TEMPO (150 μ M total concentration) for about 30 min. The experimental conditions used in this study allow us to compare the partition coefficients of the normal and cancer cells directly.

The temperature dependence of the equilibrium constant K (partition coefficient in our case) was used to calculate the free energy changes required to transfer TEMPO molecules from the aqueous to the lipid phase of the membranes of the healthy and cancer cells.

$$\log K = -\Delta G/RT$$

Similarly, the temperature dependence of the rotational correlation times of TEMPO was used to determine the activation energies for rotational motions in the membranes of the healthy and cancer cells.

Dynamics of the lipid domain of the cell membrane evaluated by spin-labeled lauric acid analog (C12SL)

Experimental procedures with C12SL, the chemical structure of which is shown below in the relevant *Figure*, were similar to that of TEMPO described in section 2.4. In contrast to TEMPO, C12SL was dissolved in ethanol. An equal amount of each cell suspension (0.1 mg/ml) was incubated with 200 μ M of C12SL for 30 min. A high concentration of C12SL was employed to monitor both the dynamics of the lipid domain and its maximal incorporation capacity in healthy and cancer cells. The attained complex EPR spectra were analyzed with a multi-component EPR program [34]. Analyses of the EPR spectra of C12SL were performed in two steps. In the first step, free C12SL, not incorporated into the cell membrane, was removed to decrease the number of fitting parameters. Removal of free C12SL spectra was performed using the EPR program “FreeRemover”, which is part of the program package [34]. In the second step, the spectra that lack “free” spectral components were analyzed by the multi-component EPR spectral analysis as described above.

RESULTS AND DISCUSSION

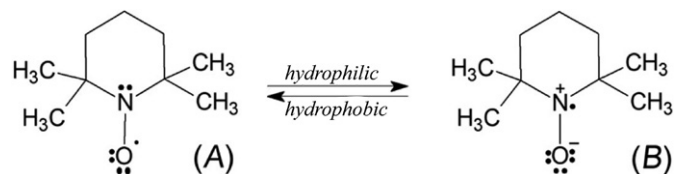
As indicated above, the lipid compositions in the healthy and cancer cells of various tissues significantly differ from each other [12–14]. The lipid compositions of the cells determine the specific properties of the cell membranes, such as membrane fluidity, permeability, the temperature of phase transition, etc. These characteristics of the membranes are essential from a therapeutic point of view, particularly for drug delivery applications. TEMPO does not show any binding properties toward the proteins. Therefore, the use of TEMPO in membrane research allows for a selective characterization of the lipid phase. Unlike the findings obtained in liposomes [26, 27], in this case, lipid phase properties are modified by the membrane proteins of the corresponding cells. Below, we provide experiments of TEMPO partitioning into the membranes of the cells at the temperature of 283–317 K interval and pH values of 7.3 and 6.2, conditions that are relevant for cancer therapeutics.

Partitioning of TEMPO into the membranes of healthy and cancer human lung cells

The EPR spectra of TEMPO incubated with human lung cancer and healthy cells at pH 7.3 are shown

in Figs. 2A,B, respectively. Components of the EPR spectra in the high magnetic field split into two peaks labeled as l (lipophylic) and h (hydrophilic). Thus, each EPR spectrum is composed of two components resulting from the partitioning of TEMPO between the cell membrane (lipophylic) and aqueous (hydrophilic) phases. The relative amplitudes of the high-field components of EPR spectra indicate that the partition of TEMPO is significantly different for cancer and healthy cells (Fig. 2). At pH 7.3, the relative amount of TEMPO in the membranes of the cancer cells is significantly higher compared to that in healthy cells. Interestingly, differences in TEMPO partitioning are even higher at pH 6.2 compared to those at pH 7.3 (Fig. 2A,C). EPR spectra in the temperature interval of 283–317 K indicate that an increase in temperature further augments the relative amount of TEMPO in the membranes of both cell types. However, compared to healthy cells, the membranes of cancer cells incorporate more TEMPO molecules in the respective conditions.

To describe the EPR spectra of TEMPO in environments with significantly different hydrophobicity values, one should consider the following aspects. The observed splits of the EPR components in a high magnetic field arise from the small differences in the isotropic hyperfine coupling constants (A_{iso}) and g factors of the nitroxide spin probe in each environment. These differences are explained as changes in the relative contribution of two canonical structures of TEMPO as shown below [37].



Polar solvents like the aqueous solution tend to stabilize the structure (B) in which the unpaired electron density is localized on the N-atom. The increased relative contribution of structure (B) gives rise to the nitrogen hyperfine coupling constant. In contrast, structure (A), in which the unpaired electron density is localized on the oxygen atom, is preferentially stabilized in a hydrophobic environment. Therefore, the nitrogen hyperfine coupling constant is lower in a hydrophobic environment compared to that of a hydrophilic environment.

Decompositions of the EPR spectra of TEMPO incubated with cancer and healthy cells of the human lung at 317K using the two-component model, as an example, are shown in Fig. 3. The composite EPR spectra simulated from the resolved parameters are indistinguishable from the experimental spectra (Fig. 3A,C,E,G). Therefore, the simulated composite EPR

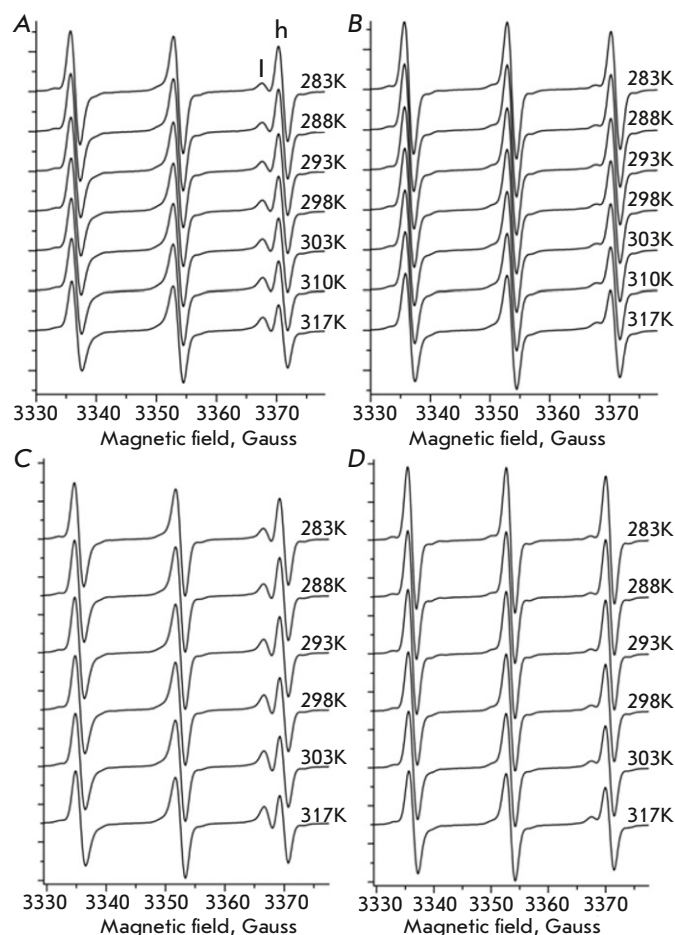


Fig. 2. EPR spectra of TEMPO resulted from the partitioning in the membranes of human lung normal and carcinoma cells. EPR spectra of TEMPO for carcinoma (A) and healthy (B) cells at pH 7.3 and at various temperature values. EPR spectra of TEMPO for carcinoma (C) and healthy (D) cells at pH 6.2 and at various temperature values. The l and h symbols denote the spectral components of the EPR spectra of TEMPO localized in lipophilic (cell membrane) and hydrophilic (aqueous) regions. The symbols l and h indicate the “lipophilic” and “hydrophobic” components of TEMPO, respectively. The temperature for each spectrum is shown in the Kelvin scale

spectra are vertically shifted for easy visualization. The EPR spectra of the resolved components (Fig. 3B,D,F,H) are in full agreement with the above-mentioned suggestion. Indeed, a mismatch in the positions of the EPR components (g values) and nitrogen hyperfine coupling constant ($2A_{\text{iso}}$, Fig. 3H) is evident. In all evaluated samples, the EPR spectra of TEMPO in the aqueous environments (thin lines in Figs. 3B,D,F,H representing healthy and cancer cells at pH values of 7.3 and 6.2) show identical $2A_{\text{iso}}$ values of 34.5 Gauss (Table 1).

However, the $2A_{\text{iso}}$ values of TEMPO incorporated into the membranes of the cells are significantly decreased and fall within an interval of 31.4–32.4 Gauss.

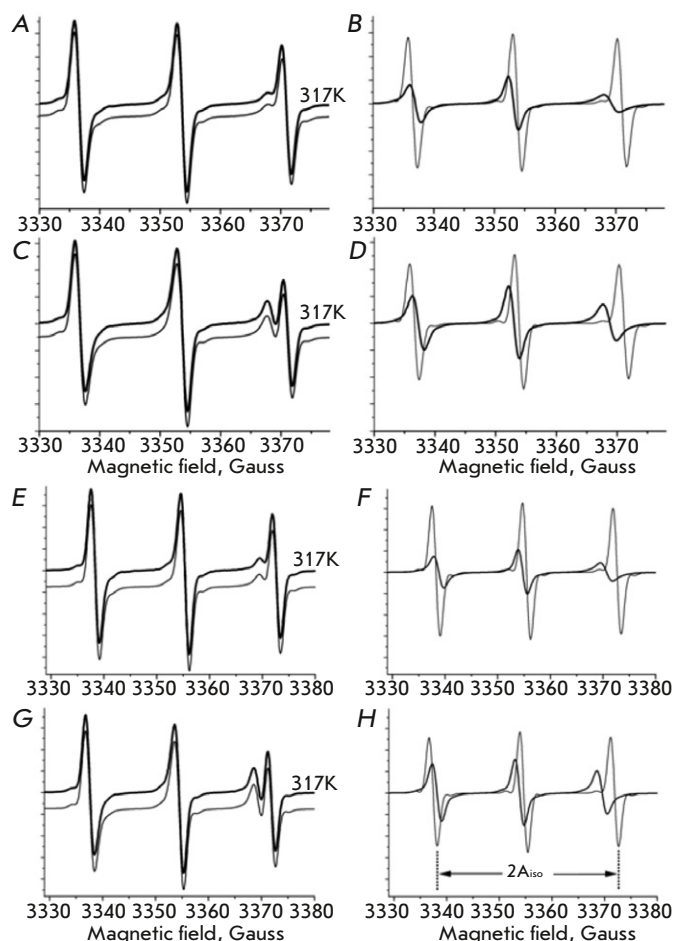


Fig. 3. Decompositions of the EPR spectra of TEMPO into components reflecting the lipophilic and hydrophilic environments. EPR spectra of TEMPO partitioning in human lung healthy and carcinoma cells at 317K and pH 7.3. (A) and (B) are the results of a two-component analysis (see Methods) and resolved components corresponding to lipophilic (sick line in B) and hydrophilic (thin line in B) for the healthy lung cells. The EPR spectrum from the fitting procedure (sick line in A) is indistinguishable from the experimental spectrum (thin line in A) and, therefore, vertically shifted for better illustration. (C) and (D) are the same as (A) and (B) but for the carcinoma cells. (E), (F), (G), and (H) indicate conditions corresponding to (A), (B), (C), and (D), respectively, but in pH 6.2. A_{iso} is the isotropic hyperfine coupling constant

At pH 7.3, $2A_{iso}$ values for the EPR spectra of TEMPO incorporated in the membrane of healthy and cancer cells are 32.4 Gauss and 31.5 Gauss, respectively. Thus, the lipid fractions of the cancer cell membrane are more hydrophobic compared to those of the healthy cells. Interestingly, as judged from the A_{iso} values of the EPR spectra of TEMPO, when increasing the pH from 6.2 to 7.3, a small increase in hydrophobicity was observed in the membranes of healthy cells (from 31.9 Gauss to 32.4 Gauss) but not in cancer cells (about

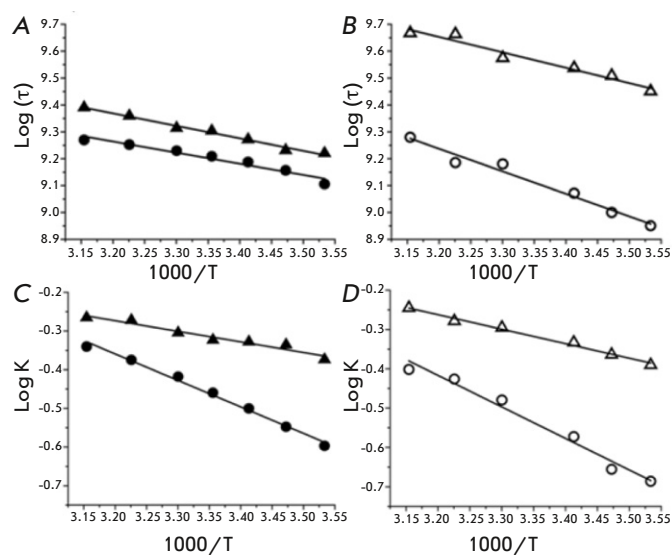


Fig. 4. Arrhenius plots for the parameters obtained from the EPR spectra of TEMPO partitioning in the healthy and carcinoma cells of the human lung tissue. Arrhenius plots for the rotational correlation times of TEMPO in the membrane environments of the cells at pH 7.3 (A) and 6.2 (B). Solid circles and solid triangles in (A) represent healthy and carcinoma cells, respectively. Open circles and triangles in (B) represent healthy and carcinoma cells, respectively. Arrhenius plots for the TEMPO partitioning coefficients in the healthy and carcinoma lung cells at pH values of 7.3 (C) and 6.2 (D). The definitions of symbols in (C) and (D) are the same as in (A) and (B), respectively. K and τ are the partition coefficient and rotational correlation time, respectively

31.5 Gauss). As a result, at pH 6.2 the difference in hydrophobicity values is shrunken between healthy and cancer cell membranes.

TEMPO does not show any binding affinity toward proteins. Therefore, the EPR spectra of TEMPO assigned to the lipophilic phase displays the characteristics of the lipid fraction of the cell membranes. The partition coefficients for the cell membranes are significantly higher compared to those obtained in liposomes fabricated from the corresponding cells [26, 27]. Thus, the proteins embedded into the membranes modify lipid phase properties, resulting in augmented partitioning of TEMPO.

Micro-viscosity of the lipid fraction of the cell membranes

Along with the decomposition of the EPR spectra of TEMPO, computer analysis also allows us to estimate the rotational correlation times of TEMPO corresponding to the spectral components in various environments. In lipid fractions, the rotational correlation times of TEMPO in cancer cells are decreased compared to those obtained in healthy cells at both pH values (7.3 and 6.2) and the used temperature range

Table 1. Parameters obtained from the EPR studies on the membranes of healthy and cancer cells of the human lung

Sample	$2A_{iso}$, Gauss		ΔG_{τ}	ΔG_K
	aqueous	membrane	kcal/mol	
Healthy cells, pH 7.3	34.5	32.4	1.9 ± 0.2	3.1 ± 0.1
Cancer cells, pH 7.3	34.5	31.5	2.1 ± 0.2	1.2 ± 0.1
Healthy cells, pH 6.2	34.4	31.9	3.8 ± 0.3	3.7 ± 0.3
Cancer cells, pH 6.2	34.5	31.4	2.6 ± 0.3	1.7 ± 0.1

(Fig. 4). For example, at room temperature and pH 7.3, rotational correlation times are about 490 ps and 617 ps (Fig. 4A) for TEMPO incorporated into cancer and healthy cell membranes, respectively. Faster rotation (corresponding to a lower correlation time) of TEMPO indicates a low viscosity of the surroundings. Since TEMPO molecules reside in the lipid fraction, the data indicate enhanced dynamics of the lipid fraction.

The Arrhenius plots for the correlation times obtained at various temperatures are shown in Fig. 4A,B. The activation energies of the rotational motions of TEMPO (ΔG_{τ}) in the membranes of healthy and cancer cells of the human lung at pH values of 7.3 and 6.2 are shown in Table 1. The values of ΔG_{τ} for the membranes of healthy and cancer cells are very similar (ΔG_{τ} values are 1.9 ± 0.2 and 2.1 ± 0.2 kcal/mol, respectively), indicating the comparable micro-viscosities of the studied lipid fractions in both cases. At pH 6.2, increased values of ΔG_{τ} were observed for both cell types. However, the micro-viscosity of the membrane fractions of the healthy lung cells was higher compared to those of the cancer cells (ΔG_{τ} values are 3.8 ± 0.3 and 2.6 ± 0.3 kcal/mol, respectively).

Efficiency of the transfer of TEMPO molecules from an aqueous to a lipid phase of cell membranes

Computer-assisted decompositions of the EPR spectra of TEMPO incubated with the healthy and cancer cells provided a means to conduct an evaluation of its partition coefficients. Several factors, such as lipid compositions, membrane dynamics, etc., may influence the partition of molecules (TEMPO in this study) between the membrane and the aqueous environment. Because TEMPO does not show any binding affinity toward proteins, equilibrium in the partitioning can be considered as a result of the passive incorporation of the molecules into the lipid fractions of the membranes. At this point, the term 'passive incorporation' indicates that the proteins localized on the cell membrane are not participating directly in this process. However, the membrane proteins may alter the properties of the lipid phase capable of influencing the partitioning characteristics of TEMPO in the cell membranes.

The Arrhenius plots for the partition coefficients (K) obtained at various temperatures are shown in Fig. 4C,D. The standard Gibbs free energy change required to transform a TEMPO from an aqueous to a lipid phase of the membrane of healthy and cancer cells is shown in Table 1. At pH 7.3, free energy changes for the transfer of TEMPO from aqueous phase to lipid phase in healthy and cancer cell membranes are 3.1 ± 0.1 kcal/mol and 1.2 ± 0.1 kcal/mol, respectively. In the acidic transition from pH 7.3 to pH 6.2, the free energy changes of TEMPO transfer for healthy and cancer cell membranes increase by about 19% and 42%, reaching the values of 3.7 ± 0.3 kcal/mol and 1.7 ± 0.1 kcal/mol, respectively. Thus, more energy is required to transfer TEMPO to the cell membranes in an acidic pH. Data indicate that in lung tissue composed of both healthy and cancer cells TEMPO molecules will preferentially incorporate the membranes of cancer cells.

It is well established that during the progression of the disease, the cancer cells in hypoxic conditions increase glucose consumption via aerobic glycolysis (termed as the Warburg effect). This process results in the creation of an acidic micro-environment [30–32, 38–41]. Cancer cells effectively use the acidic micro-environment for mesenchymal transition and metastasis. If TEMPO is considered as a model for certain drugs, then for drug delivery, it would be beneficial to create normal pH (7.3) conditions for the cancer cells. Differences in the ΔG_K values for healthy and cancer cells are almost identical for pH 7.3 and pH 6.2. However, the ΔG_K value is at its smallest for cancer cells at pH 7.3, indicating that less energy is required to transfer TEMPO from the aqueous solution to the membrane. The current study has direct clinical value. TEMPO and its derivatives show significant anti-cancer effects when applied to various types of cancer, including lung cancer [42–47]. It is highly anticipated that TEMPO-benzoate, which shows significantly enhanced partitioning in liposome studies [26, 27], will also be very effective in the membranes of the corresponding cells. A FTIR study of the lipids extracted from the normal and cancer cells supports this finding.

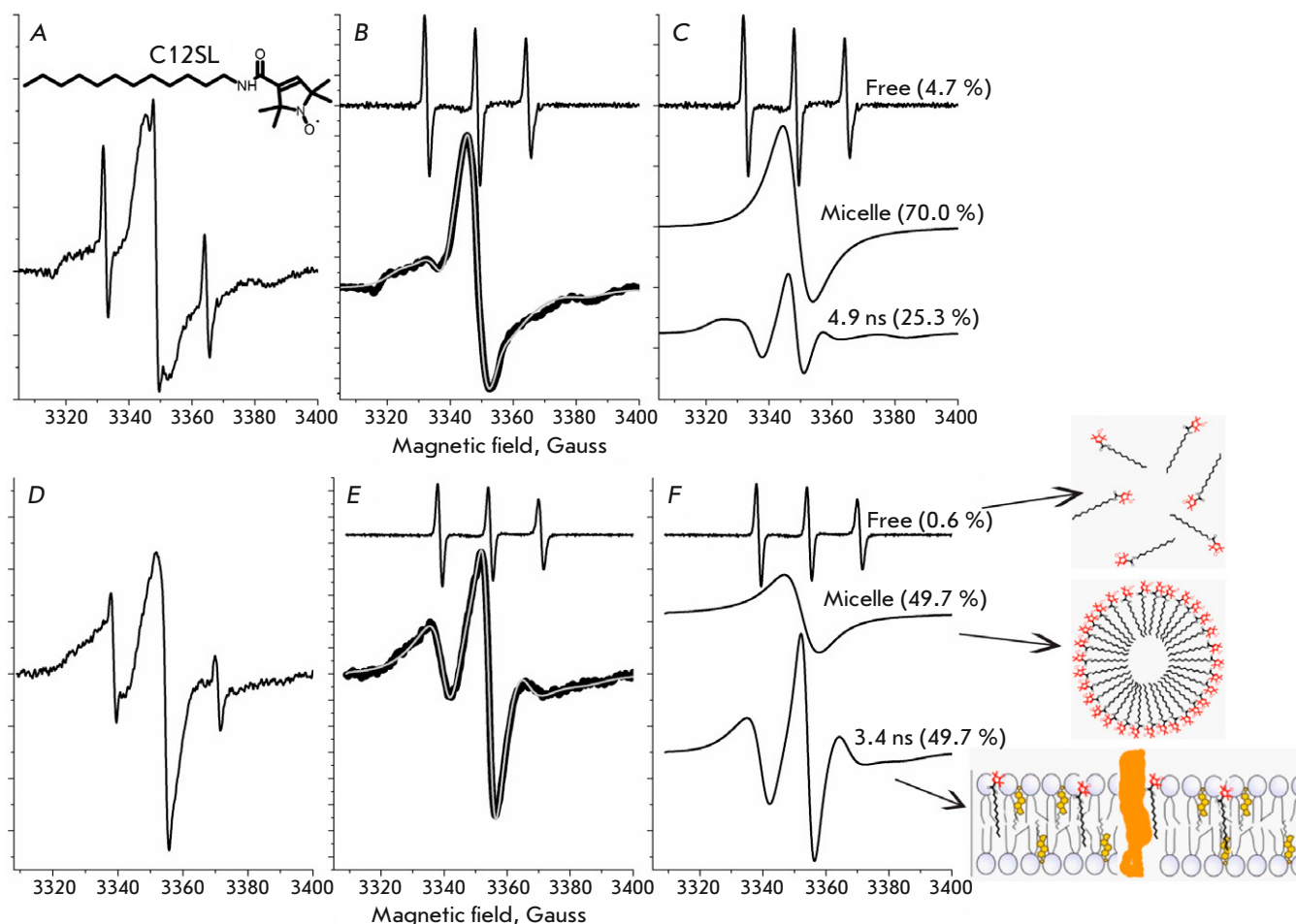


Fig. 5. EPR spectra of C12SL incorporated into the lipid domain of the membranes of healthy and cancer cells of the human lung. (A), (B), and (C) are the EPR spectrum of C12SL (shown in (A)) incubated with the cell suspension of healthy lung tissue, separation of free and composite spectral components, and the spectral component of the EPR spectrum, respectively. The grey line (in (B)) is a computer-simulated spectrum from the best fit parameters of a two-component model. (D), (E), and (F) are the same as in (A), (B), and (C), but they were obtained from the cell suspension of lung cancer cells. The EPR spectra of C12SL were measured at room temperature. The schema provided in the bottom-right corner of the *Figure* illustrates C12SL in "free", "micelle" and "membrane-incorporated" situations. C12SL is a spin-labeled analog of lauric acid, the chemical structure of which is shown in *Fig. 5A*

In contrast to normal cells, the lipid fractions from the cancer cells are in a more disordered state. In addition, lipids from the cancer cells exhibit a non-cooperative temperature transition, as opposed to the cooperative temperature transition observed for the healthy cells. The results obtained from numerous human lung cancer samples will be published elsewhere.

Evidence of increased dynamics of the lipid phase in the membranes of cancer cells compared to healthy cells

The dynamics of the lipid phase of the membranes of healthy and cancer cells were assessed using a C12SL (*Fig. 5*). C12SL molecules possessing an amphiphilic nature are predisposed to incorporate the lipid phase of the membranes. However, the efficiency of the in-

corporation depends on the physicochemical properties of the membranes, mainly based on fluidity (dynamics). Because of the position of the nitroxide spin label on C12SL, the dynamic parameters obtained from EPR spectra will be related to the surface part of the membranes [48].

The EPR spectrum of C12SL incorporated into the membranes of healthy lung cells (pH 7.3, room temperature) is shown in *Fig 5A*. The best fit spectra obtained from a computer analysis indicate that two components (besides the free components) are sufficient to describe the composite EPR spectra (*Fig. 5B,C*). About 25% of C12SL is incorporated into the membranes of healthy cells and its rotational correlation time amounts to about 4.9 ns. Because of limited solubility, about 70% of C12SL is in micelle form in

aqueous environments. The broad singlet spectrum results from strong spin-spin exchange interactions where nitroxide spin labels are too close to each other. The EPR spectrum of C12SL incorporated into the membranes of the cancer cells of human lung tissue (Fig. 5D) is significantly different from those obtained from healthy cells (Fig. 5A). In contrast, about a two-fold higher amount of C12SL was incorporated into the membranes of cancer cells of the lung. Besides that, the dynamics of the C12SL incorporated into cancer cell membranes are significantly increased, as is apparent by the decreased rotational correlation time (3.4 ns versus 4.9 ns). Data indicates that the membranes of cancer cells are more loosely packed than those of healthy cells, resulting in more permeability. Consistent with other findings, in the case of cancer cells, a lower fraction (50% versus 70%) of the C12SL is in aggregated form. Thus, the experimental data obtained with C12SL clearly indicate that, compared to healthy cells, the membranes of cancer cells are more dynamic.

The cytotoxicity values (IC₅₀) for TEMPO and its derivative compounds relevant to various applications

Nitroxides and their different derivatives exhibit numerous biologically significant functions [43]. Therefore, different objectives have been considered in their applications to various diseases, including cancer therapy. The drug applications require a unique range of IC₅₀ (the half-maximal inhibitory concentration) values. In cancer, nitroxides can be used as a radioprotector and contrast-enhancing agents in MRI (magnetic resonance imaging) [49]. For therapeutic applications, nitroxides possessing low cytotoxicity (therefore high IC₅₀ values) are preferable. TEMPO and 4-hydroxy-TEMPO (aka TEMPOL), exhibiting IC₅₀ values of 2.7 mM and 11.4 mM, respectively, are best suited for these purposes [50]. As an antiproliferative agent, the IC₅₀ values of TEMPOL for various cell lines related to breast, colon, liver, and ovary cancer fall in the range of 0.21–1.073 mM [51]. TEMPOL provides a significant adjuvant effect in cancer applications. In some cell lines for colon cancer, TEMPOL significantly enhances the cytotoxicity of the widely used anti-cancer drug doxorubicin. In the HCT116 cell lines, pretreatment with TEMPOL shows about a 7-fold decreased IC₅₀ value (from 0.38 mM to 0.053 mM). Some modified nitroxides show remarkable cytotoxicity against many cancer lines (IC₅₀ values of about 0.06 μM, including A549 cells, which are the culprit cell lines for human lung cancer [52]).

The current study is also relevant to cytotoxicity studies. It has been shown that nitroxide cytotoxicity

is strongly related to the lipid/water partition coefficients [53, 54]. Indeed, as shown above, the IC₅₀ value of the more lipophilic compound TEMPO is about 4-fold lower compared to that of the hydrophilic compound TEMPOL (just the –OH group attached to TEMPO). In line with these findings, benzoate group attachment to TEMPO dramatically enhances the partition coefficient in liposome studies [26, 27]. Thus, depending on the specific task at hand, the cytotoxicity of nitroxides (IC₅₀ values) can be considerably modified by an assortment of group attachments. The membrane partitioning values determined by the use of EPR spectroscopy can provide a preliminary, quick assessment of the cytotoxicity of nitroxide compounds.

CONCLUSIONS

TEMPO partitioning in the membranes of healthy and cancer cells of human lung tissues indicates that compared to healthy cells, the partition coefficients for the cancer cells are significantly higher. A positive correlation is observed between the temperature and the partition coefficient values for both cell types. The DG_K values determined for TEMPO suggest that, compared to healthy cells, cancer cells more readily incorporate TEMPO molecules into their membrane. The lowest free energy change required to transfer TEMPO from an aqueous to a lipid phase of the membrane was observed in cancer cells at pH 7.3. Considering TEMPO as an anti-cancer drug for various types of cancer, in addition to standard chemotherapy, complementary alkalization therapy to change the acidic microenvironment to a slightly more alkaline one could be beneficial to some cancer patients. The TEMPO partitioning experiments described above were performed on four additional lung cancer patients. The characteristics of TEMPO partitioning were similar in all cases. However, the difference between the values of the TEMPO partitioning coefficients for lung normal and cancer cells varied and was case-dependent. The benefit derived from hyperthermia and/or alkalization may not be effective in all cases. Therefore, characterization of cells by TEMPO partitioning could be a valuable tool for choosing a proficient strategy for personalized cancer chemotherapy. Our experiments with C12SL indicate that the increased membrane dynamics in cancer cells could be a mechanism of enhanced partitioning of TEMPO. ●

R. Gasanova assisted in EPR measurements.

The authors declare that they have no conflicts of interest.

This work was supported by the Azerbaijan Science Foundation (Grant No. EIF-MQM-ETS-2020-1(35)-08/07/3-M-07).

REFERENCES

1. Meacham C.E., Morrison S.J. // *Nature*. 2013. V. 501. № 7467. P. 328–337.
2. Singh A.K., Arya R.K., Maheshwari S., Singh A., Meena S., Pandey P., Dormond O., Datta D. // *Int. J. Cancer*. 2015. V. 136. № 9. P. 1991–2000.
3. Hanahan D., Weinberg R.A. // *Cell*. 2000. V. 100. № 1. P. 57–70.
4. Rakoff-Nahoum S. // *Yale J. Biol. Med.* 2006. V. 79. № 3–4. P. 123–130.
5. Casares D., Escribá P.V., Rosselló C.A. // *Int. J. Mol. Sci.* 2019. V. 20. № 9. P. 2167.
6. Lorent J.H., Levental K.R., Ganesan L., Rivera-Longsworth G., Sezgin E., Doktorova M., Lyman E., Levental I. // *Nat. Chem. Biol.* 2020. V. 16. № 6. P. 644–652.
7. Stieger B., Steiger J., Locher K.P. // *Biochim. Biophys. Acta - Mol. Basis Dis.* 2021. V. 1867. № 5. P. 166079. <https://doi.org/10.1016/j.bbadis.2021.166079>.
8. Zulueta Díaz Y.L.M., Arnsparang E.C. // *Membranes*. 2021. V. 11. № 11. P. 828.
9. van Deventer S., Arp A.B., van Spriel A.B. // *Trends Cell Biol.* 2021. V. 31. № 2. P. 119–129.
10. Raghunathan K., Kenworthy A.K. // *Biochim. Biophys. Acta Biomembr.* 2018. V. 1860. № 10. P. 2018–2031.
11. Sackmann E., Tanaka M. // *Biophys. Rev.* 2021. V. 13. № 1. P. 123–138.
12. Hristova K., Selsted M.E., White S.H. // *J. Biol. Chem.* 1997. V. 272. № 39. P. 24224–24233.
13. Zalba S., ten Hagen T.L.M. // *Cancer Treat. Rev.* 2017. V. 52. P. 48–57.
14. Szlasa W., Zendran I., Zalesińska A., Tarek M., Kulbacka J. // *J. Bioenerg. Biomembr.* 2020. V. 52. № 5. P. 321–342.
15. Karnovsky M.J., Kleinfeld A.M., Hoover R.L., Klausner R.D. // *J. Cell Biol.* 1982. V. 94. № 1. P. 1–6.
16. Owen D.M., Gaus K. // *Front. Plant Sci.* 2013. V. 4. <https://doi.org/10.3389/fpls.2013.00503>.
17. Ursell T.S., Klug W.S., Phillips R. // *Proc. Natl. Acad. Sci. USA*. 2009. V. 106. № 32. P. 13301–13306.
18. Feigenson G.W. // *Biochim. Biophys. Acta Biomembr.* 2009. V. 1788. № 1. P. 47–52.
19. Preta G. // *Front. Cell Dev. Biol.* 2020. V. 8. P. 1–10.
20. Jeon J.H., Kim S.K., Kim H.J., Chang J., Ahn C.M., Chang Y.S. // *Lung Cancer*. 2010. V. 69. № 2. P. 165–171. <http://dx.doi.org/10.1016/j.lungcan.2009.10.014>.
21. Svensson R.U., Shaw R.J. // *Cold Spring Harb. Symp. Quant. Biol.* 2016. V. 81. № 1. P. 93–103.
22. Munir R., Lisec J., Swinnen J.V., Zaidi N. // *Br. J. Cancer*. 2019. V. 120. № 12. P. 1090–1098. <http://dx.doi.org/10.1038/s41416-019-0451-4>.
23. Swinnen J.V., Brusselmans K., Verhoeven G. // *Curr. Opin. Clin. Nutr. Metab. Care*. 2006. V. 9. № 4. P. 358–365.
24. Hess D., Chisholm J.W., Igal R.A. // *PLoS One*. 2010. V. 5. № 6. <https://doi.org/10.1371/journal.pone.0011394>.
25. Du A., Wang Z., Huang T., Xue S., Jiang C., Qiu G., Yuan K. // *MedComm - Oncol*. 2023. V. 2. № 1. P. 1–22.
26. Gasymov O., Bakhishova M., Gasanova R., Aslanov R., Melikova L., Aliyev J. // *Russ. J. Biol. Phys. Chemisrty*. 2022. V. 7. № 2. P. 261–267.
27. Bakhisova M., Aslanov R.B., Gasanova R.B., Melikova L., Aliyev J.A., Gasymov O.K. // *Trans. ANAS, Phys. Astron.* 2022. V. 52. № 5. P. 56–63.
28. Guisasola E., Asín L., Beola L., De La Fuente J.M., Baeza A., Vallet-Regí M. // *ACS Appl. Mater. Interfaces*. 2018. V. 10. № 15. P. 12518–12525.
29. Kang J.K., Kim J.C., Shin Y., Han S.M., Won W.R., Her J., Park J.Y., Oh K.T. // *Arch. Pharm. Res.* 2020. V. 43. № 1. P. 46–57.
30. Anemone A., Consolino L., Arena F., Capozza M., Longo D.L. // *Cancer Metastasis Rev.* 2019. V. 38. № 1–2. P. 25–49.
31. Gatenby R.A., Gawlinski E.T., Gmitro A.F., Kaylor B., Gillies R.J. // *Cancer Res.* 2006. V. 66. № 10. P. 5216–5223.
32. Gillies R.J., Pilot C., Marunaka Y., Fais S. // *Biochim. Biophys. Acta - Rev. Cancer*. 2019. V. 1871. № 2. P. 273–280.
33. Gasanova R.B., Melikova L.A., Gasymov O.K., Aliyev J.A. // *Mod. Achiev. Azerbaijan Med.* 2020. № 4. P. 112–117.
34. Budil D.E., Sanghyuk L., Saxena S., Freed J.H. // *J. Magn. Reson. - Ser. A*. 1996. V. 120. № 2. P. 155–189.
35. Keith A., Bulfield G., Snipes W. // *Biophys. J.* 1970. V. 10. № 7. P. 618–629.
36. Wu S.H. wei, McConnell H.M. // *Biochemistry*. 1975. V. 14. № 4. P. 847–854.
37. Griffith O.H., Dehlinger P.J., Van S.P. // *J. Membr. Biol.* 1974. V. 15. № 1. P. 159–192.
38. Gillies R.J., Robey I., Gatenby R.A. // *J. Nucl. Med.* 2008. V. 49. № 6. P. 24–43. doi: 10.2967/jnumed.107.047258.
39. Tennant D.A., Durán R.V., Gottlieb E. // *Nat. Rev. Cancer*. 2010. V. 10. № 4. P. 267–277.
40. Webb B.A., Chimenti M., Jacobson M.P., Barber D.L. // *Nat. Rev. Cancer*. 2011. V. 11. № 9. P. 671–677.
41. Ribeiro Md.L.C., Silva A.S., Bailey K.M., Kumar N.B., Seller T.A., et al. // *J. Nutr. Food Sci.* 2012. V. 1. № S2. P. 1–7.
42. Soule B.P., Hyodo F., Matsumoto K.I., Simone N.L., Cook J.A., Krishna M.C., Mitchell J.B. // *Antioxidants Redox Signal.* 2007. V. 9. № 10. P. 1731–1743.
43. Lewandowski M., Gwozdziński K. // *Int. J. Mol. Sci.* 2017. V. 18. № 11. P. 2490.
44. Suy S., Mitchell J.B., Samuni A., Mueller S., Kasid U. // *Cancer*. 2005. V. 103. № 6. P. 1302–1313.
45. Park W.H. // *Molecules*. 2022. V. 27. № 21. P. 7341.
46. Andreidesz K., Szabo A., Kovacs D., Koszegi B., Vantus V.B., Vamos E., Isbera M., Kalai T., Bognar Z., Kovacs K., et al. // *Int. J. Mol. Sci.* 2021. V. 22. № 16. P. 1406.
47. Wang M., Li K., Zou Z., Li L., Zhu L., Wang Q., Gao W., Wang Y., Huang W., Liu R., et al. // *Oncol. Lett.* 2018. V. 16. № 4. P. 4847–4854.
48. Widomska J., Raguz M., Dillon J., Gaillard E.R., Subczynski W.K. // *Biochim. Biophys. Acta Biomembr.* 2007. V. 1768. № 6. P. 1454–1465.
49. Liu Y.Q., Ohkoshi E., Li L.H., Yang L., Lee K.H. // *Bioorganic Med. Chem. Lett.* 2012. V. 22. № 2. P. 920–923. <http://dx.doi.org/10.1016/j.bmcl.2011.12.024>.
50. Guo X., Seo J.-E., Bryce S.M., Tan J.A., Wu Q., Dial S.L., Moore M.M., Mei N. // *Toxicol. Sci.* 2018. V. 163. № 1. P. 214–225.
51. Gariboldi M.B., Lucchi S., Caserini C., Supino R., Oliiva C., Monti E. // *Free Radic. Biol. Med.* 1998. V. 24. № 6. P. 913–923.
52. Zhao X.-B., Wu D., Wang M.-J., Goto M., Morris-Natschke S.L., Liu Y.-Q., Wu X.-B., Song Z.-L., Zhu G.-X., Lee K.-H. // *Bioorg. Med. Chem.* 2014. V. 22. № 22. P. 6453–6458.
53. Kroll C., Langner A., Borchert H.H. // *Free Radic. Biol. Med.* 1999. V. 26. № 7–8. P. 850–857.
54. Kroll C., Borchert H.H. // *Eur. J. Pharm. Sci.* 1999. V. 8. № 1. P. 5–9.

GENERAL RULES

Acta Naturae publishes experimental articles and reviews, as well as articles on topical issues, short reviews, and reports on the subjects of basic and applied life sciences and biotechnology.

The journal *Acta Naturae* is on the list of the leading periodicals of the Higher Attestation Commission of the Russian Ministry of Education and Science. The journal *Acta Naturae* is indexed in PubMed, Web of Science, Scopus and RCSI databases.

The editors of *Acta Naturae* ask of the authors that they follow certain guidelines listed below. Articles which fail to conform to these guidelines will be rejected without review. The editors will not consider articles whose results have already been published or are being considered by other publications.

The maximum length of a review, together with tables and references, cannot exceed 50,000 characters with spaces (approximately 30 pages, A4 format, 1.5 spacing, Times New Roman font, size 12) and cannot contain more than 16 figures.

Experimental articles should not exceed 30,000 symbols (approximately 15 pages in A4 format, including tables and references). They should contain no more than ten figures.

A short report must include the study's rationale, experimental material, and conclusions. A short report should not exceed 12,000 symbols (5–6 pages in A4 format including no more than 12 references). It should contain no more than three figures.

The manuscript and all necessary files should be uploaded to www.actanaturae.ru:

- 1) text in Word 2003 for Windows format;
- 2) the figures in TIFF format;
- 3) the text of the article and figures in one pdf file;
- 4) the article's title, the names and initials of the authors, the full name of the organizations, the abstract, keywords, abbreviations, figure captions, and Russian references should be translated to English;
- 5) the cover letter stating that the submitted manuscript has not been published elsewhere and is not under consideration for publication;
- 6) the license agreement (the agreement form can be downloaded from the website www.actanaturae.ru).

MANUSCRIPT FORMATTING

The manuscript should be formatted in the following manner:

- Article title. Bold font. The title should not be too long or too short and must be informative. The title should not exceed 100 characters. It should reflect the major result, the essence, and uniqueness of the work, names and initials of the authors.
- The corresponding author, who will also be working with the proofs, should be marked with a footnote *.
- Full name of the scientific organization and its departmental affiliation. If there are two or more scientific organizations involved, they should be linked by digital superscripts with the authors' names. Abstract. The structure of the abstract should be

very clear and must reflect the following: it should introduce the reader to the main issue and describe the experimental approach, the possibility of practical use, and the possibility of further research in the field. The average length of an abstract is 20 lines (1,500 characters).

- Keywords (3 – 6). These should include the field of research, methods, experimental subject, and the specifics of the work. List of abbreviations.

• INTRODUCTION**• EXPERIMENTAL PROCEDURES****• RESULTS AND DISCUSSION****• CONCLUSION**

The organizations that funded the work should be listed at the end of this section with grant numbers in parenthesis.

• REFERENCES

The in-text references should be in brackets, such as [1].

RECOMMENDATIONS ON THE TYPING**AND FORMATTING OF THE TEXT**

- We recommend the use of Microsoft Word 2003 for Windows text editing software.
- The Times New Roman font should be used. Standard font size is 12.
- The space between the lines is 1.5.
- Using more than one whole space between words is not recommended.
- We do not accept articles with automatic referencing; automatic word hyphenation; or automatic prohibition of hyphenation, listing, automatic indentation, etc.
- We recommend that tables be created using Word software options (Table → Insert Table) or MS Excel. Tables that were created manually (using lots of spaces without boxes) cannot be accepted.
- Initials and last names should always be separated by a whole space; for example, A. A. Ivanov.
- Throughout the text, all dates should appear in the “day.month.year” format, for example 02.05.1991, 26.12.1874, etc.
- There should be no periods after the title of the article, the authors' names, headings and subheadings, figure captions, units (s – second, g – gram, min – minute, h – hour, d – day, deg – degree).
- Periods should be used after footnotes (including those in tables), table comments, abstracts, and abbreviations (mon. – months, y. – years, m. temp. – melting temperature); however, they should not be used in subscripted indexes (T_m – melting temperature; $T_{p,t}$ – temperature of phase transition). One exception is mln – million, which should be used without a period.
- Decimal numbers should always contain a period and not a comma (0.25 and not 0,25).
- The hyphen (“-”) is surrounded by two whole spaces, while the “minus,” “interval,” or “chemical bond” symbols do not require a space.
- The only symbol used for multiplication is “×”; the “x” symbol can only be used if it has a number to its

right. The “.” symbol is used for denoting complex compounds in chemical formulas and also noncovalent complexes (such as DNA·RNA, etc.).

- Formulas must use the letter of the Latin and Greek alphabets.
- Latin genera and species' names should be in italics, while the taxa of higher orders should be in regular font.
- Gene names (except for yeast genes) should be italicized, while names of proteins should be in regular font.
- Names of nucleotides (A, T, G, C, U), amino acids (Arg, Ile, Val, etc.), and phosphonucleotides (ATP, AMP, etc.) should be written with Latin letters in regular font.
- Numeration of bases in nucleic acids and amino acid residues should not be hyphenated (T34, Ala89).
- When choosing units of measurement, SI units are to be used.
- Molecular mass should be in Daltons (Da, KDa, MDa).
- The number of nucleotide pairs should be abbreviated (bp, kbp).
- The number of amino acids should be abbreviated to aa.
- Biochemical terms, such as the names of enzymes, should conform to IUPAC standards.
- The number of term and name abbreviations in the text should be kept to a minimum.
- Repeating the same data in the text, tables, and graphs is not allowed.

GUIDENESS FOR ILLUSTRATIONS

- Figures should be supplied in separate files. Only TIFF is accepted.
- Figures should have a resolution of no less than 300 dpi for color and half-tone images and no less than 600 dpi.
- Files should not have any additional layers.

REVIEW AND PREPARATION OF THE MANUSCRIPT FOR PRINT AND PUBLICATION

Articles are published on a first-come, first-served basis. The members of the editorial board have the right to recommend the expedited publishing of articles which are deemed to be a priority and have received good reviews.

Articles which have been received by the editorial board are assessed by the board members and then sent for external review, if needed. The choice of reviewers is up to the editorial board. The manuscript is sent on to reviewers who are experts in this field of research, and the editorial board makes its decisions based on the reviews of these experts. The article may be accepted as is, sent back for improvements, or rejected.

The editorial board can decide to reject an article if it does not conform to the guidelines set above.

The return of an article to the authors for improvement does not mean that the article has been accepted

for publication. After the revised text has been received, a decision is made by the editorial board. The author must return the improved text, together with the responses to all comments. The date of acceptance is the day on which the final version of the article was received by the publisher.

A revised manuscript must be sent back to the publisher a week after the authors have received the comments; if not, the article is considered a resubmission.

E-mail is used at all the stages of communication between the author, editors, publishers, and reviewers, so it is of vital importance that the authors monitor the address that they list in the article and inform the publisher of any changes in due time.

After the layout for the relevant issue of the journal is ready, the publisher sends out PDF files to the authors for a final review.

Changes other than simple corrections in the text, figures, or tables are not allowed at the final review stage. If this is necessary, the issue is resolved by the editorial board.

FORMAT OF REFERENCES

The journal uses a numeric reference system, which means that references are denoted as numbers in the text (in brackets) which refer to the number in the reference list.

For books: the last name and initials of the author, full title of the book, location of publisher, publisher, year in which the work was published, and the volume or issue and the number of pages in the book.

For periodicals: the last name and initials of the author, title of the journal, year in which the work was published, volume, issue, first and last page of the article. Must specify the name of the first 10 authors. Ross M.T., Grafham D.V., Coffey A.J., Scherer S., McLay K., Muzny D., Platzer M., Howell G.R., Burrows C., Bird C.P., et al. // Nature. 2005. V. 434. № 7031. P. 325–337.

References to books which have Russian translations should be accompanied with references to the original material listing the required data.

References to doctoral thesis abstracts must include the last name and initials of the author, the title of the thesis, the location in which the work was performed, and the year of completion.

References to patents must include the last names and initials of the authors, the type of the patent document (the author's rights or patent), the patent number, the name of the country that issued the document, the international invention classification index, and the year of patent issue.

The list of references should be on a separate page. The tables should be on a separate page, and figure captions should also be on a separate page.

The following e-mail addresses can be used to contact the editorial staff: actanaturae@gmail.com, tel.: (495) 727-38-60.